

Proceedings

15th International Workshop
on

Water Waves and Floating Bodies



27 February - 1 March 2000

DISTRIBUTION STATEMENT A
Approved for Public Release
Distribution Unlimited

Caesarea
Israel

20010430 046

Editors: T. Miloh & G. Zilman

REPORT DOCUMENTATION PAGE

Form Approved OMB No. 0704-0188

Public reporting burden for this collection of information is estimated to average 1 hour per response, including the time for reviewing instructions, searching existing data sources, gathering and maintaining the data needed, and completing and reviewing the collection of information. Send comments regarding this burden estimate or any other aspect of this collection of information, including suggestions for reducing this burden to Washington Headquarters Services, Directorate for Information Operations and Reports, 1215 Jefferson Davis Highway, Suite 1204, Arlington, VA 22202-4302, and to the Office of Management and Budget, Paperwork Reduction Project (0704-0188), Washington, DC 20503.

1. AGENCY USE ONLY (Leave blank)		2. REPORT DATE 2000		3. REPORT TYPE AND DATES COVERED Conference Proceeding	
4. TITLE AND SUBTITLE Proceedings. 15 th International Workshop on Water Waves and Floating Bodies. 17 February – 1 March, 2000, Caesarea, Israel.				5. FUNDING NUMBERS N00014-00-1-1006	
6. AUTHOR(S) T. Miloh & G. Zilman, Editors					
7. PERFORMING ORGANIZATION NAME(S) AND ADDRESS(ES) Tel-Aviv University Faculty of Engineering Israel 699 78				8. PERFORMING ORGANIZATION REPORT NUMBER ISBN 965-274-288-0	
9. SPONSORING/MONITORING AGENCY NAME(S) AND ADDRESS(ES) Office of Naval Research International Field Office PSC 802 Box 39 FPO AE 09499-0039				10. SPONSORING/MONITORING AGENCY REPORT NUMBER	
11. SUPPLEMENTARY NOTES This work relates to Department of Navy Grant N00014-00-1-1006 issued by the Office of Naval Research-Europe. The United States has a royalty free license throughout the world in all copyrightable material contained herein.					
12a. DISTRIBUTION/AVAILABILITY STATEMENT Approved for Public Release; Distribution Unlimited. Government Purpose Rights License. All other rights reserved by the copyright holders.				12b. DISTRIBUTION CODE A	
12. ABSTRACT (Maximum 200 words) A total of 49 extended abstracts are included in this volume of papers presented at the 15 th International Workshop on Water Waves and Floating Bodies, held 17 February – 1 March, 2000, Caesarea, Israel. Also see http://www.eng.tau.ac.il/~miloh/iwwwfb . The objective of the Workshop is to provide a forum for informal discussions of fundamental research, of mutual interest to both engineers and scientists, in the broad area of wave interactions with fixed, floating or submerged bodies.					
14. SUBJECT TERMS Waves, Nonlinear waves				15. NUMBER OF PAGES	
				16. PRICE CODE	
17. SECURITY CLASSIFICATION OF REPORT UNCLASSIFIED	18. SECURITY CLASSIFICATION OF THIS PAGE UNCLASSIFIED	19. SECURITY CLASSIFICATION OF ABSTRACT UNCLASSIFIED	20. LIMITATION OF ABSTRACT UL		

NSN 7540-01-280-5500

Standard Form 298 (Rev. 2-89)
Prescribed by ANSI Std. Z39-18
298-102

P r o c e e d i n g s
15th International Workshop
on
Water Waves and Floating Bodies



27 February – 1 March 2000

Dan Caesarea

ISRAEL

Edited by T. Miloh & G. Zilman

**Faculty of Engineering
Tel-Aviv University
ISRAEL 699 78**

AQ F01-07-1420

Preface

The 15th *International Workshop on Water Waves and Floating Bodies* (IWWWFB) was organized by Prof. Touvia Miloh, Assoc. Dean Faculty of Engineering, Tel-Aviv University. The Workshop was held in the Dan Caesarea Hotel, Caesarea, Israel from the 27th February to the 1st March, 2000.

A total of 49 abstracts were accepted for presentation. The abstracts were selected by a scientific committee consisting of T. Miloh and the organizers of the two previous workshops, Professors Robert Beck & William Schultz from the University of Michigan and Professor Aad Hermans of the Delft University of Technology. The following pages contain the extended abstracts. They are listed in alphabetical order of the first author's name. For the first time the abstracts of IWWWFB appear prior to the conference on the Web Site <http://www.eng.tau.ac.il/~miloh/iwwwfb>

The 15th IWWWFB was sponsored by:

Tel-Aviv University, Faculty of Engineering
Technion, Israel Institute of Technology
Minerva Center for Nonlinear Physics of Complex Systems
Henri Glasberg Extraordinary Chair for International Cooperation
Gordon Center for Energy Studies
Association of Engineers and Architects of Israel
Office of Naval Research Europe

T.M., Feb. 2000, Tel-Aviv

ISBN 965-274-288-0

Copyright © 2000. All rights reserved.

This work relates to Department of the Navy Grant N00014-00-1-1006 issued by the Office of Naval Research European Office. The United States has a royalty-free license throughout the world in all copyrightable material contained herein.

CONTENTS

Agnon, Y. and H.B. Bingham , <i>A Fourier-Boussinesq method for nonlinear wave propagation on a variable depth fluid</i>	1
Akylas, T.R. , <i>Supercritical wakes in stratified flows</i>	5
Ando, S. , <i>Wind waves and swells: probabilistic models for directions of propagation for moving ships</i>	8
Borthwick, A.G.L., M.S. Turnbull and R. Eatock Taylor , <i>Nonlinear wave loading using sigma- transformed and unstructured finite element meshing</i>	12
Brummelen, H. van and H. Raven , <i>Numerical solution of steady free-surface Navier-Stokes flow</i>	16
Cadby, J.R. and C.M. Linton , <i>Scattering of oblique waves in a two-layer fluid</i>	20
Chen, X.-B. , <i>Peculiar properties of ship-motion Green functions in water of finite depth.</i>	24
Clamond, D. and J. Grue , <i>Dynamics of the transient leading part of a wave train</i>	28
Daalen, E.F.G. van, J. Gerrits, G.E. Loots and A.E.P. Veldman , <i>Free surface anti-roll tank simulations with a volume of fluid based Navier-Stokes solver</i>	32
Dingemans, M.W. and A.C. Radder , <i>The use of the CL-equation as a model for secondary circulations</i>	36
Doctors, L.J. and A.H. Day , <i>The squat of a vessel with a transom stern</i>	40
Drimer, N., M. Glozman, M. Stiassnie and G. Zilman , <i>Forecasting the motion of berthed ships in harbors</i>	44
Evans, D.V. and B.J. Shipway , <i>A continuum model for multi-column structures in waves</i>	47
Fontaine, E., M. Landrini and M.P. Tulin , <i>On modeling the post breaking phase: splashing</i>	51
Greco, M., O. Faltinsen and M. Landrini , <i>An investigation of water on deck phenomena</i>	55
Grilli, S., P. Guyenne and F. Dias , <i>Numerical computation of three-dimensional overturning waves</i>	59
Grue, J., A. Jensen, P.-O. Rusås and J.K. Sveen , <i>Solitary waves in stratified fluid: modelling and experiments</i>	63
Gueret, R. and A.J. Hermans , <i>Behavior of a ship with elastic distortions in periodic waves</i>	67
Hamilton, J.A. and R.W. Yeung , <i>Non-linear motion of a submerged body in waves</i>	71

Huseby, M., A. Jensen and J. Grue, <i>An experimental investigation of ringing loads on a vertical cylinder in transient waves</i>	75
Iafrati, A. and A. Korobkin, <i>Liquid flow close to intersection point</i>	79
Indeitsev, D. and Yu. Mochalova, <i>Trapped modes above a die oscillating on the bottom of a wave channel</i>	83
Iwashita, H., <i>On unsteady waves generated by a blunt ship with forward speed</i>	87
Jiang, T. and R. Henn, <i>Nonlinear waves generated by a surface-piercing body using a unified shallow-water theory</i>	91
Judge, C. and A. Troesch, <i>Asymmetry and horizontal velocity during water impact</i>	95
Kashiwagi, M., <i>Wave interactions with a multitude of floating cylinders</i>	99
Kim, Y., <i>Numerical analysis of sloshing problem</i>	103
Kimmoun, O. and C. Kharif, <i>On the behaviour of steep short-crested waves in deep water and their effects on structures</i>	107
Landrini, M. and P.A. Tyvand, <i>Impulsive free-surface flow due to a steady line source at the bottom of a uniform fluid layer</i>	110
Lin, H.J. and M. Perlin, <i>The velocity and vorticity fields beneath gravity-capillary waves exhibiting parasitic ripples</i>	114
Malenica, Š. and M. Zalar, <i>An alternative method for linear hydrodynamics of air cushion supported floating bodies</i>	118
Molin, B., <i>On the sloshing modes in moonpools, or the dispersion equation for progressive waves in a channel through the ice sheet</i>	122
Mori, K. and S. Nagaya, <i>Wave making resistance of a submerged hydrofoil with downward force</i>	126
Newman, J.N., <i>Diffraction of water waves by an air chamber</i>	130
Noblesse, F., C. Yang, and D. Hendrix, <i>Steady free-surface potential flow due to a point source</i>	134
Ohkusu, M., <i>Analysis of wave force on a large and thin floating platform</i>	138
Pelinovsky, E. and C. Kharif, <i>Simplified model of the freak wave formation from the random wave field</i>	142
Peng, W. and D.H. Peregrine, <i>Pressure-impulse theory for plate impact on water surface</i>	146
Peregrine, D.H. and M. Brocchini, <i>An instantaneous measure of the strength of a breaker: "foot and toes"</i>	150

Retzler, C.H., J.R. Chaplin and R.C.T. Rainey, <i>Transient motion of a vertical cylinder: measurements and computations of the free surface</i>	154
Rognebakke, O.F. and O.M. Faltinsen, <i>Damping of sloshing due to tank roof impact</i>	158
Scolan, Y.-M. and A. A. Korobkin, <i>Design of three-dimensional bodies subject to water impact</i>	162
Shemer, L., Haiying Jiao and E. Kit, <i>Nonlinear wave group evolution in deep and intermediate-depth water: experiments and numerical simulations</i>	166
Subramani, A.K. and R.F. Beck, <i>Suppression of wave breaking in nonlinear water wave computations including forward speed</i>	170
Tuck, E.O., <i>Numerical solution for unsteady two-dimensional free-surface flows</i>	174
Ursell, F., <i>The metacentre in the stability of ships. Some difficulties</i>	178
Vanden-Broeck, J.-M. and B. Spivak, <i>Free-surface wave damping due to viscosity and surfactants</i>	181
Westhuis, J. H., E. van Groesen and R. Huijsmans, <i>Long time evolution of unstable bichromatic waves</i>	184
Wu, G.X., <i>Initial pressure distribution over a wavemaker after an impulsive motion</i>	188
Wu, G., Y. Liu and D.K.P. Yue, <i>Numerical reconstruction of nonlinear irregular wave-field using single or multiple probe data</i>	191
Zhang, J., M. McIver, P. McIver and C.M. Linton, <i>Embedded trapped modes for arrays of cylinders</i>	195

The cover images are taken from the abstract by C.H. Retzler, J.R. Chaplin & C.T. Rainey, pp.154-157.

A Fourier-Boussinesq method for nonlinear wave propagation on a variable depth fluid

Y. Agnon* and H. B. Bingham†

This abstract describes a new Boussinesq-type model which overcomes the restriction to small values of kh which is inherent in traditional Boussinesq methods ($k = |\vec{k}|$ the wavenumber and h the water depth.) The term Boussinesq-type model is used here in a broad sense to describe a two-dimensional approximation to the exact potential flow problem, where the vertical coordinate has been eliminated from the formulation. This elimination is done, without approximation, by representing the solution as an infinite power series in z . The way in which this series is truncated (as well as the particular choice of velocity variable) determines the final form of the Boussinesq-type model. Traditional Boussinesq methods obtain approximate linear dispersion relations (expressed in terms of non-dimensional wave celerity $\frac{c^2}{gh} = \frac{\omega^2}{k^2 gh} = \frac{\tanh kh}{kh}$) which are rational functions of $(kh)^2$. The exact relation is however transcendental, and tends to $\frac{1}{kh}$ as $kh \rightarrow \infty$, which can not be matched asymptotically by a function of $(kh)^2$. By introducing the FFT, and thus allowing a fast evaluation of the Hilbert transform, algebraic approximations to the dispersion relation which are asymptotically correct in both limits of kh can be investigated.

Following [5] (and others) we consider weakly nonlinear solutions to the exact Laplace problem by expressing the free-surface boundary conditions in terms of the potential at the free-surface,

$$\begin{aligned}\eta_t &= (1 + \nabla \eta \cdot \nabla \eta) \tilde{\phi}_z - \nabla \tilde{\phi} \cdot \nabla \eta \\ \tilde{\phi}_t &= -g\eta - \frac{1}{2}(\nabla \tilde{\phi})^2 - \frac{1}{2}(1 + \nabla \eta \cdot \nabla \eta) \tilde{\phi}_z^2\end{aligned}\quad (1)$$

where $\nabla = (\frac{\partial}{\partial x}, \frac{\partial}{\partial y})$ and $\tilde{\phi} = \phi(\vec{x}, \eta, t)$. The surface potential is then expressed as a perturbation expansion in the wave slope ϵ , and each perturbation potential is Taylor expanded from $z = 0$ to $z = \eta$. Thus,

$$\tilde{\phi} = \sum_{m=1}^M \sum_{k=0}^{M-m} \frac{\eta^k}{k!} \frac{\partial}{\partial z} \hat{\phi}^{(m)} \quad (2)$$

where $\hat{\phi} = \phi(\vec{x}, 0, t)$. Expressed in this form, the closure which allows us to step forward in time is a relation for the vertical component of velocity w , in terms of the horizontal component of velocity \vec{u} , where both quantities are evaluated on $z = 0$. This relationship must naturally satisfy the Laplace equation and the bottom boundary condition

$$\phi_z + \nabla \phi \cdot \nabla h = 0 \quad z = -h, \quad (3)$$

in which case the problem is solved. To be attractive computationally, the method should be of order N the number of unknowns on the free-surface.

Consider first a flat bottom. If the solution is expanded in a Taylor series about $z=0$, and the Laplace equation is invoked then

$$\phi(\vec{x}, z, t) = \sum_{n=0}^{\infty} (-1)^n \left(\frac{z^{2n}}{2n!} \nabla^{2n} \hat{\phi} + \frac{z^{2n+1}}{(2n+1)!} \nabla^{2n} w \right). \quad (4)$$

The bottom boundary condition may now be expressed as

$$\text{Cos}(h \nabla) w + \text{Sin}(h \nabla) \vec{u} = 0 \quad (5)$$

*Technion, Haifa, Israel, agnon@cameri2.technion.ac.il

†Danish Technical U., Lyngby, Denmark, hbb@imm.dtu.dk

where the Sin and Cos Taylor series operators are defined by

$$\begin{aligned}\text{Sin}(L \nabla) &= L \nabla - \frac{L^3 \nabla^3}{6} + \frac{L^5 \nabla^5}{120} + \dots \\ \text{Cos}(L \nabla) &= 1 - \frac{L^2 \nabla^2}{2} + \frac{L^4 \nabla^4}{24} + \dots\end{aligned}\quad (6)$$

and ∇ is understood as the gradient when applied to a scalar and the divergence when applied to a vector. If the operators in Equation (6) are truncated, and replaced by finite-difference operators, the result is a sparse matrix equation for w in terms of \vec{u} . This corresponds to a classical Boussinesq method. Imbedded in Equation (5) is the linear dispersion relation. To see this note that in the frequency domain the operator $\nabla = ik$ (in one horizontal dimension), so we can write $W = -\text{Tan}(h\nabla)U = -i\text{Tanh}(kh)\vec{U}$, where U, W are the frequency-domain velocity components and the Tan and Tanh operators are defined in the way of Equation (6). The linear free-surface boundary condition says that $g\nabla w = -\vec{u}_{tt}$ or $W = \frac{\omega^2}{igk}U$. Combining these two expressions gives the exact linear dispersion relation $\omega^2 = gk \tanh(kh)$. Thus a classical Boussinesq method can be thought of coming from the equation

$$W = \frac{\text{Tanh}(\vec{k}h)}{\vec{k}h} i h \vec{k} \cdot \vec{U}, \quad (7)$$

where $\text{Tanh}(\vec{k}h)/\vec{k}h$ is approximated by truncated Taylor series expansion of $\text{Sinh}\vec{k}h$ and $\text{Cosh}\vec{k}h$, and $i h \vec{k}$ is associated with $h\nabla$ to get a method in physical space. Such classical methods unfortunately diverge beyond $kh = \pi/2$ due to the first singularity of \tanh on the imaginary axis. This problem can however be avoided by replacing the Taylor expansions by Padé expansions, resulting in modified (or enhanced) Boussinesq methods. For example, the Padé(4,4) expansion of $\text{Tanh}(\vec{k}h)/\vec{k}h$ is

$$\frac{1 + \frac{1}{9}\kappa^2 + \frac{1}{945}\kappa^4}{1 + \frac{4}{9}\kappa^2 + \frac{1}{63}\kappa^4}$$

where $\kappa = \vec{k}h$, which leads to a very accurate method out to $kh = 6$ (see [3].)

Here we go one step further by introducing the Hilbert transform operator H , which is most conveniently written in Fourier space as $\mathcal{F}\{H\phi\} = -i\mathcal{F}\{\phi\}$ where \mathcal{F} indicates a Fourier transform. (The operator applies a 90° phase shift in Fourier space.) This allows even powers of κ to appear in the rational approximation for $\tanh \kappa/\kappa$. The trick is to use the identity

$$\tanh(\kappa) \equiv \frac{p_1}{1 + p_1}, \quad p_1 = \frac{\sinh(\kappa)}{\cosh(\kappa) - \sinh(\kappa)}. \quad (8)$$

By taking a Padé(m, n) expansion of p_1 with $n < m$ the correct asymptotics are obtained for both limits of κ . Figure 1 shows the relative error in linear dispersion for a Padé(4,1) and a Padé(8,2) approximation of p_1 . The specific methods obtained in these two cases are:

$$(15 + 9\kappa + 9\kappa^2 + 4\kappa^3 + \kappa^4)W = -(15 + 9\kappa + 4\kappa^2 + \kappa^3)i h \vec{k} \cdot \vec{U} \quad (9)$$

and

$$\begin{aligned}(14175 + 8505\kappa + 9135\kappa^2 + 4410\kappa^3 + 1575\kappa^4 + 420\kappa^5 + 84\kappa^6 + 12\kappa^7 + \kappa^8)W \\ = -(14175 + 8505\kappa + 4410\kappa^2 + 1575\kappa^3 + 420\kappa^4 + 84\kappa^5 + 12\kappa^6 + \kappa^7)i h \vec{k} \cdot \vec{U}\end{aligned}\quad (10)$$

respectively, where the corresponding differential equation is obtained by associating $h i \vec{k}$ with $h\nabla$ and $-i$ with H . The agreement with the exact linear dispersion relation for all wavenumbers is remarkable.

In order to create a method which is easily implemented, it is desirable perform some further manipulation. Since the left hand sides of Equations (9) and (10) represent the implicit part of

the solution, it is convenient to convert these polynomials into ones with only even powers of kh . (When odd powers are retained, the solution must be obtained iteratively.) It turns out that any polynomial $f(x)$ can be written with only even powers by multiplying it with $f(-x)$. Multiplying both sides of the equation by this polynomial produces an explicit matrix equation for w in terms of \tilde{u} , at the cost of doubling the highest order of the derivative which must be calculated. Note also that if $\kappa = \kappa_1$ is a root of the original polynomial, then both κ_1 and $-\kappa_1$ are roots of the new polynomial; so to get a stable method, the original polynomial must have no real roots. The odd powers of κ which remain in the numerator are evaluated by taking horizontal derivatives of $\nabla H \tilde{u}$ which is found using the FFT.

Our first application of the method is to the infinite depth, non linear standing wave solution of [4]. Figure 2 shows the wave elevation at the center of the tank as a function of time, calculated using the Padé(8,2) method. 65 points have been used on the free-surface and 40 points per wave period, while the non linearity retained in the free-surface boundary condition corresponds to $M = 5$ in Equation (2). After 25 periods the mass has been conserved to within 2×10^{-7} and energy to within 4×10^{-5} of the initial conditions. This is a periodic solution, and therefore well suited to a method which incorporates the FFT. In order to treat non-periodic problems, we apply the method presented in [2]. The idea is to split the solution into two potentials, one of which is known analytically (or solved by another method), while the other is found by the above described technique. The known potential corresponds to a flux into or out of the domain and can represent a wave maker or absorber for example. This solution can be any appropriate solution to the Laplace equation and the bottom boundary condition, as long as the sum of the two potentials satisfies the the free-surface boundary conditions.

When the bottom slope is retained in the bottom boundary condition, it takes the form

$$\text{Cos}(h \nabla) w_0 + \text{Sin}(h \nabla) \cdot \tilde{u}_0 + \nabla h \cdot [\text{Cos}(h \nabla) \cdot \tilde{u}_0 - \text{Sin}(h \nabla) w_0] = 0. \quad (11)$$

In this case, derivation of the approximate equation is more involved. When multiplying powers of $h \nabla$, terms involving ∇h , $(\nabla h)^2$, $\nabla^2 h$ etc. arise. Since h is variable, ∇ and h do not commute, and their ordering affects the product. The details will appear in a future publication [1]. We present however some preliminary calculations. Figure 3 shows a wave with period $T = 8$ s shoaling up a sloping beach as computed by the Padé(8,2) method using the linear free-surface boundary conditions. Also shown is the amplitude envelope predicted by linear theory, and the depth variation.

References

- [1] Agnon, Y. and Bingham, H. B. A Boussinesq type model for fully dispersive water waves. *In preparation*.
- [2] Agnon, Y. and Bingham, H. B. A non-periodic spectral method with application to nonlinear water waves. in *European J. Mech. B/Fluids* **18:3** 527–534, 1999.
- [3] Agnon, Y., Madsen, P. A. and Schäffer, H. A. A new approach to high order Boussinesq models. in *Journal of Fluid Mechanics* **399** 319–333. 1999
- [4] Agnon, Y. and Glozman, M. Periodic solutions for a complex Hamiltonian system: New standing water waves. in *Wave Motion* **24** 139–150, 1996.
- [5] Dommermuth, D. and Yue, D. K. P. A high-order spectral method for the study of nonlinear gravity waves. in *J. Fluid Mech.* **184** 267–288, 1987.

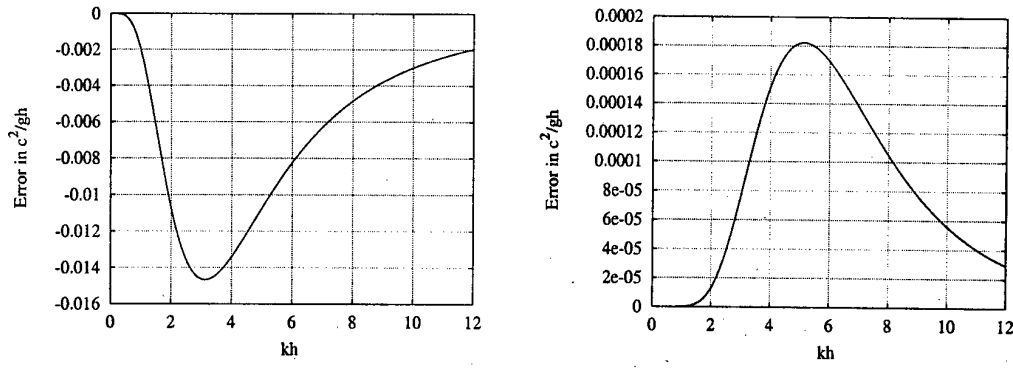


Figure 1: Relative errors in dispersion for Fourier-Boussinesq Padé(4,1) and Padé(8,2) methods.

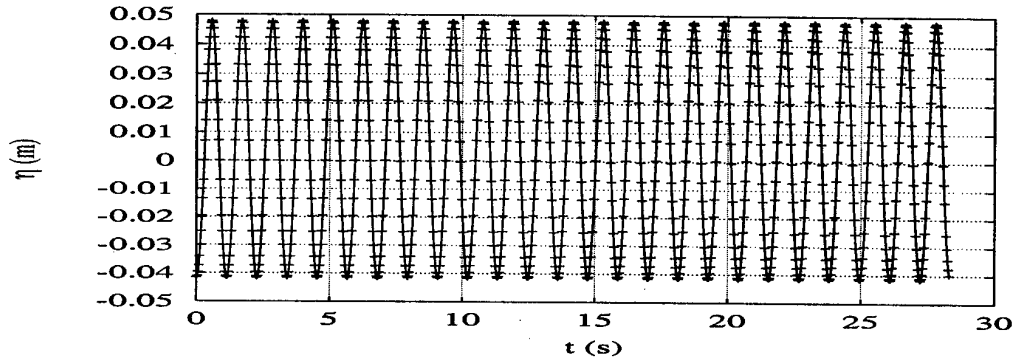


Figure 2: Time history of the elevation at the center of the tank with a non linear standing wave as the initial condition.

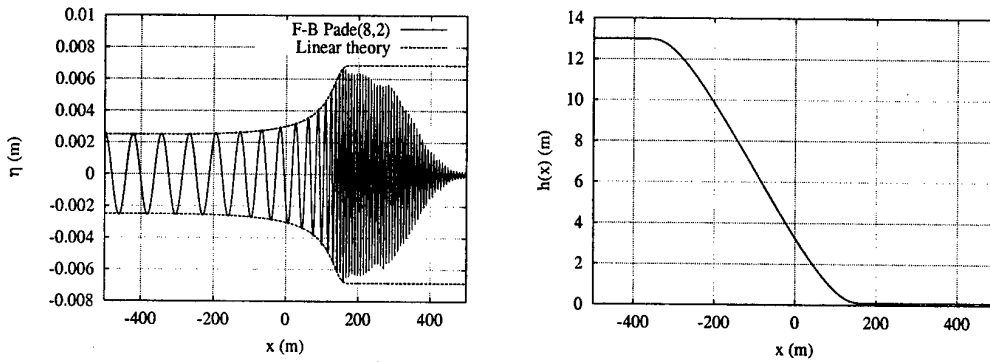


Figure 3: Linear shoaling for a wave of period $T = 8$ s over the bottom shown. A wavemaker generates the waves from the left boundary and a sponge layer absorbs them at the right boundary.

SUPERCritical WAKES IN STRATIFIED FLOWS

T. R. AKYLAS

Department of Mechanical Engineering, Massachusetts Institute of Technology, Cambridge, MA 02139, USA

1 Introduction

According to the linear hydrostatic equations of motion, supercritical free-surface flow (Froude number $F > 1$) past a locally confined obstacle gives rise to two oblique wavetrains, oriented at an angle $\cot^{-1}(F^2 - 1)^{1/2}$ to the flow direction, that form a wake downstream, and these theoretical predictions have been confirmed experimentally (see, for example, Baines [1] §2.2). We shall be concerned with analogous phenomena in stratified flow over locally confined topography that have been observed in satellite photographs of atmospheric internal-wave patterns generated by isolated islands (Gjevik & Marthinsen [2]).

In the context of stratified flow, under certain conditions, it is possible to set up a finite-amplitude theory that allows one to examine the role that nonlinear effects in the flow over the topography may play in generating supercritical wakes downstream. More specifically, when the topography is more elongated in the spanwise than in the streamwise direction, the nonlinear three-dimensional (3-D) equations of motion can be handled via a matched-asymptotics procedure. Three specific flow configurations are discussed in detail: (a) nonresonant flow of general (stable) stratification over finite-amplitude topography in a channel of finite depth; (b) resonant, uniformly stratified flow in a channel of finite depth; and (c) vertically unbounded, uniformly stratified flow over finite-amplitude topography. In all three cases, supercritical wakes are found downstream, but in (b) and (c) these wakes are induced by nonlinear interactions precipitated by 3-D effects in the flow over the topography, and are significantly stronger than their linear counterparts.

2 Formulation

We shall be concerned with steady, inviscid, incompressible, stratified flow. It is convenient to work with the streamfunctions Ψ , Φ :

$$\mathbf{u} = \nabla\Phi \times \nabla\Psi, \quad (1)$$

and take $\rho = \rho(\Psi)$ so that incompressibility and mass conservation are automatically satisfied. Furthermore, assuming that the flow starts from rest, one may show, using the circulation theorem, that the vorticity, $\boldsymbol{\omega} = \nabla \times \mathbf{u}$, lies in surfaces of constant ρ so that

$$\boldsymbol{\omega} \cdot \nabla\Psi = 0. \quad (2)$$

On the hypothesis of no upstream influence, the flow is undisturbed far upstream ($x \rightarrow -\infty$):

$$\Psi \sim U_0 z, \quad \Phi \sim y, \quad \rho \sim \rho_0(z) \quad (x \rightarrow -\infty),$$

U_0 and $\rho_0(z)$ being the background flow speed and density profile, respectively. Hence, $\rho = \rho_0(\Psi/U_0)$ and, making use of (2), the momentum equation implies that

$$\boldsymbol{\omega} \cdot \nabla\Phi = \frac{1}{\rho} \frac{d\rho}{d\Psi} \left\{ \frac{1}{2} U_0^2 - \frac{1}{2} \mathbf{u}^2 + \frac{g}{U_0} (\Psi - U_0 z) \right\}. \quad (3)$$

Having solved for the density ρ in terms of Ψ , and since $\boldsymbol{\omega} = \nabla \times \nabla\Phi \times \nabla\Psi$, equations (2) and (3) may now be viewed as two equations for determining Ψ and Φ and thereby the velocity field via

(1). This equation set is intractable, however, and, to make further analytical progress, we shall focus on long, weakly 3-D disturbances in a Boussinesq fluid:

$$\mu = \frac{H}{L}, \quad \alpha = \frac{L}{D}, \quad \beta = \frac{HN_0^2}{g} \rightarrow 0,$$

where N_0 is a characteristic Brunt–Väisälä frequency, H is a vertical lengthscale and L, D are the topography lengthscales in the streamwise (x -) and spanwise (y -) direction, respectively. On the other hand, the nonlinear parameter, $\epsilon = h/H$, h being the topography amplitude, is not assumed to be small.

Making variables dimensionless using L as the characteristic horizontal lengthscale, H as the characteristic vertical lengthscale and U_0 as the velocity scale, and after the re-scaling

$$\Psi = z + \psi(x, Y, z), \quad \Phi = y + \alpha\phi(x, Y, z),$$

the governing equations (2) and (3) become

$$\Psi_{zz} + \frac{N^2(\Psi)}{F^2} (\Psi - z) = O(\alpha^2, \mu^2), \quad (4)$$

$$J(v, \Psi) = \Psi_z \Psi_{zY} - \Psi_Y \Psi_{zz} + O(\alpha^2, \mu^2), \quad (5)$$

where $F = U_0/(N_0 H)$ is the Froude number, $Y = \alpha y$ is a stretched spanwise coordinate, and

$$v = J(\Psi, \phi)$$

is the spanwise velocity component, $J(a, b) = a_x b_z - a_z b_x$ being the Jacobian.

Based on (4) and (5), one may devise a perturbation solution scheme: first, the leading-order approximation to Ψ , $\Psi^{(0)} = z + \psi^{(0)}$ say, can be readily obtained by solving (4) subject to appropriate boundary conditions on the topography and the upper boundary of the flow. The spanwise velocity component, $v^{(0)}$, then follows from (5) by integrating along x on surfaces of constant $\Psi^{(0)}$:

$$v^{(0)} = \frac{\partial}{\partial Y} \int^x dx' \psi_z^{(0)} \Big|_{\Psi^{(0)}}.$$

This perturbation expansion becomes nonuniform, however, far upstream and downstream of the topography. It turns out that the far-field disturbance is weakly nonlinear but not weakly 3-D, invalidating the scalings chosen earlier, and it is governed by the linear 3-D hydrostatic equations to leading order. To fully determine the flow field, it is necessary to match the nonlinear, weakly 3-D disturbance over the topography with the weakly nonlinear, 3-D far-field response.

3 Summary of Results

The matching procedure indicated above was carried out for three particular flow configurations. Specifically,

(a) Non-resonant flow over finite-amplitude topography in channel of finite depth. In this instance, there is an infinity of long-wave modes and it is assumed that F is not close to any of the critical Froude numbers:

$$\dots < F_M < F < F_{M-1} < F_{M-2} < \dots < F_1.$$

The downstream response consists of an infinite number ($n \geq M$) oblique wavetrains, each oriented at angle $\tan^{-1}(F_n/\sqrt{F^2 - F_n^2})$ to the flow direction, forming multiple supercritical wakes. The amplitudes of these wakes are not affected seriously by nonlinearity in the near-field flow. On the other hand, 3-D effects inhibit breaking of the flow over the topography, increasing the critical steepness for overturning by $O(\alpha)$.

(b) Uniformly stratified, resonant flow in a channel of finite depth. When the flow speed is close to the speed of one of the long-wave modes,

$$F \approx F_M ,$$

the flow is resonant. Furthermore, when the flow is uniformly stratified, small-amplitude topography induces a finite-amplitude response under resonance conditions [3]. Qualitatively, the geometry of the wakes generated downstream is similar to those found in the non-resonant case. The generation mechanism, however, is quite different here: nonlinear interactions in the flow over the topography play an important part, and the amplitudes of the downstream wakes are much stronger than their linear counterparts (by a factor of $O(\alpha^{-2})$).

(c) Vertically unbounded, uniformly stratified flow. Here the flow may be regarded as resonant for all flow speeds because the spectrum of long-wave modes is continuous. Furthermore, according to linear theory, the 3-D wave pattern induced by locally confined topography remains locally confined. We find that, owing to the same nonlinear mechanism as in (b) above, multiple wakes are generated downstream so, in contrast to linear theory, the nonlinear wave pattern is not locally confined. The wake angles are given by $\tan^{-1}(1/\sqrt{n^2 - 1})$ ($n \geq 2$).

References

- [1] Baines, P. G. *Topographic Effects in Stratified Flows*. Cambridge University Press, 1995.
- [2] Gjevik, B. J. and Marthinsen, T. Three-dimensional lee-wave pattern. *Quart. J. Roy. Met. Soc.*, **104**, 947–957, 1978.
- [3] Grimshaw, R. H. J. and Yi, Z. Resonant generation of finite-amplitude waves by the flow of a uniformly stratified fluid over topography. *J. Fluid Mech.*, **229**, 603–628, 1991.

WIND WAVES AND SWELLS: PROBABILISTIC MODELS FOR DIRECTIONS OF PROPAGATION FOR MOVING SHIPS

Samon Ando

Defence Research Establishment Atlantic, P.O. Box 1012, Dartmouth, NS B2Y 3Z7, Canada

Barber and Ursell (1948) measured frequency spectra of ocean waves in order to develop a reliable method of predicting amplitude and period of wind waves and swell from meteorological charts and forecasts. The stroboscopic view of the sea state offered by the series of measured wave spectra at two locations off the east coast of England in their paper provide some useful insights. First, the waves will grow and decay with time at any particular point on the ocean surface. Secondly, the ocean surface is usually covered simultaneously by many wave systems of different nature, but often, predominant systems can be categorized as wind waves and swells. (Wind waves, or a sea, are generated by the wind blowing over a local area of the observer. The swell is generated in a distant storm. So, in general, swell travels in a direction different from that of sea.) Thirdly, the waves are likely to be different at different points on the ocean surface at any time.

So the sea states encountered by a moving ship are constantly changing. Classification societies and navies are concerned about how best to incorporate this fact into the design codes for ships. Researchers, mainly oceanographers, have addressed the question of how the energy of ocean waves is distributed with respect to direction of propagation. For stationary offshore structures, the directional spectrum can be measured at the site. But they have not developed a model that takes into account the relative direction of co-existing sea and swell for moving ships. Such a model is needed to better represent the attributes of a combination of local sea and swell in design wave spectra for ships. The reason is that a ship's behavior in waves is just as sensitive to the direction of oncoming waves relative to the ship's heading as to wave amplitude and period. This paper aims at probability-based characterization of the directions of propagation of sea and swell as encountered by ships operating at sea. Here the direction of sea is assumed to be that of locally-blowing wind. The probability models such as described in this paper are a necessary link between theoretical wave mechanics and practical naval architecture.

Let $\bar{\theta}_w$ and $\bar{\theta}_s$ denote the predominant directions of propagation of wind waves and swell, respectively. We wish to find the conditional probability of $\bar{\theta}_s$, given $\bar{\theta}_w$. Here, we examine a closely equivalent problem of establishing a probability law of the relative angle, say β , of propagation of swell to that of wind wave, where $\beta = \bar{\theta}_s - \bar{\theta}_w$. Questions arise: Can any or all of $\bar{\theta}_w$, $\bar{\theta}_s$, and β be considered random variables taking a value between 0 and 2π ? Are the random variables $\bar{\theta}_w$ and $\bar{\theta}_s$ statistically independent of each other? This second question is important because the answer in affirmative represents an enormous simplification of the probabilistic formulation of the problem.

At the moment, the only way to answer these questions is to collect data. This was one of the motivations for us to start compiling the data on winds and waves, among other things, recorded in the logs of Canadian Navy ships. This work is currently in progress [Ando (1999)], but what we have collected so far offers some glimpses of the answers we seek. In this paper, I present some of the results. The data come from the ship logs recorded at every four hours by two Canadian warships over a seven-year period (1969-75) while operating in the areas between North America and Europe, including the North Sea and the Mediterranean. The two ships belonged to different operational groups, and operated separately both spatially and temporally during the period. It may be pertinent to note that warships of the Canadian Navy typically spend 30 percent of their lives at sea.

Figure 1 shows the scatter diagrams of heights of swell and sea. Notice wide ranges of one variable for a given value of the other. For example, when sea is 5-ft high, swell ranges from 2 ft to 16 ft in Fig. 1a and from 2 ft to 15 ft in Fig. 1b. When swell is 5-ft high, sea ranges from 0 ft to 7 ft in Fig. 1a, and 0 ft to 35 ft in Fig. 1b. It is exactly for this kind of situation where low- and high-frequency waves co-exist that the bimodal wave spectrum of the Ochi-Hubble model is designed.

Figure 2 shows the relative frequencies of $\bar{\theta}_w$ and $\bar{\theta}_s$ (0 deg for wind blowing from due north). The data points in Fig. 1 with zero waveheight are discarded in Fig. 2. The chi-square test suggests that the hypothesis of uniform distribution of $\bar{\theta}_w$ and $\bar{\theta}_s$ between 0 and 2π must be rejected.

Figure 3 shows the relative frequencies of incremental changes, $\bar{\theta}_{w_i} - \bar{\theta}_{w_{i-1}}$ and $\bar{\theta}_{s_i} - \bar{\theta}_{s_{i-1}}$, of the directions of propagation of wind waves and swell between two consecutive observations. The data in this study are indexed in the order of observation. The observations were made every four hours (at the end of a watch) while the ships were steaming during a sortie. The set of observations from one sortie is appended to that from the preceding sortie. The elapsed time between sorties varied from days to months. Figure 3a shows a strong tendency of wind and swell to persist even after four hours. This is somewhat surprising, particularly for seas. For, as Barber and Ursell (1948) conclude, an optimum duration for recording sea states is between 17 and 45 minutes, and in general, the short-term sea spectra are expected to hold for less than two hours. Thus the four-hour period between successive observations in ship logs would be long compared with the memory time of sea states and so each point would be independent of the previous history. In contrast, the degree of persistence is considerably less in Fig. 3b than Fig. 3a. This difference is significant and the cause(s) must be investigated.

Figures 4a and 4b shows the scatter plots of $\bar{\theta}_w$ and $\bar{\theta}_s$ as observed by the two ships. They show surprisingly high degrees of linear correlation (coefficient of correlation between $\bar{\theta}_w$ and $\bar{\theta}_s$ is 0.649 and 0.575 for Figs. 4a and 4b, respectively).

The histograms in Fig. 5 show the distribution of β . They are roughly bell-shaped but highly peaked (coefficient of kurtosis is 3.54 for Fig. 5a and 2.63 for Fig. 5b). The only distribution that fits this condition is the Cauchy distribution,

$$f(x) = \frac{1}{\pi} \frac{c}{c^2 + (x - \mu)^2}, \quad \text{for } -\infty \leq x \leq \infty, \quad (1)$$

where the constant $c > 0$ is a scale parameter, which controls the shape of the probability density, and the parameter μ locates its center of symmetry. Here the sample space of the random variable is limited, $\beta \in [-\pi, \pi]$, so we need to use the conditional distribution within that space, or the truncated distribution [Ochi (1990)] such that:

$$f_*(\beta) = \frac{f(\beta)}{\int_{-\pi}^{\pi} f(\beta) d\beta}, \quad \text{for } -\pi \leq \beta \leq \pi, \quad (2)$$

$$= 0, \quad \text{otherwise,}$$

where f is given by (1). The curves in Figs. 5a and 5b show the truncated Cauchy distribution (2) with $c = 0.32$ and 0.36 respectively, and $\mu = 0$ for both, for sample space of $[-\pi, \pi]$. The same probability law agrees well with the actual distributions for both ships, even though the probability laws for the increments for sea and swell, $\bar{\theta}_{w_i} - \bar{\theta}_{w_{i-1}}$ and $\bar{\theta}_{s_i} - \bar{\theta}_{s_{i-1}}$, differ significantly between the two ships, as seen in Fig. 3. This may be construed as an indication of the ergodicity of the process represented by the set $\{\beta_i\}$. Note that although the process represented by the set $\{\beta_i\}$ is rapidly varying and highly irregular in the time scale on which observations were made, it fails to be a Brownian motion process (or Wiener process), since, for one thing, it does not possess independent increments; see, e.g. Parzen (1962).

So far in this work, $\{\beta_i\}$ has been treated as a process independent of time, so the same probability laws govern it at all times. An interesting, but challenging, possibility is to cast it in the framework of stochastic processes and to develop differential equations that include white noise (approximation of $\bar{\theta}_w$ and $\bar{\theta}_s$) as a driving-force term. Investigation of such a possibility is part of the work currently in progress.

Reference

- Ando, S. 1999. "Database for winds, waves, and speeds of CF ships," DREA Tech. Memo., in preparation.
- Barber, N.F. and Ursell, F. 1948. "The generation and propagation of ocean waves and swell," *Phil. Trans. Royal Soc. Lond., A*, **240**, 527-560.
- Ochi, M.K. 1990. *Applied Probability and Stochastic Processes in Engineering and Physical Sciences*, Wiley.
- Parzen, E. 1962. *Stochastic Processes*, Holden-Day.

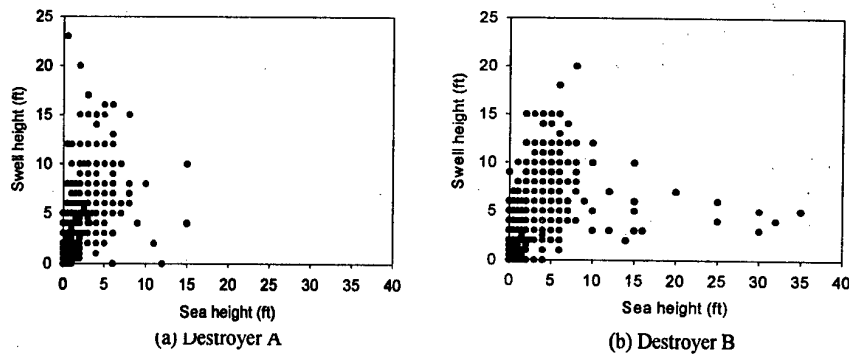


FIG. 1. Scatter plots of swell heights vs. wind-wave heights as observed every 4 hours by two destroyers at sea between 1969-75: 2596 and 2815 data points for destroyers A and B, respectively. Many data points coincide. Note the difference in maximum sea heights observed by the two ships during the same period.

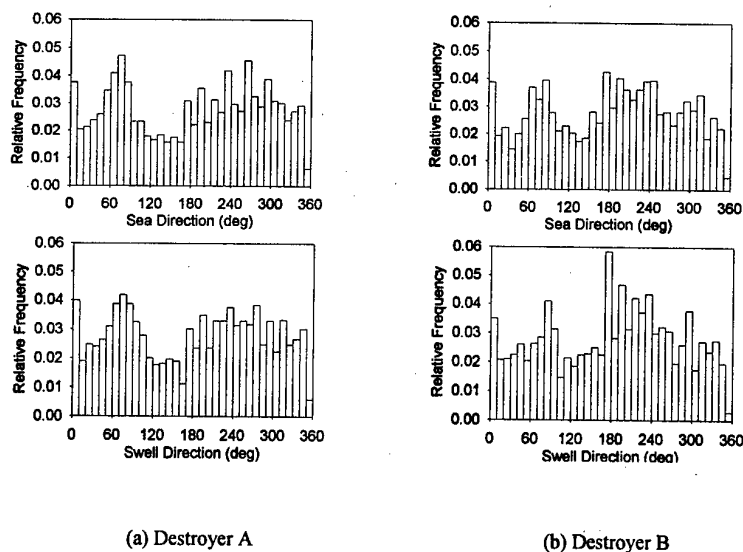


FIG. 2. Histograms of directions of wind (waves) and swells observed every 4 hours by two destroyers between 1969-75. Only data points for nonzero wave heights in Fig. 1 are taken into account: (a) 2394 data points for sea and 2587 for swell; (b) 2702 data points for sea and 2809 for swell.

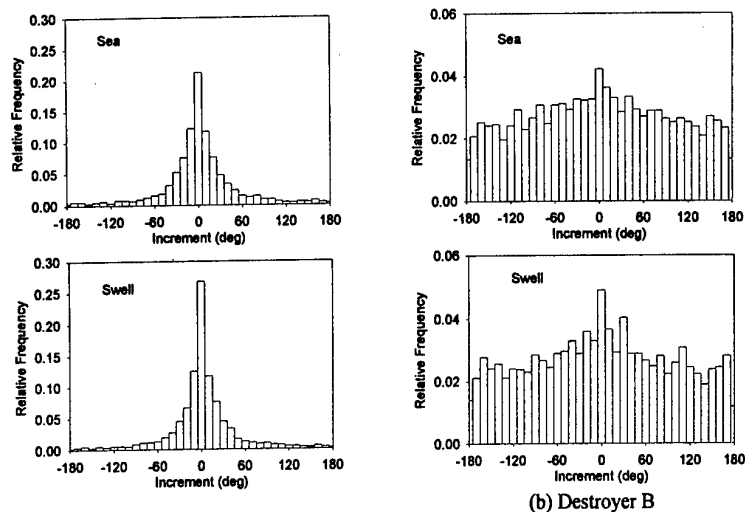


FIG. 3. Relative frequencies of changes in directions of propagation of sea and swell between successive observations) for the two destroyers. Only data points for nonzero wave heights in Fig. 1 are taken into account: (a) 2394 data points for sea and 2587 for swell; (b) 2702 data points for sea and 2809 for swell.

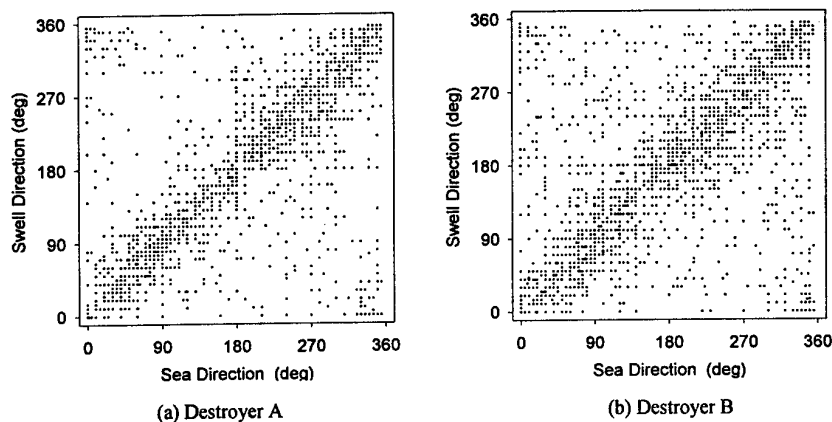


FIG. 4. Scatter plots of directions of propagation of sea and swells observed every 4 hours by the two destroyers at sea between 1969-75. Only paired data points with nonzero heights for both sea and swell are considered: (a) 2388 data points; (b) 2699 data points.

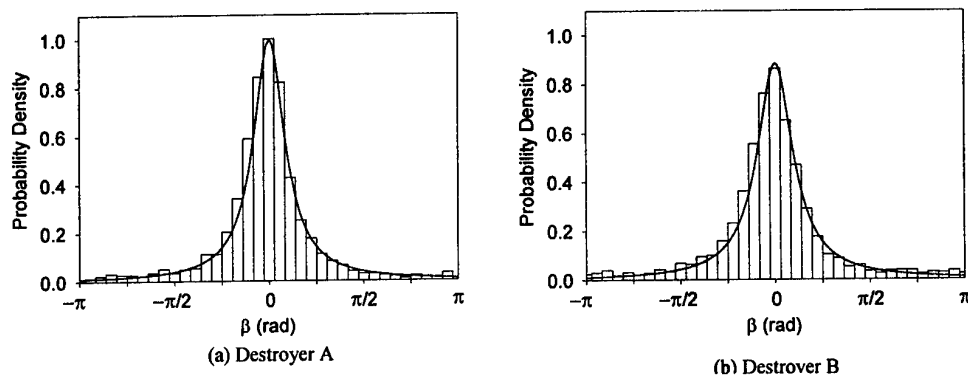


FIG. 5. Probability densities of relative angles between directions of propagation of sea and swells observed every 4 hours by two destroyers at sea between 1969-75. Only paired data points with nonzero heights for both sea and swell are considered: (a) 2388 data points; (b) 2699 data points. The histograms are observed distribution and the curves are the fitted truncated Cauchy distribution of equation (2) in the text: $\alpha = 0.32$ for (a) and $\alpha = 0.36$ for (b), and $\mu = 0$ for both.

NONLINEAR WAVE LOADING USING SIGMA-TRANSFORMED AND UNSTRUCTURED FINITE ELEMENT MESHING

A G L Borthwick, M S Turnbull & R Eatock Taylor

Department of Engineering Science, Oxford University, Parks Road, Oxford OX1 3PJ, U.K.

ABSTRACT

This paper describes a finite element numerical scheme for modelling the wave-induced loading on a horizontal cylinder. A numerical wave tank is utilised with a σ -transformation applied to regions upwave and downwave of the cylinder in order to take advantage of the mapping between free surface and bed. The region around the cylinder is discretised using a Voronoi mesh, with free surface tracking achieved using the Wu and Eatock Taylor (1994) scheme. In this case, the free surface velocities are determined using an accurate higher order interpolation scheme. A combination of the Sommerfeld radiation condition and a damping zone is used to eliminate end effects at the far radiation boundary. Results are presented for sloshing free surface motions in a rectangular tank, progressive waves with and without an immersed horizontal cylinder. Promising agreement is achieved with the analytical and experimental force data of Ogilvie (1963) and Chaplin (1984).

INTRODUCTION

For offshore structures subject to loading in the inertial regime, fully nonlinear potential theory is necessary for predicting relatively large free surface or body motions. Whereas first and second order potential theories have been developed for small amplitude motions, the effects of higher order nonlinearity become increasingly evident in steep waves or where body motions are significant. Wu and Eatock Taylor (1995) have demonstrated that the finite element method can be substantially more efficient than the boundary element method for solving such problems. This is because, although the finite element method involves discretising the entire domain unlike the boundary element method, savings can be made because the finite element matrix is sparsely populated and the coefficients are straightforward to determine. The present paper describes a continuation of the Wu and Eatock Taylor model, whereby a σ -transformation is used to stretch the mesh linearly between the bed and free surface in regions where the fluid is continuous and there is a unique mapping between the bed and free surface. In other regions where for example a horizontal cylinder is situated, Wu and Eatock Taylor's (1995) finite element solver is used with an unstructured Voronoi mesh fitted to the problem boundaries. In the former case, the mapping inherently takes care of the moving boundary. In the latter, the free surface is moved forward in time by calculating the displacements according to the surface velocity components.

MATHEMATICAL FORMULATION

Consider a two-dimensional free surface flow of an incompressible inviscid fluid without surface tension. We assume the flow is irrotational, and potential theory applies whereby the velocity vector \mathbf{u} is related to the velocity potential ϕ by $\mathbf{u} = \nabla\phi$. Invoking irrotationality, $\nabla^2\phi = 0$ throughout the fluid domain. The

boundary conditions are as follows: $\frac{\partial\phi}{\partial n} = 0$ at all solid surfaces; $\frac{\partial\phi}{\partial x} = U(t)$ at the wave-maker where

$U(t)$ is the wave-maker velocity at time t ; the kinematic free surface boundary conditions $\frac{Dx}{Dt} = \frac{\partial\phi}{\partial x}$ and

$\frac{Dz}{Dt} = \frac{\partial\phi}{\partial z}$, and dynamic free surface boundary condition $\frac{D\phi}{Dt} - \frac{1}{2}|\nabla\phi|^2 + gz = 0$ at $z = \zeta(x, t)$.

FINITE ELEMENT FORMULATION

Multiplying Laplace's equation by linear shape functions, $N_j(x, z)$, such that $\phi = \sum_{j=1}^n \phi_j N_j(x, z)$ and integrating over the domain, Wu & Eatock Taylor (1995) derived

$$\int_S N_i \frac{\partial\phi}{\partial n} dS - \int_R \nabla N_i \cdot \nabla\phi dR = 0$$

Replacing ϕ with its approximation and the potential derivative with f_2 , gives

$$\int_R \nabla N_i \cdot \sum_{j=1}^n \phi_j \nabla N_j dR \bigg|_{j \in S_1} = - \int_R \nabla N_i \cdot \sum_{j=1}^n \phi_j \nabla N_j dR \bigg|_{j \in S_1} + \int_{S_2} N_i f_2 dS$$

in which S_1 is the boundary where the velocity potential is specified, and S_2 is the boundary where the normal derivative of the velocity potential, f_2 , is known. In matrix form, this may be written

$$[A]\{\phi\} = \{B\} \text{ where } A_{ij} = \int_R \nabla N_i \cdot \nabla N_j dR \text{ or } A_{ij} = 1 \text{ if } i = j \text{ and } i \in S_1 \text{ or } A_{ij} = 0 \text{ if } i \in S_1 \text{ or } j \in S_1 \text{ and } i \neq j, \text{ and } B_i = - \int_R \nabla N_i \cdot \sum_{j=1}^n \phi_j \nabla N_j dR \bigg|_{j \in S_1} + \int_{S_2} N_i f_2 dS \text{ or } B_i = \phi_i \text{ if } i \in S_1.$$

SIGMA-TRANSFORMED FORMULATION

We choose stretched co-ordinates between the bed and free surface such that $X = \frac{x}{l}$, $\sigma = \frac{z+d}{h}$ and $T = t$, where l is the length of the domain, d is the still water depth and h is the total water depth ($h = d + \eta$).

Using the chain rule: $\frac{\partial}{\partial x} = \frac{1}{l} \frac{\partial}{\partial X} + \left(\frac{\partial \sigma}{\partial x} \right) \frac{\partial}{\partial \sigma}$; $\frac{\partial}{\partial z} = \frac{1}{h} \frac{\partial}{\partial \sigma}$; and $\frac{\partial}{\partial t} = \frac{\partial}{\partial T} + \left(\frac{\partial \sigma}{\partial T} \right) \frac{\partial}{\partial \sigma}$. In the σ -

transformed system, $dR = dx dz = l h dX d\sigma$, and $\nabla = \begin{pmatrix} \frac{\partial}{\partial x} \\ \frac{\partial}{\partial z} \end{pmatrix} = \begin{pmatrix} \frac{1}{l} \frac{\partial}{\partial X} + \left(\frac{\partial \sigma}{\partial x} \right) \frac{\partial}{\partial \sigma} \\ \frac{1}{h} \frac{\partial}{\partial \sigma} \end{pmatrix}$. The general form of a

linear shape function is $N_i = (\alpha_i + \beta_i X + \gamma_i \sigma) / 2\Delta$ where $\alpha_1 = X_2 \sigma_3 - X_3 \sigma_2$, $\alpha_2 = X_3 \sigma_1 - X_1 \sigma_3$, $\alpha_3 = X_1 \sigma_2 - X_2 \sigma_1$, $\beta_1 = \sigma_2 - \sigma_3$, $\beta_2 = \sigma_3 - \sigma_1$, $\beta_3 = \sigma_1 - \sigma_2$, $\gamma_1 = X_3 - X_2$, $\gamma_2 = X_1 - X_3$, $\gamma_3 = X_2 - X_1$, and Δ is the area of the element. The spatial derivatives of the shape functions become

$\frac{\partial N_i}{\partial X} = \frac{\beta_i}{2\Delta}$ and $\frac{\partial N_i}{\partial \sigma} = \frac{\gamma_i}{2\Delta}$. Therefore over a particular element,

$$\nabla N_i \cdot \nabla N_j = \frac{1}{l^2} \frac{\beta_i \beta_j}{4\Delta^2} + \frac{1}{l} \left(\frac{\partial \sigma}{\partial x} \right) \frac{(\beta_i \gamma_j + \beta_j \gamma_i)}{4\Delta^2} + \left(\frac{\partial \sigma}{\partial x} \right)^2 \frac{\gamma_i \gamma_j}{4\Delta^2} + \frac{1}{h^2} \frac{\gamma_i \gamma_j}{4\Delta^2}.$$

Integrating over the element,

$$\begin{aligned} & \frac{1}{l} \frac{\beta_i \beta_j}{4\Delta^2} \int_e h dX d\sigma + \frac{(\beta_i \gamma_j + \beta_j \gamma_i)}{4\Delta^2} \int_e \left(\frac{\partial \sigma}{\partial x} \right) h dX d\sigma \\ & + \frac{l \gamma_i \gamma_j}{4\Delta^2} \int_e \left(\frac{\partial \sigma}{\partial x} \right)^2 h dX d\sigma + \frac{l \gamma_i \gamma_j}{4\Delta^2} \int_e \frac{1}{h} dX d\sigma \end{aligned}$$

The integral expressions are evaluated using cubic formulae, and the matrix equation solved by Gaussian elimination.

VELOCITY CALCULATION

The velocity components are $u = \frac{\partial \phi}{\partial x} = \frac{1}{l} \frac{\partial \phi}{\partial X} + \frac{1}{lh} \left(-\sigma \frac{\partial \eta}{\partial X} + (1-\sigma) \frac{\partial d}{\partial X} \right) \frac{\partial \phi}{\partial \sigma}$ and $w = \frac{\partial \phi}{\partial z} = \frac{1}{h} \frac{\partial \phi}{\partial \sigma}$. At

the free surface, the velocity components are used to estimate rates of change of free surface elevation and velocity potential with time. The σ -transformed free surface kinematic boundary condition gives

$$\frac{\partial \eta}{\partial t} = w - u \frac{\partial \eta}{\partial x} = w - \frac{u}{l} \frac{\partial \eta}{\partial X}. \quad \text{For a uniform sea bed, } \frac{\partial \sigma}{\partial t} = -\frac{\sigma}{l} \frac{\partial \eta}{\partial t}, \quad \text{and so}$$

$$\frac{\partial \Phi}{\partial T} = \frac{\partial \Phi}{\partial t} + \frac{\sigma}{h} \frac{\partial \eta}{\partial t} \frac{\partial \Phi}{\partial \sigma} = \frac{\partial \Phi}{\partial t} + \sigma \frac{\partial \eta}{\partial t} \frac{\partial \Phi}{\partial z}. \quad \text{At the free surface, } \sigma = 1, \text{ and the dynamic free surface}$$

boundary condition gives, $\frac{\partial \Phi}{\partial T} = -g\eta - \frac{(u^2 + w^2)}{2} + \frac{\partial \eta}{\partial T} w$. A fourth-order Runge-Kutta scheme is used to step free surface elevation and potential forward in time.

RESULTS

Sloshing in a Fixed Rectangular Tank

Here, a tank of length twice that of the still water depth is considered. The initial elevation is sinusoidal such that one wavelength fits the tank. Almost exact agreement was obtained with Wu and Eatock Taylor's (1994) second order analytical solution when the wave amplitude to depth ratio $a/d = 0.001$. Fig. 1 depicts the time history of the free surface at the tank centre for a wave of greater amplitude $a/d = 0.1$. The results from both the σ -transformed and Wu and Eatock Taylor (1995) schemes are almost identical. The effect of higher order wave nonlinearity is evident with a phase shift evident and higher free surface maxima than for the second order potential solution. The effect of nonlinearity can also be seen in Fig. 2 which shows the free surface profile along the tank at different times during a cycle. There is a narrower central peak and wider trough than for a linear sinusoidal standing wave. The fixed positions of nodes that exist for small amplitude cases are not present here. These results are in close agreement with those of Chern *et al.* (1999). Fig. 3 depicts the spatial free surface profiles along the tank for a relatively large amplitude case ($a/d = 0.05$) where the wavelength of the initial sinusoidal free surface elevation is half the length of the tank. Again, the crests are clearly sharper and troughs shallower than for linear sinusoidal motions.

Sloshing in a Base-excited Tank

Wu *et al.* (1998) gave the linear solution for free surface motions of inviscid liquid in a tank where the base was oscillated horizontally. Fig. 4 illustrates the very close agreement between the finite element model predictions and the analytical solution for a near resonant case, where the excitation frequency $\omega = 1.1\omega_0$ (and ω_0 is the natural sloshing frequency of the tank). The finite element scheme predicts increasingly higher peaks than the analytical model as the initial oscillations grow in amplitude; this is again due to high order nonlinearity.

Regular Waves

Progressive waves were generated by imposing the linear theory horizontal velocity distribution at the left hand boundary of the domain. The velocity amplitude was ramped up over a predetermined period to avoid spurious oscillations. At the right hand end of the tank, wave absorption was achieved using a combination of the Sommerfeld radiation condition with a damping zone. Fig. 5 represents the free surface evolution along the tank with time, whereby spatial profiles are plotted at time intervals of twice the wave period. The overlaid plots demonstrate the repeatability of the wave generation process. The first and second order components of waves of steepness ka up to 0.194, were found to be almost identical to analytical values from Stokes' second order theory.

Horizontal Cylinder Under Regular Waves

In order to insert a horizontal cylinder in the wave tank, a combination of structured and unstructured finite element meshes was used. A typical example of the unstructured region is shown in Fig. 6. The total force may be calculated by integrating the surface pressure profile around the cylinder. The first and second order force components in the vertical and horizontal directions were determined using Fourier analysis. Reasonable agreement is obtained with Ogilvie's (1963) semi-analytical model and Chaplin's (1984) experimental data, as the following example illustrates. For a non-dimensional wave frequency $\omega = 1.8495$, non-dimensional depth of immersion $d_c = 0.18$, and non-dimensional cylinder radius $A = 0.06$, Ogilvie predicts $|F^{(1)}|/A = 0.0430$, Chaplin obtains $|F^{(1)}|/A = 0.0415$, whereas the present scheme predicts $|F_x^{(1)}|/A = 0.0435$ and $|F_z^{(1)}|/A = 0.0429$. Moreover, for the second order mean vertical force, $\overline{F_z^{(2)}}/A^2$, the corresponding results from Ogilvie, Chaplin and the present scheme are 0.0914, 0.0944 and 0.0930, respectively.

CONCLUSIONS

A numerical wave tank has been described based on finite element models with σ -transformed and unstructured mesh systems. Simulations of nonlinear sloshing waves in fixed and base-excited tanks

have been found to agree well with analytical solutions, and the numerical results of Chern *et al.* (1999). Progressive regular waves have been simulated in close agreement with Stokes' second order theory. Sensible estimates have been made of the first and second order forces on a submerged horizontal cylinder under waves, in comparison with Ogilvie (1963) and Chaplin (1984).

REFERENCES

- Chaplin, J.R. (1984) "Nonlinear forces on a horizontal cylinder beneath waves", J. Fluid Mech., 147: 449-464.
 Chern, M.J., Borthwick, A.G.L., and Eatock Taylor (1999) "A pseudospectral σ -transformation model of 2-D nonlinear waves", Journal of Fluids and Structures, 13: 607-630.
 Ogilvie, T.F. (1963) "First- and second-order forces on a cylinder submerged under a free surface", J. Fluid Mech., 16: 451-472.
 Wu, G.X., and Eatock Taylor, R. (1994) "Finite element analysis of two-dimensional nonlinear transient water waves", Appl. Ocean Res., 16: 363-372.
 Wu, G.X., and Eatock Taylor, R. (1995) "Time stepping solutions of the two-dimensional non-linear wave radiation problem", Ocean Eng., 22(8): 785-798.
 Wu, G.X., Ma, Q.W., and Eatock Taylor, R. (1998) "Numerical simulation of sloshing waves in a 3D tank based on a finite element method", Appl. Ocean Res., 20: 337-355.

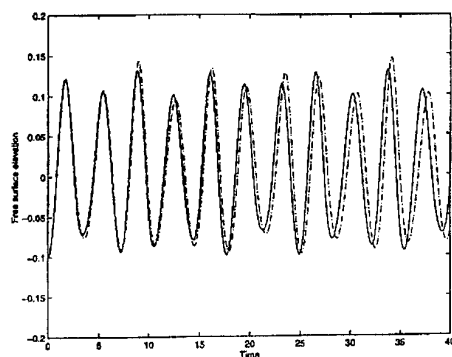


Fig. 1 Free surface motions at tank centre

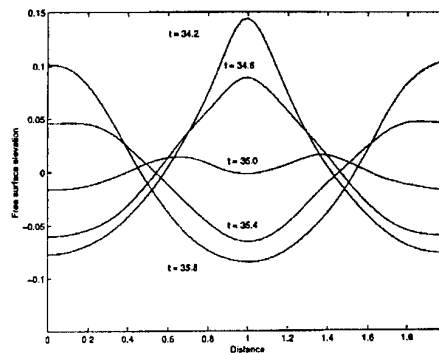


Fig.2 Wave profiles: $a = 0.1$

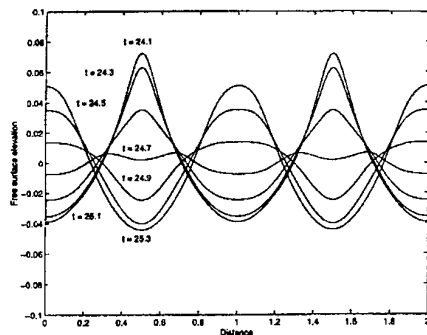


Fig. 3 Double standing wave profiles: $a = 0.05$

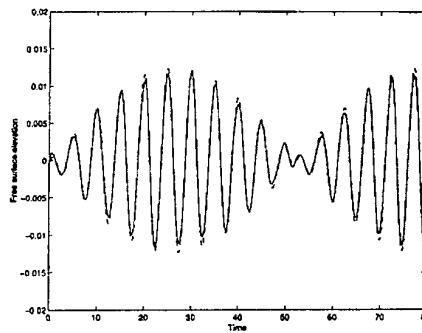


Fig.4 Free surface motions at left wall:
Base-excited tank: $\omega = 1.1 \omega_0$

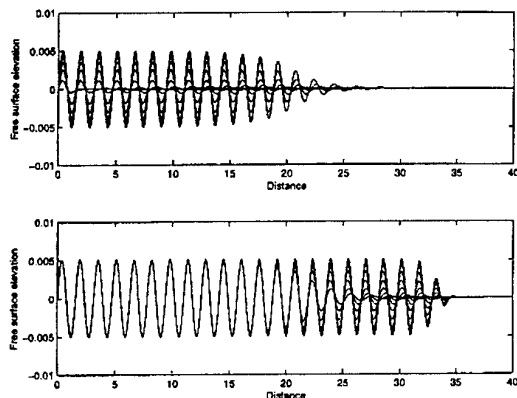


Fig. 5 Evolution of regular waves

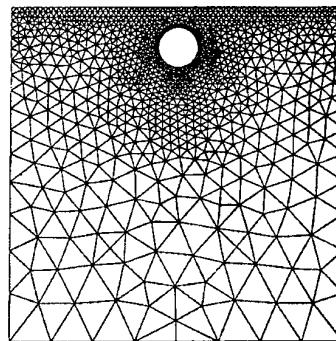


Fig. 6 Voronoi mesh about cylinder

Numerical Solution of Steady Free-Surface Navier-Stokes Flow

Harald van Brummelen*, Hoyte Raven†

Abstract

The usual time integration approach for solving steady viscous free surface flow problems has several drawbacks. We propose instead an efficient iterative method, which relies on a different but equivalent formulation of the free surface flow problem, involving a so-called quasi free-surface condition. Furthermore, we present a method for analyzing the properties of wave solutions of the discrete equations. Numerical results for flow over a bottom bump agree well with measurements and with the predictions of the analysis.

1 Introduction

The numerical solution of flows which are partially bounded by a freely moving boundary is of great practical importance. Current methods for solving steady viscous free-surface flow problems typically display two defects, viz., high computational costs due to persistent transient behavior and substantial numerical damping of gravity wave solutions. In the present work we address both of these problems.

To reduce the computational effort of solving the steady free-surface flow problem, we propose an efficient iterative solution method. Whereas dedicated techniques have been developed for the solution of steady free surface potential flow [2, 4], methods for steady Navier-Stokes flow simply continue the usual time integration process until a steady state is reached. In [5] several drawbacks of this process are discussed, such as slow convergence to steady state. In particular, one can show that at subcritical Froude numbers, dispersion causes asymptotic temporal behavior of the amplitude of transient waves in \mathbb{R}^d of $O(t^{-(d-1)/2})$. Hence, if the objective is to reduce the amplitude of transient waves to the order of spatial discretization errors, the efficiency of the time integration approach deteriorates rapidly with decreasing meshwidth. In practical computations, thousands of time steps are usually required.

The iterative method we propose relies on a different but equivalent formulation of the free-surface flow problem, involving a quasi free-surface condition. The method solves a sequence of steady Navier-Stokes subproblems with this condition imposed at an approximation to the steady free boundary. Each subproblem evaluation yields an improved approximation to the steady free surface position. For the testcase presented, the method displays linear convergence of the boundary location and the results exhibit good agreement with measurements.

To reduce numerical wave damping, a priori knowledge of the properties of the discretization scheme is imperative. We present a method for analyzing the properties of the discretized equations corresponding to the subproblems. The analysis yields valuable information on numerical wave damping and dispersion and can serve in the assessment of discretization schemes. The results of the analysis agree well with the computed results.

2 Problem Statement & Solution Method

We consider an incompressible, viscous fluid flow, subject to a constant gravitational force on a domain, \mathcal{V} . The domain is bounded by a free boundary, \mathcal{S} , and fixed boundaries $\partial\mathcal{V} \setminus \mathcal{S}$. The flow is characterized by the Froude number, Fr , and the Reynolds number, Re . The (nondimensionalized) fluid velocity and pressure are identified by $\mathbf{v}(\mathbf{x})$ and $p(\mathbf{x})$, respectively. The objective is to find $\mathcal{V}, \mathbf{v}(\mathbf{x}), p(\mathbf{x})$ such that the steady (Reynolds Averaged) Navier-Stokes equations are satisfied on \mathcal{V} , the appropriate boundary conditions hold at fixed boundaries and, moreover, at the free surface the steady kinematic condition,

$$\mathbf{v} \cdot \mathbf{n} = 0, \quad \mathbf{x} \in \mathcal{S}, \quad (1)$$

*CWI, P.O. Box 94079, 1090 GB Amsterdam, The Netherlands

†MARIN, P.O. Box 28, 6700 AA Wageningen, The Netherlands

with $\mathbf{n}(\mathbf{x})$ the unit normal vector to \mathcal{S} , and the dynamic conditions,

$$\mathbf{t}_\alpha \cdot \boldsymbol{\tau}(\mathbf{v}) \cdot \mathbf{n} = 0, \quad \mathbf{x} \in \mathcal{S}, \quad (2a)$$

$$p = 0, \quad \mathbf{x} \in \mathcal{S}, \quad (2b)$$

are fulfilled. Here, $\mathbf{t}_\alpha(\mathbf{x})$ are orthogonal tangential unit vectors to \mathcal{S} and $\boldsymbol{\tau}$ denotes the viscous stress tensor. In the derivation of the normal dynamic condition (2b) viscous effects have been ignored.

An equivalent formulation of the free-surface flow problem is obtained if the second dynamic condition (2b) is replaced by the quasi free-surface condition:

$$\mathbf{v} \cdot \nabla p = 0, \quad \mathbf{x} \in \mathcal{S}. \quad (2b^*)$$

Condition (2b*) results from a combination of the kinematic and dynamic condition. In [1] it is shown for perturbations of a uniform flow in a channel of unit depth that the Navier-Stokes equations subject to boundary condition (2b*) allow gravity wave solutions that satisfy the usual dispersion relation. Denoting by $\mathcal{C}(\mathcal{V}, \mathbf{v}, p)$ the problem corresponding to the steady (RA)NS equations on \mathcal{V} , with appropriate boundary conditions on fixed boundaries, $\partial\mathcal{V} \setminus \mathcal{S}$, and conditions (2a) and (2b*) on the free boundary, \mathcal{S} , we propose the following algorithm for solving the free-surface flow problem:

```
initialize  $\mathcal{S}$ ; solve  $\mathbf{v}, p$  from  $\mathcal{C}(\mathcal{V}, \mathbf{v}, p)$ ;
while ( $\|p(\mathbf{x})\|_{\mathcal{S}} > \epsilon$ ) {update  $\mathcal{S} := \{\mathbf{x} + \mathbf{j} \text{Fr}^2 p(\mathbf{x}) \mid \mathbf{x} \in \mathcal{S}\}$ ; solve  $\mathbf{v}, p$  from  $\mathcal{C}(\mathcal{V}, \mathbf{v}, p)$ };
```

Here, \mathbf{j} stands for the vertical unit vector. The method relies on use of boundary condition (2b*) in each subproblem. Contrary to the kinematic condition (1) and the dynamic condition (2b), condition (2b*) permits a nonzero normal velocity and a nonconstant pressure at the approximate free boundary. Condition (2b*) is smooth in the sense that it holds to close approximation in a neighborhood of the actual free surface. Consequently, the adjustment of the boundary induces only small disturbances in the solution. Then, the update improves the approximation to the free-surface location. One may note that this approach is analogous to methods for solving steady free-surface potential flow, e.g., [4]. Results of the method for a testcase from [2] are presented in section 4.

3 Wave solutions of the discrete equations

To solve the free-surface (RA)NS problem numerically, at the expense of a discretization error, the continuous differential equations and boundary conditions are replaced by a system of discrete equations. By consistency, these discrete equations permit surface gravity wave solutions that obey a dispersion relation that is similar to that of the continuous equations. Analysis of the difference between solutions of the discrete equations and of the continuous equations yields valuable information on the properties of the discretization scheme. Moreover, such an analysis can serve in the development of discretization schemes with special behavior, e.g., low numerical damping of surface gravity waves. Subsequently, we present the results of such an analysis.

We consider perturbations of magnitude ϵ , $\epsilon \ll 1$, of a uniform horizontal flow with velocity V_0 in a channel of unit depth. Through asymptotic expansion and Fourier analysis, one can show that the system of equations resulting from the discretization of the incompressible NS equations and the boundary condition (2b*) on a uniform mesh with meshsize h , allows a steady gravity wave solution that is proportional to $\exp(\theta_1 x_1 + \theta_2 x_2)$, $(\theta_1, \theta_2) \in \mathbb{C}^2$, provided that the dispersion relation

$$V_0^2 \partial_{ch}^1(\theta_1) \partial_{sh}^1(\theta_1) = -\text{Fr}^{-2} \frac{E(-\theta_2) - E(\theta_2)}{\frac{E(-\theta_2)}{\partial_{ph}^2(\theta_2)} - \frac{E(\theta_2)}{\partial_{ph}^2(-\theta_2)}} \quad (3)$$

is obeyed. Here, $\partial_{ch}^1(\theta_1)$ denotes the symbol of the discrete approximation to the x_1 -derivative of the velocity in the convective term of the momentum equations, $\partial_{sh}^1(\theta_1)$ stands for the symbol of the x_1 -derivative of the pressure in the quasi free-surface condition, $\partial_{ph}^2(\theta_2)$ represents the symbol of the x_2 -derivative of the pressure in the momentum equations and $E(\theta_2)$ denotes the symbol of the impermeability condition, $v = 0$, at the bottom boundary. Solutions of (3) should be compared to solutions of the dispersion relation corresponding to the continuous problem, viz., $(\theta_1, \theta_2) = (ik, k)$ with $V_0^2 = \text{Fr}^{-2} k^{-1} \tanh(k)$. Indeed, it can be verified by Taylor expansion of the Fourier symbols that for a consistent discretization, (θ_1, θ_2) by (3) approach (ik, k) as h tends to 0.

For the discretization employed in the numerical experiments, figure 1(l) displays the relative difference between the wavelength of a stationary wave solution of the continuous equations, $\lambda = 2\pi/k$, and the wavelength of a stationary wave solution of the discrete equations, $\lambda^h = 2\pi/\Im(\theta_1)$, with θ_1 according to (3), versus the Froude number, for various values of the meshwidth h . Figure 1(r) shows the associated wave attenuation per wavelength, $\nu^h = \exp(\Re(\theta_1) \lambda^h)$.

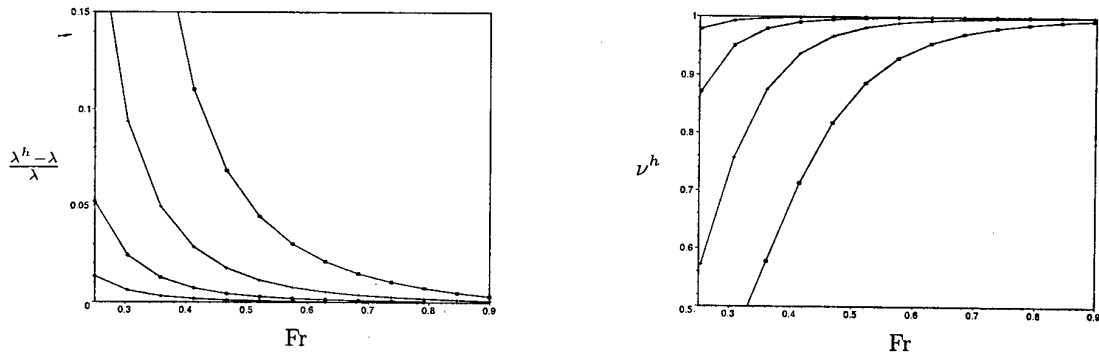


Figure 1: Relative difference in wavelength of stationary wave solutions of the discrete equations and of the continuous equations (l) and numerical wave damping (r), versus the Froude number for meshwidth $h = 1/10$ (\square), $h = 1/20$ ($+$), $h = 1/40$ (\circ) and $h = 1/80$ (\diamond).

4 Numerical Experiments & Results

To test the algorithm described in section 2 and verify the results of the analysis presented in section 3, we conducted numerical experiments for the subcritical flow over a bump in a channel of unit depth at $Fr = 0.43$ and $Re = 3 \times 10^6$, with bumpheight $E = 0.2$, as described in [2] and, to reduce the non-linearity, with $E = 0.18$. The experiments were performed on grids with different meshwidths. In each case, exponential grid stretching was applied to resolve the boundary layer at the bottom. The steady RANS problems were solved by the method described in [3]. After each evaluation, the grid was adapted using relative vertical stretching and an initial estimate on the adapted grid was generated by linear interpolation from the solution on the previous grid.

Figure 2 displays the computed wave-elevation and the measurements from [2]. In [2] a (nondimensionalized) wavelength $\lambda = 1.1 \pm 10\%$ and an amplitude $a = 4.5 \times 10^{-2} \pm 15\%$ is stated for the measurements of the trailing wave. The numerical results on a grid with horizontal meshwidth $h = 1/32$ yield $\lambda = 1.09$ and $a = 6.4 \times 10^{-2}$. Hence, the computed amplitude is slightly overestimated and the wavelength is within the uncertainty interval.

The table in figure 3 lists the wavelength and the wave-attenuation according to the numerical results, for $E = 0.18$, and according to dispersion relation (3). The numerical results and the predictions by (3) exhibit good agreement. The differences are within the uncertainty that is introduced by determining the wavelength and the wave-attenuation from the computed wave-elevation.

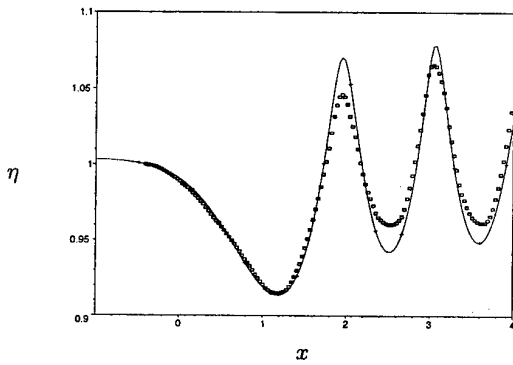


Figure 2: Computed wave elevation for $h = 1/32$ and measurements from [2].

h	wavelength		attenuation	
	comput.	analysis	comput.	analysis
1/10	1.30	1.27	0.74	0.75
1/20	1.22	1.19	0.94	0.95
1/40	1.18	1.17	0.99	0.99
1/80	1.17	1.16	1.00	1.00

Figure 3: Wavelength and wave attenuation of the numerical results, for $E = 0.18$, and by dispersion relation (3) for $h = 1/10, 1/20, 1/40, 1/80$.

Figure 4 displays the computed wave-elevation on the $h = 1/80$ grid after consecutive subproblem evaluations, when the initial estimate of the free boundary is the undisturbed surface. Observe that already after a single evaluation a wave-solution is obtained.

The table in figure 5 lists the pressure defect at the free surface after successive subproblem evaluations, with $\|p\|_S = h \sum |p_i|$. The results reveal that 2 evaluations suffice to reduce the pressure defect by an order of magnitude. This indicates that the pressure defect and, hence, the boundary position converge linearly

with the number of subproblem evaluations. However, the evaluations become increasingly less expensive, because the error in the initial estimate that is obtained from the previous solution, decreases proportional with the pressure defect. As a consequence, for the testcase with $E = 0.18$, the computations were only marginally more expensive than a fixed domain computation; see also [5].

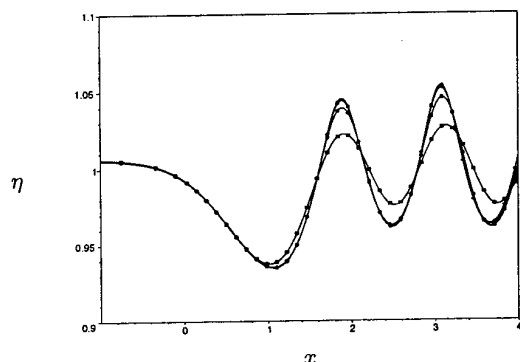


Figure 4: Wave elevation obtained after consecutive subproblem evaluations for $E = 0.18$ and $h = 1/80$.

#	$\ p\ _s$
1	5.38×10^{-1}
2	1.62×10^{-1}
3	3.46×10^{-2}
4	7.96×10^{-3}
5	2.47×10^{-3}
6	7.66×10^{-4}
7	2.17×10^{-4}
8	9.51×10^{-5}

Figure 5: Number of subproblem evaluations and corresponding pressure defect at the free surface for $E = 0.18$.

5 Conclusions

We presented a computational method for the efficient numerical solution of steady free-surface Navier-Stokes flow and a method for analyzing the properties of the discretization scheme.

The computational method solves a sequence of subproblems, with a quasi free-surface condition imposed at the free surface. After each subproblem evaluation, an improved approximation to the free-surface location is obtained. Numerical results were presented for the flow over a bottom-bump. The results agree well with measurements. Moreover, for the testcase presented, the method displays linear convergence of the boundary position with the number of subproblem evaluations. The results indicate that the method indeed permits efficient solution of steady free-surface Navier-Stokes flows.

The method for analyzing the properties of the discretization scheme employs asymptotic expansion techniques and Fourier analysis to determine the dispersion relation for the system of discrete equations. Results of the analysis were compared with numerical results on grids with different meshwidths. The comparison reveals good agreement between the predictions from the analysis and the numerical results. We expect that the method can serve in the development and assessment of discretization schemes.

References

- [1] H. v. BRUMMELEN, *Analysis of the incompressible navier-stokes equations with a quasi free-surface condition*, tech. rep., CWI, 1999. Available at <http://www.cwi.nl/static/publications/reports/MAS-1999.html>.
- [2] J. CAHOUE, *Etude numérique et expérimentale du problème bidimensionnel de la résistance de vagues non-linéaire*, PhD thesis, ENSTA, Paris, 1984. (In French).
- [3] M. HOEKSTRA, *Numerical Simulation of Ship Stern Flows with a Space-Marching Navier-Stokes Method*, PhD thesis, Delft University of Technology, Netherlands, 1999.
- [4] H. RAVEN, *A Solution Method for the Nonlinear Ship Wave Resistance Problem*, PhD thesis, Delft University of Technology, Netherlands, 1996.
- [5] H. RAVEN AND H. v. BRUMMELEN, *A new approach to computing steady free-surface viscous flow problems*, in 1st MARNET-CFD Workshop, Barcelona, 1999. Available at http://www.marin.nl/projects/cph_parnassos_720.html.

SCATTERING OF OBLIQUE WAVES IN A TWO-LAYER FLUID

J.R. Cadby & C.M. Linton

Loughborough University, Loughborough, Leicestershire, LE11 3TU, U.K.

Introduction

The research presented here investigates the interaction of oblique waves with a horizontal cylinder in a two-layer fluid consisting of a layer of finite thickness bounded above by a free surface and below by a fluid of greater density and infinite depth. The free surface and the interface between the two fluids provide two surfaces on which waves can exist. The case of normal incidence was considered previously by Linton and McIver (1995) who were interested in such interactions following proposals to build submerged floating tunnels across Norwegian fjords. Such fjords typically consist of a layer of fresh water above a deep expanse of salt water.

Formulation

Cartesian coordinates are chosen such that the (x, y) -plane coincides with the undisturbed interface between the two fluids. The z -axis points vertically upwards with $z = 0$ and $z = d$ corresponding to the undisturbed interface and free surface respectively. The upper fluid, $0 < z < d$, will be referred to as region *I* and have density ρ^I , whilst the lower fluid, $z < 0$, will be referred to as region *II* and have density ρ^{II} . We also define $\rho = \rho^I / \rho^{II} < 1$. Under the usual assumptions of linear water wave theory we can write the velocity potential as $\Re\{\phi(x, z)e^{i\ell y}e^{-i\omega t}\}$ where

$$(\nabla^2 - l^2)\phi = 0 \quad \text{in the fluid,} \quad (1)$$

$$\phi_z^I = \phi_z^{II} \quad \text{on } z = 0, \quad (2)$$

$$\rho(\phi_z^I - K\phi^I) = \phi_z^{II} - K\phi^{II} \quad \text{on } z = 0, \quad (3)$$

$$\phi_z^I = K\phi^I \quad \text{on } z = d, \quad (4)$$

and $K = \omega^2/g$. The dispersion relation is given by

$$(u - K)(K(\sigma + e^{-2ud}) - u(1 - e^{-2ud})) = 0, \quad (5)$$

where $\sigma = (1 + \rho)/(1 - \rho)$. It follows that either $u = K$ or $u = k > K$ where

$$K(\sigma + e^{-2kd}) = k(1 - e^{-2kd}). \quad (6)$$

The potential of an incident plane wave of wavenumber K making an angle α_{inc} with the positive x -axis takes the form

$$\phi_{\text{inc}} = e^{iKx \cos \alpha_{\text{inc}}} e^{Kz}, \quad (7)$$

from which

$$l = K \sin \alpha_{\text{inc}} \quad (8)$$

and hence we clearly must have $l < K$. For incident wavenumber k we simply have to replace K with k in (8) and such waves can exist provided $l < k$. A general scattering potential has the far-field behaviour described by

$$\phi^I \sim A^\pm e^{\pm i\beta x} e^{Kz} + B^\pm e^{\pm i\beta x} g(z) + C^\pm e^{\mp i\beta x} e^{Kz} + D^\pm e^{\mp i\beta x} g(z), \quad (9)$$

$$\phi^{II} \sim A^\pm e^{\pm i\beta x} e^{Kz} + B^\pm e^{\pm i\beta x} e^{kz} + C^\pm e^{\mp i\beta x} e^{Kz} + D^\pm e^{\mp i\beta x} e^{kz}, \quad (10)$$

as $x \rightarrow \pm\infty$, where $\beta = \sqrt{K^2 - l^2}$ and $b = \sqrt{k^2 - l^2}$. Equations (9) & (10) can be characterised by

$$\phi \sim \{A^-, B^-, C^-, D^-; A^+, B^+, C^+, D^+\}. \quad (11)$$

For incident waves of wavenumber K we have $\beta = K \cos \alpha_{\text{inc}}$ and $b = \sqrt{k^2 - K^2 \sin^2 \alpha_{\text{inc}}}$ which are real for all K and $0 < \alpha_{\text{inc}} < \pi/2$ since $K < k$. For the case of an incident wave of wavenumber k we have $\beta = \sqrt{K^2 - k^2 \sin^2 \alpha_{\text{inc}}}$ and $b = k \cos \alpha_{\text{inc}}$. In this case, given α_{inc} there is a critical value of K for which $\beta = 0$. For values of K less than this critical value β is complex and hence scattered waves of wavenumber K do not exist.

Using Green's theorem and (3) we can derive the general identity

$$\int_B \left(\phi_i \frac{\partial \phi_j}{\partial n} - \phi_j \frac{\partial \phi_i}{\partial n} \right) ds = J_K (A_i^+ C_j^+ - C_i^+ A_j^+ + A_i^- C_j^- - C_i^- A_j^-) + J_k (B_i^+ D_j^+ - D_i^+ B_j^+ + B_i^- D_j^- - D_i^- B_j^-), \quad (12)$$

where

$$J_K = i\beta \left[\frac{1}{K} + 2\rho \int_0^d e^{2Kz} dz \right], \quad J_k = ib \left[\frac{1}{k} + 2\rho \int_0^d [g(z)]^2 dz \right], \quad (13)$$

and B is the set of body boundaries which are assumed for simplicity to all lie in the lower fluid. If we consider the scattering of waves by a fixed obstacle then in general there are two problems. These are the scattering of an incident wave of wavenumber K , which we shall refer to as problem 1; and the scattering of an incident wave of wavenumber k (problem 2). For each of these problems we use R and T to represent reflection and transmission coefficients corresponding to waves of wavenumber K and r and t are used for waves of wavenumber k . The problems are thus characterised, in the notation of (11), by

$$\phi_1 \sim \{R_1, r_1, 1, 0; T_1, t_1, 0, 0\}, \quad (14)$$

$$\phi_2 \sim \{R_2, r_2, 0, 1; T_2, t_2, 0, 0\}. \quad (15)$$

Applying (12) to $\phi_i, \bar{\phi}_i, i = 1, 2$, we obtain identities representing energy conservation, namely

$$|R_1|^2 + |T_1|^2 + J(|t_1|^2 + |r_1|^2) = 1, \quad (16)$$

$$|R_2|^2 + |T_2|^2 + J(|t_2|^2 + |r_2|^2) = J. \quad (17)$$

where $J = J_k/J_K$.

Circular cylinder in lower fluid layer

Let us consider the case of an infinite cylinder of radius a in the lower fluid centred at $z = f < 0$ with its generator parallel to the y -axis. The scattering problem for such a geometry can be solved using multipole expansions. Multipoles are singular solutions of (1) which satisfy all the boundary conditions of the problem except that on the cylinder. Symmetric and antisymmetric multipoles can be constructed for this problem and when expanded about $z = f$ they take the form

$$\phi_m^s = K_m(lr) \cos m\theta + \sum_{n=0}^{\infty} A_{mn}^s I_n(lr) \cos n\theta, \quad (18)$$

$$\phi_m^a = K_m(lr) \sin m\theta + \sum_{n=1}^{\infty} A_{mn}^a I_n(lr) \sin n\theta, \quad (19)$$

where

$$A_{mn}^s = (-1)^{m+n} \epsilon_n \int_0^{\infty} \cosh mu \cosh nu e^{2lf \cosh u} C_L(u) du, \quad (20)$$

$$A_{mn}^a = (-1)^{m+n} 2 \int_0^{\infty} \sinh mu \sinh nu e^{2lf \cosh u} C_L(u) du. \quad (21)$$

Here $\epsilon_0 = 1, \epsilon_n = 2, n \geq 1$,

$$C_L(u) = \frac{(l \cosh u + K)[(l \cosh u + K\sigma)e^{-2ld \cosh u} - l \cosh u + K]}{(l \cosh u - K)h(l \cosh u)}, \quad (22)$$

and

$$h(u) = (u + K)e^{-2ud} - u + K\sigma. \quad (23)$$

From (6) we have $h(k) = 0$. The integrands in (20) & (21) have poles at $u = \gamma_1$ and $u = \gamma_2$ where

$$\cosh \gamma_1 = K/l, \quad \text{and} \quad \cosh \gamma_2 = k/l. \quad (24)$$

To solve the scattering problem we write the velocity potential in terms of the incident wave and the multipoles as follows

$$\phi = \phi_{\text{inc}} + \sum_{m=0}^{\infty} a^m (\alpha_m \phi_m^a + \beta_m \phi_m^s), \quad (25)$$

where $\alpha_0 = 0$ is included for convenience. To find the unknowns α_m and β_m we apply the body boundary condition $\partial\phi/\partial r = 0$ on $r = a$. For an incident wave of wavenumber K we obtain

$$\alpha_n + \frac{I'_n(la)}{K'_n(la)} \sum_{m=1}^{\infty} \alpha_m a^{m-n} A_{mn}^a = \left(\frac{-1}{a}\right)^n 2i \frac{I'_n(la)}{K'_n(la)} e^{Kf} \sinh n\gamma, \quad n=1, 2, \dots \quad (26)$$

$$\beta_n + \frac{I'_n(la)}{K'_n(la)} \sum_{m=0}^{\infty} \beta_m a^{m-n} A_{mn}^s = -\left(\frac{-1}{a}\right)^n \epsilon_n \frac{I'_n(la)}{K'_n(la)} e^{Kf} \cosh n\gamma, \quad n=0, 1, \dots, \quad (27)$$

where $\cosh \gamma = 1/\sin \alpha_{\text{inc}}$. Truncation of the systems to $N \times N$ systems is required to find solutions. Convergence is rapid and for the results below a value of $N = 4$ was used. The reflection and transmission coefficients are obtained from the far field form of the velocity potential:

$$T_1 = 1 - \pi e^{Kf} \text{Res}[C_L : \gamma_1] \sum_{m=0}^{\infty} (-a)^m [\alpha_m \sinh m\gamma_1 - i\beta_m \cosh m\gamma_1], \quad (28)$$

$$R_1 = \pi e^{Kf} \text{Res}[C_L : \gamma_1] \sum_{m=0}^{\infty} (-a)^m [\alpha_m \sinh m\gamma_1 + i\beta_m \cosh m\gamma_1], \quad (29)$$

$$t_1 = \pi e^{kf} \text{Res}[C_L : \gamma_2] \sum_{m=0}^{\infty} (-a)^m [-\alpha_m \sinh m\gamma_2 + i\beta_m \cosh m\gamma_2], \quad (30)$$

$$r_1 = \pi e^{kf} \text{Res}[C_L : \gamma_2] \sum_{m=0}^{\infty} (-a)^m [\alpha_m \sinh m\gamma_2 + i\beta_m \cosh m\gamma_2]. \quad (31)$$

For an incident wave of wavenumber k we have $l = k \sin \alpha_{\text{inc}}$ and the equations for α_m, β_m are simply (26), (27) with K replaced with k . The equations for R_2 and r_2 are the same as those for R_1 and r_1 , but for the transmission coefficients we have

$$T_2 = \pi e^{Kf} \text{Res}[C_L : \gamma_1] \sum_{m=0}^{\infty} (-a)^m [-\alpha_m \sinh m\gamma_1 + i\beta_m \cosh m\gamma_1], \quad (32)$$

$$t_2 = 1 - \pi e^{kf} \text{Res}[C_L : \gamma_2] \sum_{m=0}^{\infty} (-a)^m [\alpha_m \sinh m\gamma_2 - i\beta_m \cosh m\gamma_2]. \quad (33)$$

Results and discussion

There are many different features of this problem that could be explored. Here we will concentrate on just one, the occurrence of zeros of transmission for particular parameter values. Figure 1 shows the reflection and transmission energies for an incident wave of wavenumber k . The transmission and reflection coefficients for waves of wavenumber K cut in at $Ka \sim 0.313$ which is the critical frequency for this case. For a frequency of $Ka \sim 0.288$ we observe there is zero transmission and full reflection of the waves of wavenumber k . Given that circular cylinders are known to reflect no energy in a single layer fluid of infinite depth this is perhaps a surprising result. Figure 2 shows reflection energies for an incident wave of wavenumber k with varying submergence of the cylinder in the lower layer. The depth of the upper layer, d/a , is fixed and the angle of incidence, α_{inc} , is set greater than the critical angle so that there are no waves of wavenumber K propagating on the free surface. We can see from the figure that there is a value of f/a which gives total reflection for a particular frequency Ka . For cylinders closer to the interface two frequencies at which total reflection occurs exist. A similar effect is observed when fixing the submergence and varying the depth of the upper fluid. The existence of zeros of transmission at certain frequencies raises the possibility that trapped modes may exist in the presence of a pair of circular cylinders submerged in a two layer fluid. This will be the subject of further research. It is also possible to examine scattering by a cylinder in the upper fluid by exactly the same method and results for this case will be presented at the workshop.

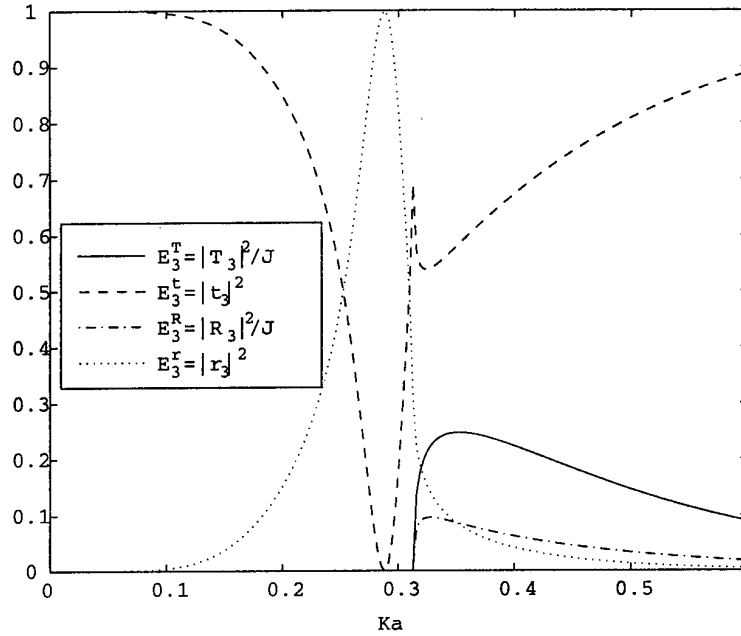


Figure 1: Transmission and reflection energies due to a wave of wavenumber k incident on a cylinder in the lower layer; $\rho = 0.5$, $d/a = 2.0$, $f/a = -1.1$ and $\alpha_{inc} = 0.33$.

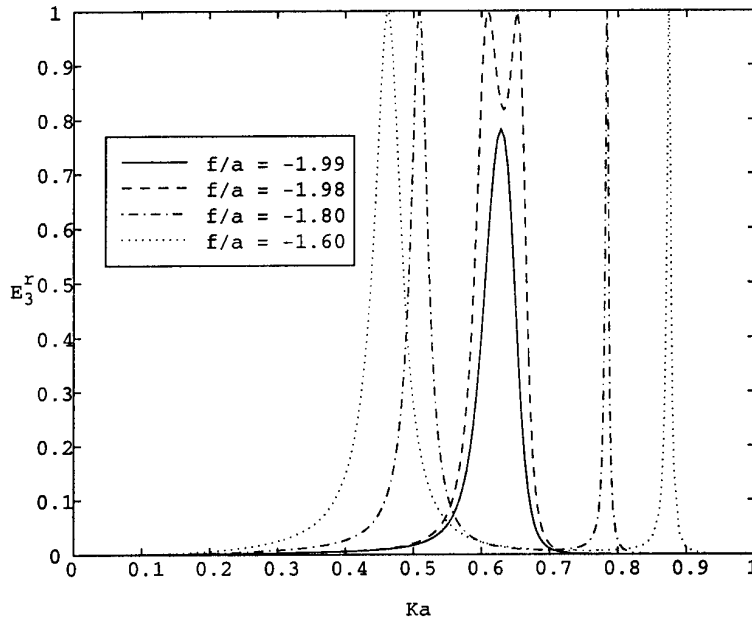


Figure 2: Reflection energies due to a wave of wavenumber k incident on a cylinder in the lower layer; $\rho = 0.5$, $d/a = 2.0$ and $\alpha_{inc} = 0.34$.

References

Linton, C.M. & McIver, M. 1995 'The interaction of waves with horizontal cylinders in two-layer fluids.' *J. Fluid Mechanics*, Vol. 304, pp. 213-229.

PECULIAR PROPERTIES OF SHIP-MOTION GREEN FUNCTIONS IN WATER OF FINITE DEPTH

XIAO-BO CHEN

Bureau Veritas, DTA, 17bis, Place des Reflets, 92400 Courbevoie (France)
Fax: 33-1-4291.3395 Email: xiao-bo.chen@bureauveritas.com

The potential flows generated by a source pulsating with constant frequency and advancing at constant horizontal speed are called ship-motion Green functions as they are involved in the kernel of integral equations established in the ship-motion problems, and include time-harmonic flows with forward speed and the special cases of Neumann-Kelvin steady flow (at zero frequency) and time-harmonic flows without forward speed. Further to an introductory treatise by Chen (1999) in the case of deep water, ship-motion Green functions in water of finite depth is considered here. Based on the formal decomposition of free-surface effects given by Noblesse & Chen (1995), the wave component (dominant in the far field) of ship-motion Green functions expressed as a single integral along the dispersion curves defined in the Fourier plane by the dispersion relation is analyzed. Especially, the peculiar properties of the wave component near the track of the source point located close to or at the free surface are studied by an asymptotic analysis.

1 Ship-motion Green functions in water of finite depth

Under the reference system moving with the source at the speed U along the positive x -axis defined by its (x, y) plane coinciding with the mean free surface and z -axis oriented positively upward, the ship-motion Green functions $G(\vec{\xi}, \vec{x}_s)$ representing the velocity potential of the flow created at a point $\vec{\xi} = (\xi, \eta, \zeta)$ by a pulsating-advancing source of unit strength located at a point $\vec{x}_s = (x_s, y_s, z_s)$, can be expressed as

$$G = G^S + G^F \quad (1)$$

where G^F accounts for free-surface effects and G^S is defined in terms of simple singularities

$$4\pi G^S = \sum_{n=-\infty}^{\infty} (-1)^n \left\{ -1/\sqrt{r^2 + (\zeta - z_s + 2nh)^2} + 1/\sqrt{r^2 + (\zeta + z_s + 2nh)^2} \right\} \quad (2)$$

in which $r = \sqrt{(\xi - x_s)^2 + (\eta - y_s)^2}$ and $h = H/L$ is the adimensional waterdepth with respect to the reference length L . The simple part G^S defined by (2) satisfies $G^S = 0$ at the free surface ($\zeta = 0$) and $\partial G^S / \partial \zeta = 0$ at the sea bed ($\zeta = -h$). The free-surface part G^F in (1) is defined by a double integral representing the Fourier superposition of elementary waves

$$4\pi^2 G^F = \lim_{\epsilon \rightarrow +0} \int_{-\infty}^{\infty} d\beta \int_{-\infty}^{\infty} d\alpha \frac{A e^{-i(\alpha x + \beta y)}}{D + i\epsilon \operatorname{sign}(D_f)} \quad (3)$$

with $(x, y) = (\xi - x_s, \eta - y_s)$ and A defined by

$$A = \cosh k(\zeta + h) \cosh k(z_s + h) / \cosh^2 kh \quad \text{with} \quad k = \sqrt{\alpha^2 + \beta^2} \quad (4)$$

Furthermore, the dispersion function D in (3) is given by

$$D = (f - F\alpha)^2 - k \tanh kh \quad (5)$$

in which $f = \omega \sqrt{L/g}$ and $F = U/\sqrt{gL}$ are respectively called adimensional frequency and Froude number, as ω and U stand respectively for wave encounter frequency and ship's speed, and L and g for ship's length (taken as the reference length) and the acceleration of gravity. The function $\operatorname{sign}(D_f)$ is given by

$$\operatorname{sign}(D_f) = \operatorname{sign}(\partial D / \partial f) = \operatorname{sign}(f - F\alpha) \quad (6)$$

Following the analysis by Noblesse & Chen (1995), the free-surface part G^F can be decomposed as $G^F = G^W + G^N$ with G^W the wave component and G^N the nonoscillatory component negligible in the far field. The wave component is defined by the single Fourier integral along the dispersion curves defined by the dispersion relation $D = 0$

$$4\pi G^W = -i \sum_{D=0} \int ds (\Sigma_1 + \Sigma_2) e^{-i(\alpha x + \beta y)} A / \|\nabla D\| \quad (7)$$

where $\sum_{D=0}$ means summation over all the dispersion curves and ds is the differential element of arc length of a dispersion curve. The function $\Sigma_1 = \text{sign}(D_f)$ is associated with the limit $\epsilon \rightarrow +0$ in (3) and ensures the satisfaction of the radiation condition, while the sign function Σ_2 is given in [2]

$$\Sigma_2 = \text{sign}(xD_\alpha + yD_\beta) \quad \text{with} \quad (D_\alpha, D_\beta) = (\partial D / \partial \alpha, \partial D / \partial \beta) \quad (8)$$

and used in the following analysis.

2 Dispersion relation and far-field waves

The dispersion function D defined by (5) is associated with the boundary condition on the free surface of wave diffraction-radiation with forward speed in water of finite depth. The dispersion relation $D = 0$ can be written as

$$(\tau - a)^2 - c \tanh(c/F_h^2) = 0 \quad \text{with} \quad \tau = fF \quad \text{and} \quad F_h = U/\sqrt{gH} \quad (9)$$

by using the speed-scaled Fourier variables $(a, b, c) = (\alpha, \beta, k)F^2$ and $H = Lh$ the waterdepth.

The equation (9) defines several distinct dispersion curves symmetric with respect to the axis $\beta = 0$ depending on both the value of τ and that of F_h . In deep water ($F_h = 0$), there exist two or three distinct dispersion curves at a value of τ smaller or larger than $1/4$. For $\tau < 1/4$, two open dispersion curves are located on the left and right half Fourier planes and one closed dispersion curve in between around the origin, as shown in Fig.1 by solid lines. At $\tau = 1/4$, the left open dispersion curve is connected to the closed dispersion curve. For $\tau > 1/4$, the left open dispersion curve goes on the right half Fourier plane near the origin while the right open dispersion curve keeps its similar form on the right half Fourier plane.

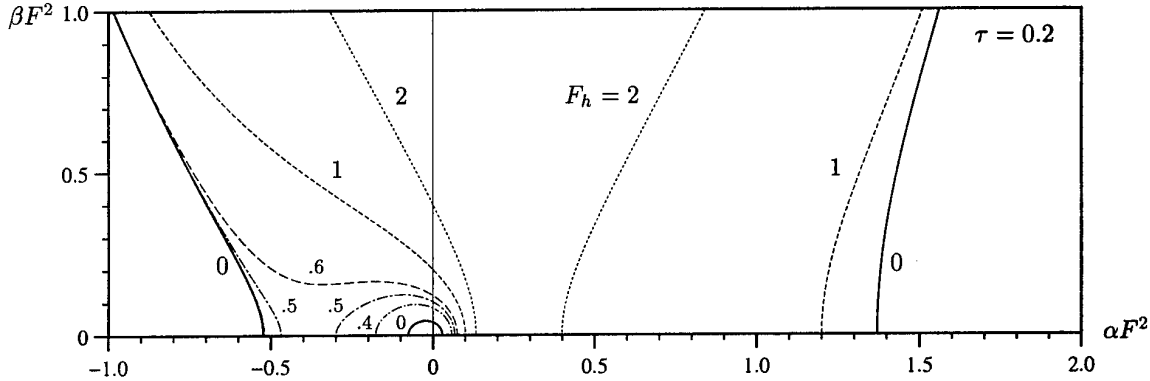


Fig.1 Dispersion curves at $\tau = 0.2$ for various values of F_h

In water of finite depth ($F_h > 0$), the dispersion curves change their form even for a constant value of τ as shown by Fig.1 which depicts the dispersion curves at $\tau = 0.2$ for different values of $F_h = 0, 0.4, 0.5, 0.6, 1$ and 2 . The left open dispersion curve and the closed dispersion curve are distinct for small values of F_h and connected to become one open dispersion curve for large values of F_h . The two open dispersion curves at large values of F_h become more and more vertical in the region near the axis $\beta = 0$ and their intersection points with the axis tend to $a = \tau$, i.e. $\alpha = f/F$. An interesting feature of dispersion curves is that the variations of the geometrical form associated with the variation of F_h at a constant $\tau > 0$ are quite similar to those associated with the variation of τ in deep water ($F_h = 0$).

The analysis by Chen & Noblesse (1997) shows that each dispersion curve is related to a wave system, and establishes a direct relationship between the geometrical properties of a dispersion curve and important aspects of the corresponding far-field waves including wavelength, direction of propagation, phase and group velocities and cusp angles. Applying to the case of finite-depth water, we have similar wave systems as in deep water: the inner-V waves are associated with the right open dispersion curve for $F > 0$, the ring waves associated with the closed dispersion curve and the outer-V waves with the left open dispersion curve for small values of both $\tau < 1/4$ and F_h while the partial ring and fan waves appear and are associated with the left open dispersion curve at larger values of F_h even at $\tau < 1/4$. Following the analysis in [4], the transverse and divergent waves associated with the open dispersion curves are respectively corresponding to the part of dispersion curves between two inflection points (symmetrical with respect to $\beta = 0$) and the part from the inflection points to infinity. Unlike the case of steady flows ($\tau = 0$) where the transverse waves disappear for super-critical flows $F_h > 1$, there exist still time-harmonic transverse waves (included in the inner-V wave system) and partial-ring waves (in partial-ring and fan waves) in the downstream for $F_h > 1$.

3 Wave component near the track of a source point

Similar to the analysis in [3] on the wave component of time-harmonic flows in deep water near the track of the source point close to or at the free surface, the asymptotic expansion of the open dispersion curves at large wavenumber is developed first. In fact, the dispersion relation (9) is found to be asymptotically

$$b = -1/2 + \tilde{a}^2 - \tau/\tilde{a} + O(\tilde{a}^{-2}) \quad \text{as } |\tilde{a}| \rightarrow \infty \quad \text{with } \tilde{a} = a - \tau \quad (10)$$

in which the first two terms on the right hand side represent a parabola with the axis $a = \tau$ and the vertex located at $(a, b) = (\tau, -1/2)$, and the parameter F_h disappears as the hyperbolic tangent function in (9) tends to the unity exponentially at large values of c . The open dispersion curves at $\tau = 0.2$ are depicted by Fig.2 which shows that all dispersion curves for different values of F_h tend to coincide at large wavenumber.

In (7), the values of $\Sigma_1 = \text{sign}(D_f)$ are equal to ± 1 respectively for the left ($a < a^-$) and right ($a > a^+$) open dispersion curves where $a^- (< \tau)$ and $a^+ (> \tau)$ are intersection points of the left and right open dispersion curves with the axis $\beta = 0$. At large wavenumber, $|D_\beta/D_\alpha| \approx 0$ along $D = 0$ so that $\Sigma_2 = \text{sign}(x D_\alpha) = \pm 1$ respectively for the left and right open dispersion curves, since we consider $x < 0$ and $y \rightarrow 0$ near the track of a source point. Furthermore, the identity

$$ds/\|\nabla D\| = d\alpha/|D_\beta| = F^{-2} da(c/b)C \quad (11)$$

with

$$C = 2 \cosh^2(c/F_h^2)/[2c/F_h^2 + \sinh(2c/F_h^2)] \quad (12)$$

valid for any point (a, b) along open dispersion curves can be used in (7) to define the wave component associated with the two open dispersion curves

$$2\pi F^2 G^W = -i \left(\int_{-\infty}^{a^-} - \int_{a^+}^{\infty} \right) AC \frac{c}{b} (E^+ + E^-) da \quad (13)$$

with $E^\pm = \exp(-iXa \pm iYb)$ and $(X, Y) = (x, y)/F^2$

The function A given by (4) can be expressed as

$$A = \frac{\exp(2c/F_h^2)}{4 \cosh^2(c/F_h^2)} (e^{-cZ_1} + e^{-cZ_2} + e^{-cZ_3} + e^{-cZ_4}) \quad (14)$$

with

$$Z_1 = -(\zeta + z_s)/F^2, \quad Z_2 = (\zeta + z_s)/F^2 + 4/F_h^2, \quad Z_3 = -(\zeta - z_s)/F^2 + 2/F_h^2, \quad Z_4 = (\zeta - z_s)/F^2 + 2/F_h^2 \quad (15)$$

By making use of (10), (12) and (14), the wave component defined by (13) can be expressed as

$$2\pi F^2 G^W = G_0^W + G_1^W + G_R^W \quad (16)$$

in which the first two terms are defined by

$$G_0^W = -ie^{-i\tau X} \left(\int_{-\infty}^{\tilde{a}^-} - \int_{\tilde{a}^+}^{\infty} \right) \sum_{n=1}^4 (\mathcal{E}_n^+ + \mathcal{E}_n^-) d\tilde{a} \quad \text{and} \quad G_1^W = \tau Y e^{-i\tau X} \left(\int_{-\infty}^{\tilde{a}^-} - \int_{\tilde{a}^+}^{\infty} \right) \sum_{n=1}^4 \frac{\mathcal{E}_n^+ - \mathcal{E}_n^-}{\tilde{a}} d\tilde{a} \quad (17)$$

with $\mathcal{E}_n^\pm = \exp[-(Z_n \pm iY)\tilde{a}^2 - iX\tilde{a} \pm iY/2]$ where $\tilde{a} = a - \tau$, and the remaining term defined by

$$G_R^W = \left(\int_{-\infty}^{\tilde{a}^-} - \int_{\tilde{a}^+}^{\infty} \right) \left[O(\tilde{a}^{-2}) + O(e^{-2\tilde{a}^2/F_h^2}) \right] d\tilde{a} \quad (18)$$

can be shown to yield a finite and non-oscillatory value near the source's track, since the integrand is absolutely integrable. The terms G_0^W and G_1^W defined by (17) can be further expressed by using the complex error function given in Abramowitz & Stegun (1967). By considering the asymptotic behavior of the complex error function obtained in [3], the leading terms of the wave component can be written asymptotically as $Y \rightarrow 0$

$$G_0^W = e^{-i\tau X} \sum_{n=1}^4 \widetilde{G}_{0n}^W + O(1) \quad \text{and} \quad G_1^W = \tau e^{-i\tau X} \sum_{n=1}^4 \widetilde{G}_{1n}^W + O(1) \quad (19)$$

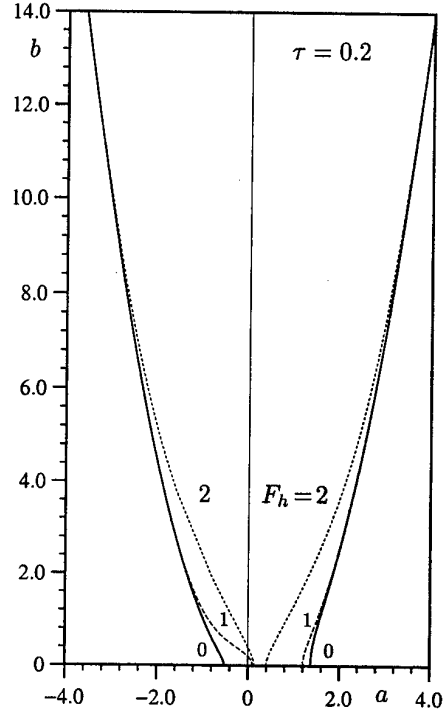


Fig.2 Open dispersion curves

$$\text{with } \widetilde{\mathcal{G}}_{0n}^W = \frac{e^{-Z_n X^2/(4R_n^2)}}{\sqrt{R_n/\pi/2}} \sin\left(\frac{\theta_n - Y}{2} - \frac{X^2 Y}{4R_n^2}\right) \quad \text{and} \quad \widetilde{\mathcal{G}}_{1n}^W = -i \frac{4Y e^{-Z_n X^2/(4R_n^2)}}{X \sqrt{1/(\pi R_n)}} \cos\left(\frac{\theta_n + Y}{2} + \frac{X^2 Y}{4R_n^2}\right) \quad (20)$$

in which the notations $R_n = \sqrt{Z_n^2 + Y^2}$ with Z_n defined by (15) and $\theta_n = \arctan(Y/Z_n)$ are used.

In summary, the wave component near the track of a pulsating-advancing source is expressed as

$$2\pi F^2 G^W = \widetilde{\mathcal{G}}^W + \widetilde{\mathcal{G}}_R^W \quad \text{with} \quad \widetilde{\mathcal{G}}^W = e^{-i\tau X} \left(\sum_{n=1}^4 \widetilde{\mathcal{G}}_{0n}^W + \tau \sum_{n=1}^4 \widetilde{\mathcal{G}}_{1n}^W \right) \quad (21)$$

in which the principal part $\widetilde{\mathcal{G}}^W$ is defined with the leading terms given by (20) and the remaining part $\widetilde{\mathcal{G}}_R^W = 2\pi F^2 G^W - \widetilde{\mathcal{G}}^W$ is finite with a magnitude of order $O(1)$ and non-oscillatory with respect to Y . The leading terms $\widetilde{\mathcal{G}}_{0n}^W$ and $\widetilde{\mathcal{G}}_{1n}^W$ are highly-oscillatory as $Y \rightarrow 0$ due to the term $X^2 Y/(4R_n^2)$ in the trigonometric functions which associates Y with an increasing wavenumber $X^2/(4R_n^2)$ for small R_n especially as $R_1 \rightarrow 0$ (when $Y \rightarrow 0$ and $Z_1 \rightarrow 0$). Furthermore, the leading term $\widetilde{\mathcal{G}}_{01}^W$ is singular near the track as $Y \rightarrow 0$ of the source located at the free surface ($Z_1 = 0$).

4 Discussions and conclusions

The singular and highly-oscillatory properties of ship-motion Green functions in water of finite depth represented by $\widetilde{\mathcal{G}}^W$ in (21) are illustrated in Fig.3 for a source point located at the free surface (left part) and for an immersed source point close to the free surface (right part) at $\tau = 0.2$ and $F_h = 1$ along $X = -5$. The real and imaginary parts are depicted respectively by the solid and dashed lines. This result can be considered as an extension of the study in [3] on deep-water Green functions to the more general case of finite-depth water. Furthermore, the formulations developed in [1] in deep-water case are useful in developing formulations for finite-depth Green functions since they possess similar properties.

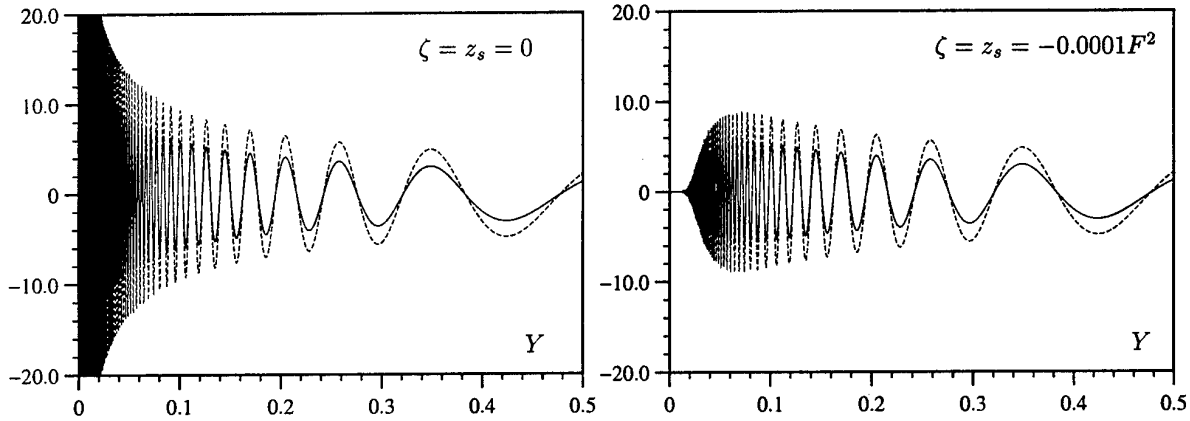


Fig.3 Wave component near the track of a source at the free surface (left) and an immersed source (right)

These peculiar properties of ship-motion Green functions indicate that usual panel methods based on a constant or linear distribution of sources and dipoles may not be reliable since the waterline integral carried out by numerical quadrature cannot be accurate, due to dramatic cancellations of highly-oscillatory values. The new results obtained in the present study are critically important in understanding all aspects of free-surface dispersive flows and very useful in providing a robust and consistent method based on a higher-order distribution of singularities and analytical integrations of the singular and highly-oscillatory terms such as studied in [6], to solve 3D ship-motion problems in a fully satisfactory way.

References

- [1] CHEN X.B. 1999 An introductory treatise on ship-motion Green functions. *Proc. 7th Intl Conf. on Num. Ship Hydro. Nantes (France)*, 1-21.
- [2] NOBLESSE F. & CHEN X.B. 1995 Decomposition of free-surface effects into wave and near-field components. *Ship Tech. Res.* 42, 167-185.
- [3] CHEN X.B. 1998 On singular and highly-oscillatory properties of ship-motion Green functions.
- [4] CHEN X.B. & NOBLESSE F. 1997 Dispersion relation and far-field waves. *12th IWWF*.
- [5] ABRAMOWITZ M. & STEGUN I.A. 1967 Handbook of mathematical functions. *Dover Publications*.
- [6] DOUTRELEAU Y. & CHEN X.B. 1999 Line integrals on the free surface in ship-motion problems. *14th IWWF*.

DYNAMICS OF THE TRANSIENT LEADING PART OF A WAVE TRAIN

DIDIER CLAMOND & JOHN GRUE

Department of Mathematics, University of Oslo, Norway

1 Introduction

The dynamics of waves along the ocean surface determines the input parameters in wave analysis of stationary offshore structures and moving ships, and in the calculation of induced loads in tension legs and risers. Recent experimental investigations at the University of Oslo have shown that the leading waves in a wave group may introduce special loads on the structures. This includes in particular high-frequency loads (ringing). The experimental studies have prompted the present investigation. Questions we have in mind include why leading waves of a wave train can reach appreciable heights? What are the induced velocities and accelerations of the waves? Do moderately steep to steep waves exhibit special features compared with small amplitude waves?

To analyze these questions we derive a very accurate model for a wave train generated by a pneumatic wavemaker.

2 Mathematical formulations

The classical two-dimensional gravity wave equations for a potential flow over a horizontal bottom are

$$\phi_{xx} + \phi_{yy} = 0 \quad \text{for} \quad -h \leq y \leq \eta, \quad (1)$$

$$\phi_y = 0 \quad \text{at} \quad y = -h, \quad (2)$$

$$\phi_y - \eta_t - \eta_x \phi_x = 0 \quad \text{at} \quad y = \eta, \quad (3)$$

$$\tilde{p} + g\eta + \phi_t + \frac{1}{2}\phi_x^2 + \frac{1}{2}\phi_y^2 = 0 \quad \text{at} \quad y = \eta, \quad (4)$$

where ϕ is the velocity potential, h is the mean depth, g is the acceleration due to gravity, η is the surface elevation from rest and \tilde{p} is a forcing pressure at the surface.

To numerically solve the equations, it is convenient to rewrite the system (1)–(4) in a form which involves quantities at the surface only. Using the derivative laws

$$\tilde{\phi}_x = \widetilde{\phi_x} + \eta_x \widetilde{\phi_y}, \quad \tilde{\psi}_x = \widetilde{\psi_x} + \eta_x \widetilde{\psi_y}, \quad \tilde{\phi}_t = \widetilde{\phi_t} + \eta_t \widetilde{\phi_y},$$

(ψ being the stream function, $\psi=0$ at the bottom, and we denote quantities at the surface by tildes), and the flow conservation law, equations at the surface can be rewritten as:

$$\eta_t + \tilde{\psi}_x = 0, \quad (5)$$

$$\tilde{\phi}_t + g\eta + \frac{1}{2} \frac{\tilde{\phi}_x^2 - \tilde{\psi}_x^2 + 2\eta_x \tilde{\phi}_x \tilde{\psi}_x}{1 + \eta_x^2} = -\tilde{p}. \quad (6)$$

These two equations give temporal evolutions of η and $\tilde{\phi}$. To complete the system we need an equation for ψ . Using the holomorphy of $\phi+i\psi$, the equation for $\tilde{\psi}$ is obtained from the Cauchy integral formula. An infinite tank does not exist in the real world and

it is not convenient for computations. We then consider a tank of a finite length L , in which $0 \leq x \leq L$. Since we shall use a forcing pressure with an even symmetry, the tank is extended for $x < 0$ by symmetry. Moreover, it is advantageous to periodise the fluid domain to compute solutions with Fast Fourier Transforms. We therefore consider a $2L$ -periodic problem. The bottom impermeability is taken into account *via* a Schartzian symmetry. Finally, the equation for ψ is

$$\begin{aligned} \tilde{\psi}(x, t) = & \frac{1}{2L} \text{PV} \int_{-L}^L \frac{(\tilde{\phi}' - \eta'_x \tilde{\psi}') \sin \frac{x'-x}{L/\pi} + (\tilde{\psi}' + \eta'_x \tilde{\phi}') \sinh \frac{\eta'-\eta}{L/\pi}}{\cosh \frac{\eta'-\eta}{L/\pi} - \cos \frac{x'-x}{L/\pi}} dx' \\ & - \frac{1}{2L} \int_{-L}^L \frac{(\tilde{\phi}' - \eta'_x \tilde{\psi}') \sin \frac{x'-x}{L/\pi} + (\tilde{\psi}' + \eta'_x \tilde{\phi}') \sinh \frac{2h+\eta'+\eta}{L/\pi}}{\cosh \frac{2h+\eta'+\eta}{L/\pi} - \cos \frac{x'-x}{L/\pi}} dx', \end{aligned} \quad (7)$$

where PV is the principal value and $\tilde{\phi}' = \tilde{\phi}(x', t)$, etc. The system (5)–(7) is equivalent to the original one and it involves quantities at the surface only. Moreover, it is purely Eulerian.

To generate from rest a wave of angular frequency σ , we choose a localized pneumatic wavemaker of the form

$$\tilde{p} = gA \sin(\sigma t) H(t) \exp(-x^2/2\lambda^2), \quad (8)$$

where H is the Heaviside function, and parameters A and λ are tuned to obtain a wave-maker of maximum efficiency (Wehausen & Laitone 1960).

The analytic solution of the linearized equations is (for $L = \infty$)

$$\eta = \frac{A\lambda\sigma t}{\sqrt{2\pi}} \int_{-\infty}^{\infty} \frac{\omega e^{-\frac{k^2\lambda^2}{2}}}{\omega + \sigma} \left[\text{sinc} \frac{(\omega - \sigma)t}{2} \cos \frac{(\omega + \sigma)t}{2} - \text{sinc} \sigma t \right] e^{ikx} dk, \quad (9)$$

$$\tilde{\phi} = \frac{-gA\lambda\sigma t}{\sqrt{2\pi}} \int_{-\infty}^{\infty} \frac{\omega e^{-\frac{k^2\lambda^2}{2}}}{\omega + \sigma} \text{sinc} \frac{(\omega - \sigma)t}{2} \sin \frac{(\omega + \sigma)t}{2} e^{ikx} dk, \quad (10)$$

$$\tilde{\psi} = \frac{-iA\lambda\sigma t}{\sqrt{2\pi}} \int_{-\infty}^{\infty} \frac{\omega^3 k^{-1} e^{-\frac{k^2\lambda^2}{2}}}{\omega + \sigma} \text{sinc} \frac{(\omega - \sigma)t}{2} \sin \frac{(\omega + \sigma)t}{2} e^{ikx} dk, \quad (11)$$

with $\omega^2 = gk \tanh kh$ and $i^2 = -1$. This solution is used in the numerical scheme.

3 Numerical resolution

Our goal was to obtain a highly accurate approximation, even for long time evolution.

The periodic tank is discretized with a constant spatial step. Derivatives are computed with FFT (pseudo-spectral method). The scheme is hence of infinite order in space and very fast.

The Cauchy integral is discretized with the trapezoidal formula, which is of infinite order for a periodic regular function. This leads to the resolution of an implicit linear system. Calculations are achieved with an optimized SSOR method.

The temporal resolution is carried out in Fourier space. The resolution is very stiff for high frequencies, and thus the time step must be very small. Moreover, the amount of phase error increases with the Fourier wavenumbers and with the length of the time interval. The accuracy condition is more demanding than the stability condition. To avoid this problem, we split equations in linear and nonlinear parts, and we make an

analytical integration of the linear part (e.g. (9)–(11)). Only the nonlinear terms remain. Fornberg & Whitham (1978) have used this type of transformation to solve the Korteweg & de Vries equation. The treatment of the linear term is both unconditionally stable and exact. The stability limit and the accuracy are considerably increased. The evolution of nonlinear terms are computed with the fourth-order Runge–Kutta–Gill algorithm.

This scheme is very accurate and relatively fast. It is written in MATLAB and runs on a PC.

4 Preliminary results

We have computed transient short waves in relative deep water. First we can compare the surface elevations given by the exact numerical solution and the linear solution. In the quasi-steady part of the wave train, the linear and nonlinear solutions are not very different (Fig. 1). This means that a high-order analytical theory can predict correctly the wave field. On the other hand, in the transient leading part, differences in amplitudes and phases are very important. In the far field where the elevation is small, linear and nonlinear solutions are comparable in both amplitudes and phases. This proves that the significant differences in the transient leading part are not due to numerical inconsistencies. We observe that the first significant crest focuses energy. It has an oscillating motion, increasing and decreasing alternatively with an amplification until breaking. Such behavior seems to be difficult to describe with classical high-order theories.

We can also consider the horizontal acceleration at the surface (Fig. 2). The back side of the leading crest has an important negative acceleration, which is not the case for the quasi-steady part of the wave train. This phenomenon could have important effects on an obstacle.

Our work is still in progress. Further and more definite results will be presented at the workshop.

References

- FORNBERG, B., WHITHAM, G. B. (1978) A numerical and theoretical study of certain nonlinear wave phenomena. *Phil. Trans. Soc. Lon.*, **289**, 373–404.
- WEHAUSEN, J. V., LAITONE, E. V. (1960) *Handbuch der Physik*, vol. **9**, 446–776, Springer-Verlag.

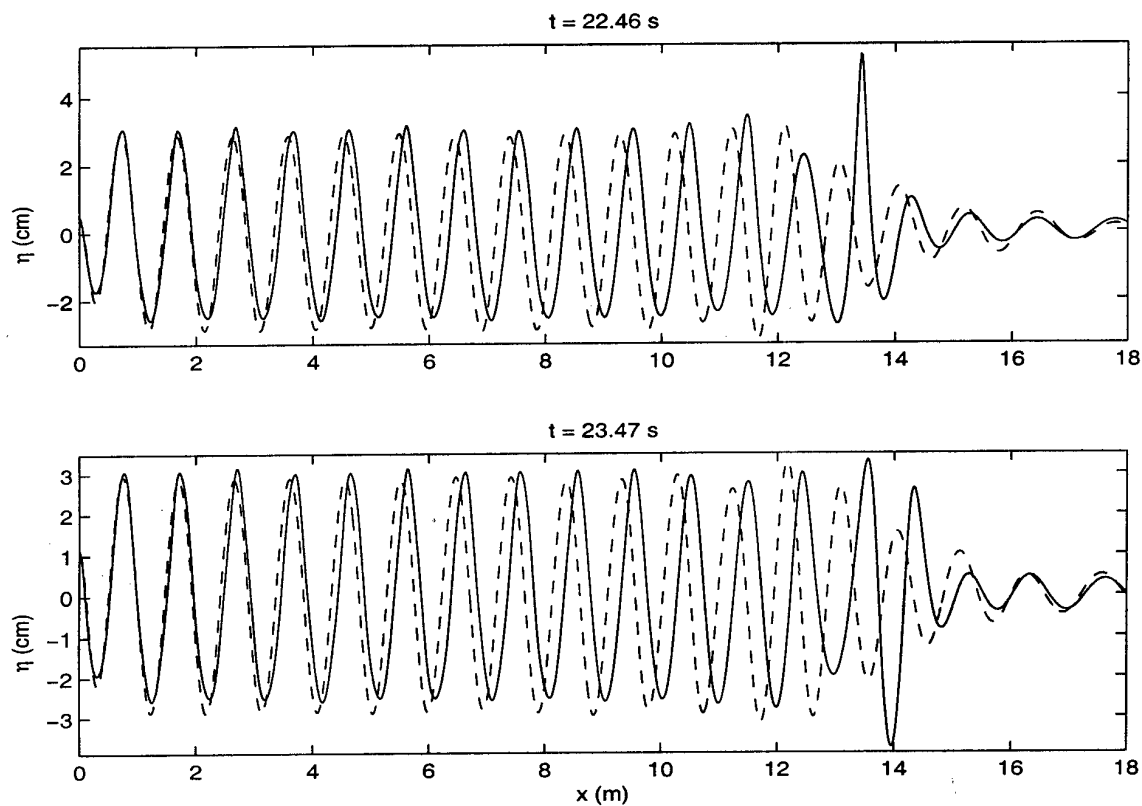


Figure 1: *Surface elevations at two different times.*

(—) exact, (---) linear, for $g = 9.8 \text{ m s}^{-2}$, $h = 0.6 \text{ m}$, $\sigma = 8 \text{ rad s}^{-1}$.

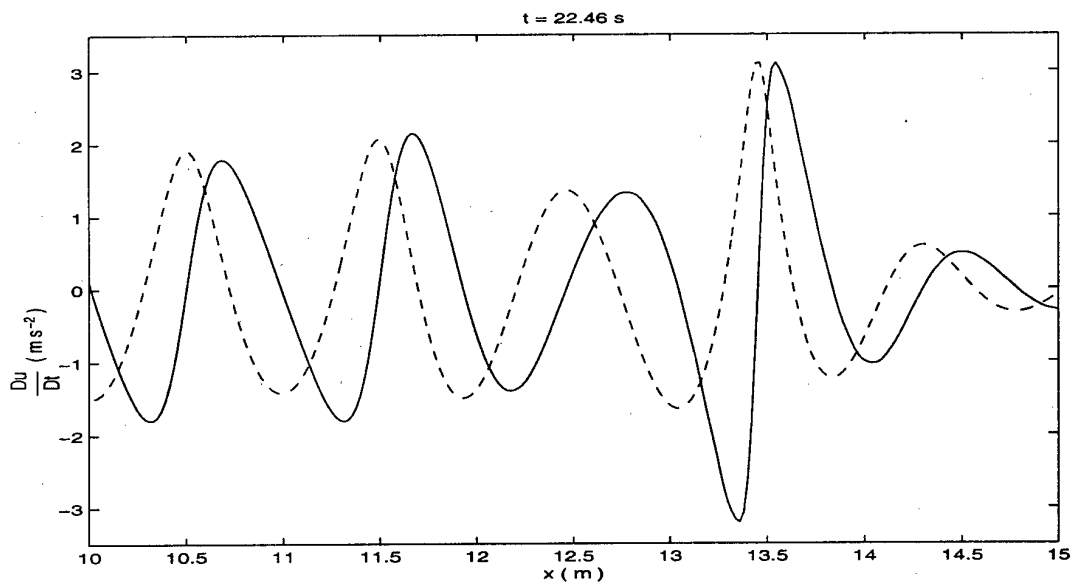


Figure 2: *Horizontal acceleration at the surface.*

(—) acceleration, (---) surface elevation, for $g = 9.8 \text{ m s}^{-2}$, $h = 0.6 \text{ m}$, $\sigma = 8 \text{ rad s}^{-1}$.

FREE SURFACE ANTI-ROLL TANK SIMULATIONS WITH A VOLUME OF FLUID BASED NAVIER-STOKES SOLVER

E.F.G. van Daalen¹, J. Gerrits², G.E. Loots², A.E.P. Veldman²

¹) Maritime Research Institute Netherlands (MARIN)

P.O. Box 28, 6700 AA Wageningen, The Netherlands

²) University of Groningen, Department of Mathematics

P.O. Box 800, 9700 AV Groningen, The Netherlands

1. Introduction

Ship roll stabilization has received attention for more than a century. From a wide variety of anti-roll devices, the anti-roll tank (ART) is considered for its simplicity, low cost and action at low or even zero speed. In the past several types of ARTs have been proposed and tried in practice. The simplest type of ART is the free surface ART (FS-ART), see Figure 1.

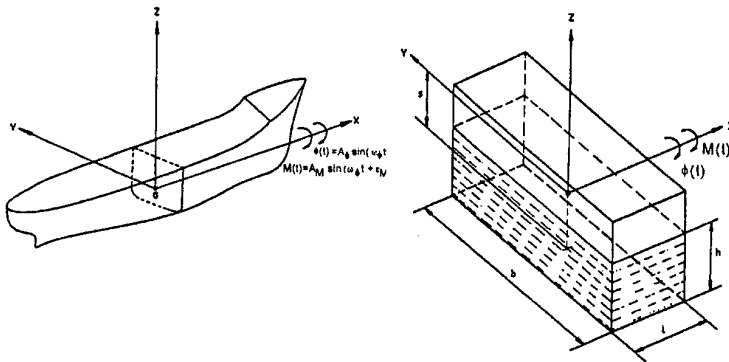


Figure 1: Definition of geometry and tank dimensions.

The physical phenomenon in a FS-ART must be classed in the group of wave problems in shallow water. The main stabilizing action is created by a bore travelling up and down the tank, which is a strongly non-linear phenomenon. Therefore it is unlikely that any linear or weakly non-linear theory will produce reliable approximations for the FS-ART action. For this reason an experimental procedure was followed by Van den Bosch and Vugts (1966) to collect information about the performance of the FS-ART. It was forced to execute sinusoidal oscillations about a fixed axis while amplitude and phase of the moment about this axis were measured. Systematic measurements were done for a wide range of tank and motion parameters. This experimental data set is used at MARIN to account for the effect of a FS-ART on the rolling motion of a ship. Since these frequency domain results are useful in regular wave conditions only, there is a need for a numerical time domain method to predict the tank forces and moments for a ship sailing in irregular waves.

The computer program ComFlo solves the Navier-Stokes equations for unsteady incompressible fluid flow in complex geometries. The method is based on the Volume Of Fluid (VOF) method - see Hirt and Nichols (1981). ComFlo has found many applications in a variety of flow problems, ranging from sloshing in fuel containers onboard satellites to green water loading on the fore deck of a ship. The program has proven to be robust and accurate. All experiments of Van den Bosch and Vugts were simulated with ComFlo as a first step in an extensive validation program. The results are presented in this abstract. For a description of the mathematical model and the numerical implementation in ComFlo we refer to Gerrits (1996) or Loots (1997).

2. Free surface anti-roll tank simulations

Figure 2 presents the non-dimensional amplitude $A_M/(\rho g b^3 l)$ and phase angle ε_M of the roll moment as functions of the non-dimensional roll frequency $\omega_\phi/(g/b)^{1/2}$, for one combination of the position s of the tank, the undisturbed water depth h and the roll amplitude A_ϕ . This level of agreement is observed throughout the entire parameter space, see Van Daalen et al (1999). The influence of some of the tank and motion parameters is discussed next.

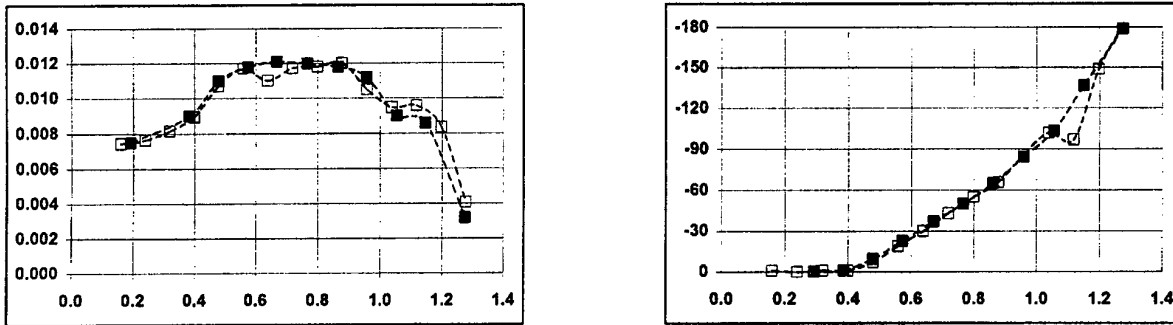


Figure 2: Roll moment amplitude (left) and phase (right) as function of roll frequency. Open and closed symbols denote calculated resp. measured results. $h/b=0.08$, $A_\phi=5.7^\circ$.

When the *amplitude of oscillation* increases, the strength of the bore and thereby the roll moment amplitude increases too. This influences the curve of the phase angles as well. An example is given in Figure 3. The dependence of the roll moment amplitude on the roll angle can be approximated by the square root, as shown in Figure 4.

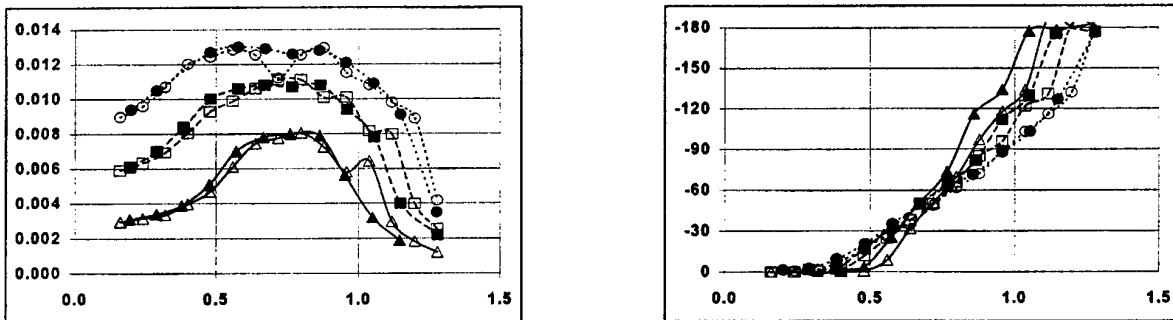


Figure 3: Roll moment amplitude (left) and phase (right) as function of roll frequency. Open and closed symbols denote calculated results and measured results respectively. $\triangle A_\phi=1.9^\circ$; $\blacksquare A_\phi=3.8^\circ$; $\bullet A_\phi=5.7^\circ$.

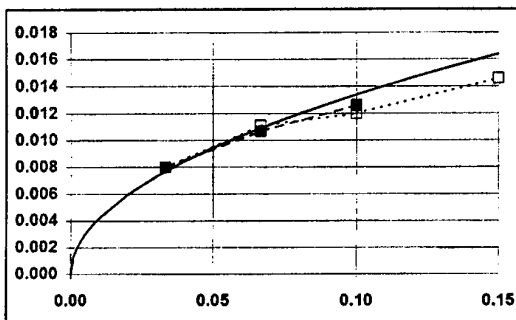


Figure 4: Roll moment amplitude at the actual (measured or calculated) resonance frequency as function of roll amplitude. Open and closed symbols denote calculated results and measured results respectively. Solid line denotes square root approximation.

The *water depth* is a particularly important parameter, because it is clear that for a certain tank width the only possibility to change the natural period of the water transfer is a change in water depth. And it is equally clear that at or near this natural period the water transfer is largest and circumstances are most favorable for roll damping. The effect of increasing water depth is twofold as shown in Figure 5: In the first place the curve of phase angles versus roll frequency is shifted to the higher frequency range. When they are plotted versus the frequency - to - resonance frequency ratio, then there is hardly any noticeable difference except for the higher frequencies, that is for the region in which the bore transforms into the solitary wave. In the second place the moment amplitude increases because of the larger amount of water in the tank. But here again the increase is not linear, but can be approximated by the square root, as shown in Figure 6.

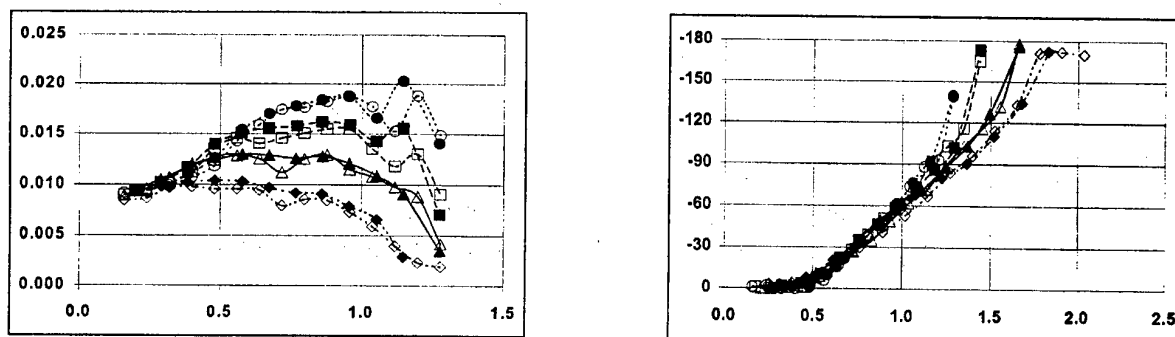


Figure 5: Roll moment amplitude (left) and phase (right) as function of roll frequency. Open and closed symbols denote calculated resp. measured results.

◆ $h/b=0.04$; ▲ $h/b=0.06$; ■ $h/b=0.08$; ● $h/b=0.10$. $A_\phi=5.7\text{deg}$.

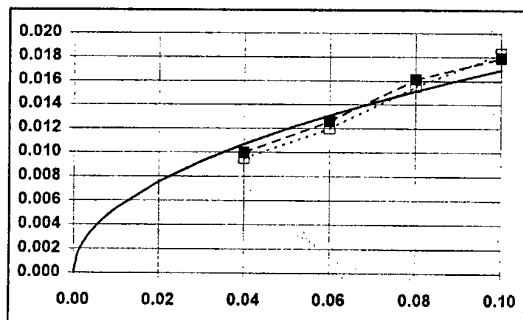


Figure 6: Roll moment amplitude at actual resonance frequency as function of water depth. Open and closed symbols denote calculated results and measured results respectively. Solid line denotes square root approximation.

The fact that physically the phenomenon in the tank is a wave problem implies that for scaling up Froude's law has to be followed. Therefore it can be expected that the moment exerted by the tank fluid is proportional to the fourth power of the model scale. Or, considering the moment per unit tank length in a two-dimensional problem this will be proportional to the third power of the model scale, which will be clearly governed by the *tank breadth*. To create a comparable flow pattern the tanks should be filled according to the same ratio of water depth to tank breadth. When plotted in a non-dimensional way, it appears that the results fully confirm the expectations, as can be observed from Figure 7.

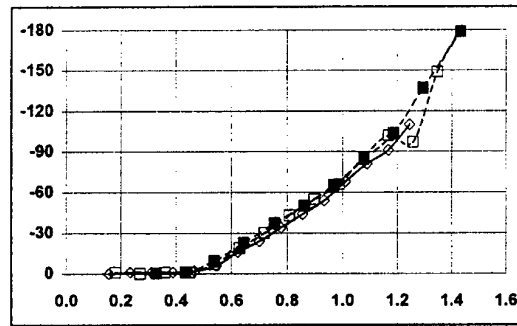
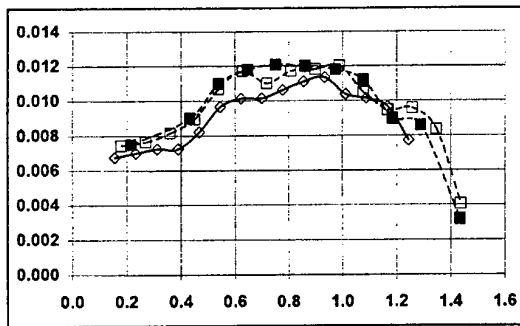


Figure 7: Roll moment amplitude (left) and phase (right) as function of roll frequency. Open and closed symbols denote calculated results and measured results respectively. ■ $b=1.00\text{m}$; ◆ $b=0.75\text{m}$. $h/b=0.08$, $A_\phi=5.7\text{deg}$.

3. Discussion and future work

We have presented the application of the computer program ComFlo to the problem of water sloshing in a free surface anti-roll tank. For various combinations of motion and tank parameters the measured and calculated results for the roll moment amplitude and phase were found to be in good agreement.

This promising result is the first step in a validation program to demonstrate the applicability of ComFlo in the design of ARTs. Numerical simulations of a free surface ART in coupled sway-roll motion have been done as well and will be validated using the results from ongoing experiments.

Numerical simulations of the water motion inside a U-tube ART will be reported at the workshop as well: These results indicate that the method can be applied to U-tube ARTs as well.

As a third step in the validation process, the three-dimensional water motion in ARTs will be simulated and validated using experimental results.

The ultimate goal of this research is the fully nonlinear six degree of freedom coupling of the ART action with a time domain ship motion program.

References

1. Gerrits, J.: Three-dimensional liquid sloshing in complex geometries. Master's thesis, University of Groningen, Department of Mathematics, August 1996.
2. Hirt, C.W. and Nichols, B.D.: Volume of Fluid (VOF) method for the dynamics of free boundaries. Journal of Computational Physics, Vol. 39, pp. 201-225, 1981.
3. Loots, G.E.: Free surface flow in three-dimensional complex geometries using enhanced boundary treatment. Master's thesis, University of Groningen, Department of Mathematics, June 1998.
4. Van Daalen, E.F.G., Van Doeveren, A.G., Driessen, P.C.M., Visser, C.: Two-dimensional free surface anti-roll tank simulations with a Volume Of Fluid based Navier-Stokes solver, MARIN Report No. 15306-1-OE, October 1999.
5. Van den Bosch, J.J. and Vugts, J.H.: Roll damping by free surface tanks. Shipbuilding Laboratory of the Technical University of Delft, Report No. 83S, April 1966.

THE USE OF THE CL-EQUATION AS A MODEL FOR SECONDARY CIRCULATIONS

M.W. DINGEMANS AND A.C. RADDER

WL|DELFT HYDRAULICS AND RIJKSWATERSTAAT-RIKZ, THE NETHERLANDS

1. Introduction. In problems of interaction of waves and currents, it is customary that the influence of the current on the waves gets most attention. However, waves also influence the current itself. The most general and precise way to formulate this is via the so-called generalised Lagrangian mean (GLM) method, introduced by Andrews and McIntyre (1978a,b); for an introduction we refer to McIntyre (1980) and §2.10.6 of Dingemans (1997). As shown by Leibovich (1980), see also Radder (1994) and Dingemans et al. (1996), the mean-current equation in GLM coordinates simplifies under mild conditions to the Craik-Leibovich equation in Eulerian coordinates (also denoted as CL equation), which reads:

$$(1.1) \quad \partial_t \bar{\mathbf{u}} + (\bar{\mathbf{u}} \cdot \text{grad}) \bar{\mathbf{u}} + \text{grad} \bar{\pi} = \bar{\mathbf{u}}^S \wedge \bar{\boldsymbol{\omega}} + \rho^{-1} \text{div} \bar{\boldsymbol{\sigma}}',$$

where $\text{div} \bar{\boldsymbol{\sigma}}' \equiv \partial \bar{\sigma}'_{ik} / \partial x_k$, the pressure term $\bar{\pi}$ is given by $\bar{\pi} = \bar{p} / \rho + gz + \frac{1}{2} \langle \tilde{\mathbf{u}} \cdot \tilde{\mathbf{u}} \rangle$, $\bar{\mathbf{u}}$ is the (Eulerian) mean velocity, $\bar{\mathbf{u}}^S$ is the Stokes drift, defined as the difference between the Lagrangian and Eulerian mean velocity, and $\tilde{\mathbf{u}}$ is the wave part of the velocity (the total velocity is considered the sum of the current and the wave part and the Stokes part of the velocity: $\mathbf{u} = \bar{\mathbf{u}} + \tilde{\mathbf{u}} + \bar{\mathbf{u}}^S$). Notice that we have $\bar{\mathbf{u}}^S = (\bar{u}^S, \bar{v}^S, 0)^T$, $\bar{\mathbf{u}} = (\bar{u}, \bar{v}, \bar{w})^T$ and $\bar{\boldsymbol{\omega}} = \text{curl} \bar{\mathbf{u}}$. It has been shown that Langmuir circulations can be generated through an instability mechanism of this CL equation; for a review is referred to Leibovich (1983). Essential for this to happen is the existence of the Stokes drift and the shear of the mean current, i.e., the vortex force $\bar{\mathbf{u}}^S \wedge \bar{\boldsymbol{\omega}}$ is instrumental in the generation of these Langmuir vortex rolls. Because the Stokes drift is a wave-related quantity, it can be argued that one of the effects of waves on currents is the generation of Langmuir circulations.

Although no viscosity is taken into account in the usual CL-equation-formulations, it is advantageous to do so. This has to do with the so-called Large Eddy Simulation (LES) programs. Viscosity in these equations is needed for obtaining shear in the mean-current equations, which, in its turn, is needed to generate the vortex-force term. We take the (eddy) viscosity coefficient to be isotropic because of the scales on which the flow occurs here. Applying the Boussinesq-hypothesis, the stresses $\bar{\sigma}'_{ik}$ are approximated as¹ $\rho^{-1} \bar{\sigma}'_{ik} = \nu_T (\partial \bar{u}_i / \partial x_k + \partial \bar{u}_k / \partial x_i)$, while the eddy viscosity ν_T has still to be determined.

2. The equations for primary and secondary flow. One of the explanations of Langmuir circulations rests upon the supposition that an instability mechanism in the CL equation is responsible for the generation of these vortex rolls. We suppose that the mean current $\bar{\mathbf{u}}$ is disturbed. These perturbations are supposed to be of periodic nature, i.e., $\hat{\mathbf{u}}$ obeys a WKBJ-type of behaviour which is natural, also in view of the resulting (periodic) vortex-roll motions. We then have the situation that $\bar{\mathbf{u}}$ can be written as $\bar{\mathbf{u}} = \mathbf{U} + \hat{\mathbf{u}}$, where $\hat{\mathbf{u}}$ is the disturbance which is responsible for the formation of the vortex rolls and \mathbf{U} is the velocity of the basic state. For the other quantities $\bar{\pi}$ and $\bar{\boldsymbol{\omega}}$ in the CL equation the same kind of perturbations are assumed to exist, viz. a basic state (denoted with capitals) and a perturbed state (denoted by hatted variables).

Because the eddy viscosity is a function of the velocity $\bar{\mathbf{u}}$ and the depth z , a perturbation of ν_T is also necessary. It is shown by Dingemans (1999) that the perturbation of ν_T has no effect on the present results, for the order considered. We now simply write $\bar{\nu}_T$ in order to stress the approximation.

We now insert the expressions $\bar{\mathbf{u}} = \mathbf{U} + \hat{\mathbf{u}}$, $\bar{\boldsymbol{\omega}} = \boldsymbol{\Omega} + \hat{\boldsymbol{\omega}}$, $\bar{\boldsymbol{\sigma}}' = \boldsymbol{\Sigma}' + \hat{\boldsymbol{\sigma}}'$, $\bar{\mathbf{u}}^S = \mathbf{U}^S$ in the CL equation and the continuity equation. Notice that the wave-related quantities, $\bar{\mathbf{u}}^S$ and $\tilde{\mathbf{u}}$, are not perturbed. Because of the periodicity of the perturbed quantities, averaging over a period and length large to the characteristic period and length of the perturbations, yields for the basic state:

$$(2.1) \quad \partial_t \mathbf{U} + (\mathbf{U} \cdot \text{grad}) \mathbf{U} + \langle (\hat{\mathbf{u}} \cdot \text{grad}) \hat{\mathbf{u}} \rangle + \text{grad} \Pi = \mathbf{U}^S \wedge \boldsymbol{\Omega} + \rho^{-1} \text{div} \boldsymbol{\Sigma}',$$

Notice that $\langle (\hat{\mathbf{u}} \cdot \text{grad}) \hat{\mathbf{u}} \rangle$ are the Reynolds stresses. The evaluation of these stresses is the subject of this study. The equation for the perturbation is obtained by subtraction of (2.1) from the full equation:

$$(2.2) \quad \partial_t \hat{\mathbf{u}} + (\hat{\mathbf{u}} \cdot \text{grad}) \mathbf{U} + (\mathbf{U} \cdot \text{grad}) \hat{\mathbf{u}} + (\hat{\mathbf{u}} \cdot \text{grad}) \hat{\mathbf{u}} - \langle (\hat{\mathbf{u}} \cdot \text{grad}) \hat{\mathbf{u}} \rangle + \text{grad} \hat{\pi} = \mathbf{U}^S \wedge \hat{\boldsymbol{\omega}} + \rho^{-1} \text{div} \hat{\boldsymbol{\sigma}}'.$$

The continuity equation splits in one for the basic state and one for the perturbed velocity:

$$(2.3) \quad \text{div} \mathbf{U} = 0 \quad \text{and} \quad \text{div} \hat{\mathbf{u}} = 0.$$

¹We write σ'_{ik} with the prime, denoting the part of the stress tensor without the pressure, see Dingemans (1997, p. 4.)

3. Simplified equations. We now adopt a number of simplifications. Firstly, we suppose that the basic current \mathbf{U} is uniform in the horizontal directions, $\mathbf{U} = \mathbf{U}(z, t)$ and, moreover, no vertical component exists: $\mathbf{U} = (U(z, t), V(z, t), 0)^T \equiv \mathbf{U}^h$. This means that (nearly) horizontal nearly-uniform shear flows are considered. As pointed out in Dingemans (1997, pp. 193 and 201), the vertical component of the mean current can only be neglected when the bottom is (nearly) horizontal. It is therefore also supposed that *the bottom is horizontal*, i.e. $\nabla h(x, y) = 0$ where $\nabla = (\partial_x, \partial_y)^T$. Secondly, the wave-induced perturbation $\hat{\mathbf{u}}$ is supposed to be single-periodic in one specific direction θ . Thirdly, with θ the angle between the positive x -axis and the path of propagation s and n the lateral direction, we also suppose that $\partial \hat{\mathbf{u}}(x, y, z, t) / \partial n = 0$. Fourthly, the Stokes drift \mathbf{U}^S is supposed to be only a function of depth, i.e., $\mathbf{U}^S = \mathbf{U}^S(z) = (U^S(z), V^S(z), 0)^T$. As the eddy viscosity is also a function of space and time through its dependence on the friction velocity, we now suppose that $\bar{\nu}_T = \bar{\nu}_T(|\mathbf{U}^*(\mathbf{X}, T)|, z)$ with $\mathbf{X} = \delta \mathbf{x}$ and $T = \delta t$ and $\delta \ll 1$. The simplified momentum equations then become (details in Dingemans, 1999):

$$(3.1) \quad \partial_t \mathbf{U}^h + \langle \partial_{x_j} (\hat{u}_j \hat{\mathbf{u}}) \rangle^h + \nabla \Pi_0 = \partial_z (\bar{\nu}_T \partial_z \mathbf{U}^h) \quad \text{where} \quad \Pi_0 = \bar{P}/\rho + \frac{1}{2} \langle \hat{\mathbf{u}} \cdot \hat{\mathbf{u}} \rangle.$$

We note that in the present approximation the vortex force has only a vertical component and therefore plays no role in the horizontal mean momentum equations. For the perturbed velocity we get:

$$(3.2a) \quad \partial_t \hat{\mathbf{u}}^h + \hat{w} \partial_z \mathbf{U}^h + (\mathbf{U}^h \cdot \nabla) \hat{\mathbf{u}}^h + \nabla \hat{\pi} = (\mathbf{U}^S \wedge \hat{\omega})^h + \rho^{-1} (\text{div } \hat{\sigma}')^h$$

where the viscosity term is a function on $\hat{\mathbf{u}}$ and $\bar{\nu}_T$. The vertical momentum equation becomes:

$$(3.2b) \quad \partial_t \hat{w} + (\mathbf{U}^h \cdot \nabla) \hat{w} + \partial_z \hat{\pi} = (U^S \hat{\omega}_2 - V^S \hat{\omega}_1) 2 \partial_z (\bar{\nu}_T (\partial_z \hat{w})) + \bar{\nu}_T \partial_{x_j} (\partial_{x_j} \hat{w} + \partial_z \hat{u}_j) \quad j = 1, 2.$$

4. Linear stability analysis. A solution of Eqs. (3.2) is sought now. Following Cox (1997) an asymptotic solution is sought by applying a long-wave expansion. This expansion is based on the observation that Langmuir circulations have a much larger horizontal extent (in the direction perpendicular to the circulation) than the extent of the circulation cells. The boundary conditions for the perturbed velocities then are:

$$(4.1) \quad \partial_z \hat{\mathbf{u}} = \partial_z \hat{\mathbf{v}} = w = 0 \quad \text{at} \quad z = 0 \quad \text{and} \quad \partial_z \hat{\mathbf{u}} = \partial_z \hat{\mathbf{v}} = w = 0 \quad \text{at} \quad z = -h.$$

It is noted that the conditions (4.1) do not comply with the no-slip conditions, which should apply for viscous flow as is considered here. It seems reasonable to limit this stability analysis to the bulk of the fluid, just outside the bottom boundary layer. We now assume a slow growth rate σ and the expansions of $\hat{\mathbf{u}}$ is:

$$(4.2a) \quad \hat{\mathbf{u}}(\mathbf{x}, z, t) = \mathbf{u}'(z) e^{\vartheta} \quad \text{with} \quad \mathbf{u}'(z) = \hat{\mathbf{u}}_0(z) + \varepsilon \hat{\mathbf{u}}_1(z) + \varepsilon^2 \hat{\mathbf{u}}_2(z) + \dots \quad \text{where}$$

$$(4.2b) \quad \vartheta(\mathbf{x}, t) = i \varepsilon \tilde{\mathbf{k}} \cdot \mathbf{x} + \varepsilon \sigma t \quad \text{and} \quad \sigma = \sigma_1 + \varepsilon \sigma_2 + \dots$$

with $\tilde{\mathbf{k}} = (\tilde{k}_1, \tilde{k}_2)^T$ the scaled wave number vector: $\tilde{\mathbf{k}} = \mathbf{k}/\varepsilon$ and $|\tilde{\mathbf{k}}| = \mathcal{O}(1)$. For $\hat{\pi}$ we use a similar expansion. In this way one focusses attention to the most unstable wave numbers \mathbf{k} , which are $\mathcal{O}(\varepsilon)$.

The expansions (4.2) are substituted in the linearised momentum equations for the perturbed velocities (3.2a) and (3.2b). The continuity equation yields $\varepsilon i \tilde{\mathbf{k}} \cdot \mathbf{u}' + \partial w' / \partial z = 0$. In the zeroth-order equation the continuity equation yields $w_0 = \text{constant}$, and from the boundary conditions it then follows that $w_0 \equiv 0$. The zeroth-order momentum equations then simplify to $\partial_z u_0 = \partial_z v_0 = 0$. Using the boundary conditions it follows that u_0 and v_0 are constant in the fluid domain. It then also follows that π_0 is constant.

In first-order the continuity equation is $\tilde{\mathbf{k}} \cdot \mathbf{u}_0 + \partial_z w = 0$ and the boundary conditions in first order are $\partial_z u_1 = \partial_z v_1 = w_1 = 0$ at $z = -h$ and $z = 0$. This results in $w_1 \equiv 0$. From the bottom condition we have the condition $\tilde{k}_1 u_0 + \tilde{k}_2 v_0 = 0$ which serves as a relation between the unknown constants u_0 and v_0 . The horizontal first-order momentum equations are integrated over depth (from $z = -h$ to $z = 0$). We introducing vertically-averaged quantities, denoted by a double overbar by $\overline{\overline{\mathbf{U}}} = (\overline{\overline{U}}, \overline{\overline{V}})^T = h^{-1} \int_{-h}^0 \mathbf{U}(z) dz$ and similarly for $\overline{\overline{\mathbf{U}^S}}$. These vertically-averaged equations are solved for σ_1 and π_0 . It is clear that σ_1 is imaginary, otherwise it had to be zero since $u_0 \neq 0$ and $v_0 \neq 0$. We therefore write $\sigma_1 = i \sigma_1^{(i)}$. We obtain as solutions $\pi_0 = \mathbf{u}_0 \cdot \overline{\overline{\mathbf{U}^S}}$ and $\sigma_1^{(i)} = -\tilde{\mathbf{k}} \cdot (\overline{\overline{\mathbf{U}}} + \overline{\overline{\mathbf{U}^S}})$.

In second order we proceed as follows. Differentiation of the second-order continuity equation yields $i \tilde{k}_1 \partial_z (\bar{\nu}_T \partial_z u_1) + i \tilde{k}_2 \partial_z (\bar{\nu}_T \partial_z v_1) + \partial_z (\bar{\nu}_T \partial_z^2 w_2) = 0$. Expressions for $\partial_z (\bar{\nu}_T \partial_z u_1)$ and $\partial_z (\bar{\nu}_T \partial_z v_1)$ follow from the (unaveraged) first-order equations. For w_2 we then obtain the differential equation:

$$(4.3) \quad \partial_z (\bar{\nu}_T \partial_z^2 w_2) = |\tilde{\mathbf{k}}|^2 \mathbf{u}_0 \cdot (\overline{\overline{\mathbf{U}^S}} - \mathbf{U}^S).$$

The right-hand side is thus zero when no shear is present (i.e., when U^S is constant over the depth). Recapitulating, we have the unknown constants u_0 and v_0 with relation $\tilde{k}_1 u_0 + \tilde{k}_2 v_0 = 0$ between them, and solutions for π_0 and σ_1 . For the first non-zero vertical velocity component we have the differential equation (4.3). In next section we consider the energy equation for the perturbed velocities in order to close the system.

5. The Landau-Stuart equation. The energy equation for the perturbed velocities \hat{u} follows by scalar multiplication of the momentum equation for the perturbed velocities with \hat{u} . Introducing the mean kinetic energy by $\mathcal{K} = \iiint dx dy dz \frac{1}{2} \hat{u} \cdot \hat{u} \equiv \int_{-h}^0 dz \langle \frac{1}{2} \hat{u} \cdot \hat{u} \rangle$, the total change in kinetic energy may be written down, e.g. Joseph (1976, pp. 11-12). Using the simplifications of §3, the result is:

$$(5.1) \quad \frac{d\mathcal{K}}{dt} \equiv \frac{d}{dt} \left\{ \int_{-h}^0 dz \left\langle \frac{1}{2} \hat{u} \cdot \hat{u} \right\rangle \right\} = - \int_{-h}^0 dz \left\{ \langle \hat{w} \hat{u}_j \rangle \frac{\partial}{\partial z} (U_j^h + U_j^S) \right\} - \int_{-h}^0 dz \left\{ \bar{v}_T \left\langle \left(\frac{\partial \hat{u}_i}{\partial x_j} \right)^2 \right\rangle \right\}.$$

An amplitude $A_0 = \sqrt{u_0^2 + v_0^2}$ is introduced and we also write $\varepsilon^2 w_2(z) = \varepsilon^2 \tilde{k}^2 m_2(z) = k^2 m_2(z)$ where $\tilde{k}^2 = \tilde{k}_1^2 + \tilde{k}_2^2$. Instead of expansion (4.2) we now have the expansion

$$(5.2) \quad \hat{u}(x, z, t) = \frac{1}{2} \left(\tilde{k}_2 / \tilde{k}, -\tilde{k}_1 / \tilde{k}, \varepsilon^2 \tilde{k}^2 m_2(z) \right)^T A_0 e^{\vartheta} + CC$$

with $\vartheta = i\varepsilon \tilde{k} \cdot x + i\sigma_1^{(i)} t$. For m_2 we have the differential equation

$$(5.3) \quad \partial_z (\bar{v}_T(z) \partial_z^2 m_2) = \tilde{k}^{-1} \left[\tilde{k}_2 (\overline{U^S} - U^S) - \tilde{k}_1 (\overline{V^S} - V^S) \right] \equiv G,$$

with the boundary conditions $m_2(z) = \partial_z^2 m_2(z) = 0$ at $z = -h$ and $z = 0$. Introducing the notation $q = \tilde{k}_1 / \tilde{k}_2$, the solution for $m_2(z; q)$ may be written as

$$(5.4) \quad m_2(z; q) = \int_0^z d\hat{z} f(\hat{z}; q) + \frac{z}{h} \int_0^{-h} d\hat{z} f(\hat{z}; q) \quad \text{with} \quad f(\hat{z}; q) = \int_0^{\hat{z}} dz' \frac{1}{\bar{v}_T(z')} \int_{-h}^{z'} dz'' G(z''; q).$$

We consider the simplified energy equation (5.1). Following Stuart (1958), we now suppose the amplitude A_0 to be a function of time, $A_0 = A_0(t)$. Using the expansion (5.2) in this energy equation leads to the so-called Landau-Stuart equation:

$$(5.5) \quad \frac{dA_0^2}{dt} = 2\alpha A_0^2 - \ell A_0^4 \quad \text{with exact solution} \quad A_0^2 = 1 / \left[\frac{\ell}{2\alpha} + \left(\frac{1}{A_0^2} - \frac{\ell}{2\alpha} \right) e^{-2\alpha t} \right],$$

where the coefficients α and ℓ consist of expressions in m_2 , the Stokes drift, etc., see Dingemans (1999). We have $\ell > 0$, but the sign of α is not clear beforehand. An exact solution is found by rewriting Eq. (5.5) in one for A_0^{-2} , which equation turns out to be linear. When $\alpha > 0$, the solution (5.5) approaches the equilibrium solution, $A_0^2 \rightarrow A_e^2 = 2\alpha / \ell$ for $t \rightarrow \infty$. When $\alpha < 0$, $A_0 \rightarrow 0$ for $t \rightarrow \infty$.

6. The alignment of the vortex rolls. To obtain the direction of the axis of the vortex rolls we now use the *principle of exchange of stability* (PES). Some remarks on PES can be found in Joseph (1976, pp. 26, 27 and 55). The method was originally proposed by Stuart (1958). We have investigated the stability of perturbations of the form $\hat{u}(x, z, t) = u' \exp[\vartheta(x, t)]$. Here is $\vartheta = i\tilde{k} \cdot x + \varepsilon\sigma t$, indicating that in horizontal space the solution is periodic and in time growth or decay of the solutions may occur. It was found that only an imaginary part of σ resulted. When this part is unequal to zero, then neutrally-stable solutions exist. When the imaginary part is also zero for one or more of the solutions of σ , then a bifurcation of the basic flow into a secondary flow may result. This secondary flow may be stable or unstable, depending on the prevailing conditions. Because we look for the generation of secondary currents due to the instability of the basic current, PES may well be valid in our case. We have $\sigma_1^{(i)} = 0$ when $\tilde{k}_c \cdot (\overline{U} + \overline{U^S}) = 0$, or, in terms of q , $q_c (\overline{U} + \overline{U^S}) + (\overline{V} + \overline{V^S}) = 0$.

The wave number vector \tilde{k} points in the direction with the smallest periodicity of the periodic structure. In the perpendicular direction the component is very small, signifying that the extent of the periodicity is very large. The axis of the vortex roll is thus in a direction perpendicular to \tilde{k} . For the special case that both \overline{U} and $\overline{U^S}$ are in the x -direction so that $\tilde{k}_2 = 0$, we have $\tilde{k}_1 = 0$, signifying infinitely long rolls in the x -direction.

7. Maximal growth of the perturbations and the Reynolds stresses. Instead of PES we use a different method to determine the critical direction given by $q_c = \tan \varphi_c$ for which maximum growth of the perturbations occurs. When considering infinitesimal perturbations, the Landau-Stuart equation can be linearised to give $\max_q dA_0^2/dt = 2\alpha A_0^2$. Maximum growth is obtained for $d\alpha/dq = 0$ together with the condition that $d^2\alpha/dq^2 < 0$. Using the expressions for the coefficients of the Landau-Stuart equation, the value of q_c can be determined, see Dingemans (1999).

The Reynolds stresses $\langle \hat{w}\hat{u} \rangle = \varepsilon^2 \langle w_2\hat{u} \rangle$ and $\langle \hat{w}\hat{v} \rangle$ can now be calculated. Returning to unscaled variables we see that for the case that $\alpha > 0$ we have $\langle \hat{w}\hat{u} \rangle = \frac{1}{2}k^2 A_0^2 m_2 / \sqrt{1+q^2}$ and $\langle \hat{w}\hat{v} \rangle = \frac{1}{2}k^2 A_0^2 q m_2 / \sqrt{1+q^2}$. When $\alpha < 0$ the Reynolds stresses are zero. For the amplitude A_0 we now use the equilibrium solution $A_e = \sqrt{2\alpha/\ell}$. From the resulting expressions (see Dingemans, 1999) it appears that, to leading order, the Reynolds stresses do not depend on $k = \varepsilon \tilde{k}$, meaning that they are independent of the extent of the circulation cells (the size being proportional to $1/k$).

8. An example. We consider an example from flume experiments by Klopman (1994). Measurements show the influence of waves on currents, see Figure 8.1. Taking the logarithmic velocity profile $U(z) = (\bar{u}^*/\kappa) \log \{(z+h)/z_0\}$ for $-h+z_0 \leq z \leq 0$, we have $\bar{u}^*/\kappa = 0.018$ with $z_0 = 0.4$ mm and $h = 0.5$ m. For this case an approximate calculation of the radiation stress, using long-wave approximations, yields a current contribution $u_w = -0.24h \log(2+z/h)$. Determination of the mean current to be the same in the no-waves and waves case yields a constant $c = 0.0464$ m/s. In Figure 8.1 is given the $U(z)$ and the curve for $U(z) + u_w(z) + c$. It is clear that the effect of a backwards leaning velocity profile for following waves is included in the present theory.

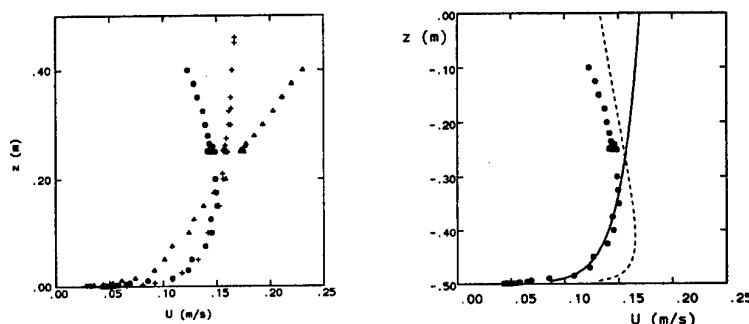


FIGURE 8.1. Left: Klopman's (1994) measurements; +: current without waves, o: waves following the current, Δ: waves opposing the current. Right: drawn line: logarithmic current profile, interrupted line: total velocity, circles: Klopman's measurements for following waves.

REFERENCES

- [1] Andrews, D.G. and McIntyre, M.E., 1978a. An exact theory of nonlinear waves on a Lagrangian mean flow. *J. Fluid Mechanics* **89**(4), pp. 609-646.
- [2] Andrews, D.G. and McIntyre, M.E., 1978b. On wave action and its relatives. *J. Fluid Mechanics* **89**(4), pp. 647-664.
- [3] Cox, S.M., 1997. Onset of Langmuir circulation when shear flow and Stokes drift are not parallel. *Fluid Dynamics Research* **19**, pp. 149-167.
- [4] Dingemans, M.W., 1997. *Water Wave Propagation over Uneven Bottoms*. World Scientific, Singapore, 967 pp.
- [5] Dingemans, M.W., 1999. 3D wave-current modelling; a model for secondary circulations. *WL|Delft Hydraulics Report Z2612*, 68 pp.
- [6] Dingemans, M.W., van Kester, J.A.Th.M., Radder, A.C. and Uittenbogaard, R.E., 1996. The effect of the CL-vortex force in 3D wave-current interaction. *Proc. 25th Int. Conf. on Coastal Engineering, Orlando*, pp. 4821-4832.
- [7] Drazin, P.G. and Reid, W.H., 1981. *Hydrodynamic Stability*. Cambridge University Press, 527 pp.
- [8] Joseph, D.D., 1976. *Stability of Fluid Motion*, Vol. I. Springer Tracts in Natural Philosophy, Vol. 27, Springer Verlag, Berlin, 282 pp.
- [9] Klopman, G., 1994. Vertical structure of the flow due to waves and currents. *Delft Hydraulics*, Report H840.30 Part II.
- [10] Leibovich, S., 1980. On wave-current interaction theories of Langmuir circulations. *J. Fluid Mechanics* **99**(4), pp. 715-724.
- [11] Leibovich, S., 1983. The form and dynamics of Langmuir circulations. *Ann. Rev. of Fluid Mech.* **15**, pp. 391-427.
- [12] McIntyre, M.E., (1980). Towards a Lagrangian-mean description of stratospheric circulations and chemical transports. *Phil. Trans. Roy. Soc. London* **A296**, 129-148.
- [13] Radder, A.C., 1994. A 3D wave-current interaction theory based on the CL equation. *Rijkswaterstaat/RIKZ report RIKZ/OS-94.163x*, Dec. 1994.
- [14] Rodi, W., 1980. *Turbulence Models and their Application in Hydraulics*. IAHR, Delft, 104 pp.
- [15] Stuart, J.T., 1958. On the non-linear mechanics of hydrodynamic stability. *J. Fluid Mech.* **4**, pp. 1-21.

The Squat of a Vessel with a Transom Stern

Lawrence J. Doctors and Alexander H. Day

The University of New South Wales, Sydney, NSW 2052, Australia

The University of Glasgow, Glasgow, G12 8QQ, Scotland

Summary

The inviscid linearized near-field solution for the flow past a vessel with a transom stern is developed within the framework of classical thin-ship theory. However, the hollow in the water behind the stern is represented here by an extension to the usual centerplane source distribution employed to model the hull itself. As a consequence, the resistance, sinkage, and trim can be computed by means of an integration of the resulting pressure distribution over the wetted surface of the vessel. Comparison of the theoretical results with a systematic series of twelve models shows good correlation with the towing-tank data.

1 Introduction

Previous work on the subject of prediction of resistance of marine vehicles, such as monohulls and catamarans, has shown that the *trends* in the curve of total resistance with respect to speed can be predicted with excellent accuracy, using the traditional Michell (1898) wave-resistance theory.

These principles were advanced in the research of Doctors and Day (1997). There, transom-stern effects were included in the theory by accounting for the hollow in the water behind the vessel in an approximate manner. The wave resistance was assumed to be simply that of the vessel plus its hollow in the water behind the transom. To this drag they added the so-called hydrostatic resistance, which represents the drag associated with the transom stern not being wetted. A good level of correlation between the predictions and the experimental data for a large set of conditions for the tests on a towing-tank catamaran model was demonstrated.

In the current work, we will compute the near-field solution to the flow using the classical thin-ship approximation. This idea clearly represents a considerable addition to the complexity of the solution which contrasts with the traditional far-field method.

2 Mathematical Formulation

Figure 1(a) shows the main geometric features representing a typical hull. The hollow that is developed in the water behind the transom stern is also depicted. A regular meshing, consisting of flat panels or "facets" possessing a rectangular base, is employed for the purpose of the numerical calculation of the pressure, or profile, resistance. This type of panel is algebraically simpler than the "pyramids" or "tents" which were previously employed. The use of flat facets implies a higher level of discontinuity on the hull surface. On the other hand, numerical convergence tests for wave resistance, based on the two types of panels, showed that a similar number of panels was required in either case; namely, 40 panels in the longitudinal direction and 8 panels in the vertical direction.

The solution for the potential due to a point source of strength Q , obtained by Wehausen and Laitone (1960, p. 484, Equation (13.36)), is

$$\phi = -\frac{Q}{4\pi r} + \frac{Q}{4\pi r'} + \varphi, \quad (1)$$

where we have defined

$$r = \sqrt{(x-x')^2 + (y-y')^2 + (z-z')^2}, \quad (2)$$

$$r' = \sqrt{(x-x')^2 + (y-y')^2 + (z+z')^2}, \quad (3)$$

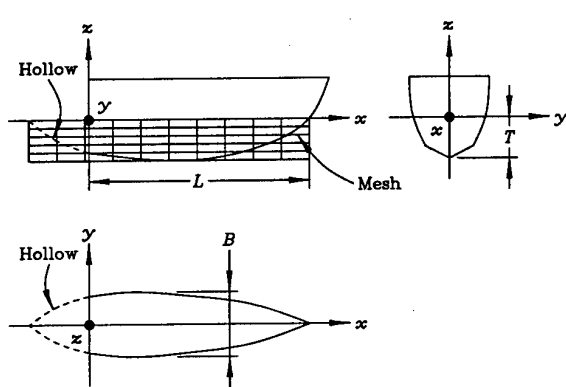


Figure 1: Definition of the Problem
(a) Fitting Mesh to the Vessel

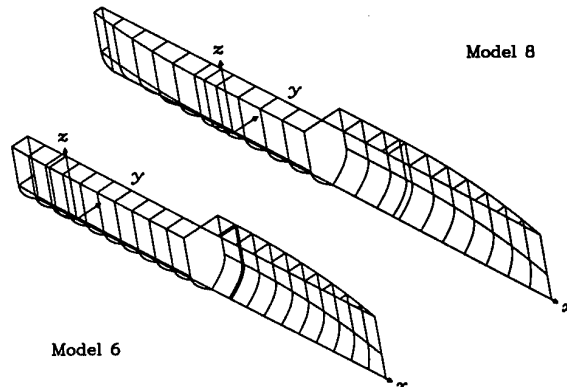


Figure 1: Definition of the Problem
(b) Lego Model 6 and Model 8

and

$$\varphi = -\frac{Qk_0}{4\pi^2} \int_{-\pi}^{\pi} d\theta \int_0^{\infty} dk \frac{\exp\{k[z+z' + i(x-x')\cos\theta + i(y-y')\sin\theta]\}}{k_0 - k\cos^2\theta - i\mu\cos\theta}. \quad (4)$$

The first term in Equation (1) can be integrated for a constant-strength source panel and a constant-slope field panel in the so-called Galerkin manner. The result for the induced longitudinal gradient of the potential at the field panel is

$$\phi_{x,1} = -\frac{1}{4\pi} \sigma_j \sum_{l=-1}^1 w_l \sum_{m=-1}^1 w_m \cdot G_4(i, j, l, m), \quad (5)$$

in which G_4 is the third integral of the $1/r$ function, with respect to z , x , and z , and is just

$$G_4(x, z) = \frac{1}{2} z^2 \sinh^{-1}(x/|z|) + xz \sinh^{-1}(z/|x|) - \frac{1}{2} x \sqrt{x^2 + z^2}. \quad (6)$$

The weighting factor is given by the formula

$$w_l = \begin{cases} -1 & \text{for } l = -1 \\ 2 & \text{for } l = 0 \\ -1 & \text{for } l = 1 \end{cases} \quad (7)$$

and the required arguments in Equation (6) are defined by

$$x = x_i - x_j + l\Delta x, \quad (8)$$

$$z = z_i - z_j + m\Delta z. \quad (9)$$

The third term can also be integrated with respect to the wavenumber k , as well as with respect to the spatial coordinates, to yield

$$\phi_{x,3} = -\frac{i}{2\pi^2 k_0^2} \sigma_j \int_{-\pi/2}^{\pi/2} \cos^3\theta \sum_{l=-1}^1 w_l \sum_{m=-1}^1 w_m \cdot F_4(Z(i, j, l, m)) d\theta. \quad (10)$$

Here, the special complex wave function F_4 is closely related to the exponential integral and was defined by Doctors and Beck (1987). The argument is given by

$$Z(i, j, l, m) = k(z_i + z_j + m\Delta z) + ik_x(x_i - x_j + l\Delta x). \quad (11)$$

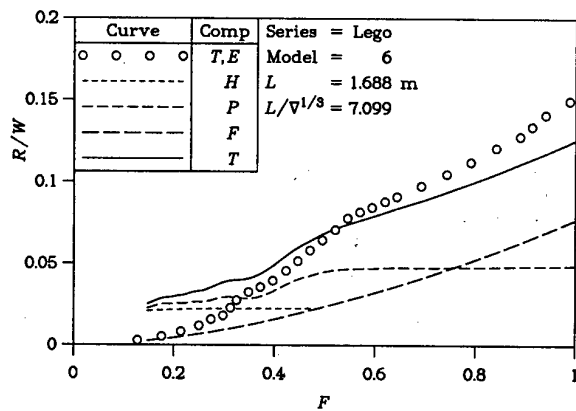


Figure 2: Resistance Components
(a) Lego Model 6

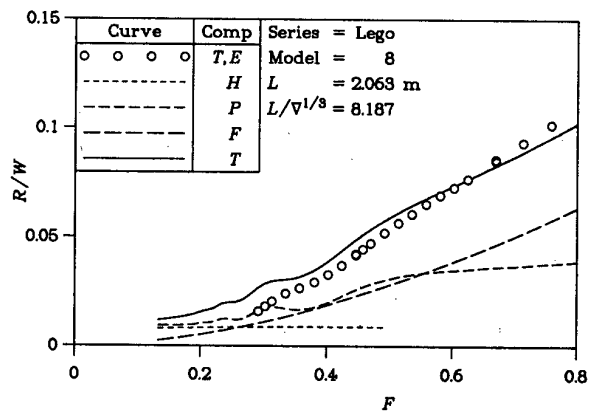


Figure 2: Resistance Components
(b) Lego Model 8

Once the total gradient of the potential at the field panels has been computed, one can determine the pressure on the surface of the hull. The forces and moments on the vessel are then found from this pressure distribution. Initially, the vessel will not be in equilibrium. Numerical experiments showed that using the traditional *hydrostatic stiffness* coefficients worked well for iterating the sinkage and trim of the vessel.

3 Experiments and Numerical Results

The twelve so-called Lego towing-tank ship models were constructed from up to seven segments. The philosophy behind the models is the original Wigley (1934) simple ship. The bow and stern segments have parabolic waterplanes. The bow segments, stern segments, and the parallel middle-body segments all possess parabolic cross sections. Figure 1(b) shows pictorial views of two of the test models. Each model had a beam of 0.150 m and a draft of 0.0938 m. Model 6 had a length of 1.688 m and a prismatic coefficient of 0.8494. Model 8 had a length of 2.063 m and a prismatic coefficient of 0.8275.

Figure 2 shows the resistance components for the two models. The curves show respectively the total-experimental, low-speed hydrostatic, pressure, frictional, and total-theoretical resistance, as functions of the Froude number. The calculations include the effects of sinkage and trim and employ the near-field theory. One sees that the total-theoretical resistance correctly approaches the theoretical hydrostatic resistance at sufficiently low speeds. Of course, the theory ignores real-fluid effects of a partially filled transom hollow; hence the total-theoretical resistance overestimates the total-experimental resistance at low speeds. The correlation could no doubt be improved at higher speeds by employing a form factor to the 1957 International Towing Tank Committee (ITTC) formula for the frictional resistance.

Four theories are compared with experiments on Model 6 in Figure 3(a). In two of the theoretical cases, the model has been free to sink and trim. In two of the theoretical cases, the current near-field approach has been used, while in the other two theoretical cases it is has not (the traditional far-field approach has been used, instead). It is seen that the worst prediction occurs if the experimental sinkage and trim are used in a far-field method, while the current approach apparently gives the second best agreement. Consideration of a form factor would alter the veracity of this statement. Figure 3(b) shows data for Model 8, where one sees that the current theory provides the best correlation.

Finally, we present a comparison for the dimensionless sinkage and the dimensionless trim in Figure 4. Remarkably good agreement is demonstrated for both Model 6 and Model 8.

4 Conclusions

Future research should be directed toward a refinement of the model detailing the precise shape of the transom-stern hollow. Details of the numerical procedure can also be improved, particularly by establishing a data bank of near-field influence functions.

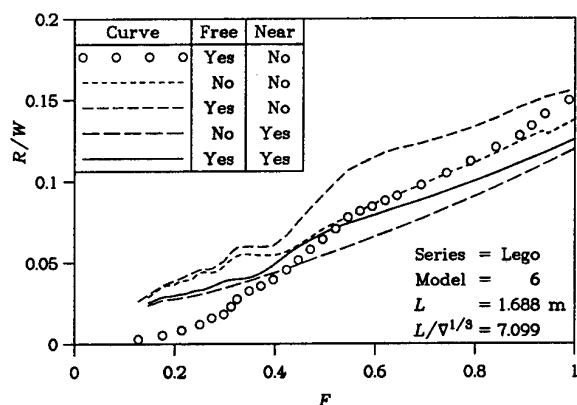


Figure 3: Total Resistance Predictions
(a) Lego Model 6

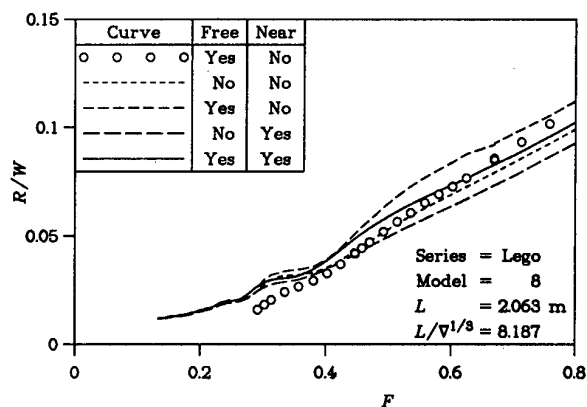


Figure 3: Total Resistance Predictions
(b) Lego Model 8

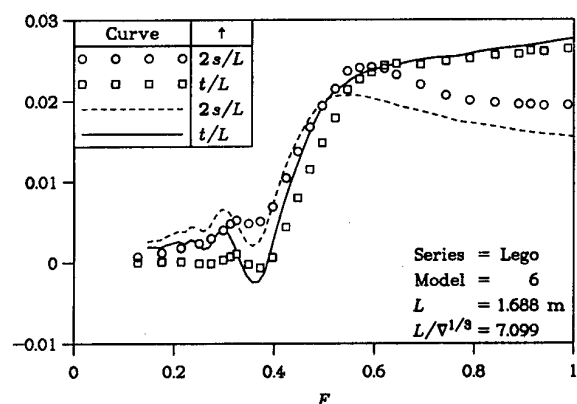


Figure 4: Sinkage and Trim Predictions
(a) Lego Model 6

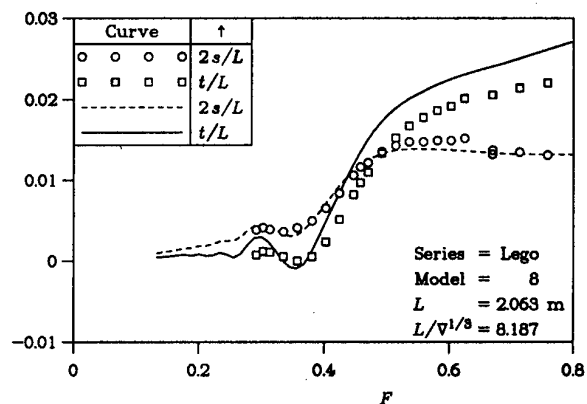


Figure 4: Sinkage and Trim Predictions
(b) Lego Model 8

5 Acknowledgments

The authors would like to thank the Directorate of Naval Platform Systems Engineering, Department of Defence, for its support through Contract 9627MZ. They also gratefully acknowledge the assistance of the Australian Research Council (ARC) Large Grant Scheme (via Grant Number A89917293).

6 References

- DOCTORS, L.J. AND BECK, R.F.: "Convergence Properties of the Neumann-Kelvin Problem for a Submerged Body", *J. Ship Research*, Vol. 31, No. 4, pp 227-234 (December 1987)
- DOCTORS, L.J. AND DAY, A.H.: "Resistance Prediction for Transom-Stern Vessels", *Proc. Fourth International Conference on Fast Sea Transportation (FAST '97)*, Sydney, Australia, Vol. 2, pp 743-750 (July 1997)
- MICHELL, J.H.: "The Wave Resistance of a Ship", *Philosophical Magazine*, London, Series 5, Vol. 45, pp 106-123 (1898)
- WEHAUSEN, J.V. AND LAITONE, E.V.: "Surface Waves", *Encyclopedia of Physics: Fluid Dynamics III*, Ed. by S. Flügge, Springer-Verlag, Berlin, Vol. 9, pp 445-814 (1960)
- WIGLEY, W.C.S.: "A Comparison of Experiment and Calculated Wave-Profiles and Wave-Resistances for a Form Having Parabolic Waterlines", *Proc. Royal Society of London*, Series A, Vol. 144, No. 851, pp 144-159 + 4 plates (March 1934)

FORECASTING THE MOTION OF BERTHED SHIPS IN HARBORS

N. DRIMER, M. GLOZMAN, M. STIASSNIE AND G. ZILMAN¹

CAMERI - Coastal and Marine Engineering Research Institute, Technion City, Haifa 32000, Israel

1 Introduction

This paper describes a numerical model for forecasting the motion of berthed ships in harbors, excited by waves. The model simulates the whole process, from a deep sea storm, to the motion of a berthed ship. The model together with a complementary module, which draws input data from a weather center, and a graphical user interface, are the main components of a system called Sea-21, which enables to forecast the operability conditions of a marine installation.

2 The physical process and its simulation

In order to simplify the simulation, we decompose the problem into three physical processes: wave shoaling from deep sea to the harbor entrance, wave diffraction and harbor oscillations, and wave-ship interaction in the harbor. Generally, the periods of harbor resonances and of the horizontal modes of motion of a moored ship are in the range of long waves (about one minute). Long waves are better transmitted into a harbor. Thus, the contribution of long waves to the motion of a moored ship becomes considerable and important. Most of the energy in the long waves range, observed at the harbor mouth, is a result of nonlinear wave-wave interaction which takes place in the shoaling zone. The substantial attenuation of wind waves by the breakwaters of the harbor justify the neglecting of nonlinear interaction within the harbor. An illustration of the process is presented in Figure 1.

3 The shoaling model

Agnon *et al.* [1] derived an evolution equation describing the shoaling of unidirectional wide spectra at normal incidence which takes into account second order wave-wave interaction. The present model extends [1] in order to include wave refraction.

While for other components of the process the non linear effects may be neglected, the evolution of the waves from deep into relatively shallow water is an essentially nonlinear process. At open sea the long waves are nearly absent from the spectrum. They are generated through nonlinear interaction among wind waves mostly close to the shore and within a domain of at most several tens of lengths of the short wave.

The near shore wave evolution was described using a nonlinear deterministic model which takes into account the refraction and second order quadratic nonlinear interaction. This model describes the evolution of wide spectra from deep into shallow water and requires the information about spectral density and the modal phases at deep water. Typically the spectral density is known whereas the phases are unknown. The mathematical model generates a set of uniformly distributed random phases which are used in each particular run. The average of 100 - 200 runs gives the mean characteristics of the process.

¹Permanent address: School of Engineering, Dept. of Fluid Mechanics and Heat Transfer, Tel Aviv University, Ramat Aviv 69978, Israel

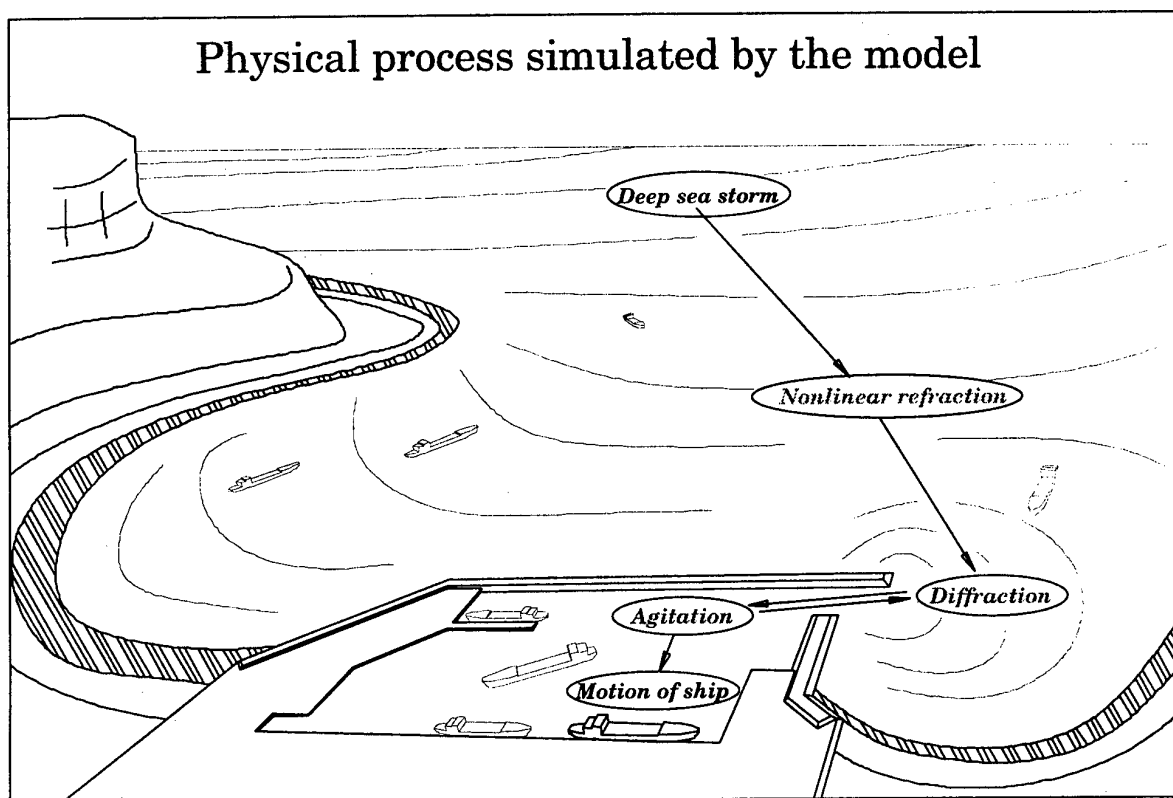


Figure 1: Illustration of the physical process simulated by the model

4 The Agitation Model

To simulate wave diffraction and harbor oscillations, we use the MIKE-21 EMS Model of the Danish Hydraulic Institute. It is a linear model in the frequency domain, which solves the mild-slope equations as described by Madsen & Larsen [2]. The wave spectrum at the harbor entrance obtained by the shoaling model is decomposed into a set of 23 monochromatic waves with periods: $320 \text{ seconds} / n, n = 2, 3, 4, 5, 6, 7, 8, 10, \dots, 40$.

For each of those periods the mathematical model computes the wave amplification factors, and the components of the particles velocity vectors at the grid points inside the harbor. This information is later used by an interface program, to obtain the boundary conditions for the wave-ship interaction problem.

5 The wave-ship interaction model

This model was developed for the current project and is called the VIP (Vessel In Port) model. Basically, it is a program for solving the linear wave-body interaction problem. The program uses the Boundary Elements Method with the wave source Green's function. In order to solve the diffraction problem for a VIP an interface program reads the binary output file of MIKE 21 EMS and calculates the values of the velocity potential function and its derivatives at the centroids of the boundary elements of the ship's model. Those values are used as an input to evaluate the exciting forces acting on the vessel. The scattering problem, as well as the six radiation problems, are solved with boundary conditions of constant depth and long vertical quay at which the vessel is berthed. In such an approach the re-reflection by the sea-walls which are far from the vessel are neglected.

6 Additional developments

Due to nonlinear reactions of mooring lines and fenders, in many practical situations the linear frequency-domain approach is limited. The linear model can be extended by invoking the time domain simulations. The principle of this approach is first to solve the linear hydrodynamic problem for a set of frequencies, and then using Fourier transform to obtain a set of nonlinear integro-differential equations of ship motion in the time domain. The equations of motion in the time domain may consider nonlinear effects such as nonlinear reactions of mooring lines and fenders, nonlinear roll damping and others. The time domain approach is now under intensive development at CAMERI, and significant progress has already been achieved.

7 Conclusions

We presented a method for numerical simulation of the transformation process of deep sea storms that shoals toward a harbor entrance, propagates into the harbor and excites motion of berthed ships. The mathematical model was used to predict the operability of cargo handling of berthed vessels.

The presented mathematical model is also a practical tool for port designers. It may assist to select among design alternatives which may differ in the layout of breakwaters and quays, bathymetry, and other design parameters.

System Sea-21 has been installed at the ports of Haifa and Ashdod and provides real time forecasting of operability conditions for these installations.

References

- [1] 1. Agnon, Y. Sheremet, A. Gonsalves, J. & Stiassnie, M. A unidirectional model for shoaling gravity waves, *Coastal Engineering*, 1993, **20**, 29–58.
- [2] 2. Madsen, P.A. & Larsen, J. An efficient finite-difference approach to the mild-slope equation, *Coastal Engineering*, 1987, **11**, 329–351.

A CONTINUUM MODEL FOR MULTI-COLUMN STRUCTURES IN WAVES

D.V. EVANS AND B.B. SHIPWAY

School of Mathematics, University of Bristol, University Walk, Bristol BS8 1TW

At the last Workshop Phil McIver showed how ideas commonplace in solid-state physics, and in particular in lattice theory for crystals, could be used in connection with the problems of ocean wave interaction with periodic multi-column configurations such as might be used to support massive off-shore structures such as aircraft run-ways. During the discussion it was remarked that an alternative approach might be to look at homogenisation theory in which the (very large number of) columns were replaced by a continuous medium having some averaged different properties from the column-free medium, which describes in some global sense the effect of the columns. Just such an approach is presented here, drawing on a model which has been used with success in modelling the acoustic resonances which can occur in banks of heat exchangers in the form of a large number of periodic closely-spaced cylindrical tubes having axes at right-angles to the air flow.

To fix ideas we assume that the multi-column configuration occupies the region $|x| < a$, $0 < z < h$, i.e. extends indefinitely in the y -direction. The undisturbed free surface is $z = 0$ and the velocity of the fluid normal to the surface of each of the cylinders vanishes. It is thus possible to remove the vertical z -dependence by writing the three-dimensional harmonic velocity potential $\Phi(\mathbf{r}, t)$ in the form

$$\Phi(\mathbf{r}, t) = \Re \phi(x, y) \cosh k(h - z) e^{-i\omega t}. \quad (1)$$

Then $\phi(x, y)$ satisfies

$$\phi_{xx} + \phi_{yy} + k^2 \phi = 0, \quad |x| > a, \quad -\infty < y < \infty. \quad (2)$$

Also, the linearised free surface condition is satisfied provided the wavenumber k is the real, positive root of

$$w^2 = gk \tanh kh \quad (3)$$

where $w/2\pi$ is the assumed harmonic wave frequency. Thus the reduced potential ϕ satisfies the Helmholtz equation in $|x| > a$, all y , and in $|x| < a$ external to the region of the $x - y$ plane occupied by the cross-sections of the columns. In addition

$$\phi_n = 0 \text{ on each of the column boundaries.} \quad (4)$$

Suitable conditions need to be satisfied by ϕ as $|x| \rightarrow \infty$, depending on the problem under consideration.

Now if $k = w/c_0$, where c_0 is the speed of sound, then equations (2), (4) also describe the two-dimensional small perturbations, restricted to the $x - y$ plane, in sound pressure of a compressible fluid having frequency $w/2\pi$ in the presence of an array of rigid cylinders in $|x| < a$, $-\infty < y < \infty$, $0 < z < h$, on which a 'hard' condition is satisfied. This follows since the linearised continuity equation

$$\frac{\partial \rho}{\partial t} + \rho_0 \nabla \cdot \mathbf{u} = Q \quad (5)$$

where ρ_0 is the mean and ρ the actual density of the fluid and Q is any mass flux per unit volume and the linearised momentum equation

$$\rho_0 \frac{\partial \mathbf{u}}{\partial t} + \nabla p = \mathbf{F} \quad (6)$$

where \mathbf{F} is any external force per unit volume, reduce, if $Q = \mathbf{F} = 0$ to

$$\frac{\partial^2 \rho}{\partial t^2} = \nabla^2 p. \quad (7)$$

Now assuming $p = p(\rho_0) + (\rho - \rho_0)p'(\rho_0) + \text{smaller terms}$ gives

$$\frac{\partial p}{\partial t} = p'(\rho_0) \frac{\partial \rho}{\partial t} \equiv c_0^2 \frac{\partial \rho}{\partial t}, \text{ say} \quad (8)$$

so that (7) becomes

$$\frac{1}{c_0^2} \frac{\partial^2 p}{\partial t^2} = \nabla^2 p \quad (9)$$

Finally, by letting

$$p(x, y, t) = \Re \phi(x, y) e^{-i\omega t} \quad (10)$$

we recover (2) with $k = \omega/c_0$.

Thus the water wave problem for the 'reduced' potential ϕ and the acoustic problem in the x, y plane are identical and we may adapt a homogenisation technique used successfully for the latter problem, and described by Blevins [1], to the former problem.

The aim is to replace the region $|x| < a$, $0 < z < h$ occupied by the array of cylinders, by a homogeneous medium satisfying a modified wave equation. Thus, following Blevins [1], the region $|x| < a$, $-\infty < y < \infty$ is divided into adjacent cells, each cell of volume V containing a single cylinder of volume v so that the solidity factor $\sigma = \frac{v}{V} < 1$. (It is convenient to regard each cell and cylinder as having unit length in the z -direction.) We now replace each rigid fixed cylinder by a cylinder of compressible fluid of density ρ similar to that in the rest of the cell. This 'virtual' cylinder will compress and experience forces on its boundaries. By choosing an appropriate mass flux Q in (5), and an appropriate external body force \mathbf{F} in (6), we seek to (i) prevent compression of the cylinder of fluid, and (ii) ensure it remains stationary, thereby modelling the fixed rigid cylinder. Such mass fluxes and body forces will then be smeared out over the whole cell. Now in time δt the volume v of a cylinder of fluid changes by an amount δv where $\delta v/v = -\delta\rho/\rho$ so the rate of change in mass per unit cylinder volume is $(\rho\delta v/v)/\delta t = -\partial\rho/\partial t$ whence the rate of change in mass per unit cell volume is $-vV^{-1}\partial\rho/\partial t = -\sigma\partial\rho/\partial t$. Thus we choose a mass flux

$$Q = \sigma \frac{\partial \rho}{\partial t} \quad (11)$$

in (6) in order to counter this compression.

Now the unsteady inertia force on a fluid cylinder per unit volume may be written

$$\mathbf{f} = \rho_0(\mathbf{I} + \mathbf{A})\dot{\mathbf{u}}, \quad \mathbf{A} = \begin{pmatrix} a_{11} & a_{12} \\ a_{21} & a_{22} \end{pmatrix}, \quad \mathbf{u} = \begin{pmatrix} u_1 \\ u_2 \end{pmatrix} \quad (12)$$

where \mathbf{A} is the added inertia matrix and \mathbf{I} the 2×2 identity matrix. Equation (12) assumes $ka \ll 1$ and wide-spacing between adjacent cylinders. Also for lines of symmetry parallel to x and y , $a_{12} = a_{21} = 0$. So the total force which needs to be applied by the fluid cylinder to the rest of the fluid in the cell per unit volume of that fluid is

$$\mathbf{F} = -\frac{v\mathbf{f}}{(V-v)} = -\frac{\sigma}{1-\sigma}\rho_0(\mathbf{I} + \mathbf{A})\dot{\mathbf{u}}. \quad (13)$$

Using (11) and (13) in (5) and (6) gives, using (10),

$$\nabla \cdot \{(\mathbf{I} + \sigma\mathbf{A})^{-1} \nabla \phi\} + k^2 \phi = 0, \quad k = \omega/c_0$$

or

$$(1 + \sigma a_{22})\phi_{xx} + (1 + \sigma a_{11})\phi_{yy} - \sigma(a_{12} + a_{21})\phi_{xy} + k^2 \Delta \phi = 0 \quad (14)$$

where $\Delta = \det(\mathbf{I} + \sigma\mathbf{A})$.

If we assume lines of symmetry of the columns parallel to x and y , then $a_{12} = a_{21} = 0$ and (14) reduces to

$$(1 + \sigma a_x)^{-1} \phi_{xx} + (1 + \sigma a_y)^{-1} \phi_{yy} + k^2 \phi = 0 \quad \text{in } |x| < a \text{ for all } y \quad (15)$$

where $a_{11} \equiv a_x$, $a_{22} \equiv a_y$. Numerical computation reported by Burton [2] suggest that a_x/a_y varies linearly with aspect ratio $\alpha = s_x/s_y$ where s_x, s_y are the spacings between adjacent cylinders in the x and y direction respectively and that $a_x a_y$ varies roughly linearly with σ . However experimental results of Blevins [1] suggest it is sufficient to assume that $a_x = a_y = 1$ so that in $|x| < a$ we have

$$(\nabla^2 + k_1^2)\phi = 0 \quad (16)$$

where $k_1 = k(1 + \sigma)^{\frac{1}{2}}$ an increased wavenumber or $c_1 = w/k_1 = c_0(1 + \sigma a)^{-\frac{1}{2}}$ a reduced sound speed.

We shall assume (15) is valid in $|x| < a$ and (2) in $|x| > a$, all y and apply continuity of ϕ , ϕ_x at $x = \pm a$.

The Scattering Problem

Symmetry suggests splitting the problem by writing $\phi(x, y) = \phi_s(x, y) + \phi_a(x, y)$ where $\phi_s(\phi_a)$ is even (odd) in x .

Appropriate forms are then

$$\phi_{s,a} = (e^{-iKx} + R_{s,a}e^{iKx})e^{i\alpha y} \quad |x| > a$$

for an incident wave at an angle θ_0 with the negative x direction if $\alpha = k \sin \theta_0$, $K = k \cos \theta_0$, and

$$\left. \begin{aligned} \phi_s &= A_s \cos K_1 x e^{i\alpha y} & |x| < a \\ \phi_a &= A_a \sin K_1 x e^{i\alpha y} \end{aligned} \right\} \quad (17)$$

$$\text{if } K_1 = (1 + \sigma a_x)^{\frac{1}{2}} \left\{ k^2 - \frac{\alpha^2}{(1 + \sigma a_y)} \right\}^{\frac{1}{2}} > 0.$$

The continuity conditions then show that

$$R_s e^{2iK_1 a} = \frac{iK - K_1 \tan K_1 a}{iK + K_1 \tan K_1 a}, \quad R_a e^{2iK_1 a} = \frac{iK + K_1 \cot K_1 a}{iK - K_1 \cot K_1 a} \quad (18)$$

Trapped modes

Trapped modes can exist in $|x| < a$ if $k < \alpha < (1 + \sigma a_y)^{\frac{1}{2}} k$ since now $K \equiv i\beta = i(\alpha^2 - k^2)^{\frac{1}{2}}$, $\beta > 0$ and, consistent with (17) in $|x| < a$ are solutions

$$\phi_{s,a} = e^{-\beta x} e^{i\alpha y} \quad \text{in } |x| > a \quad (19)$$

whence continuity requires

$$\beta = K_1 \tan \left(K_1 a - \frac{j\pi}{2} \right) \quad \begin{aligned} j &= 0, \text{ even solution} \\ &= 1 \text{ odd solution} \end{aligned} \quad (20)$$

and

$$\frac{K_1^2}{(1 + \sigma a_x)} + \frac{\beta^2}{(1 + \sigma a_y)} = \sigma a_y k^2. \quad (21)$$

A sketch of (20), (21) in the β, K_1 plane makes clear that for each value of

$$\lambda \equiv \sigma a_y (1 + \sigma a_x)^{\frac{1}{2}} k \quad (22)$$

there exist pairs (β_i, K_{1i}) $i = 1, 2, \dots, n$ corresponding to trapped modes and

$$(r-1)\frac{\pi}{2a} < K_{1r} < \frac{r\pi}{2a}, \quad r = 1, 2, \dots, n$$

whenever

$$(n-1)\frac{\pi}{2a} < \lambda < \frac{n\pi}{2a}.$$

Returning to the water-wave problem, given a frequency $\omega/2\pi$ we can determine k from $\omega^2 = gk \tanh kh$ and hence λ from (22) which in turn determines β_i from which the trapped mode wavenumbers α_i along the y -direction can be derived from

$$\alpha_i = (\beta_i^2 + k^2)^{\frac{1}{2}}.$$

Excitation of trapped modes

It is not possible to excite these trapped modes by a wave incident from infinity since in that case $\alpha = k \sin \theta_0 < k$. However a localised source of energy can be shown to excite trapped modes. For example the presence of a sharp headland could act as a radiator of an incident wave towards $|x| < a$. Thus a simple model is to assume that in $|x| > a$ the governing equation is $\phi_{xx} + \phi_{yy} + k^2\phi = -\delta(x-b)\delta(y)$ i.e. there is a line source at $x = b, y = 0$. We can now ask how much energy from this source is fed into trapped modes producing possibly large modes of oscillation, and how much gets radiated out to sea? A related problem in electromagnetic theory is discussed in Collin [3].

The mathematical solution to this problem is simply

$$\phi(x, y) = -\frac{1}{4\pi i} \int_C \left(\frac{2e^{i\mathcal{K}|x-b|}}{\mathcal{K}} + \frac{(R_s + R_a)}{\mathcal{K}} e^{i\mathcal{K}(x+b)} \right) e^{-i\alpha y} d\alpha \quad (23)$$

where C is a contour chosen to satisfy appropriate radiation conditions. The contribution to the trapped modes arises from the poles of the integrand or the zeros of the denominators of R_s, R_a in (18) whilst the contribution to the energy radiated away from the columns out to sea, arises from the branch cuts at $\alpha = \pm k$.

Further details of the derivation of the solution (23) and its implications will be presented at the workshop.

References

- [1] Blevins, R.D. Acoustic modes of heat exchanges tube bundles. *J. Sound and Vibration*, 1986, **109** (1), 19-31.
- [2] Burton, T.E. Sound speed in a heat exchanger tube bank. *J. Sound and Vibration*, 1980, **71** (1), 157-160.
- [3] Collin, R.E. *Field Theory of Guided Waves*, IEEE Press, 1991 p. 725.

ON MODELING THE POST BREAKING PHASE: SPLASHING

E. Fontaine, M. Landrini and M.P. Tulin

Ocean Engineering Laboratory, UCSB, CA93106-1080, USA

Wave breaking is known to play a crucial role in explaining various phenomena such as the down-shifting evolution of ocean wind waves [1], high impact loads on structures [2], the observed high RCS return at low grazing angles [3], or the existence of a visible surface wake behind ships [4]. In the latter case, part of the persisting surface disturbance is the result of bow wave breaking, and it is desirable to understand and quantify this process. As a wave breaks, several regimes have been identified, [5], [6]:

- Steepening-cresting phase. The wave is deforming asymmetrically, its crest and trough rise, the front face steepens, and the crest eventually sharpens.
- Plunging-jet phase. A jet forms at the crest of the deformed wave and moves forward and downward in a ballistic trajectory.
- Splashing-ploughing phase. The plunging jet has splashed into the front face of the wave, throwing water upwards as it ploughs forward. Air entrainment usually occurs during this phase.
- Decaying scar phase. The turbulent underwater structure created during the previous phase is slowly dissipated under the action of viscosity.

The steepening-cresting and plunging-jet phases can be accurately simulated within the framework of potential flow theory, and using Boundary Element Method (BEM) in a Mixed Eulerian Lagrangian (MEL) approach. Simulation of energetic ocean breaking waves have been carried out successfully up to the early beginning of the splashing-ploughing phase, i.e. as the tip of the jet starts to re-enters the front face of the wave, [5], [6]. Similarly, bow breaking waves have been simulated within the framework of $2D + t$ theory, [7], [8]. Despite attempts to directly simulate the overall breaking process [9], little is known about the detailed mechanisms that lead to air entrainment and to the formation of the resulting post-breaking vortical structures which give rise to the visible wake.

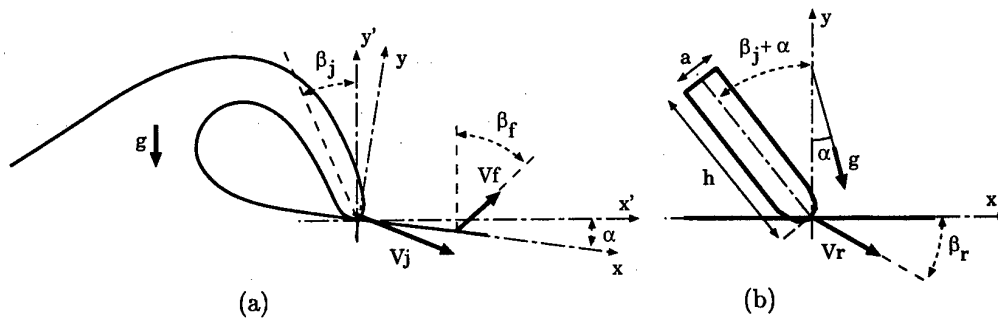


Figure 1: (a) Breaking wave at the beginning of the splashing-ploughing phase, and (b) the associated simplified model with gravity and neglecting surface tension.

The aim of the present study is to extend our knowledge of the splashing-ploughing phase through the simplified modeling presented in Fig. 1, preparatory to calculating the complete

problem, (a), using a hybrid method. The jet is here represented by a two-dimensional slug of water in free-fall which hits the surface (front face of the wave) at some angle from the vertical. In a frame of reference moving upwards with the front face, the gravity and relative velocity of the jet appear to be tilted with respect to the vertical and the jet axis directions, respectively. The main parameters in the problem are the aspect ratio of the jet, $r = h/a$, the Froude number $F = V_r/\sqrt{ga}$, and the angles α , β_j and β_r .

The simplified problem, (b), can be studied within the framework of potential flow theory and using BEM [10], but this approach is limited both by necessary theoretical assumptions and technical difficulties associated with following highly distorted free-surface configurations. In particular, fluid fragmentation is observed during the splashing phase.

Here, the Smoothed Particle Hydrodynamics (SPH) method [11] was adopted. This fully Lagrangian method was initially designed for the resolution of compressible Euler equations with applications to astrophysical problems [12]. The key concept of the method is to give a local approximation of a generic physical variable $f(\vec{x}, t)$ in terms of the values $f_i(t)$ carried by a finite number of particles, i.e.

$$f(\vec{x}, t) = \iint f(\vec{x}', t) \delta(\vec{x} - \vec{x}') ds \simeq \iint f(\vec{x}', t) W(\vec{x} - \vec{x}') ds \simeq \sum_j \frac{m_j}{\rho_j} f(\vec{x}_j, t) W(\|\vec{x}_j - \vec{x}\|) \quad (1)$$

where the smoothing kernel $W(\vec{x})$ is an approximation to the Dirac δ function, m_i and ρ_i are the mass and density of the fluid particle. Upon identifying f with the variables ρ and \vec{U} , Euler equations reduce to a set of ODEs that are integrated with respect to time to give the evolution of the fluid dynamic system. Spatial derivatives of the quantities are obtained by differentiating eq. (1), i.e. using analytical kernel derivatives. The compact support of the kernel leads each particle to interact only with its close neighbours. Mass and momentum conservation are explicitly enforced by requiring each particle to have a constant mass and symmetric interactions between them, respectively. The pressure is computed by using the density and a suitable equation of state for water which is considered a weakly compressible fluid. Simulations are performed at a low Mach number (typically $M = 0.1$), leading to non essential perturbations in density during the simulation (typically of the order of $O(M^2) = 0.01$). As in most numerical methods, artificial viscosity is introduced to stabilize the scheme. Changes in the total energy, typically within a few percent, are representative of the global accuracy of the simulations. The method has been implemented and successfully tested against both analytical and BEM results for different problems: the evolution of a patch of fluid, the propagation of a bore, the wedge entry problem, and the generation and propagation of shallow water waves. Results will be presented.

A particular SPH simulation of the prototype problem, (b), is shown in Fig. 2, where the parameters are based on the LONGTANK simulation of an energetic breaker [5], using 100^K particles distributed in the water with variable initial spacings, densest near the surface. Hydrostatic pressure is imposed on the outer boundary of the flow domain (not shown).

The jet does not decelerate significantly after impact, and the impacting fluid is deflected upwards on the left covering the previous surface, and similarly on the right, where it spills over together with some of the former surface, forming a visible splash up. After some time, the observed shape of the impacting jet and the new surface tend to become unchanging, see Fig. 2 lower right corner, and the particles on the upper side of the new cavity surface are almost motionless. The very thin jet formed on the right is seen to be stretching, fragmenting and falling downwards. The observed behaviour has important implications for the generation of vorticity.

Simulations have also been conducted for a range of jet parameters with interesting results. For $F > O(10)$ and $\beta < O(20^\circ)$, Fig. 3, the impacting jet flow into the cavity on the left tends to disappear and the slug is deflected along the surface; ricochet is indicated. For $F < O(3)$ the cavity eventually collapses creating an upward splash (see Fig. 4).

Finally, a hybrid numerical procedure is under development where the the splashing jet region, modeled by SPH numerics, is driven by the surrounding wave field described by BEM

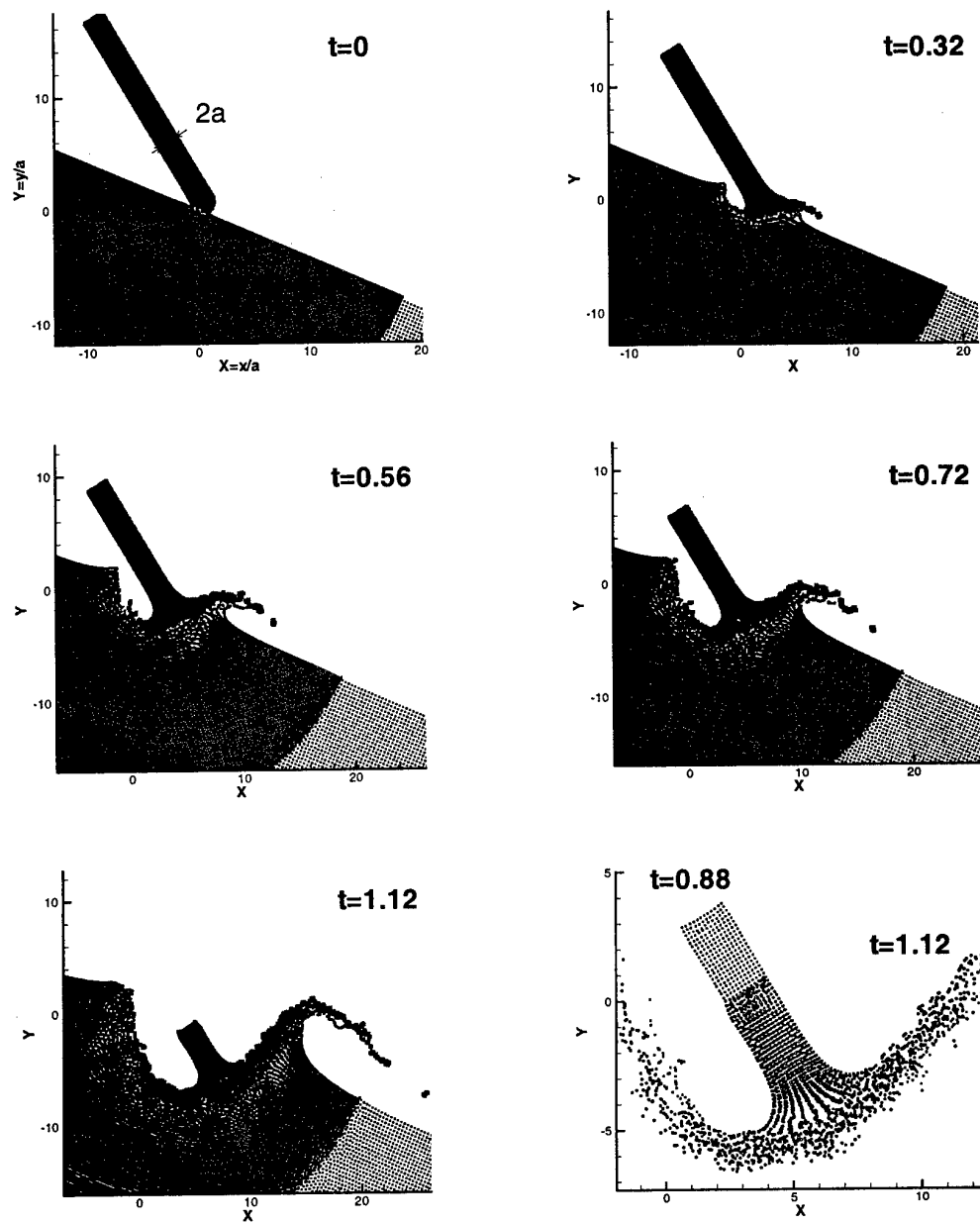


Figure 2: Jet breaking wave at the beginning of the splashing-ploughing phase for $\alpha = 23^\circ$, $\beta_j = 31^\circ$, $\beta_r = 30^\circ$, $F = 10$, and $r = 10$.

numerics. Coupling is achieved by partial overlapping of the two subdomains. The SPH method allows the eventual inclusion of multiphase effects due to air entrapment.

The authors are grateful for the support of the ONR, Dr Ed Rood, Program Manager.

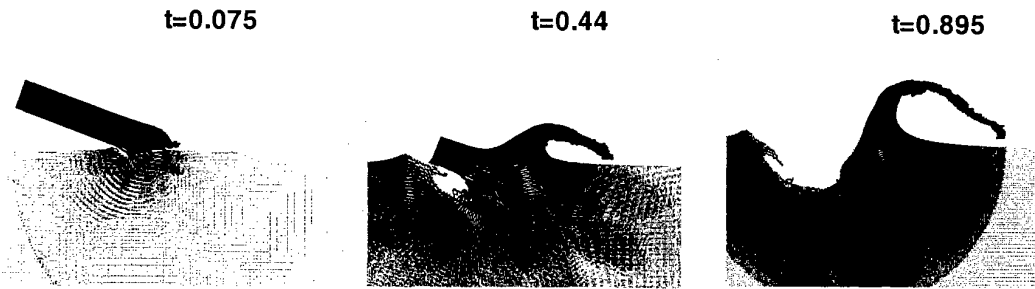


Figure 3: Jet breaking wave at the beginning of the splashing-ploughing phase for $\alpha = 0^\circ$, $\beta_j = 70^\circ$, $\beta_r = 20^\circ$, $F = 10$, and $r = 10$. The scales differs in each plot.

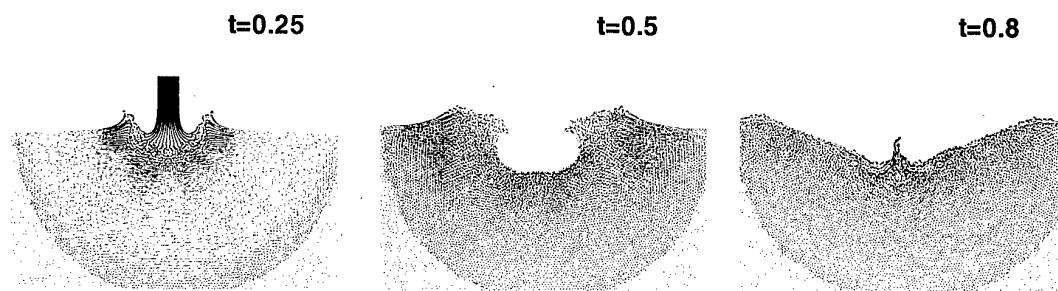


Figure 4: Jet breaking wave at the beginning of the splashing-ploughing phase for $\alpha = 0^\circ$, $\beta_j = 0^\circ$, $\beta_r = 90^\circ$, $F = 1$, and $r = 10$. BEM simulation stops [10] after $t=0.5$ as the cavity collapses.

References

- [1] M.P. Tulin, Y. Yao, A.K. Magnusson, 1996. The evolution and structure of energetic wind waves, *Proc. of ISOPE'96*.
- [2] S. Welch, C. Levi, E. Fontaine, M.P. Tulin, 1999. Experimental loads on a flexibly mounted vertical cylinder in breaking waves groups. *International Journal on Offshore and Polar Engineering* (in Press).
- [3] J. Fuchis, D. Regas, T. Waseda, S. Welch and M.P. Tulin, 1999. Correlation of hydrodynamics features with LGA Radar Backscatter from breaking waves. *IEEE transactions on Geoscience and remote sensing*, Vol. 37, No 5, pp. 2442-2460.
- [4] I. Miyata and T. Inui, 1984. Nonlinear ship waves, *Advances in Applied Mechanics*, Vol. 24, pp. 215-289.
- [5] M.P. Tulin, Y. Yao, and P. Wang, 1994. The simulation of the deformation and breaking of ocean waves in wave groups. *BOSS'94*, Boston-Ma, pp. 383-392.
- [6] M.P. Tulin and T. Waseda, 1999. Laboratory observations of wave group evolution, including breaking effects. *J. Fluid Mech.*, vol. 378, pp. 197-232.
- [7] M.P. Tulin and T. Wu, 1996. Divergent Bow Waves. In *Twenty first Symposium on Naval Hydrodynamics*, Trondheim, Norway, pp. 99-117.
- [8] E. Fontaine and M.P. Tulin, 1998. On the prediction of nonlinear free-surface flows past slender hulls using $2D + t$ approximation: the evolution of an idea. *Proc. Symp. NATO/RTO/AVT*, pp. 26-1,11, Amsterdam.
- [9] I. Miyata, 1995. Potential flow of fluids, CMP, Ed. M. Rahman.
- [10] A. Prosperetti and H. N. Oguz, 1997. Air entrainment upon liquid impact. *Phil. Trans. R. Soc. Lond. A*, Vol. 355, pp. 491-506.
- [11] J.J. Monaghan and A. Kos, 1999. Solitary Waves on a Cretan Beach. *Journal of Waterway, Port, and Ocean Engineering*, May/June, pp. 145-154.
- [12] J.J. Monaghan, 1992. Smoothed Particle Hydrodynamics. *Annu. Rev. Astron. Astrophys.*, 30, pp. 543-574.

An Investigation of Water on Deck Phenomena

M. Greco* O. Faltinsen* M. Landrini**

* Department of Marine Hydrodynamics NTNU, Trondheim – Norway.

** INSEAN, Italian ship model basin, Roma – Italy.

Shipping of water on deck represents a danger both for moored (as FPSO) and for advancing ships. When a compact mass of water ('green water') is shipped onto the deck, the fluid moves with high speed, being able to damage superstructures and equipments and to be a risk for human lives. Also, the shipped water can significantly alter the dynamics of smaller vessels. Such events make the green water loads an important parameter to take into account even at design stage and call for predictive tools. However, knowledge about the physics involved is still limited and motivates increasing research effort.

At present, we are not able to deal with the problem as a whole and, moreover, the physical and numerical complexity can easily obscure the underlying fundamental aspects. Therefore we devised a set of basic prototype phenomena and, although in reality they are strongly coupled, we analyzed them separately. In this framework, the main stages to be considered are wave-body interaction, shipping of water, flow onto the deck, impact of water with superstructures.

Though the problem is three-dimensional, we learned from the water entry problem that physical insight can be gained through a two-dimensional analysis and provide a guidance on how to approximate numerically the more complex three-dimensional one. We assume in addition inviscid fluid, which is known to be a proper approximation, but we fully retain nonlinearities due to the motion of the free surface and solid body. A potential flow model results and a mixed Eulerian-Lagrangian approach is adopted to solve the unsteady interaction between the body and the free surface. Briefly, the fluid velocity \mathbf{u} is evaluated in terms of the potential $\varphi(\mathbf{P}, t)$, which in turn satisfies the Laplace equation with mixed Dirichlet-Neumann boundary conditions. This kinetic problem is solved by a direct boundary integral formulation. The numerical solution is achieved by a collocation method with piecewise linear shape functions and collocation points at the edges of each element. At the contact point body-free surface, a weak regularity of the solution is assumed by enforcing the continuity of the potential. Though no rigorous justification is available, this procedure guarantees convergence of the numerical results under grid refinement (cfr. [4]). However when the angle between the free surface and the body surface is very small numerical problems may always occur. The time dependence enters through the evolution of boundary data, ruled by kinematic conditions on free and moving boundaries, and a dynamic condition for the free surface. A Lagrangian description is adopted and the problem is stepped forward in time by using a Runge-Kutta fourth order algorithm.

The first step to predict the deck wetness at the bow region (the most severe in head sea conditions) is an adequate estimate of the wave elevation near the bow. Here, due to nonlinear interactions, wave forms are strongly deformed relative to the incident waves. As a very preliminary study, we have considered the run-up of solitary waves on plane walls with different slopes. In particular, figure 1 shows the numerical maximum run-up, defined as the maximum vertical distance R between the still-water level and the intersection between wall and free surface, in the case of a vertical wall. Results are compared with experiments [3] and analytical values [1]. For (initial) wave height-to-depth ratio H/h sufficiently small all the results are in a reasonable agreement, while for larger amplitudes only the numerical results follow the experiments.

When the wave elevation exceeds the freeboard, the water can flow over the deck. According to experimental observations [2], the considered flow field resembles the one after a dam breaking. Therefore we have assumed the latter suitable to check our model of the evolution of the water on deck. Figure 2 gives numerical and analytical [6] pressure distributions on the 'deck' just after the dam breaking. The initial height of the water is h and $\tau = t\sqrt{g/h}$ is the non-dimensional time. As we can observe, the two solutions fit well and show a sudden departure of the pressure from the initial hydrostatic value. Free surface profiles as time increases are examined in figure 3. In this case we compared the numerical solution with experiments from [5], with satisfactory agreement during the whole considered time interval. Though in the initial stages dispersive wave effects matter, for large times the evolution can be adequately described by the shallow water solution, also presented in figure.

While flowing over the deck, the fluid can violently impact against obstacles and cause damage of superstructures. In general, the flow field will depend on the motion of the deck but the characteristics of the original incoming waves are expected to be weak because of the small time and space scales involved. On this ground, it is reasonable to focus only on the impact problem and we adopted the dam breaking flow as initial condition. The initial stage of the phenomenon is shown in figure 4, where a vertical obstacle is placed $3.366h$ far from a dam which initially limits a region of water with height h and length $2h$ (see top plot in figure 5). The flow field is not modified except in a small region close to the structure, where the flow behaves like a half-wedge of fluid hitting the wall. Further gravity effects are modest since the vertical acceleration of the contact point is $\mathcal{O}(5g)$

for small times after initial impact. Both these aspects are confirmed by the satisfactory comparison with a gravity-less similarity solution from [7]. At the latest time considered the numerical contact point moves with a higher vertical velocity than the analytical one (see right plot). However, as in the two previous instants, the numerical mass flux related to the jet flow is in quite good agreement with the analytical one. Qualitatively, just after the impact the water deviates by 90° and evolves in the form of a tiny jet. At this stage, spray formation is expected which can not be handled by the present method. Anyway we believe that this detail is not relevant for structural loads. To avoid numerical problems associated with the intersection between the free surface and the wall, the jet was partly cut.

Later evolution is presented in figure 5 where, due to the gravity, the vertical velocity of the water decreases, eventually becomes negative and the free surface overturns. In the same figure, for $h = 0.6$ m, the two bottom plots show the time history of the water level h_w at the two locations $(x/h)_A = 3.721$ and $(x/h)_B = 4.542$. Good agreement between numerical results and experiments [8] is observed until the breaking occurs. Because of the lack of a detailed description of the experiments in [8], we have shifted the time axis of the experimental curves so that numerical and experimental h_w become different than zero at the same instant. When using the predicted pressure distribution on the wall, this has to be analyzed from a structural point of view and possible hydroelastic effects have to be considered.

Clearly, 'water on deck' arises by the coupling of all the problems mentioned above. As a last item, we focus on a simple problem in which incoming waves in deep water can interact with straight walls with different slopes and possibly wetting the deck. The vertical extension of the obstacle is large with respect to the wavelength λ . Different values of the height-to-wavelength ratio (H/λ) have been considered. When the water reaches the freeboard (f) of the wall it is forced to leave it tangentially upwards. In figure 6, the case of a vertical wall and an incident wave with $H/\lambda = 0.06$ is shown. Horizontal and vertical scales are nondimensionalized in terms of the maximum exceedance (h) of the freeboard by the free surface. At first, the water near the wall gets mainly a vertical velocity and the exceedance of the freeboard increases quicker than the horizontal displacement of the water. Later on, horizontal velocity of the fluid already on the deck increases while the vertical velocity of the water approaching the structure reduces because of gravity. This causes two wave flows. One is a reflected system and the other propagates along the deck. The latter phenomenon is qualitatively like the flow caused by dam breaking. This is also confirmed by a reasonable agreement of the numerical free surface profiles with the corresponding experimental data [5] for the dam breaking. The final sequence 7 analyzes the water on deck for a wall at 45° with $f/H = 0.36$ and $f/H = 0.55$, respectively. Still incoming waves with $H/\lambda = 0.06$ are considered. For the larger value of f/H just a little amount of the water wets the deck. The maximum exceedance of the freeboard is smaller than in the other case and the gravity matters before the water on the deck reaches a sufficient horizontal velocity. In this case most of the water returns back leaving the deck.

In the latest figures both the stem overhang and the freeboard are involved, however many other parameters enter the problem as well as three-dimensional effects making it much more complicated. As an example, if the body moves when water reaches the freeboard, the relative vertical velocities involved can be large enough to cause a jet flow leaving the bow without occurrence of water on deck. The analysis presented gives a certain confidence about future possibilities to attack more realistic conditions.

1. BYATT-SMITH, J. G. B. (1971) *An integral equation for unsteady surface waves and a comment on the Boussinesq equation*, J. Fluid Mech., 49.
2. BUCHNER, B. (1995) *On the impact of green water loading on ship and offshore unit design*, PRADS'95.
3. CAMFIELD, F. E. AND STREET, R.L. (1967) *An investigation of the deformation and breaking of solitary waves*, Dep. of Civil Eng. Tech. Rep., N. 81, Stanford Univ.
4. DOMMERMUTH D.G. AND YUE D.K.P. (1987) *Numerical simulations of nonlinear axisymmetric flows with a free surface*, J. Fluid Mech., 178.
5. DRESSLER, R. F. (1954) *Comparison of theories and experiments for the hydraulic dam-break wave*, Assemblée Générale de Rome.
6. POHLE, F. V. (1950) *The Lagrangian equations of hydrodynamics: solutions which are analytic functions of time*, Ph.D. Thesis, New York Univ.
7. ZHANG, S., YUE, D. K. P. AND TANIZAWA, K. (1996) *Simulation of plunging wave impact on a vertical wall*, J. Fluid. Mech., 327.
8. ZHOU, Z. Q., DE KAT, J. O. AND BUCHNER, B. (1999) *A nonlinear 3-D approach to simulate green water dynamics on deck*, 7th Int. Conf. Numer. Ship Hydrodyn.

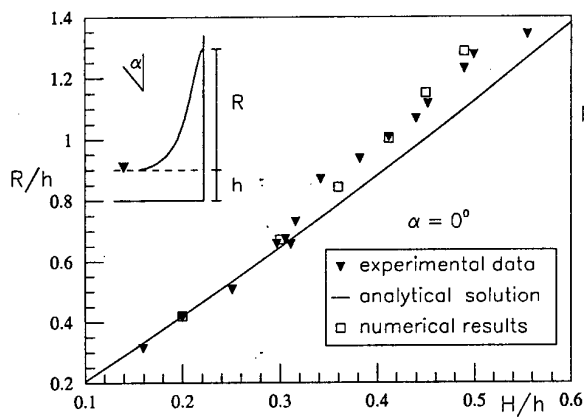


Figure 1: Maximum run-up R on a vertical wall of a solitary wave with amplitude H .

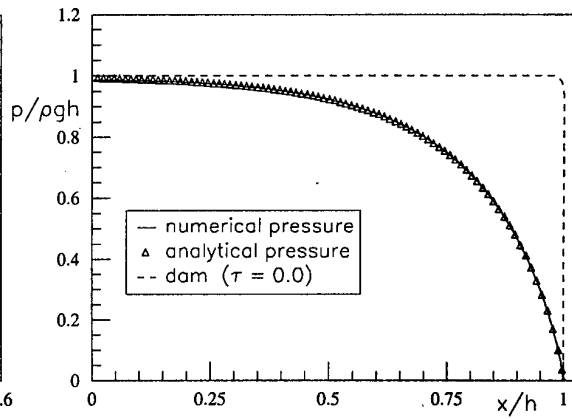


Figure 2: Comparison of analytical [6] and numerical pressure distributions at the beginning of dam breaking.

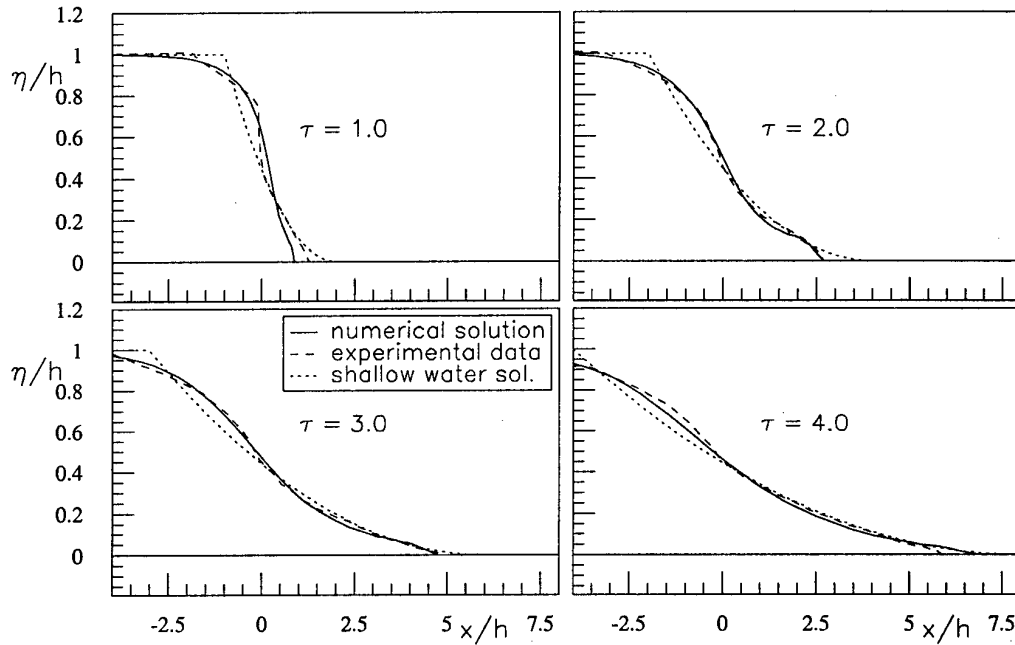


Figure 3: Free surface profiles after the dam breaking. Experimental data [5] and fully nonlinear and shallow water solutions ($\tau = t\sqrt{g/h}$).

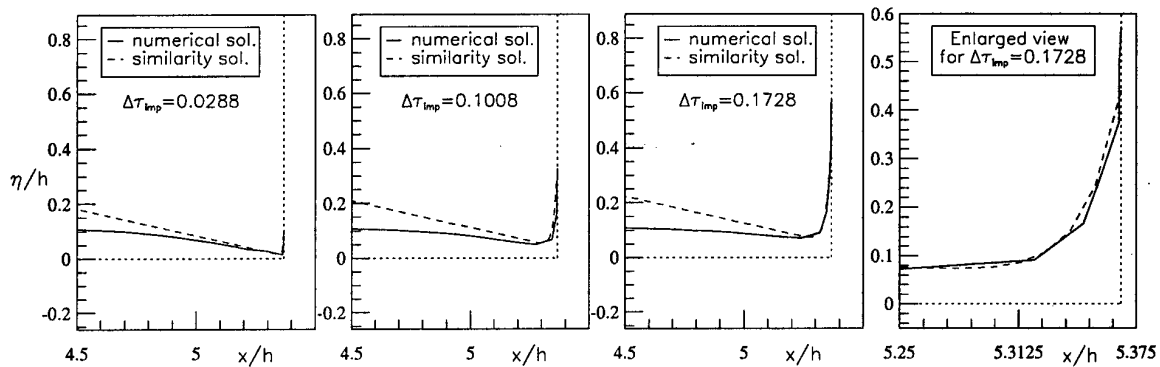


Figure 4: Initial stages of the impact problem after the dam breaking. Numerical results are compared with similarity solution of [7]. $\Delta\tau_{imp}$ is the dimensionless temporal distance from the impact. In the right plot the horizontal scale is magnified by a factor 4.18 with respect to the vertical one.

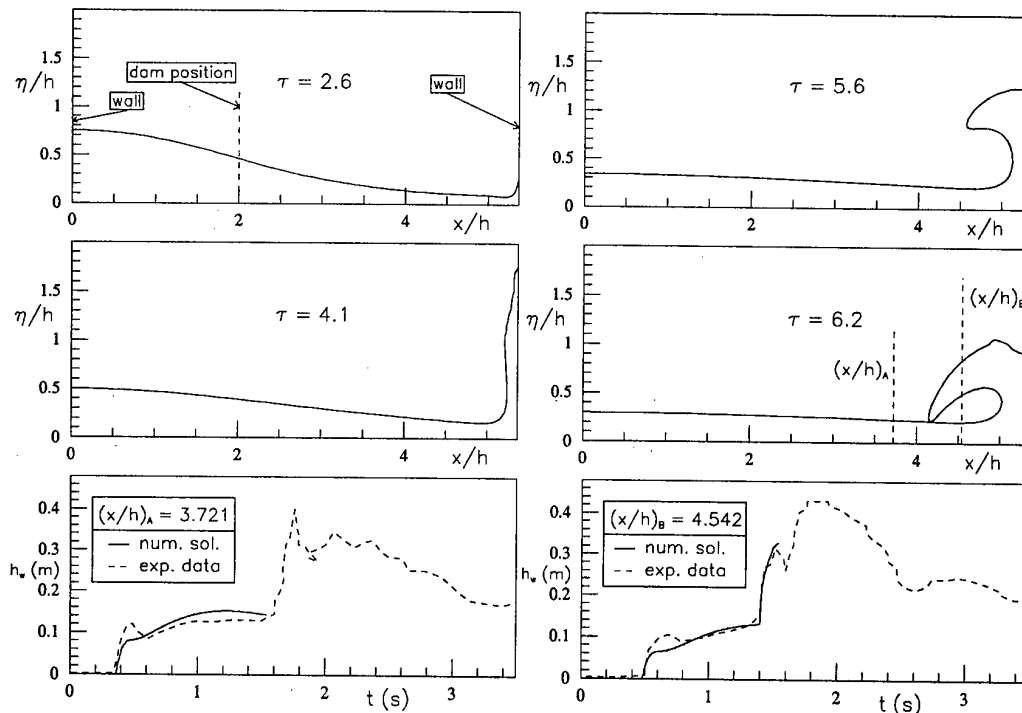


Figure 5: Simulation of dam breaking and impact with a vertical structure (top and central plots). Experimental [8] and numerical level of water at $(x/h)_A = 3.721$ and $(x/h)_B = 4.542$ as a function of time (bottom plots).

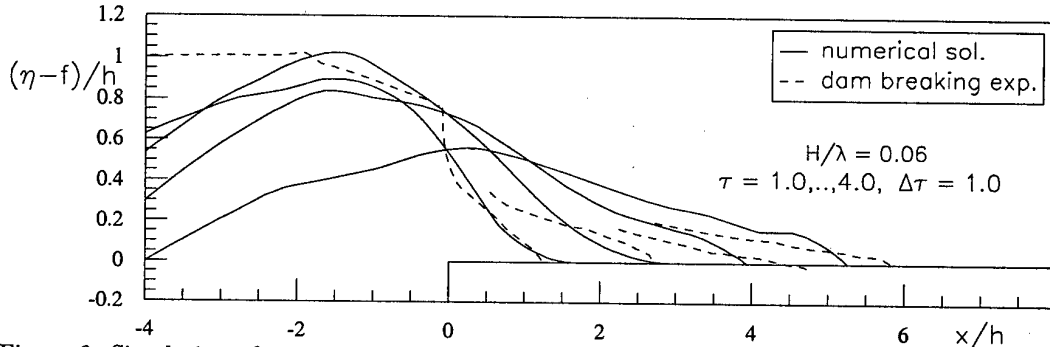


Figure 6: Simulation of water on deck due to incoming waves with $H/\lambda = 0.06$ for a 'deep' vertical wall. f is the 'freeboard' and $h = (\eta - f)_{\max}$. Numerical free surface profiles are compared with experimental data [5] for the dam breaking.

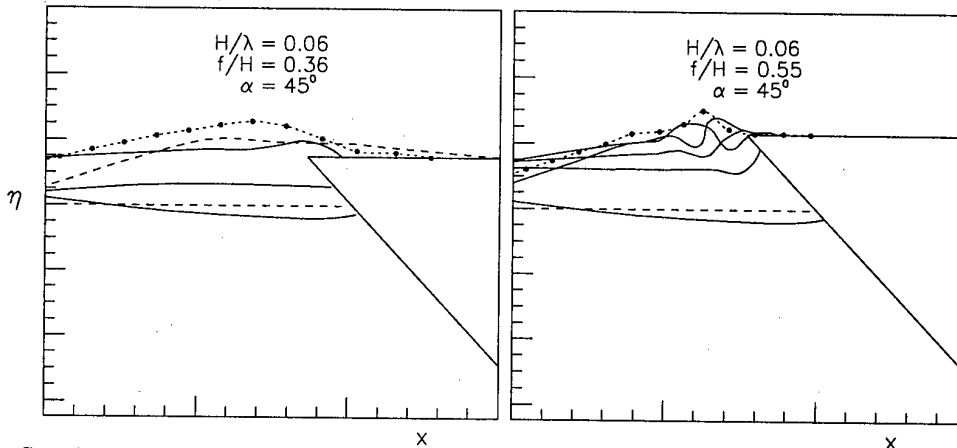


Figure 7: Simulation of water on deck due to incoming waves with $H/\lambda = 0.06$ for a 'deep' wall at 45° with $f/H = 0.36$ (left plot) and $f/H = 0.55$ (right plot).

NUMERICAL COMPUTATION OF THREE-DIMENSIONAL OVERTURNING WAVES

S. GRILLI ¹, P. GUYENNE ², F. DIAS ³

¹ Department of Ocean Engineering
University of Rhode Island, Narragansett, RI 02882, USA

² Institut Non-Linéaire de Nice
1361 route des Lucioles, 06560 Valbonne, FRANCE

³ Centre de Mathématiques et de Leurs Applications
ENS-Cachan, 61 avenue du Président Wilson, 94235 Cachan cedex, FRANCE

Abstract

We present accurate three-dimensional (3D) numerical computations for strongly nonlinear waves. The program solves fully nonlinear potential flow equations with a free surface, using a higher-order 3D Boundary Element Method (BEM) and a Mixed-Eulerian-Lagrangian time updating. An application to overturning waves over a non-uniform bottom is shown.

1 Introduction

So far, fully nonlinear potential flow (FNPF) equations of water waves have been successfully solved by two-dimensional (2D) Boundary Element methods (BEM). Among many applications, wave shoaling over arbitrary bottom topography up to overturning of a wave crest has been extensively studied (e.g., Grilli *et al.*, 1996, 1997). By comparing results with laboratory experiments (e.g., Bonmarin, 1989), FNPF formulation has been shown to model the physics of wave overturning in deep and intermediate water (e.g., Dommermuth *et al.*, 1988) as well as wave shoaling and breaking over slopes (e.g., Grilli *et al.*, 1997) with a high degree of accuracy. Most recent results on 2D waves deal with a numerical wave tank (NWT) where incident waves are generated at one extremity and reflected, absorbed or radiated at the opposite extremity (e.g., Grilli and Horillo, 1997). Although some 3D NWT have been developed for non-overturning waves over constant depth (e.g., Ferrant, 1998; Celebi *et al.*, 1998), only a few attempts have been reported, which solve FNPF problems for overturning waves in deep water (Xü and Yue, 1992) or over arbitrary bottom (e.g., Broeze, 1993). In general, 3D computations involve more difficult geometric and far-field representation problems than in 2D. In this study, we propose an efficient 3D NWT for calculating nonlinear surface waves according to FNPF theory (Fig. 1). In particular, it is applicable to the simulation of overturning waves over arbitrary bottom topography Γ_b .

2 Numerical approach

The model is based on a higher-order 3D BEM and a Mixed-Eulerian-Lagrangian time updating of the free surface Γ_f . Namely, we consider an incompressible, inviscid and irrotational 3D flow with a free surface. Green's second identity then transforms the Laplace's equation for the velocity potential into the boundary integral equation

$$\alpha(\mathbf{x}_l) \phi(\mathbf{x}_l) = \int_{\Gamma(\mathbf{x})} \left\{ \frac{\partial \phi}{\partial n}(\mathbf{x}) G(\mathbf{x}, \mathbf{x}_l) - \phi(\mathbf{x}) \frac{\partial G}{\partial n}(\mathbf{x}, \mathbf{x}_l) \right\} d\Gamma(\mathbf{x}), \quad (2.1)$$

where $\phi(\mathbf{x}_l)$ is the velocity potential, $G(\mathbf{x}, \mathbf{x}_l) = 1/4\pi r$ the 3D free space Green's function, \mathbf{n} the outward normal unit vector to the boundary $\Gamma(\mathbf{x})$ and $\alpha(\mathbf{x}_l) = \theta_l/(4\pi)$ with θ_l the exterior solid angle at point \mathbf{x}_l . The formulation is completed with the nonlinear kinematic and dynamic boundary conditions on the free surface expressed in Mixed-Eulerian-Lagrangian form. Both spatial and temporal discretizations are direct extensions of Grilli and Subramanya's 2D model (1996). Geometry and field variables in (2.1) are represented on the boundary by 16-node cubic "sliding" 2D elements with continuous slopes. Accurate and efficient numerical integrations are developed for these elements. Discretized boundary conditions at intersections (corner/edges) between the free surface and the lateral walls are well-posed in all cases of mixed boundary conditions. The dense and nonsymmetric linear system resulting from (2.1) is solved iteratively using a preconditioned GMRES (Generalized Minimal Residual) algorithm. For the time integration, we adopt an second-order explicit scheme with adaptive time steps, based on Taylor expansions of the fluid particle position and the velocity potential

$$\mathbf{r}(t + \Delta t) = \mathbf{r}(t) + \Delta t \frac{D\mathbf{r}}{Dt}(t) + \frac{(\Delta t)^2}{2} \frac{D^2\mathbf{r}}{Dt^2}(t) + \mathcal{O}[(\Delta t)^3],$$

$$\phi(\mathbf{r}(t + \Delta t)) = \phi(t) + \Delta t \frac{D\phi}{Dt}(t) + \frac{(\Delta t)^2}{2} \frac{D^2\phi}{Dt^2}(t) + \mathcal{O}[(\Delta t)^3].$$

Higher-order tangential derivatives required for the time stepping are calculated in a local curvilinear coordinate system $(\mathbf{s}, \mathbf{m}, \mathbf{n})$, using 25-node fourth-order "sliding" 2D elements. Arbitrary waves can be generated in the tank by wavemakers on Γ_{r1} , or directly on the free surface. If needed, absorbing boundary conditions are specified on lateral walls Γ_{r2} of the computational domain. Node regridding to a finer resolution can also be performed at any time step in selected areas of the free surface. Details can be found in Grilli, Guyenne and Dias.

3 Results

As an example, Fig. 2 depicts a 3D overturning wave calculated over a sloping 1:15 bottom having a ridge/bump in the y direction, thus focusing wave energy in the middle part of the NWT ($y = 0$). In addition, Fig. 3 shows the vertical cross-section $y = 0$ of the same overturning wave as in Fig. 2 at time t_2 and at an earlier time t_1 before a horizontal tangent occurs beneath the plunging jet.

References

- BONMARIN P. 1989 Geometric properties of deep-water breaking waves. *J. Fluid Mech.* **209**, 405–433.
- BROEZE J. 1993 Numerical modelling of nonlinear free surface waves with a 3D panel method, Ph.D. dissertation, Enschede, The Netherlands.
- CELEBI M. S., KIM M. H. & BECK R. F. 1998 Fully nonlinear 3D numerical wave tank simulations. *J. Ship Res.* **189** (1), 33–45.
- DOMMERMUTH D. G., YUE D. K. P., LIN W. M. & RAPP R. J. 1988 Deep-water plunging breakers: a comparison between potential theory and experiments. *J. Fluid Mech.* **189**, 423–442.
- FERRANT P. 1998 Runup on a cylinder due to waves and currents: potential flow solution with fully nonlinear boundary conditions. In *Proc. 8th Intl. Offshore and Polar Engng. Conf.* (Montreal) **3**, 332–339.

- GRILLI S., GUYENNE P. & DIAS F. A fully nonlinear model for three-dimensional overturning waves over arbitrary bottom. submitted to *Numerical Methods in Fluids*
- GRILLI S. T. & HORILLO J. 1997 Numerical generation and absorption of fully nonlinear periodic waves. *J. Engineering Mech.* **123**, 1060–1069.
- GRILLI S. T. & SUBRAMANYA R. 1996 Numerical modeling of wave breaking induced by fixed or moving boundaries. *Computational Mech.* **17**, 374–391.
- GRILLI S. T., SVENDSEN I. A. & SUBRAMANYA R. 1997 Breaking criterion and characteristics for solitary waves on slopes. *J. Waterway Port Coastal and Ocean Engineering* **123**, 102–112.
- TSAI W.-T. & YUE D. K. P. 1996 Computation of nonlinear free-surface flows. *Ann. Rev. Fluid Mech.* **28**, 249–278.
- XÜ H. & YUE D. K. P. 1992 Computations of fully nonlinear three-dimensional water waves. *Proc. 19th Symp. on Naval Hydrodynamics*. (Seoul), 24 pps.

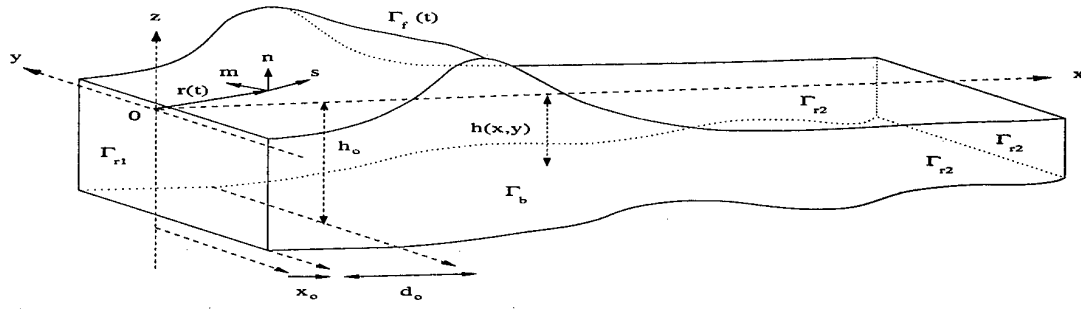


Figure 1: Sketch of the computational domain for 3D BEM solution of FNPF equations.

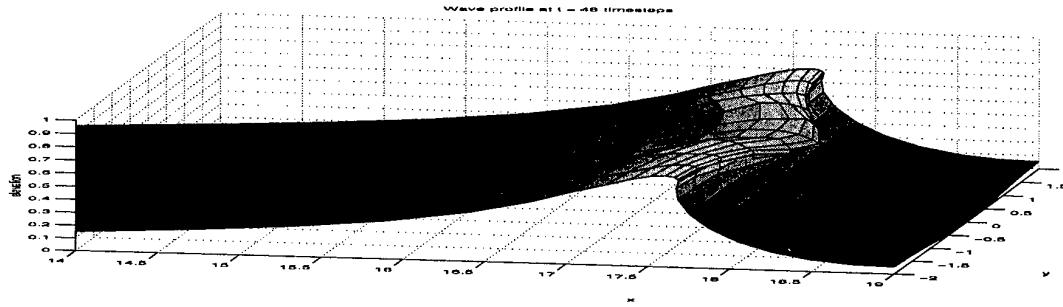


Figure 2: Overturning wave over a ridge modeled as a sloping 1:15 bottom with a $sech^2$ modulation in the y direction.

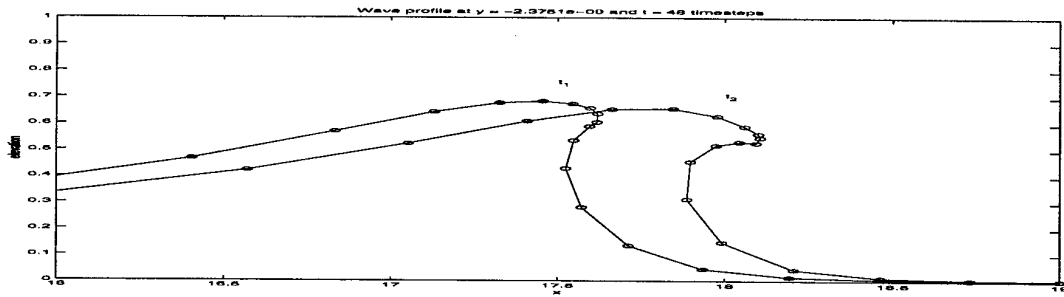


Figure 3: Vertical cross-section at $y = 0$ of the overturning wave of Fig. 2 at time t_2 and an earlier time t_1 .

SOLITARY WAVES IN A STRATIFIED FLUID: MODELLING AND EXPERIMENTS

JOHN GRUE, ATLE JENSEN, PER-OLAV RUSÅS AND JOHAN KRISTIAN SVEEN

Mechanics Division, Department of Mathematics, University of Oslo, Norway

This study concerns solitary waves in a stratified fluid and is motivated by possible effects of sub-surface waves in a layered ocean on compliant offshore units. Such offshore units may be floating platforms or ships at the sea surface with connecting risers and cables to wells and equipment at the sea floor. The concern is the possible loads and induced vibrations of the risers and cables caused by sub-surface waves.

The ocean often has a shallow upper layer with a stratification that is relatively close to a linear function and a deep lower layer with constant density. This motivates for developing a two-layer model where the Brunt-Väisälä frequency is constant in the upper layer and zero in the lower. The basic equations of the fully nonlinear model are derived along the lines of previous studies, most notably Yih (1960) and Turkington et al. (1991). Coordinates $O-xy$ are introduced, with the x -axis horizontal and the y -axis vertical, and with unit vectors \mathbf{i} and \mathbf{j} accordingly. We consider motion in two dimensions where waves of permanent form are propagating with speed c horizontally in the fluid. Viewing the problem in a frame of reference which follows the waves, the motion becomes steady, with a horizontal current with speed c along the negative x -axis in the far-field. The undisturbed fluid has a vertical density profile

$$\rho(y) = \begin{cases} \rho_0 - \Delta\rho y/h_2, & \text{for } 0 < y < h_2, \\ \rho_0, & \text{for } -h_1 < y < 0, \end{cases} \quad (1)$$

We assume that the fluid is incompressible and inviscid. The former means that $\nabla \cdot \mathbf{v} = 0$ where $\mathbf{v} = (u, v)$ denotes the fluid velocity. Conservation of mass, $\nabla \cdot (\rho\mathbf{v}) = 0$, then gives that $\mathbf{v} \cdot \nabla\rho = 0$. Following the procedure of Yih (1960) we introduce pseudo velocities $u' = (\rho/\rho_0)^{1/2}u$, $v' = (\rho/\rho_0)^{1/2}v$. Furthermore we introduce a pseudo stream function Ψ' such that $\mathbf{v}' = \nabla\Psi' \times \mathbf{k}$ where $\mathbf{k} = \mathbf{i} \times \mathbf{j}$. It follows that $\rho = \rho(\Psi')$. From the equations of motion the following relation may be derived

$$\rho_0 \nabla^2 \Psi' + gy \frac{d\rho}{d\Psi'} = \frac{dH(\Psi')}{d\Psi'} = h(\Psi'), \quad (2)$$

where $-\nabla^2 \Psi'$ determines the pseudo vorticity and $H = p + \frac{1}{2}\rho(u^2 + v^2) + \rho gy$ is the Bernoulli constant being conserved along a streamline determined by $\Psi' = \text{constant}$. Furthermore, p denotes pressure and g the acceleration due to gravity. $dH/d\Psi'$ is determined in the far-field, giving

$$\frac{dH}{d\Psi'} = \left(\frac{dp}{dy} + \rho g \right) \frac{dy}{d\Psi'} + \frac{c^2}{2} \frac{d\rho}{d\Psi'} + gy \frac{d\rho}{d\Psi'}, \quad (3)$$

The vertical component of the equation of motion becomes in the far-field $p_y + \rho g = 0$, which means that the first term on the right of (3) is zero. The pseudo stream function is then decomposed by $\Psi' = \Psi'_\infty + \psi'$, where Ψ'_∞ satisfies

$$\frac{d\Psi'_\infty}{dy} = -c \left(\frac{\rho}{\rho_0} \right)^{1/2} \quad (4)$$

giving

$$\nabla^2 \Psi'_\infty = \frac{c^2}{2\rho_0} \frac{d\rho}{d\Psi'}. \quad (5)$$

Since $d\rho/d\Psi'$ is constant along each streamline, (2) becomes

$$\rho_0 \nabla^2 \psi' + g(y - y_\infty) \frac{d\rho}{d\Psi'} = 0, \quad (6)$$

where y and y_∞ are vertical coordinates on the same streamline, with y_∞ in the far-field.

From now on we apply the Boussinesq approximation, i.e. exploit that $\Delta\rho/\rho$ is small. Integrating (4) we find $\Psi'_\infty = -cy[1 + O(\Delta\rho/\rho)]$, giving $y - y_\infty = \psi'/c$. Furthermore we have

$$\frac{g}{\rho_0} \frac{d\rho}{d\Psi'} = \frac{g}{\rho_0} \frac{d\rho}{dy} \frac{dy}{d\Psi'} \simeq \frac{N^2}{c} [1 + O(\Delta\rho/\rho)], \quad (7)$$

where $N^2 = -(g/\rho_0)(d\rho/dy)$ determines the Brunt-Väisälä frequency. Within the Boussinesq approximation we may also replace the pseudo stream function by the stream function Ψ such that $\mathbf{v} = \nabla\Psi \times \mathbf{k}$. Correspondingly, Ψ'_∞ and ψ' are replaced by Ψ_∞ and ψ , respectively. Let $\psi = \psi_2$ in the upper layer and $\psi = \psi_1$ in the lower. Then ψ_2 satisfies the Helmholtz equation in the upper layer, i.e.

$$\nabla^2 \psi_2 + \frac{N^2}{c^2} \psi_2 = 0. \quad (8)$$

ψ_1 satisfies the Laplace equation in the lower layer, i.e.

$$\nabla^2 \psi_1 = 0. \quad (9)$$

The upper boundary of the upper layer is a free surface. With $\Delta\rho/\rho$ small this boundary may be approximated by a horizontal rigid lid. We assume that the bottom of the lower layer is horizontal at $y = -h_1$. Thus, $\psi_2 = 0$ at $y = h_2$, $\psi_1 = 0$ at $y = -h_1$. The two layers are separated by the streamline with vertical coordinate η where $\eta \rightarrow 0$ for $x \rightarrow \pm\infty$. The kinematic boundary condition requires that the fluid velocity is continuous at the boundary between the layers, i.e. that

$$\nabla(\psi_1 - cy) = \nabla(\psi_2 - cy) \quad \text{at} \quad y = \eta. \quad (10)$$

The formulation is fully nonlinear, where the stream functions $\psi_{1,2}$, the stream line η and the wave speed c shall be determined.

We solve the nonlinear problem (8)–(10) by means of integral equations and introduce two Green functions G_1 and G_2 . The first Green function is a pole at $(x, y) = (x', y')$ and satisfies the Laplace equation (9), i.e.

$$G_1(x, y, x', y') = \ln \frac{r}{r_1}. \quad (11)$$

The second Green function is a pole at $(x, y) = (x', y')$ and satisfies the Helmholtz equation (8), i.e.

$$G_2(x, y, x', y') = \frac{\pi}{2} [Y_0(Kr) - Y_0(Kr_2)], \quad (12)$$

where Y_0 denotes the Bessel function of second kind of order zero and $K = N/c$. Furthermore,

$$r = [(x - x')^2 + (y - y')^2]^{1/2}, \quad r_{1,2} = [(x - x')^2 + (y + y' \pm 2h_{1,2})^2]^{1/2}. \quad (13)$$

The stream functions are determined by

$$\psi_{1,2} = \int_I \sigma_{1,2}(s') G_{1,2}(x, y, x'(s'), y'(s')) ds', \quad (14)$$

where $\sigma_1(s)$ and $\sigma_2(s)$ denote yet unknown distributions, I denotes the contour $y = \eta$ and s arclength.

Choosing h_2 as length scale and the linear long wave speed c_0 as velocity scale (and h_2/c_0 as time scale) we determine Nh_2/c_0 from a linearized set of equations. Then the nondimensional quantities Kh_2 , σ_1/c_0 , σ_2/c_0 , η/h_2 and c/c_0 depend on the parameters h_1/h_2 and η_{max}/h_2 , and not on $\Delta\rho/\rho$. Thus, within the Boussinesq approximation, the actual value of $\Delta\rho/\rho$ enters only in the problem through c_0 . Velocity profiles are visualized in figure 1.

The investigation combines theory and experiments. The latter are performed in a wave tank with a stable two-layer fluid with a shallow fluid of linear stratification above or below a deeper

fluid of homogeneous density. We generate solitary waves of mode one which propagate along the wave tank. The amplitude of the waves, defined by the maximal excursion of the stratified layer, is in a rather large range. Particle tracking velocimetry (PTV) and particle image velocimetry (PIV) are employed to make detailed recordings of the induced velocities due to the waves.

Particular focus is paid to the role of the breaking of the waves observed in the experiments. For the large waves the breaking occurs in a region in the centre of the waves in the thin layer with linearly stratified fluid. The breaking serves to limit the fluid velocity. The latter is in the region with breaking found to be of the form $\mathbf{v} = c\mathbf{i} + \mathbf{v}'$ where $c\mathbf{i}$ denotes the wave velocity and \mathbf{v}' a velocity field where $|\mathbf{v}'| \ll c$. This means that the wave speed provides an upper bound of the fluid velocity induced by the wave, practically speaking. The wave breaking occurs similarly in the experiments with the inverted two-layer model, when the waves are large. A fluid velocity approximately equal to the wave speed means that the wave transports mass.

The experimental and theoretical velocity fields exhibit good agreement up to breaking, generally speaking. Intensive breaking is found to occur for a wave amplitude a less than about 0.8 times the depth h_2 of the linearly stratified layer. This is in agreement with the theoretical model which predicts an induced fluid velocity being less than the wave speed when $a/h_2 < 0.855$. For larger waves the theory does not fit with the experimental observations. We find that the experimental waves broaden when the non-dimensional wave amplitude exceeds 0.8–0.9 (figure 2). The experiments suggest that the broadening is caused by the wave breaking which limits the magnitude of the fluid velocity. The broadening is not reproduced by the theory. The broadening effect found here is entirely different from the one taking place in a two-fluid system with constant densities in each of the layers.

In the present two-layer model a solitary wave always exhibits an excursion out of the layer with linear stratification.

This work was conducted under the Strategic University Programme 'General Analysis of Realistic Ocean Waves' funded by the Research Council of Norway.

References

- Turkington, B., Eydeland, A. & Wang, S. 1991 A computational method for solitary internal waves in a continuously stratified fluid. *Stud. Appl. Math.*, **85**, 93.
- Yih, C.-S. 1960 Exact solutions for steady two-dimensional flow of a stratified fluid. *J. Fluid Mech.*, **9**, 161.

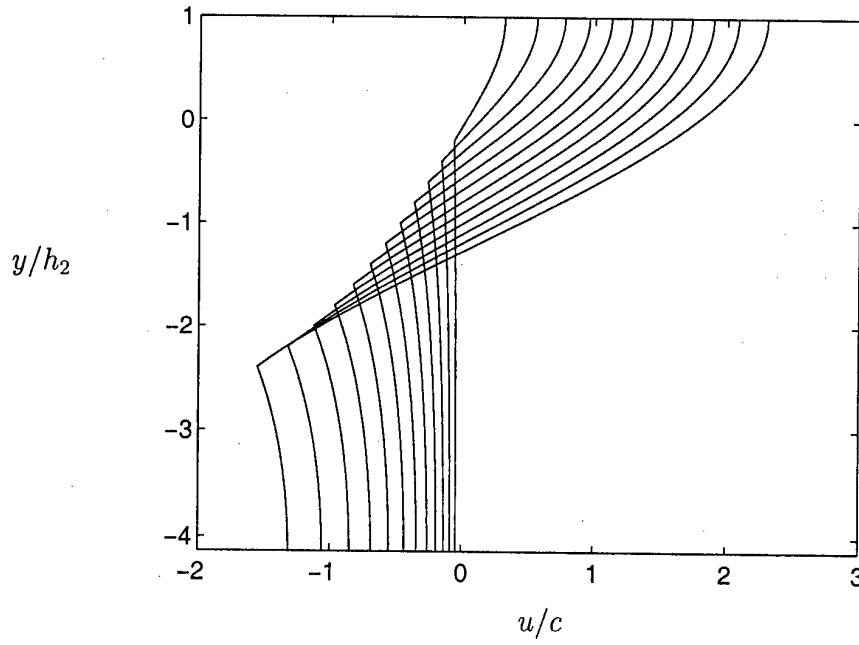


Figure 1: Velocity profiles at wave crest. $a/h_2 = 0.2, 0.4, 0.6, \dots, 2.4$. $h_1/h_2 = 4.13$.

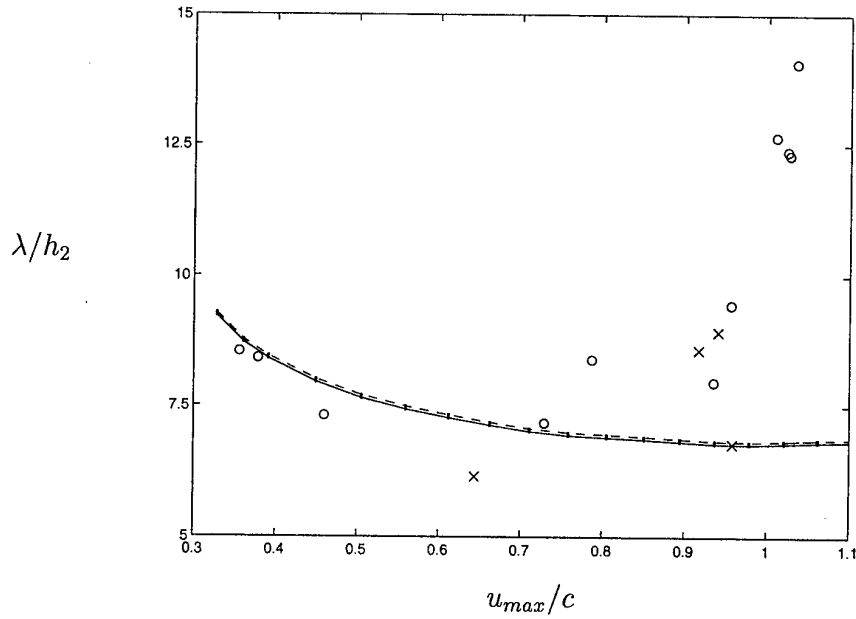


Figure 2: Nondimensional wave length λ/h_2 vs. nondimensional velocity u_{max}/c . Small circles and crossed (experiments) Solid and dashed line (theory).

BEHAVIOR OF A SHIP WITH ELASTIC DISTORTIONS IN PERIODIC WAVES

R. Gueret and A. J. Hermans

Department of Applied Mathematics, Delft University of Technology, The Netherlands

1 Introduction

In this presentation we study the rigid body motion and the elastic behaviour of a ship in periodic waves. In an earlier paper on the motion of large elastic platforms it was found that it is possible to derive a formulation to describe the rigid body motion and the elastic behaviour by means of one differential-integral equation. This equation for the elevation can be solved numerically, without splitting the problem in the various rigid motion and eigenmode components, as is standard in the field of linear ship motions. One of the goals of this project is to apply similar ideas to an elastic ship.

In our case the ship is not a rigid structure and we focus on the shears, bending moments and distortion due to the waves excitation. We consider the ship as an elastic beam and we only study the time dependent distortions in the hull. It means that we don't take in account the strains due to gravity and buoyancy forces in still water. In this presentation we finally restrict ourselves to the influence of head-seas on the heaving and pitching rigid-body motions. Furthermore, to obtain the bending motion we take an elastic beam as an elastic model for the ship.

We first derive a general formulation for a 3D ship, and then give some results for a ship in head waves for heave and pitch motion, and associated elastic distortion of the hull. In principle we can extend the formulation for the effect of waves on a ship travelling with steady forward speed.

2 Mathematical model

In this section we derive a formulation for a ship without forward speed. We assume the flow to be a potential flow and introduce the velocity potential $\mathbf{V} = \nabla\Phi(x, t)$ where \mathbf{V} is the fluid velocity vector. We get for the potential $\Phi(x, t)$ the Laplace equation $\Delta\Phi = 0$ in the fluid domain Ω .

We have at the linearized free surface $z = 0$, the linearized kinematic condition $\Phi_z = \eta_t$, and the dynamic condition $\Phi_t = -g\eta$ where $\eta(x, t)$ denotes the wave elevation. On the hull, we have the following kinematic and dynamic conditions:

$$\frac{\partial\Phi}{\partial n} = v_n = \tilde{w}_t(x, t) \vec{e}_z \cdot \vec{n} + \tilde{\theta}_t(x, t) y \vec{e}_z \cdot \vec{n} - \tilde{\theta}_t(x, t) z \vec{e}_y \cdot \vec{n} \quad (1)$$

$$\frac{p}{\rho} = -\Phi_t - g(\tilde{w}(x, t) + \tilde{\theta}(x, t) y) \quad (2)$$

where v_n is the normal velocity of a point at the hull of the ship, $\tilde{w}(x, t)$ the deflection and $\tilde{\theta}(x, t)$ the angular rotation due to torsion respectively.

The ship is assumed to behave like a beam with no thickness. We use the linear beam theory to describe its deflection $\tilde{w}(x, t)$ and its angular rotation $\tilde{\theta}(x, t)$. Then we have the equations:

$$\mu(x) \frac{\partial^2 \tilde{w}(x, t)}{\partial t^2} + \frac{\partial^2}{\partial x^2} \left(D(x) \frac{\partial^2 \tilde{w}(x, t)}{\partial x^2} \right) = Z(x, t) \quad (3)$$

$$I_s \frac{\partial^2 \tilde{\theta}(x, t)}{\partial t^2} - \frac{\partial}{\partial x} \left(c \frac{\partial \tilde{\theta}(x, t)}{\partial x} \right) = \Gamma(x, t) \quad (4)$$

where D is the flexural rigidity, μ the mass per length, I_s the rotational inertia, Z and Γ the vertical force and the moment per length acting on the ship. The shear and bending moment vanish at the ends of the beam. Thus, we have for the boundary conditions:

$$D \frac{\partial^2 \tilde{w}}{\partial x^2} = 0 \quad \frac{\partial}{\partial x} \left(D \frac{\partial^2 \tilde{w}}{\partial x^2} \right) = 0 \quad (5)$$

$$\frac{\partial \tilde{\theta}}{\partial x} = 0 \quad (6)$$

We consider a harmonic wave propagating in the direction β with respect with the main axis of the ship. The harmonic wave potential, deflection and angular rotation can be written as $\Phi(\mathbf{x}, t) = \phi(\mathbf{x}) e^{-i\omega t}$, $\tilde{w}(x, t) = w(x) e^{-i\omega t}$ and $\tilde{\theta}(x, t) = \theta(x) e^{-i\omega t}$. The incident plane wave potential equals:

$$\phi^{inc} = \frac{g\zeta_0}{\omega_0} \exp\{ik_0(x \cos \beta + y \sin \beta) + k_0 z\} \quad (7)$$

The potential function is split in a incident wave potential and a diffracted wave potential.

$$\phi(\mathbf{x}) = \phi^{inc}(\mathbf{x}) + \phi^D(\mathbf{x}) \quad (8)$$

We notice that in most theories the diffracted potential is defined for the fixed ship, while here it also contains the effect of the rigid- and elastic-body motions.

We finally introduce the Green's function that fulfills $\Delta \mathcal{G}(\mathbf{x}, \xi) = 4\pi \delta(\mathbf{x} - \xi)$, the free surface condition and the radiation condition.

For $\mathbf{x} \in \partial\Omega$:

$$2\pi \phi^D = \int_{\partial\Omega} \left(\phi^D \frac{\partial \mathcal{G}}{\partial n} - \mathcal{G} \frac{\partial \phi^D}{\partial n} \right) dS \quad (9)$$

Equations (1), (2) and (7) lead to a system of integral equations:

$$-\mu\omega^2 w + \frac{\partial^2}{\partial x^2} \left(D \frac{\partial^2 w}{\partial x^2} \right) - i\rho\omega \left\{ \int_{\mathcal{C}(x)} \phi^D \vec{n} dl \right\} \cdot \vec{e}_z + \rho g b(x) w = i\rho\omega \left\{ \int_{\mathcal{C}(x)} \phi^{inc} \vec{n} dl \right\} \cdot \vec{e}_z \quad (10)$$

$$-I_s \omega^2 \theta - \frac{\partial}{\partial x} \left(c \frac{\partial \theta}{\partial x} \right) - i\rho\omega \left\{ \int_{\mathcal{C}(x)} \vec{OM} \wedge \phi^D \vec{n} dl \right\} \cdot \vec{e}_x + \mathcal{K}(x) \theta = i\rho\omega \left\{ \int_{\mathcal{C}(x)} \vec{OM} \wedge \phi^{inc} \vec{n} dl \right\} \cdot \vec{e}_x \quad (11)$$

where $b(x)$ is the width of the ship at abscis x , $\mathcal{K}(x)$ the restoring moment for a slice at abscis x and \mathcal{C} the line integral over the wetted hull at abscis x .

$$2\pi \phi^D - \int_{\partial\Omega} \left\{ \phi^D \frac{\partial \mathcal{G}}{\partial n} + i\omega \mathcal{G} (w \vec{e}_z \cdot \vec{n} + \theta y \vec{e}_z \cdot \vec{n} - \theta z \vec{e}_y \cdot \vec{n}) \right\} dS = \int_{\partial\Omega} \mathcal{G} \frac{\partial \phi^{inc}}{\partial n} dS \quad (12)$$

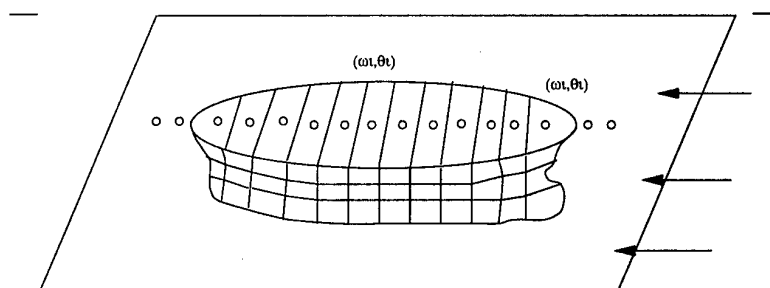
3 Numerical method

The differential equations are discretised by means of a difference scheme, while the integral equation is discretised by means of a piece-wise constant panel distribution. The final set of equations is a matrix equation for the coupled unknowns. For the purpose of calculation, the hull is divided into N slices. Each slice is supposed to have a constant displacement (w_i, θ_i) .

As we are using a finite difference approach to solve the dynamic equations for the beam, we introduce 4 supplementary points for the mesh describing the beam in order to represent the fourth order derivative for the beam equation. We denote the diffracted potential on each of the M panels of the mesh describing the ship's hull by ϕ_i^D .

Equations (3), (4), (5), (6) (10) and (11) lead to a linear system for the discretized problem. The solution vector is written in the form

$$\vec{X} = \{\phi_1^D, \phi_2^D, \dots, \phi_M^D, w_{-1}, w_0, w_1, w_2, \dots, w_N, w_{N+1}, w_{N+2}, \theta_0, \theta_1, \theta_2, \dots, \theta_N, \theta_{N+1}\} \quad (13)$$



4 Numerical results for a paralepipedic barge

We present some numerical results for a thin barge of dimension $l_x=100\text{m}$, $l_y=10\text{m}$, $l_z=5\text{m}$. The ship is cut in 30 slices and has a constant flexural rigidity of 10^{11}Nm^2 . The computations are carried out for a wave direction parallel to the ship direction, hence, $\theta(x) \equiv 0$. The incoming wave has a wave length of 45m and a unit amplitude. We are so here only interested in the motion associated with the heave and pitch motion and confined in a vertical plane. The first two graphics represent the real part and the imaginary part of the total vertical deflection, ie the deflection at $t = 0$ and $t = T/2$ including the heave, pitch motion and the bending distortion due to the flexibility of the ship.

The graphs of figure (2) represent the bending distortion and moment.

We can clearly see the first two principal bending modes of an elastic vibrating uniform beam.

The graphs of figure (3) represent the amplitude of the bending moment. for a wave length equal to the length of the ship, the amplitude is maximal at mid-point of the ship.

References

- [1] Aad J. Hermans. A boundary element method for the interaction of free-surface waves with a very large floating flexible platform, *J. of fluids and structures*, to appear.
- [2] R.E.D Bishop and W.G Price (1978) . *Hydroelasticity of ships*, Cambridge University Press.

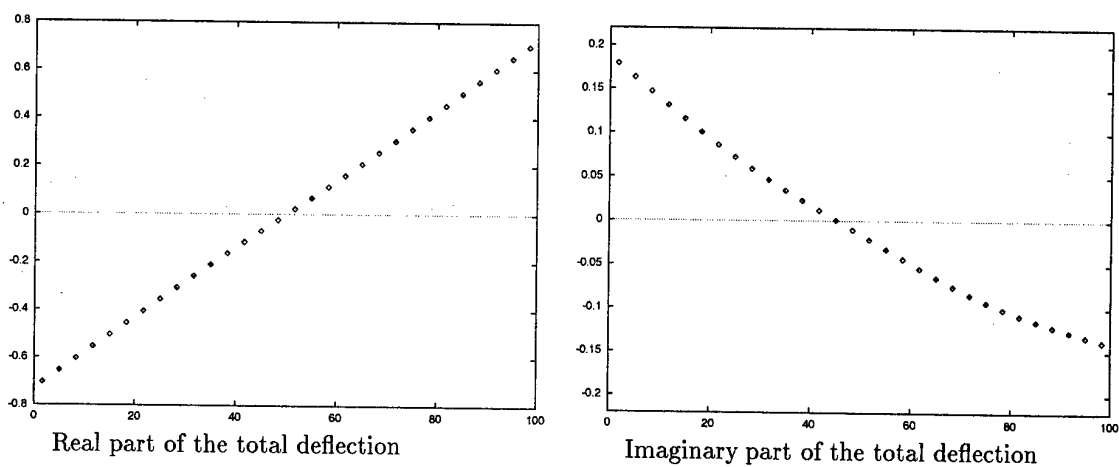


Figure 1: total deflection

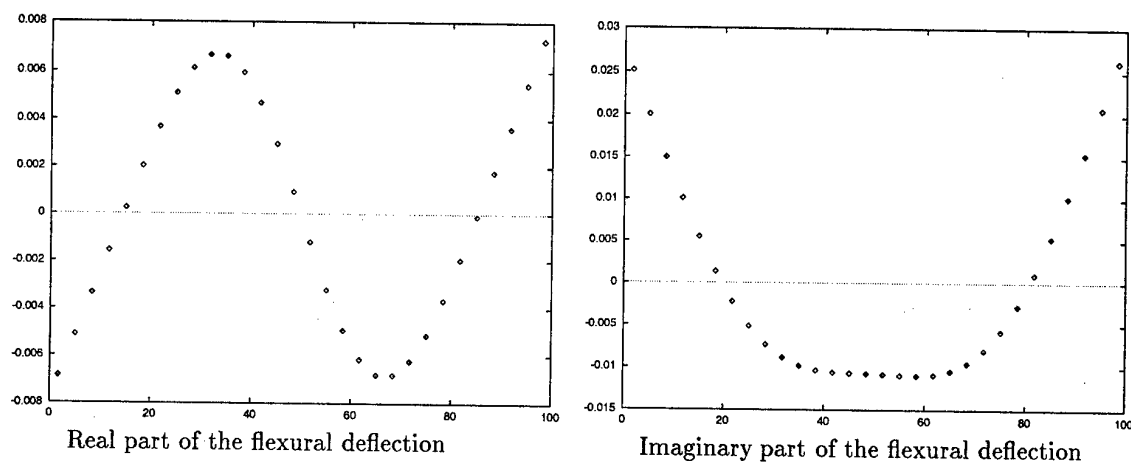


Figure 2: flexural deflection

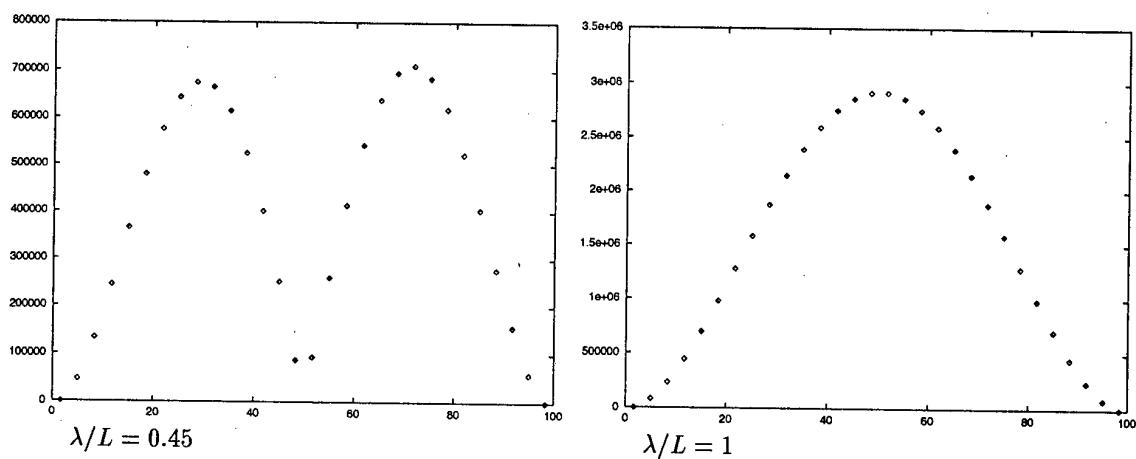


Figure 3: Amplitude of the bending moment

NON-LINEAR MOTION OF A SUBMERGED BODY IN WAVES

J. Andrew Hamilton and Ronald W. Yeung

Department of Mechanical Engineering
University of California at Berkeley, Berkeley, CA 94720, USA.

Background and Introduction

In this paper the time-domain solution of wave diffraction and the unsteady free motion of a body in waves are addressed. The 'shell-function' method of solution, described in Hamilton & Yeung [3], is extended to handle the diffraction problem and the exact kinematic boundary condition on the body under wave-excited motion. The simplification of a linear free surface condition is retained. The radiation problem with prescribed body motion was solved in [3], and as noted therein, the method has excellent computational efficiency and the shell coefficients constitute a perfect radiation boundary. The essential features of this solution method are briefly reviewed below.

The shell function method is a hybrid integral equation method which combines a Rankine source integral equation formulation with a time-dependent free-surface Green-function formulation. As is well known, a Rankine singularity as the source function yields integrals over all boundaries of the fluid domain. The resulting numerical method requires discretization of the entire area of the disturbed free surface in addition to discretization of the body geometry. The major advantage of this formulation is the low computational requirements of such a source function, making the inclusion of nonlinear effects more accessible. Alternatively, a more sophisticated choice of Green function eliminates the need to discretize any surfaces except that of the body. Typically, this function satisfies the linearized free-surface condition and an appropriate far-field condition. The computational effort required to evaluate this function is high, making the treatment of nonlinear body boundary conditions rather impractical.

The shell function method combines these two integral equation formulations in a way that retains the advantages of both. The fluid domain is split into two regions separated by an imaginary surface surrounding the body, labeled the shell surface. The simple source method is used in the resulting interior region and the time-dependent Green-function formulation is used to represent the exterior problem. Matching the two solutions on the shell surface provides a complete solution for the flow exterior to the body. Additionally, choosing an axisymmetric shell surface geometry and a constant time-step size reduces the number of unique integrals of the unsteady Green function to a number that can be readily pre-computed and stored. An axisymmetric shell imposes no restriction on the body geometry.

If the body is surface piercing, the shell surface separating the interior and exterior regions will be surface piercing and the free-surface boundary condition will need to be advanced by numerical integration. If a non-linear free-surface condition is desired, a mixed Eulerian-Lagrangian method can advance the position of the free surface. The non-linear solution of the free-surface solution in the interior region will also have to be matched to the linear solution in the exterior region. This is sensible in three-dimensions as the height of wave disturbances will diminish as they travel away from the body. To date, the three dimensional shell method has only been implemented for bodies and shells that do not pierce the surface but the surface-piercing case is not a difficult hurdle to overcome (see Figure 1).

Formulation and Numerical Procedure

Considered here are the effects of an incident wave on a submerged body which responds freely to the wave excitation. Figure 1 illustrates the problem geometry and indicates the separation of the two fluid domains by the imaginary shell surface. In each domain the velocity potential must satisfy the usual boundary conditions as well as a matching condition on the shell surface. Applying Green's theorem to the interior region with a simple source Green function provides:

$$C(P)\phi(P, t) + \int_{B \cup F \cup S} \phi(Q, t) \left(\frac{1}{r} \right)_{\nu} dS_Q = \int_{B \cup F \cup S} \phi_{\nu}(Q, t) \left(\frac{1}{r} \right) dS_Q \quad P \in S \quad (1)$$

In the discrete form of a typical panel method, this implies:

$$A_{nm}\phi_m = B_n \quad (2)$$

where,

$$A_{nm} = C(P_n)\delta_{nm} + \int_{S_m} \left(\frac{1}{r} \right)_{\nu} dS_Q \quad B_n = \sum_{m=1}^M (\phi_m)_{\nu} \int_{S_m} \left(\frac{1}{r} \right) dS_Q \quad (3)$$

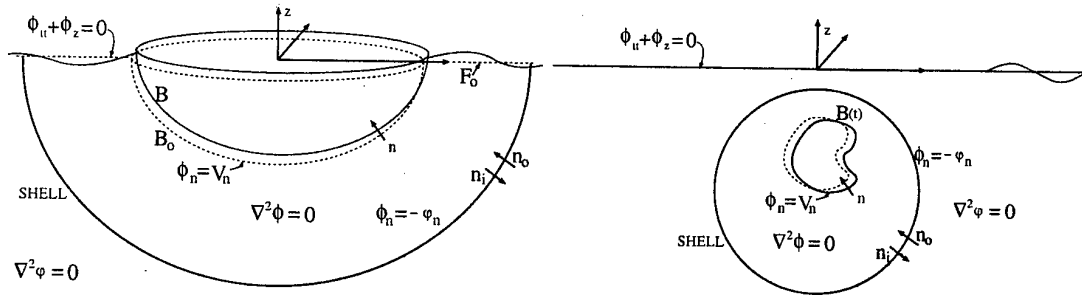


Figure 1: Schematics of the surface piercing shell method and the fully submerged shell method.

with m being the index associated with the surface unknown, and n the point at which the integral equation is satisfied. For this source formulation, ϕ_ν is provided by the boundary conditions of the domain, equal to the normal velocity of the body on the body surface, and provided by the shell coefficients on the shell surface. A perfect shell would represent the appropriate radiation and memory effects associated with wave motion.

Application of Green's theorem in the exterior region to the usual time-dependent Green function G [2] and φ_τ provides:

$$-C(P)\varphi(P,t) = \int_S [G_\nu(P,Q,0)\varphi(Q,t) - G\varphi_\nu] dS_Q + \int_0^t d\tau \int_S [\varphi_\nu(Q,\tau)H_\tau(P,Q,t-\tau) - \varphi H_{\nu\tau}] dS_Q \quad (4)$$

Discretization of this integral equation provides a linear relationship between φ and φ_ν on the shell surface (see [3] for details).

$$C_{nm}[\varphi(t_K)]_m + D_{nm}[\varphi_\nu(t_K)]_m = E_n \quad (5)$$

The matrices C_{nm} , D_{nm} , and the vector E_n are summations of integrals of the free-surface Green function. If an axisymmetric shell is selected, and if the time-step is chosen as constant, the number of distinct integrals (in C_{nm} , D_{nm} , E_n) that need to be calculated is greatly reduced. When these "shell coefficients" are pre-computed and stored, evaluations of the free-surface Green function during (*any subsequent*) time-domain simulations is eliminated. E_n is a convolution of the velocity potential with respect to past time, involving integrals of the unsteady Green function. This term contains the "memory effects" of the fluid problem.

Solving (5) for φ_ν and applying the matching conditions between the two domains provides the necessary terms to complete the formation of the right hand side of (2) for the shell surface. If a superposition of solutions in the exterior region is needed, then the matching conditions are modified to reflect this. For example, in our case of an incident wave potential being present (φ^i), the matching conditions are:

$$\phi(\mathbf{x},t) = \varphi(\mathbf{x},t) + \varphi^i(\mathbf{x},t) \quad \frac{\partial \phi(\mathbf{x},t)}{\partial n_i} = -\frac{\partial \varphi(\mathbf{x},t)}{\partial n_o} - \frac{\partial \varphi^i(\mathbf{x},t)}{\partial n_o} \quad (6)$$

Thus, the linear equations for ϕ_ν provided by the exterior solution become:

$$[\phi_\nu]_m = -[D_{nm}]^{-1}E_n + [D_{nm}]^{-1}C_{nm}([\phi]_m - [\varphi^i]_m) + [\varphi_\nu^i]_m \quad (7)$$

This equation provides the necessary terms on the right hand side of (2) in terms of quantities that are either known or are being solved for. Time-stepping of the solution is thus possible. It is well known that the effects of incident waves can be incorporated by directly modifying the body boundary condition, but it is envisioned that such a manner of treating the incident wave potential will provide more effective extensions of the method described in the conclusion section.

For the free body motion problem, the equations of motion for the body must be solved in conjunction with the hydrodynamic problem. On the body surface, ϕ_ν on the right hand side of equation 2 is provided by the normal velocity of the body surface

$$\phi_\nu = V_n = \dot{\mathbf{x}} \cdot \mathbf{n} \quad (8)$$

For the radiation problem this term is known but is unknown for the free motion problem. Thus, allowing translational motion creates three additional unknowns on the left hand side of the linear system (2). Numerical integration of the equations of motion of the body provides the required three additional equations.

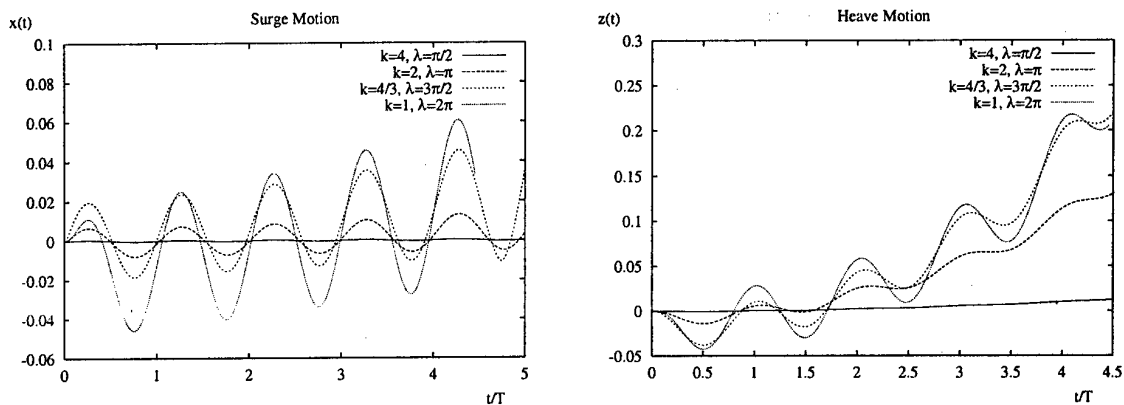


Figure 2: Submerged sphere in incident waves, motion relative to initial position, time is measured relative to incident wave period.

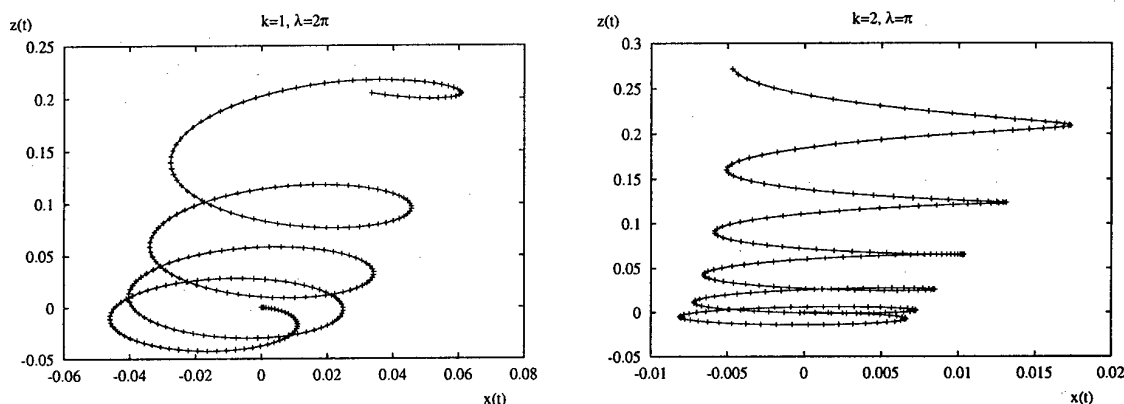


Figure 3: Path of motion for body free to move for $k=1$ and $k=2$.

This procedure is similar to that employed in two dimensions by Yeung [6]. An explicit Adams-Bashforth multi-step method is well suited to integrating the equations of motion because of the shell method's constant time step restriction.

In this work, no rotational motion of the body is considered. The results below are for a sphere and so the pressure on the body is always directed towards the center of buoyancy, resulting in no angular moments.

Demonstrative Results

The method described is used to compute a variety of results for the motion of a sphere submerged in the presence of plane progressive waves. All quantities shown are nondimensionalized by the primary variables density $\bar{\rho}$, body radius \bar{a} , and gravity \bar{g} . The incident wave potential is comprised of simple plane progressive waves whose amplitude grows smoothly from zero to 0.15 in the first one quarter wave period. Transient effects of this are minimal. The test cases consist of a sphere submerged $1\frac{1}{2}$ radii below the free surface, this provides an initial vertical gap between the sphere and the calm water surface of $\frac{1}{2}$.

Two situations are considered, one in which the sphere is free to move in all directions, and one in which it is restrained to move only in surge. Figures 2 and 3 shows the surge and heave motions at different wave numbers. The amplitudes are proportional to the fluid motion at the depth of the sphere. i.e. The $k = 4$ case corresponds to shorter wavelengths and the body is largely below the $\lambda/2$ depth of wave effects. In each case, the body experiences drift in the direction of the waves but also in the vertical direction, towards the free-surface. As the body rises closer to the free surface, the amplitudes of motion increase. When the sphere has risen 0.3, it hits the submerged shell surface and the simulation has to be halted.

Figure 4 shows results for the same geometry but with the motion restricted to the surge direction. As expected, there is drift in the direction of the waves, however, the amplitude of the motion does not increase because the body is not free to rise to the free surface. Again the longer wavelengths produce larger motions and after a few periods of oscillations, the drift velocity has become constant. The vertical force on the body is also computed. As seen in figure 4, this force has a small positive average, causing the body to rise if not restrained.

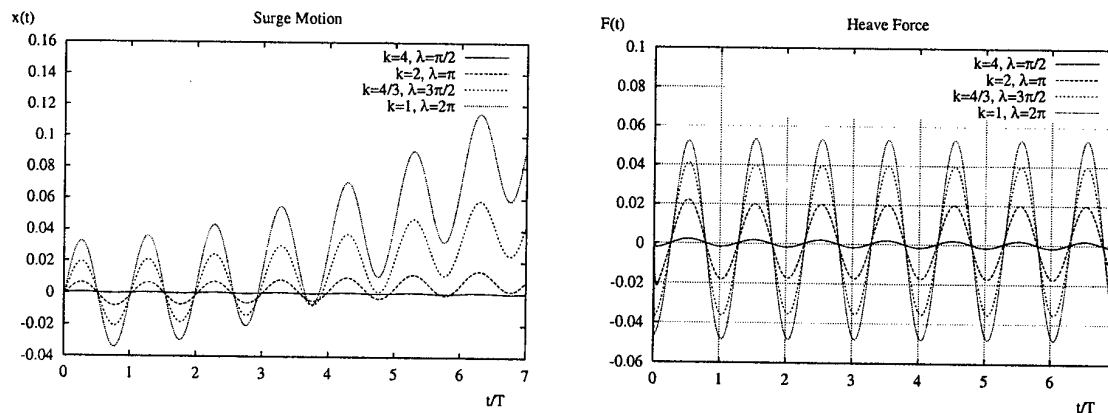


Figure 4: Submerged sphere restricted to surge motion.

Conclusion

Although results presented here are limited to the submerged case, the shell method can be implemented for a surface piercing shell. The shell function method provides a far-field boundary condition which limits the size of the region near the body for which the hydrodynamic problem needs to be solved. To date, a 'simple source' boundary integral method has been used for the interior region. Extension of the method to include a more nonlinear treatment of the interior region, such as that used by Scorpio and Beck [4], is a possibility. The inclusion of effects of viscosity by a Navier-Stokes solver such as [9] or a three-dimensional analog of the FSRVM [8] is also a viable alternative. The superior feature of this formulation is that no real-time computations of the unsteady free-surface Green function and its memory effects are needed during the simulations. All the runs presented here used the same file of shell coefficients and runs of 1000 time-steps can be completed within one day on a medium power workstation with no restrictions on the body geometry.

References

- [1] Clement, A. and Domgin, J.F., (1995). "Wave absorpsion in a 2-D wave basin by coupling two methods", *Journal of Computational Physics*.
- [2] Finkelstein, A.B., (1957). "The initial value problem for transient water waves", *Communications on Pure and Applied Math*, **10**.
- [3] Hamilton, J.A. and Yeung, R.W., (1997). "Shell-Function Solutions for Three-Dimensional Nonlinear Body-Motion Problems", *Ship Technology Research*, **44**.
- [4] Scorpio, S.M. and Beck, R.F., (1998). "A Multipole Accelerated Desingularized Method for Computing Nonlinear Wave Forces on Bodies", *Journal of Offshore Mechanics and Arctic Engineering*, **120**.
- [5] Sierevogel, L.M. and Hermans, A.J., (1995). "Absorbing boundary condition for floating objects in current and waves", *10th International Workshop on Water Waves and Floating Bodies*, Oxford, England.
- [6] Yeung, R.W., (1982). "The transient heaving motion of floating cylinders", *J. Eng. Math*. **16**.
- [7] Yeung, R.W. and Cermelli, C., (1993). "The shell functions: A global method for computing time dependent free surface flows", *8th International Workshop on Water Waves and Floating Bodies*, St. Johns, Newfoundland.
- [8] Yeung, R.W. and Liao, S.-W., (1999). "Time-Domain Solution of Freely-Floating Cylinders in a Viscous Fluid", *9th International Conference of Society of Offshore and Polar Engineers*, vol. III, Brest, France.
- [9] Yeung, R.W. and Xu, X., (1995). "Wave-Structure Interaction in a Viscous Fluid", *Offshore Mechanics and Arctic Engineering*.

An experimental investigation of ringing loads on a vertical cylinder in transient waves

by
Morten Huseby, Atle Jensen and John Grue

Mechanics Division, Department of Mathematics
University of Oslo, Norway

Over the last ten years considerable efforts have been made to analyze wave loads which lead to sudden high frequency responses of floating or stationary offshore platforms. Several model tests and small scale experiments have been undertaken. Perturbation methods and fully nonlinear methods have been developed to deal with the phenomenon (see the reference list). It seems, however, that a thorough understanding of this problem is still lacking.

Recently, we have performed several small scale experiments on slender vertical circular cylinders in incoming periodic waves (Huseby & Grue, 2000). The periodic results are, however, not the focus here. We observed in these experiments that rather intense higher harmonic oscillations of the force acting on the cylinder happen due to the transient leading part of the wave train. The oscillations of the resulting forces are much more pronounced in the transient part of the waves than in the periodic part. This typically occurs for rather steep waves. The behavior of the measured forces is similar to the forces observed in focused waves with large elevation (Grue *et al.*, 1993; Chaplin *et al.*, 1997).

This has motivated us to study these waves and the resulting forces more closely. The leading wave of a periodic wave train is large and transient. We use PIV to measure velocity and acceleration fields of the waves, considering variation in both time and space. The PIV measurements are combined with amplitude and force measurements on cylinders of different radii.

Experiments and results

The measurements are carried out in a wave tank which is 24.6 m long, 0.5 m wide and filled with water to a depth of 0.6 m. In one end of the tank there is an absorbing beach. At the other end there is a wave maker which is a vertical plate controlled and monitored by a computer. The movement of the wave maker can be described by the displacement $\xi(t)$ from the mean position, as a function of time (t). This displacement is given as sine function multiplied by a time dependent amplitude function, i.e.

$$\xi = \xi_1 \left(\frac{1}{2} + \frac{1}{2} \tanh \left[(2t - 1) \tanh^{-1} (0.98) \right] \right) \sin(2\pi ft), \quad (1)$$

where f is the frequency of the wave maker and ξ_1 the amplitude for large t . This means that $\max(\xi) = 0.99\xi_1$ after 1 second.

We consider the leading transient part of the wave train and the resulting force on the cylinder. We use PIV to measure the velocity and acceleration fields of the waves for several different frequencies. Here we present results for two frequencies. These wave measurements are performed without the cylinder present in the tank. When the wave measurements are completed, the cylinder is mounted in the tank for subsequent force recordings. The incoming waves were measured at the position of the cylinder.

We use two cylinders of radius $R = 3$ and $R = 6$ cm. Both cylinders extend to the entire water depth. The distance from the wave maker to the cylinder is 13.12 m. The

total force $F(t)$ in the horizontal direction is recorded by two force transducers, and we refer to the sum of these two as the total force.

For the small cylinder we get a large rapid oscillation of the force for both frequencies (figure 1). This is an oscillation that we believe will lead to ringing behavior of offshore structures. The oscillation of the force appears as the wave leaves the cylinder. For the large cylinder a rapid oscillation occurs for the longest waves, while no such oscillation occurs for the shorter waves. This indicates that the oscillation of the force is not only caused by the incoming waves, but also depends on the presence of the cylinder in the waves. Typically the larger cylinder experiences these kind of “ringing loads” for a range of wave lengths that is larger than for the smaller cylinder.

Measurements of the fluid accelerations of the incoming waves, at the position of the cylinder, are then shown. The accelerations are shown as a time series at a geometric point in the wave tank. The accelerations are a mean over 1 cm in depth, 4.4 cm under the mean water level, at the position of the cylinder. In order to obtain the time series, the PIV system is triggered each 1/100 of a second. For each 31 time steps a mean of 5 independent runs in the wave tank is obtained. The lower plot in figure 2 represents 155 independent PIV measurements. There do not seem to be any rapid oscillations of the accelerations, as a function of time, indicating that the rapid oscillations of the force are not caused by oscillations in the incoming acceleration field.

At the workshop more results will be presented.

This work was partly conducted under the DEEPER JIP with financial support from the Research Council of Norway and a consortium of industrial sponsors, and partly under the the Strategic University Programme “General Analysis of Realistic Ocean Waves”.

References

- CHAPLIN, J. R., RAINEY, R. C. T. & YEMM, R. W. 1997 Ringing of a vertical cylinder in waves. *J. Fluid Mech.* **350**, 119–147.
- FALTINSEN, O. M., NEWMAN, J. N. & VINJE, T. 1995 Nonlinear wave loads on a slender vertical cylinder. *J. Fluid Mech.* **289**, 179–199.
- FERRANT, P. 1998 Fully non linear interactions of long-crested wave packets with a three dimensional body. In *Provisional proceedings, 22nd ONR Symposium in Naval Hydrodynamics, Tuesday/wednesday sessions*, pp. 59–72.
- GRUE, J., BJØRSHOL, G. & STRAND, Ø. 1993 Higher harmonic wave exciting forces on a vertical cylinder. Preprint, No. 2. ISBN 82-553-0862-8, Institute of Mathematics, University of Oslo.
- HUSEBY, M. & GRUE, J. 2000 An experimental investigation of higher harmonic wave forces on a vertical cylinder. *J. Fluid Mech.* (to appear).
- MALENICA, S. & MOLIN, B. 1995 Third-harmonic wave diffraction by a vertical cylinder. *J. Fluid Mech.* **302**, 203–229.

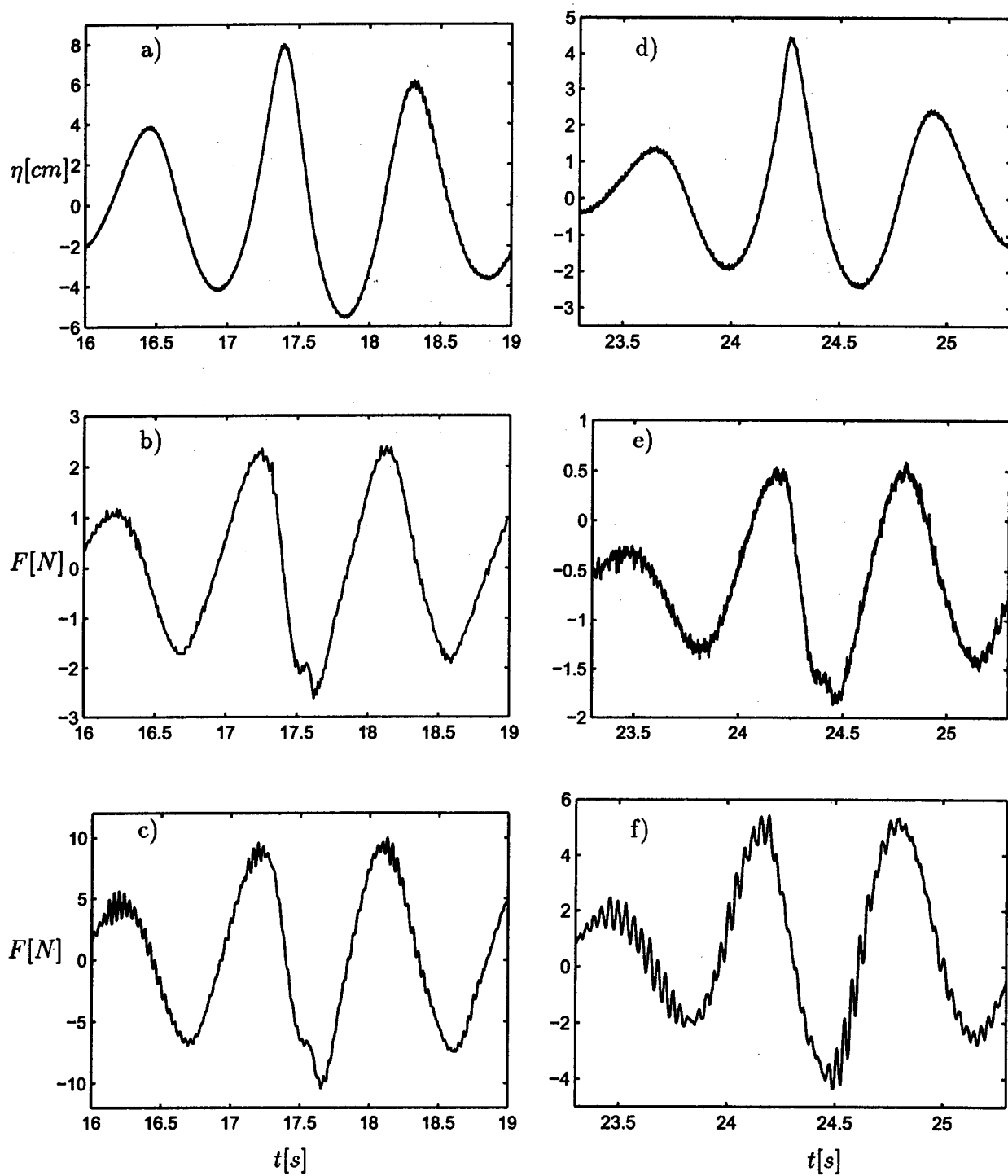
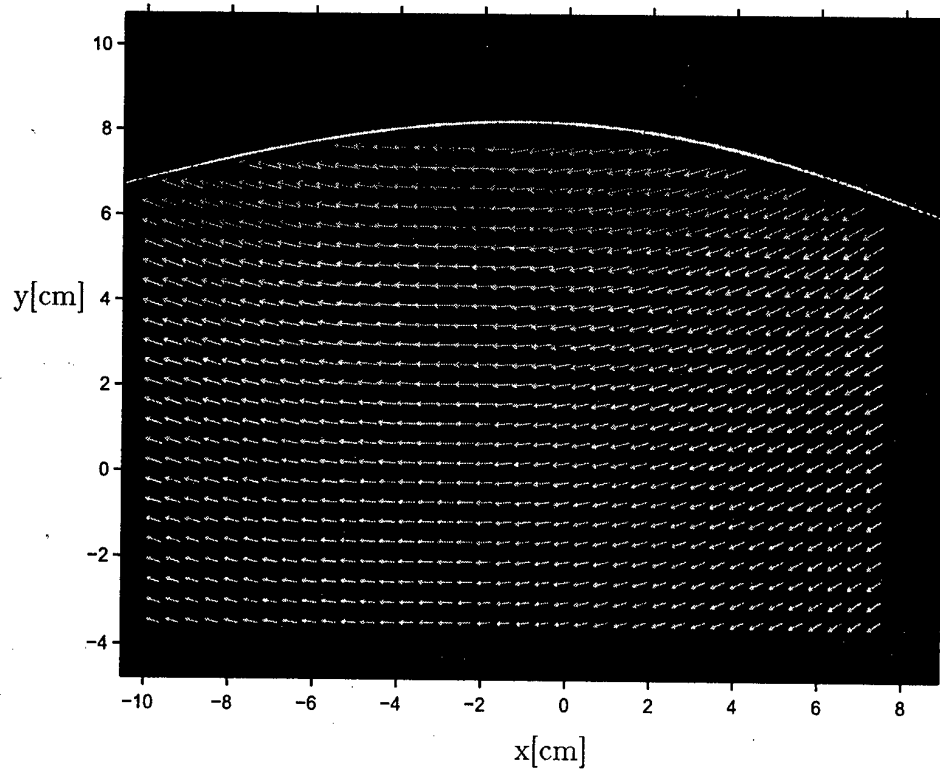
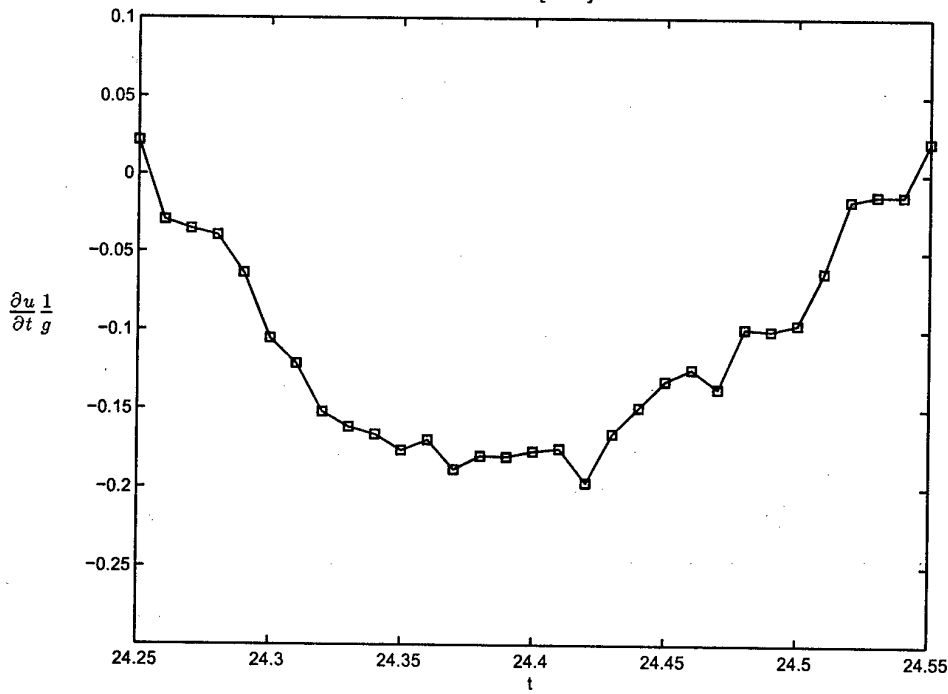


Figure 1: a), b) and c): $f=1.0$ Hz, $ak = 0.19$ (ak from the steady wave train). d), e) and f): $f=1.425$ Hz, $ak = 0.18$. a) and d): Time history of the wave elevation. b) and e): Time history of the force for the small cylinder ($R = 3$ cm). c) and f): Time history of the force for the large cylinder ($R = 6$ cm).



a)



b)

Figure 2: a): Velocity field. Waves with $f=1.0$ Hz, $ak = 0.19$ (ak from the steady wave train) and $g/\omega = 156$ cm/s. b): Time development of the acceleration. Each point is a separate run and is the mean of 1 cm in depth. Waves with $f=1.425$ Hz, $ak = 0.18$.

LIQUID FLOW CLOSE TO INTERSECTION POINT

A. IAFRATI¹ AND A. KOROBKIN²

¹*INSEAN - Italian Ship Model Basin - Rome, Italy*

²*Laurentyev Institute of Hydrodynamics - Novosibirsk, Russia*

1 Introduction

The plane unsteady problem of water impact is considered with focusing the attention on the flow near the intersection point between a liquid free surface and a rigid contour. The correct description of the flow field in this region is highly expensive in spite of its small influence on the total hydrodynamic load. On the other hand, in numerical study of the slamming problem accurate treatment of jet flow can improve numerical algorithms in use and increase accuracy of the numerical solutions.

We stay within the non-linear potential theory of ideal incompressible liquid flow generated by a floating wedge impact. The liquid initially occupies a lower half-plane ($y < 0$) and is at rest. Initial draft of the wedge is h_0 and the deadrise angle of the wedge is γ . The parts of the liquid boundary $y = 0$, $x < -x_c$ and $x > x_c$, where $x_c = h_0 \cot \gamma$, correspond to the initial position of the liquid free surface. At some instant of time which is taken as the initial one, the wedge begins to move down at a constant velocity V . We shall determine the liquid flow, position of the free surface and the pressure distribution at each instant of time $t > 0$.

The numerical method proposed by Longuet-Higgins and Cokelet for free-surface flows with non-linear boundary conditions is employed. The free surface position is updated at each time step with the help of numerical solution of the corresponding mixed boundary-value problem. This solution may be singular at the intersection points, where the type of the boundary condition changes, and which are usually corner points of the flow domain. The singularities at the intersection points influence the numerical solution at all subsequent time steps, and thus can have disastrous cumulative effects.

In order to avoid the difficulties with the time-stepping numerical method, it is suggested to distinguish small vicinities of the intersection points at each time step and to build there approximate analytical solutions matching them with the numerical solution in the main flow region (section 2). The numerical solution is obtained by the boundary-element method. Initial conditions for the numerical solution are obtained by the method of matched asymptotic expansions in section 3.

Several models have been suggested in the past, which are based on the idea to cut off the jet and to replace it with a suitable boundary condition to be applied on the jet cut. Zhao & Faltinsen [1] suggested to cut the jet there, where the angle between the tangential to the free surface and that to the body contour drops below a small given value. The flow in the jet region is not considered. The cut is orthogonal to the body contour and a linear variation of the velocity potential along the cut is assumed. The normal derivative of the velocity potential obtained by solving the discretized boundary integral equation is used to move the cut. A slightly different approach has been suggested by Fontaine & Cointe [2]. Within this approach it is suggested to cut off the jet there, where the jet thickness becomes smaller than a given limiting value. The normal velocity on the jet cut is assumed to be equal to the tangential velocity on the body contour. Both these models have been found to work well and in good agreement with similarity solutions [3]. It is expected that both models are approximately equivalent to each other for small deadrise angle, which follows from the asymptotic analysis of the wedge-entry problem. On the other hand, both models are not easy to justify for moderate and large deadrise angles, where the "cut-off" technique is also attractive to use. It should be noted that the reliabilities of these models are highly dependent on the limiting values for the jet angle or the jet thickness. The values cannot be too small and, generally speaking, cannot be arbitrary. The best choice of these values is up to the experience of a researcher.

The aim of this study is to develop a more physical way to decompose the flow region without forcing neither the jet angle or the jet thickness. In this paper the velocity potential in the jet region is expressed as a suitable expansion around the intersection point. The coefficients of the expansion are evaluated from the numerical solution of the boundary-value problem, enforcing a matching with the outer solution.

2 Numerical simulation of the water entry

The flow about a symmetric wedge plunging the water surface is numerically studied in the frame of the potential flow assumption. A boundary integral formulation is employed to solve the Laplace's equation in terms of the velocity potential. On the body contour the normal derivative of the velocity potential is

assigned while on the free surface the velocity potential is updated according to the unsteady Bernoulli's equation.

The main issue concerns the treatment of the intersection between the free surface and the body contour. In order to avoid an excessive computational effort, the shape of the flow region close to the intersection point is approximated by a wedge and the velocity potential is expressed there as follows:

$$\phi = V \cos \gamma r [\sin \theta - \tan \beta \cos \theta] + \sum_{k=0, k|\cos k\beta \neq 0}^N a_k r^k \frac{\cos k\theta}{\cos k\beta} + \sum_{k=0}^M c_k r^{\sigma_k} \cos(\sigma_k \theta), \quad (1)$$

where

$$\sigma_k = \frac{\pi}{2\beta} + k \frac{\pi}{\beta}.$$

Here β is the angle between the body contour and the free surface at the intersection point and r, θ are polar coordinates with origin at this point (Fig. 1).

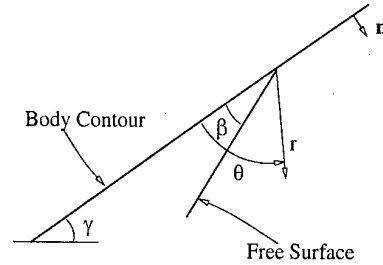


Fig.1 Sketch of the jet region

The first term in equation (1) is to satisfy the boundary condition on the body contour, the second term to satisfy the boundary condition on the free surface side and the last term represents the eigen solutions of the Laplace's equation in the liquid-wedge region. This term is of major importance for $\beta > \pi/2$ leading in this case to a singular velocity field at the intersection. For small values of β the eigen-solution part can be neglected in a low-order approximation. The coefficients in expansion (1) are computed directly by solving the boundary-value problem and enforcing the matching between the 'inner' expansion (1) and the 'outer' numerical solution along the matching line. The coefficients c_k are determined by introducing $M + 1$ panels on the matching curve while the coefficients a_k can be recovered either by extrapolation from the computational domain, where the dynamic boundary condition is satisfied, or by introducing additional $N + 1$ panels on the matching curve.

In the case of constant entry velocity, the behaviour of the angle β as function of the wedge deadrise angle was recovered. Besides to the case of constant entry velocity, also the free fall impact is analysed. In this case the unsteady contribution to the pressure field on the body contour is computed by solving another boundary-value problem in terms of the time derivative of the velocity potential. The hydrodynamic load is then used as a forcing term for the dynamic equation of the body motion that is integrated in time to provide the actual entry velocity.

3 Small time analysis

Besides the treatment of the jet region, one problem that causes troubles is the initial transient. Numerical approaches usually start from the undisturbed free surface configuration with the body partially submerged. In this condition a singular velocity field occurs at the intersection and the numerical treatment of this singularity is not straightforward. Due to the velocity singularity at the intersection, the solution that can be obtained up to the time at which the jet develops is not reliable. This unphysical behaviour of the initial transient may affect the solution in the case of free fall impact when a correct estimate of the hydrodynamic load is needed to accurately compute the dynamics of the impacting body [4]. For this reason a small-time analysis of the flow when the body impulsively starts to move down is done. It was shown that, at the leading order as $t \rightarrow 0$, the flow close to the contact point is self-similar. The solution of this problem is helpful to derive the initial conditions for the following numerical simulation.

The 'outer' solution of the floating wedge impact problem, which is valid outside the intersection point vicinities, was obtained by Sedov [5] in the form

$$\phi + i\psi = iV(z - \frac{l}{a}\sqrt{\tau^2 - 1}),$$

where $\psi(x, y)$ is the stream function, $z = x + iy$, $l = h_0/\sin \gamma$, τ is the complex variable connected to z by the formula

$$z = \frac{l}{a} e^{i\gamma} \int_0^\tau \left(\frac{\tau_0^2}{1 - \tau_0^2} \right)^{\frac{\gamma}{\pi}} d\tau_0 - ih_0, \quad a = \frac{1}{\sqrt{\pi}} \Gamma\left(\frac{1}{2} + \frac{\gamma}{\pi}\right) \Gamma\left(1 - \frac{\gamma}{\pi}\right).$$

Asymptotic behaviour of the complex potential near the right-hand side intersection point $z = x_c(0) = h_0 \cot \gamma$ is

$$\phi + i\psi \approx -iVf(\gamma)h_0^{\gamma-\frac{\gamma}{\pi}}(z - x_c)^{\frac{\pi}{2(\pi-\gamma)}} + iVx_c, \\ f(\gamma) = \left(\frac{2\beta}{\pi}\right)^{\sigma_0} (a \sin \gamma)^{\sigma_0-1}.$$

As stated above, a singularity of the velocity field at the contact point occurs as it can be recognized from the leading term of the Sedov's solution

$$\phi \simeq Ar^{\sigma_0} \cos \sigma_0 \theta \quad \text{as } r \rightarrow 0, \quad (2)$$

where $\sigma_0 = \pi/(2\beta)$ with $\beta = \pi - \gamma$. The constant A can be readily evaluated from the 'outer' Sedov's solution. Equation (2) can also be recovered from expansion (1).

To perform the small-time analysis, local stretched coordinates λ, μ and the 'inner' velocity potential $\varphi(\lambda, \mu, t)$ are introduced as follows

$$x = x_c + a(t)\lambda, \quad y = a(t)\mu, \quad \phi = a^\nu(t)\varphi(\lambda, \mu, t)$$

with $a(t) \rightarrow 0$ as $t \rightarrow 0$. Using the methods of asymptotic analysis and the matching conditions, we obtain

$$a(t) = [(2 - \sigma_0)t]^{\frac{1}{2-\sigma_0}}, \quad \nu = \sigma_0.$$

Matching the behaviour of the velocity potential in the 'outer' region expressed by equation (2) with that in the 'inner' region, gives the condition at infinity for the 'inner' velocity potential

$$\varphi(\lambda, \mu, t) \simeq A\rho^{\sigma_0} \cos \sigma_0 \theta \quad \text{as } \rho \rightarrow \infty, \quad (3)$$

with $\rho = \sqrt{\lambda^2 + \mu^2}$.

In terms of the new stretched variables the dynamic and kinematic boundary conditions on the free surface take the forms

$$\sigma_0 \varphi + \frac{1}{2} |\nabla \varphi|^2 = (\lambda \varphi_\lambda + \mu \varphi_\mu) - a^{2-\sigma_0} \varphi_t, \quad (4)$$

$$\nabla \eta \cdot \nabla \varphi = (\lambda \eta_\lambda + \mu \eta_\mu) - a^{2-\sigma_0} \eta_t, \quad (5)$$

where the equation $\eta(\lambda, \mu, t) = 0$ describes the free surface shape. Since $2 - \sigma_0 > 0$, the shape of the free surface and the velocity potential do not depend on time in the leading order as $t \rightarrow 0$, which means that the flow close to the contact point is approximately self-similar.

In terms of the stretched velocity potential the boundary condition on the body surface is

$$\varphi_\mu = \varphi_\lambda \tan \gamma - Va^{1-\sigma_0}$$

and, as $t \rightarrow 0$, the last term can be neglected leading to the following boundary condition on the body:

$$\frac{\partial \varphi}{\partial n} = 0. \quad (6)$$

Equations (4) and (5) indicate that it is convenient to introduce new unknown function $S(\lambda, \mu)$ instead of the velocity potential

$$S(\lambda, \mu) = \varphi(\lambda, \mu, t) - \frac{1}{2}(\lambda^2 + \mu^2),$$

with the help of which the 'inner' problem is reduced to the boundary-value problem for the Poisson's equation

$$\Delta S = -2 \quad \text{in the flow region,}$$

$$\frac{\partial S}{\partial n} = 0 \quad \text{on the boundary of the flow region,}$$

$$\left(\frac{\partial S}{\partial \tau}\right)^2 + 2\sigma_0 S = (1 - \sigma_0)\rho^2 \quad \text{on the free surface,}$$

$$S \simeq -\frac{1}{2}\rho^2 + A\rho^{\sigma_0} \cos \sigma_0 \theta \text{ as } \rho \rightarrow \infty ,$$

where $\partial S/\partial \tau$ is the tangential derivative of the function $S(\lambda, \mu)$ along the free surface (Fig. 2). It is important to note that the dynamic condition in this formulation can be exactly integrated leading to the direct relation between the value of the function S on the free surface and the free surface shape. The problem for the Poisson's equation is solved by iterations dealing with the corresponding mixed boundary-value problems at each step. The technique outlined in section 2 can be employed to improve the convergence.

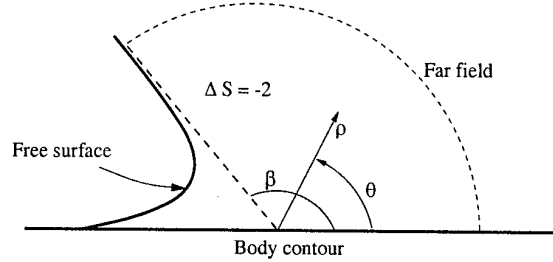


Fig.2 Sketch of the inner region for the small time analysis

Acknowledgments

This work was supported by the *Ministero dei Trasporti e della Navigazione* in the frame of INSEAN research plan 2000-02.

References

- [1] Zhao, R. and Faltinsen, O., *Journal of Fluid Mechanics*, **246**: 593-612, 1993
- [2] Fontaine, E. and Cointe, R., *Proceedings of High Speed Body Motion in Water*. AGARD REPORT 827, 1997
- [3] Dobrovolskaya, Z.N., *Journal of Fluid Mechanics*, **36**: 805-829, 1969
- [4] Iafrati, A., Carcaterra, A., Ciappi, E., and Campana, E.F., *Submitted to publication*.
- [5] Sedov, L.I., *Tr. Tsentr. Aerodin. Inst.*, **152**: 27-31, 1935.

TRAPPED MODES ABOVE A DIE OSCILLATING ON THE BOTTOM OF A WAVE CHANNEL

D. Indeitsev and Yu. Mochalova

Institute of Mechanical Engineering Problems, Russian Academy of Sciences
V.O., Bol'shoy pr., 61, St. Petersburg, 199178, Russia

1. Introduction

The problem of body's oscillation in water confined in a channel is often considered in the framework of the shallow water theory. However there are cases when trapped modes exist if the linear finite-depth solution applies and do not exist in the model by the shallow water theory. Trapped modes represent a localized oscillation of finite energy which does not propagate away to infinity.

In the paper [1] the existence of trapped modes travelling along the plate placed on the bottom of the channel was established. This problem was reduced to the two-dimensional boundary value problem, and its continuous spectrum is above a non-zero cut-off frequency. It was shown that at least one trapped mode exists occurring at frequency which is less than the cut-off value. The same result was obtained for shallow water. The case when frequency is above the cut-off was not discussed.

If there is no cut-off value in the problem, the model of shallow water fails to prove the existence of trapped modes. For example Zilman & Miloh [2] showed that oscillation of a buoyant circular plate in shallow water leads to formation only outgoing surface waves. On the other hand, for deep water the same velocity potential defined with the help of the Green function [3] gives both standing and outgoing waves, and the evidence of the trapped modes existence can be obtained numerically.

In the note we consider a circular die on the bottom of a channel. The simple geometry of the die allows us to find the analytic solution of the problem. The cut-off frequency of the boundary-value problem is zero and there exist only progressive waves in shallow water. The purpose of this work is to establish the existence of trapped modes occurring at frequencies which are point eigenvalues of the problem embedded in the continuous spectrum.

2. Formulation

We consider a three-dimensional channel of constant depth h occupied by an inviscid and incompressible fluid. The moving part of the bottom is modeled by a circular die of radius a . Cartesian coordinates are chosen so that the origin is in the mean the center of the die at rest and y -axis points vertically upwards and x_1 and x_2 are in plane of the unperturbed bottom.

It is assumed that all motions are simple harmonic in the time and have the radian frequency ω . The vertical displacement of the die can be written as $\text{Re}\{\zeta_0 e^{-i\omega t}\}$ and ζ_0 is the amplitude of die oscillations. The velocity potential which describes the fluid motion is given by $\text{Re}\{\varphi(x_1, x_2, y) e^{-i\omega t}\}$, where φ satisfies Laplace's equation

$$\nabla^2 \varphi = 0, \quad \text{in the fluid,} \quad (1)$$

and boundary conditions

$$\varphi_y - \frac{\omega^2}{g}\varphi = 0 \quad \text{on } y = h, \quad (2)$$

$$\frac{\partial \varphi}{\partial y} = -i\omega\zeta_0 \quad \text{on } |x| < a, \quad y = 0, \quad (3)$$

$$\frac{\partial \varphi}{\partial y} = 0 \quad \text{on } |x| > a, \quad y = 0, \quad (4)$$

where g is the acceleration due to gravity and $|x| = (x_1^2 + x_2^2)^{1/2}$. If trapped modes are sought then the radiation condition is replaced by

$$\varphi \rightarrow 0 \quad \text{as } |x| \rightarrow \infty. \quad (5)$$

The displacement of the die ζ_0 is determined by the equation

$$(\bar{C} - M\omega^2)\zeta_0 = -\frac{i\rho\omega}{\pi a^2} \int_{S_a} \varphi dx_1 dx_2, \quad y = 0, \quad (6)$$

where ρ is the fluid density, M is the die mass per unit area, C is the elastic foundation rigidity, $\bar{C} = C - \rho g$, $S_a = \{|x| < a, \quad y = 0\}$ is the wetted surface of the die.

3. The velocity potential and trapped frequencies

It is convenient to use horizontal polar coordinates (r, θ) defined by

$$x_1 = r \cos \theta, \quad x_2 = r \sin \theta, \quad r > 0.$$

A trapped mode solution of the problem (1)–(6) may be constructed with the help of the ring Green functions which give the potential of a ring source of radius ρ in the bottom of the channel. The representation of the ring Green function can be found in papers [4] and [5]. Then the velocity potential has the form

$$\begin{aligned} \varphi(r, y) = 4\pi i \zeta_0 \omega \left\{ iC_0 \int_0^a \rho J_0(k_0 r_<) H_0^{(1)}(k_0 r_>) d\rho + \right. \\ \left. 2 \sum_{m=1}^{\infty} C_m \int_0^a \rho I_0(k_m r_<) K_0(k_m r_>) d\rho \right\} \end{aligned} \quad (7)$$

where J_0 , I_0 , K_0 , $H_0^{(1)}$ denote standard Bessel, modified Bessel and Hankel function of zero order,

$$r_< = \min\{r, \rho\}, \quad r_> = \max\{r, \rho\}$$

and

$$C_0 = \frac{2\pi(k_0^2 - \nu^2)}{h(k_0^2 - \nu^2) + \nu} \cosh k_0 y, \quad C_m = \frac{(k_m^2 + \nu^2)}{h(k_m^2 + \nu^2) - \nu} \cos k_m y,$$

where

$$k_0, \pm i k_1, \pm i k_2, \dots, \pm i k_n, \dots$$

is a sequence of roots of the dispersion relation

$$k \tanh kh = \nu; \quad (8)$$

the parameter $\nu = \omega^2/g$.

Hence (7) gives an expansion of the velocity potential in terms of cylindrical waves. The character of those waves is clear from the asymptotic representation of Bessel functions. At large distance the first term in (7) gives an outgoing progressive wave as a result of Hankel function. The waves described by the second term in (7) behave like standing waves which decay as $r \rightarrow \infty$. The outgoing wave in $r > a$ is annulled by taking $k_0 a$ to satisfy

$$J_1(k_0 a) = 0. \quad (9)$$

that is $k_0 a = j_n$ ($n = 1, 2, \dots$), where j_n is a zero of Bessel function J_1 . Thus from (8) we obtain the sequence of the frequencies

$$\omega_n = \left(\frac{j_n g}{a} \tanh \left(\frac{j_n h}{a} \right) \right)^{1/2}, \quad n = 1, 2, \dots \quad (10)$$

For $\omega = \omega_n$ outgoing wave becomes zero in $r > a$ and radiation condition (5) is fulfilled.

The aim now to find the set of the parameters $\{a, h, M, C\}$ for which the trapped frequency is fundamental one. Then (7) gives the trapped modes solution at ω_n .

Substituting the formula (7) for the velocity potential into the integral in (6) we get for $\omega = \omega_n$

$$\bar{C}' - M' \omega_n'^2 = R'_g + R'_{in}, \quad n = 1, 2, \dots \quad (11)$$

where the nondimensional parameters $\bar{C}' = \bar{C}/\rho g$, $M' = M/\rho a$, $R' = R/\rho g$, $\omega_n' = j_n \tanh j_n \delta$, $\delta = h/a$, and

$$R'_g = -\frac{4 \tanh j_n \delta}{2 j_n \delta + \sinh 2 j_n \delta}, \quad n = 1, 2, \dots, \quad (12)$$

$$R'_{in} = 4 j_n \tanh(j_n \delta) \sum_{m=1}^{\infty} \frac{1 - 2 I_1(k_{mn} a) K_1(k_{mn} a)}{k_{mn} a (2 k_{mn} h + \sin 2 k_{mn} h)}, \quad n = 1, 2, \dots \quad (13)$$

and $\pi(m - \frac{1}{2})/h < k_{mn} < \pi m/h$, ($n = 1, 2, \dots$). The right part of (11) $R' = R'_g + R'_{in}$ is a function of δ and represents a dynamical reaction of the fluid on die oscillations. The first term $R'_g < 0$ is a result of the gravity action caused by the standing waves and $R'_g = -1 + O(\delta)$ as $\delta \rightarrow 0$, and decays as $\delta \rightarrow \infty$. The second term $R'_{in} > 0$ is induced by inertial of the fluid and $R'_{in} = O(\delta^2)$ as $\delta \rightarrow 0$ and $R'_{in} = j_n M'_{\rho_n}$ ($n = 1, 2, \dots$) as $\delta \rightarrow \infty$, where M'_{ρ_n} is the sum of the series (13). The constant M'_{ρ_n} ($n = 1, 2, \dots$) is the added mass of the die oscillating with n -th trapped frequency. Thus $R'(\delta)$ is a continuous function with alternating sings and R' tends to -1 as $\delta \rightarrow 0$ and R' equals to $j_n M'_{\rho_n}$, ($n = 1, 2, \dots$) as $\delta \rightarrow \infty$.

Evaluating \bar{C}' from (11) and taking into account the behavior of $R'(\delta)$ we can formulate the following statement.

For any n , $\delta > 0$, and $M' > 0$ we can find the finite $C' > 0$ such that the equation (11) is an identity and the trapped frequency ω_n' (10) is the fundamental one.

Thus there exist the sequence $\omega_n \rightarrow \infty$ ($n = 1, 2, \dots$) given by (10), which are point eigenvalues of the problem (1)–(6) embedded in its continuous spectrum. The trapped mode solutions $\varphi(\omega_n)$ are defined by (7).

4. Conclusion

The trapped mode solutions embedded in the continuous spectrum have been constructed for the circular die oscillating on the bottom of deep water. In the case when the geometry

of the die is arbitrary, the solution of the boundary value problem is purely numerical. We can apply the same methods in order to prove the existence of trapped modes. The condition of the outgoing wave destruction has the form

$$\int_S H_0^{(1)}(k|x - \xi|) dS = 0 \quad \text{as } |x| \rightarrow \infty$$

where $\xi = (\xi_1, \xi_2)$ and S is the die area. Defining k from the last equation we get a spectrum of trapped frequencies, which can be written as

$$\omega_{tr} = (kg \tanh kh)^{1/2}$$

For the evidence of trapped modes it is necessary to find parameters of the problem such that the frequency equation

$$\overline{C} = \left[M + \frac{2\rho}{S} \int_S \int_S G(x, y; \xi) dS dS \right] \omega_{tr}^2$$

is the identity. Here $G(x, y; \xi)$ is the Green function which describes the velocity potential of a source placed at a point $(\xi, 0)$ given by [3].

Acknowledgments. The authors are indebted to Prof. N.G. Kuznetsov and Prof. T. Miloh for substantive discussions and assistance.

References

- [1] Indeitsev, D. & Mochalova, Yu. Trapped modes in wave channel with an elastic plate on the bottom. Proc. of 13th Int. Workshop on Water Waves and Floating Bodies (1998) 47-50.
- [2] Zilman G. & Miloh T. Hydroelasticity of a buoyant circular plate in shallow water: a closed form solution. Proc. of 14th Int. Workshop on Water Waves and Floating Bodies (1999) 179-181.
- [3] John, F., On the motion of floating bodies. II. Comm. Pure Appl. Math. 3(1950) 45-101.
- [4] Hulme, A., A ring-source/integral-equation method for the calculation of hydrodynamic forces exerted on floating bodies of revolution. J. Fluid Mech. 128 (1983) 387-412.
- [5] Kuznetsov, N.G., Maz'ya, V.G. & Vainberg, B.R., Linear Time-Harmonic Water Waves (unpublished manuscript).

ON UNSTEADY WAVES GENERATED BY A BLUNT SHIP WITH FORWARD SPEED

Hidetsugu IWASHITA

Engineering Systems, Hiroshima University
1-4-1 Kagamiyama, Higashi-Hiroshima 739-8527, JAPAN

INTRODUCTION

Now plenty of studies on the seakeeping problem of ships based on the potential theories are performed by applying the Rankine panel methods (RPMs) in frequency domain and/or recently in the time domain to capture the nonlinear effects. Most of reports have treated slender ships and suggested some improvements of the estimation accuracy at least for the slender ships and for the global hydrodynamic forces and ship motions. However it has not been made so clear whether or not the methods are effective also for the blunt ships and for the estimation of local forces.

Iwashita et al. (1993) highlighted the wave pressure distribution locally acting on a blunt ship and found a significant discrepancy between computed and measured wave pressure at the bow part. Their consecutive studies show that this discrepancy can not be reduced so much even if the influence of the steady flow is taken into account more accurately, *Iwashita & Ito (1998)*. *Iwashita (1999)* adopted a diffraction wave instead of the wave pressure itself and applied one of the most sophisticated RPMs to another kind of blunt ship and compared the computed diffraction wave with measured one. Notwithstanding the computation method applied there could take account of the influence of the fully nonlinear steady wave field, the theoretical computation underestimated experiment more than 50% as well as previous wave pressure.

In this paper we perform a systematic experiment for a Series-60 ($C_b = 0.8$) and measure not only the hydrodynamic forces but also radiation and diffraction waves at a same time, in order to provide the experimental data to all the researchers concerned with. The conventional hydrodynamic forces correspond to global forces and unsteady waves represent the local physical values in the wave field around the ship. Numerical calculations by strip method, Green function method (GFM) and RPM are also carried out and obtained results are compared with experiments. Then we discuss how those computation methods can predict experiments.

FORMULATION

We consider a ship advancing at constant forward speed U in oblique regular waves encountered at angle χ , Fig.1. The ship motions $\Re[\xi_j e^{i\omega_e t}]$ ($j = 1 \sim 6$) and the wave amplitude A of the incident wave are assumed to be small. ω_0 is the circular frequency and K the wave number of the incident wave. The encounter circular frequency is $\omega_e (= \omega_0 - KU \cos \chi)$. The linear theory is employed for this problem assuming ideal potential flow.

The total velocity potential Ψ of the fluid governed by Laplace's equation can be expressed as

$$\Psi(x, y, z; t) = U\Phi(x, y, z) + \Re[\phi(x, y, z)e^{i\omega_e t}] \quad (1)$$

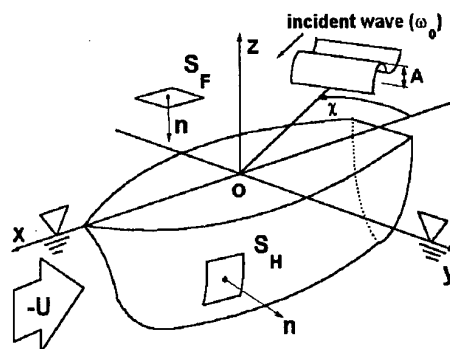


Fig. 1 Coordinate system

where

$$\phi = \frac{gA}{\omega_0}(\phi_0 + \phi_7) + i\omega_e \sum_{j=1}^6 \xi_j \phi_j, \quad \phi_0 = ie^{Kz - iK(x \cos \chi + y \sin \chi)} \quad (2)$$

Φ means the steady wave field and ϕ the unsteady wave field which consists of the incident wave ϕ_0 , the diffraction wave ϕ_7 and the radiation wave $\phi_j (j = 1 \sim 6)$. The kinematic and dynamic boundary conditions to be satisfied on the exact free surface $z = \zeta(x, y; t)$ yields

$$\frac{\partial^2 \Psi}{\partial t^2} + 2\nabla \Psi \cdot \nabla \frac{\partial \Psi}{\partial t} + \nabla \Psi \cdot \nabla \left(\frac{1}{2} (\nabla \Psi)^2 \right) + g \frac{\partial \Psi}{\partial z} = 0 \quad \text{on } z = \zeta \quad (3)$$

By substituting (1) into (3), the problem can be decomposed into the steady and the unsteady problems.

Then the steady wave field is solved so that

$$\frac{1}{2} \nabla \Phi \cdot \nabla (\nabla \Phi)^2 + K_0 \frac{\partial \Phi}{\partial z} = 0 \quad \text{on } z = \zeta_s = \frac{1}{2K_0} [1 - (\nabla \Phi)^2], \quad K_0 = g/U^2 \quad (4)$$

is satisfied on the exact steady free surface $z = \zeta_s(x, y)$ and $\partial \Phi / \partial n = 0$ on the body surface S_H . A RPM developed by *Jensen et al. (1986)* is used to solve this problem numerically. The nonlinear free surface condition (4) is satisfied by iteration scheme and the radiation condition by shifting the collocation points one panel upward.

Assuming small amplitude of the incident wave and ship motions, we can linearize the free surface condition for ϕ_j around the steady free surface $z = \zeta_s(x, y)$ obtained by solving the previous steady problem. The final form can be written with corresponding body boundary condition as follows (*Newman (1978), Bertram (1990)*):

$$\begin{aligned} -K_e \phi_j + i2\tau \nabla \Phi \cdot \nabla \phi_j + \frac{1}{K_0} \left[\nabla \Phi \cdot \nabla (\nabla \Phi \cdot \nabla \phi_j) + \nabla \phi_j \cdot \nabla \left(\frac{1}{2} (\nabla \Phi)^2 \right) \right] + \frac{\partial \phi_j}{\partial z} \\ - \frac{\frac{\partial}{\partial z} \left[\frac{1}{2} \nabla \Phi \cdot \nabla (\nabla \Phi)^2 + K_0 \frac{\partial \Phi}{\partial z} \right]}{K_0 + \nabla \Phi \cdot \nabla \frac{\partial \Phi}{\partial z}} \left(i\tau + \frac{1}{K_0} \nabla \Phi \cdot \nabla \right) \phi_j = 0 \quad \text{on } z = \zeta_s \end{aligned} \quad (5)$$

$$\frac{\partial \phi_j}{\partial n} = n_j + \frac{U}{i\omega_e} m_j \quad (j = 1 \sim 6), \quad \frac{\partial \phi_7}{\partial n} = -\frac{\partial \phi_0}{\partial n} \quad \text{on } S_H \quad (6)$$

where $K_e = \omega_e^2/g$, $\tau = U\omega_e/g$ and

$$\begin{aligned} (n_1, n_2, n_3) &= \mathbf{n}, & (m_1, m_2, m_3) &= -(\mathbf{n} \cdot \nabla) \mathbf{V}, & \mathbf{r} &= (x, y, z), \\ (n_4, n_5, n_6) &= \mathbf{r} \times \mathbf{n}, & (m_4, m_5, m_6) &= -(\mathbf{n} \cdot \nabla)(\mathbf{r} \times \mathbf{V}), & \mathbf{V} &= \nabla \Phi \end{aligned}$$

m_j and $\mathbf{V} (= \nabla \Phi)$ in (5) and (6) are evaluated by using the steady nonlinear wave field, Φ .

Once ϕ_j is obtained, the unsteady pressure $\Re[p e^{i\omega_e t}]$ is given as follows (*Timman & Newman (1962)*):

$$p = -\rho(i\omega_e + U\mathbf{V} \cdot \nabla)\phi - \rho \frac{U^2}{2} \sum_{j=1}^6 \xi_j (\beta_j \cdot \nabla)(\mathbf{V} \cdot \mathbf{V}), \quad \beta_j = \begin{cases} \mathbf{e}_j & (j = 1, 2, 3) \\ \mathbf{e}_{j-3} \times \mathbf{r} & (j = 4, 5, 6) \end{cases} \quad (7)$$

$\mathbf{e}_j (j = 1, 2, 3)$ are the unit vectors of x, y, z axes. The added mass & damping coefficients and wave exciting forces are computed by substituting the first and the second term of (2) into (7) respectively and integrating the pressure over the ship surface.

The radiation and diffraction waves $\Re[\zeta_j e^{i\omega_e t}]$ are calculated by

$$\left\{ \begin{matrix} \zeta_j / \xi_j \\ \zeta_7 / A \end{matrix} \right\} = \frac{1}{1 + \frac{1}{K_0} \nabla \Phi \cdot \nabla \frac{\partial \Phi}{\partial z}} \left(1 + \frac{1}{iK_0 \tau} \nabla \Phi \cdot \nabla \right) \left\{ \begin{matrix} K_e \phi_j \\ (-i\tau/\nu) \phi_7 \end{matrix} \right\} \quad \text{on } z = \zeta_s \quad (8)$$

where $\nu = U\omega_0/g$. The influence of the steady flow is introduced through the terms multiplied by $1/K_0$.

EXPERIMENT AND NUMERICAL METHODS

The experiment was carried out for Series-60 model of $C_b = 0.8$ at RIAM, Kyushu University. The length of the model is $L = 2\text{m}$. Added mass & damping coefficients, wave exciting forces and both of radiation wave (due to heave and pitch motion) and diffraction wave were measured. Unsteady waves were measured by Multifold Method developed by Ohkusu (1977).

In the numerical calculation based on RPM, both the steady and unsteady potentials, Φ and ϕ_j , are expressed by the source distributions on the body surface S_H and the free surface S_F . The body surface and the free surface are discretized into the finite number of constant panels, and numerical solutions for steady and unsteady problems are obtained such that a corresponding set of the free surface condition and the body boundary condition are satisfied at collocation points. The collocation points on S_H coincides with the geometric center of each panel and those on S_F are shifted one panel upward in order to force the radiation condition numerically. From the practical point of view, it has been confirmed that this numerical radiation condition is valid only for $\tau > 0.5$ where waves do not propagate to the forward direction of the ship. Not only the RPM but also the GFM and the strip method are also applied and compared.

RESULTS

Fig.2 illustrates the ship hull form and a computation grid of Series-60 of $C_b = 0.8$. Using 660 panels on S_H and additional 1840 panels on S_F , the steady problem is solved at first. Fig.3 shows the obtained steady wave distribution along a longitudinal axis near the ship. The fully nonlinear calculation predicts the experiment in good accuracy along the ship-side, but it overestimates transverse wave behind the ship. The difference can be considered to be caused by the viscous effect.

By using the solution of the steady problem the unsteady problem is solved consecutively. Figs.4 and 5 are examples of obtained hydrodynamic forces and ship motions. The present calculation can improve the estimation accuracy of the heave motion by taking account of the influence of fully nonlinear steady wave field. Figs.6 and 7 show the unsteady wave fields. The present calculation can not predict unsteady wave with large amplitude in vicinity of the bow. The discrepancy will not be caused by the nonlinear effect because the experiment shows the first term of Fourier series of obtained experimental data.

Further calculations based on the GFM are now in progress and the results will be presented in the workshop.

REFERENCES

- BERTRAM, V. (1990), *Fulfilling Open-Boundary and Radiation Condition in Free-Surface Problems Using Rankine Sources*, Ship Technology Research, Vol. 37/2
- IWASHITA, H., ITO, A., OKADA, T., OHKUSU, M., TAKAKI, M., MIZOGUCHI, S. (1993), *Wave Forces Acting on a Blunt Ship with Forward Speed in Oblique Sea (2nd Report)*, J. Soc. Naval Arch. Japan, Vol. 173 (in Japanese)
- IWASHITA, H., ITO, A. (1998), *Seakeeping Computations of a Blunt Ship Capturing the Influence of the Steady Flow*, Ship Technology Research, Vol. 45/4
- IWASHITA, H. (1999), *Diffraction Waves of a Blunt Ship with Forward Speed Taking account of the Steady Nonlinear Wave Field*, 14th WWWFB, Michigan
- JENSEN, G., MI, Z.-X., SÖDING, H. (1986), *Rankine Source Methods for Numerical Solutions of the Steady Wave Resistance Problem*, 16th Symp. on Nav. Hydrodyn., Berkeley
- NEWMAN, J. N. (1978), *The Theory of Ship Motions*, Advances in Applied Mechanics 18.
- OHKUSU, M. (1977), *Analysis of Waves Generated by a Ship Oscillating and Running on a Calm Water with Forward Velocity*, Journal of The Society of Naval Architects of Japan, Vol.142

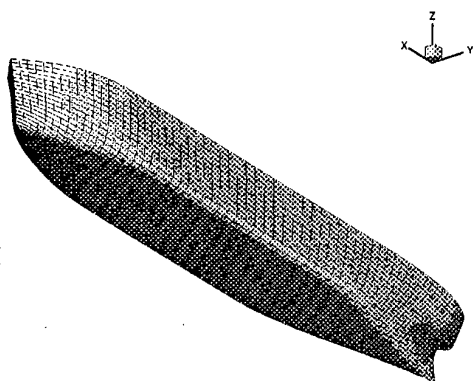


Fig.2 Perspective view of Series-60 ($C_b = 0.8$)

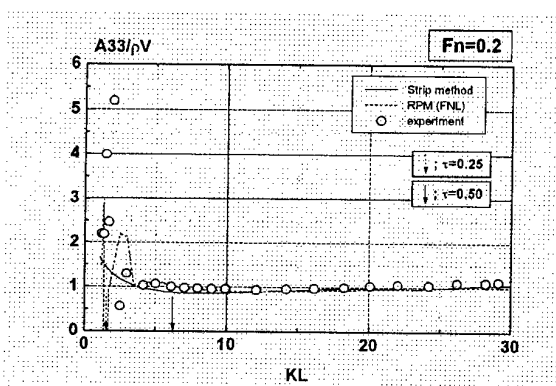


Fig.4 Added mass coefficient for heave

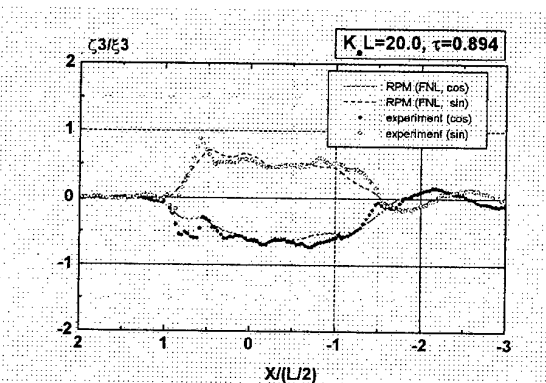


Fig.6 Heave radiation wave at $F_n = 0.2$

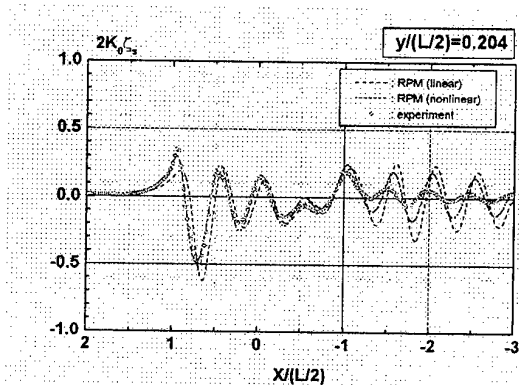


Fig.3 Steady wave distribution along longitudinal axis at $F_n = 0.2$

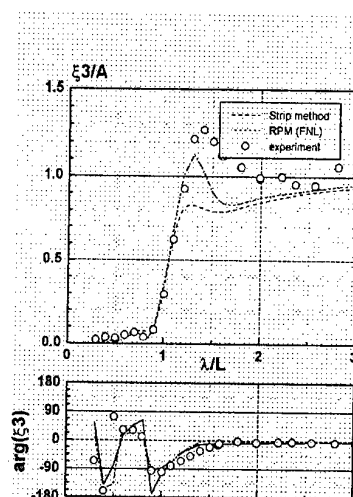


Fig.5 Heave motion at $F_n = 0.2$, $\chi = 180$ degs.

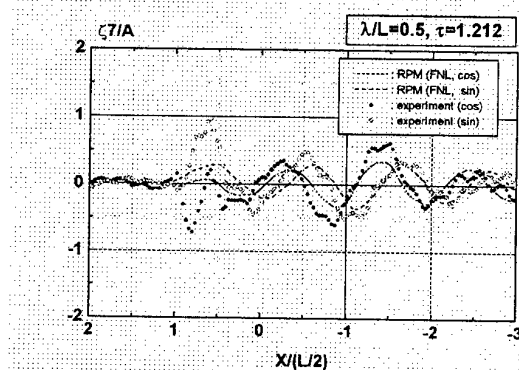


Fig.7 Diffraction wave at $F_n = 0.2$, $\chi = 180$ degs.

NONLINEAR WAVES GENERATED BY A SURFACE-PIERCING BODY USING A UNIFIED SHALLOW-WATER THEORY

Tao Jiang & Rupert Henn ¹

Institute of Ship Technology
Mercator University, Duisburg, Germany

Introduction

Modified Boussinesq's equations have been successfully applied in coastal engineering for simulating wave propagation from the deep sea to a shallow-water region, e.g. Nwogu (1993) and Schröter (1995), and in naval architecture for computing ship waves in shallow water, e.g. Jiang (1998) for a slender ship and Jiang & Sharma (1998) for a flat ship. But practical application to a general ship-form and to ship-form optimization was not possible because neither the slender-body theory nor the hydrostatic pressure assumption, used to approximate the ship's influence on the ambient flow, satisfies the tangential-flow condition on the wetted ship-surface. To overcome this fundamental difficulty in applying Boussinesq's equations to wave-body interactions, a new theory was recently derived by Jiang (1999) in which the tangential-flow condition on the wetted body-surface is explicitly included in a set of equations of Boussinesq type for the flow region under the body. After interfacial coupling of these equations for the flow inside the waterline with the associated Boussinesq's equations for the flow outside the waterline, a unified shallow-water theory emerges for many wave-related problems in shallow water.

A Unified Shallow-Water Theory for 2-D Wave-Body Interactions

For the sake of record we give here only the final formulation of the unified shallow-water theory for two-dimensional wave-body interactions. The mathematical derivation for general three-dimensional cases of varying water depth is fully documented in the work by Jiang (1999).

This unified shallow-water theory comprises a set of Boussinesq's equations

$$\left. \begin{aligned} \zeta_t + [(\zeta + h)\bar{u}]_x &= 0 \\ \bar{u}_t + \bar{u} \bar{u}_x + g\zeta_x - \frac{h^2}{3}\bar{u}_{txx} &= 0 \end{aligned} \right\}, \quad (1)$$

for the flow outside the waterline with the unknown depth-averaged horizontal velocity \bar{u} and wave elevation ζ , and a set of nonlinear partial-differential equations of Boussinesq type

$$\left. \begin{aligned} -T_t + [(h - T)\bar{u}]_x &= 0 \\ \bar{u}_t + \bar{u} \bar{u}_x + \left(\frac{p_s}{\rho}\right)_x - \frac{(h-T)^2}{3}\bar{u}_{txx} - \frac{h-T}{3}T_t\bar{u}_{xx} + (h-T)T_x\bar{u}_{tx} &= gT_x \end{aligned} \right\}, \quad (2)$$

for the flow inside the waterline with the unknown depth-averaged horizontal velocity \bar{u} and pressure p_s acting on the wetted body-surface. Herein g denotes the acceleration of gravity, ρ the water density, T the local instantaneous draft and h the constant water-depth; t is the independent time variable and x the horizontal coordinate.

¹We thank Professor Sharma for his steady support and helpful discussions.

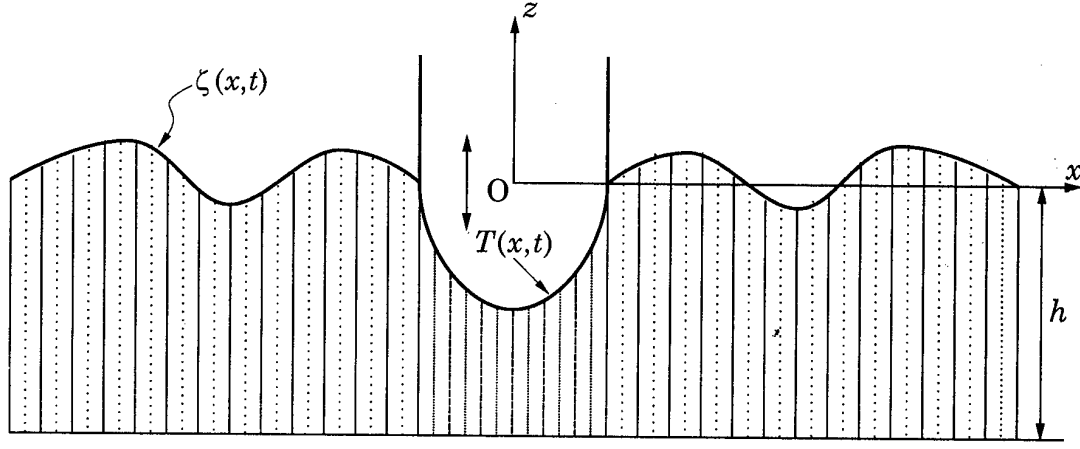


Figure 1: Schematic of space discretization using staggered grid

These two sets of equations are coupled by the interfacial condition at the waterline $x = x_w$

$$\left. \begin{aligned} \bar{u}_I(x_w, t) &= \bar{u}_O(x_w, t) \\ p_s(x_w, t) &= 0 \end{aligned} \right\}, \quad (3)$$

without a vertical sidewall, i.e. $T_w = T(x_w, t) = -\zeta(x_w, t)$, and

$$\left. \begin{aligned} (h - T_w)\bar{u}_I(x_w, t) &= (h + \zeta)\bar{u}_O(x_w, t) \\ p_s(x_w, -T_w, t) &= p_O(x_w, -T_w, t) \end{aligned} \right\}, \quad (4)$$

with a vertical sidewall, i.e. $T_w = T(x_w, t)$, where the subscripts I and O denote the flow fields inside and outside the waterline, respectively. The pressure at $z = -T_w$ can be approximated by

$$p_O(x_w, -T_w, t) = \rho g(\zeta + T_w) + \rho \left(\frac{T_w^2}{2} - hT_w \right) \bar{u}_{tx}, \quad (5)$$

which is obtainable from the outside flow.

Nonlinear Waves Generated by a Vertically Oscillating Body

Considering the analogy of the decoupling of the pressure p_s on the wetted body-surface from the depth-averaged continuity equation to that familiar from the Euler's equations, the well-established concept of a staggered grid, see Figure 1, is implemented in our computer code based on a full Crank-Nicolson scheme.

In our preliminary study we apply this unified theory to simulate the waves generated by two vertically oscillating bodies. One has the shape

$$T_s = T_o \cos^2 \pi \frac{x}{L} \quad \text{for } |x| \leq \frac{L}{2}, \quad (6)$$

where T_o and L denotes the maximum draft and the body length, respectively. The second has a rectangular shape with a constant draft $T_s = T_o$ and with the same length as the first one. These two bodies, both having a wall-sided freeboard over the still waterline, are forced to

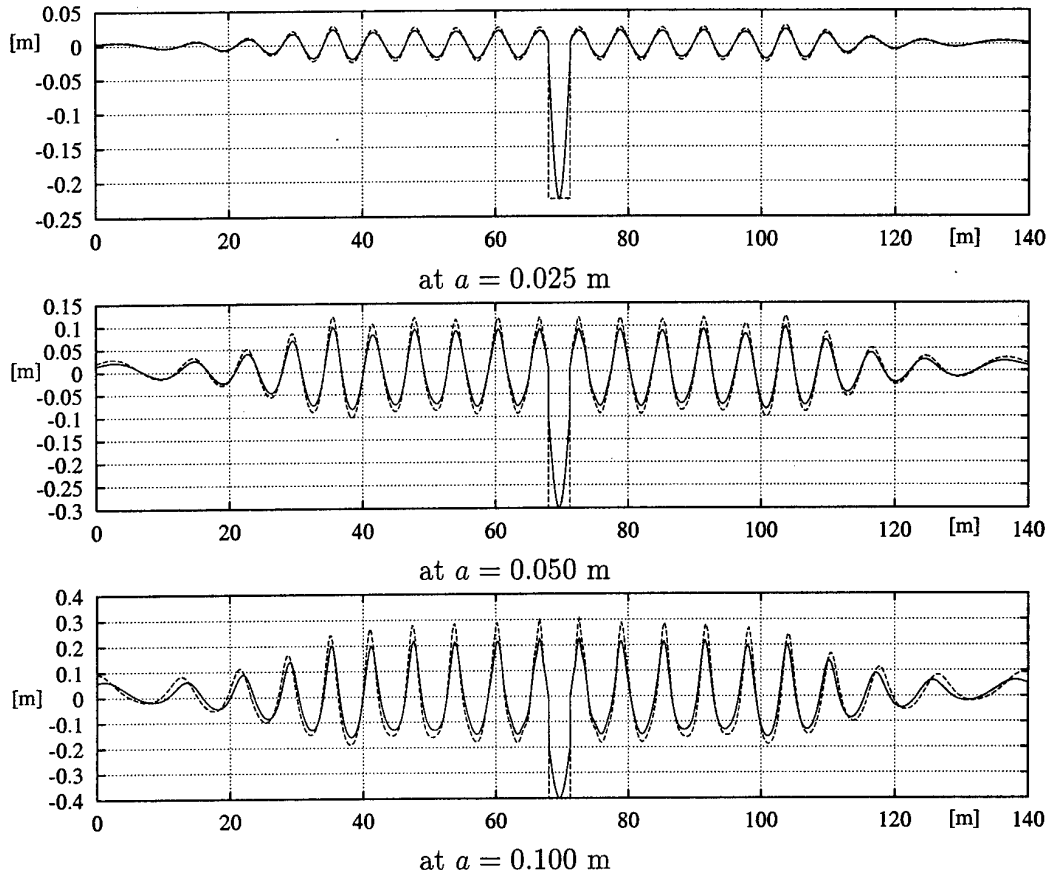


Figure 2: Comparison of waves generated by a rectangular body (dashed lines) with those by a trigonometric one (solid lines) oscillating in shallow water of depth $h = 1$ m

oscillate harmonically in shallow water of depth $h = 1$ m. The associated instantaneous local draft is then defined by

$$T = T_S + a(1 - \cos \omega t), \quad (7)$$

where ω is the forcing frequency and a the forcing amplitude.

For a combination of parameter values $L = 3.14$ m, $T_0 = 0.2$ m, and $\omega = 2.73$ s⁻¹, Figure 2 compares the waves generated by a rectangular body (dashed lines) with those by a trigonometric one (solid lines) for three forcing amplitudes $a = 0.025, 0.05$, and 0.10 m. As expected, for the same forcing amplitude, the rectangular body with larger displacement generates also waves with higher amplitudes. For the small forcing amplitude in graph (a), the waves behave more harmonically. For the large forcing amplitude in graph (c), the waves are characterized by steeper wave crests and by flatter hollows. This is typical for nonlinear shallow-water waves.

More fundamentally, Figure 3 shows the total pressure, corresponding to eight representative phases within a full period for the forcing amplitude $a = 0.10$ m. This reasonable looking pressure distribution, acting on the wetted-body surface, could be calculated for the first time by a shallow-water wave theory, namely the unified one.

Based on these preliminary results, which need to be theoretically verified and experimentally validated, we do believe in a large potential for the application of the new unified theory, consisting of two sets of Boussinesq type equations interfacially coupled at the waterline, for many wave-related 3-D problems in shallow water, reduced to the 2-D horizontal plane.

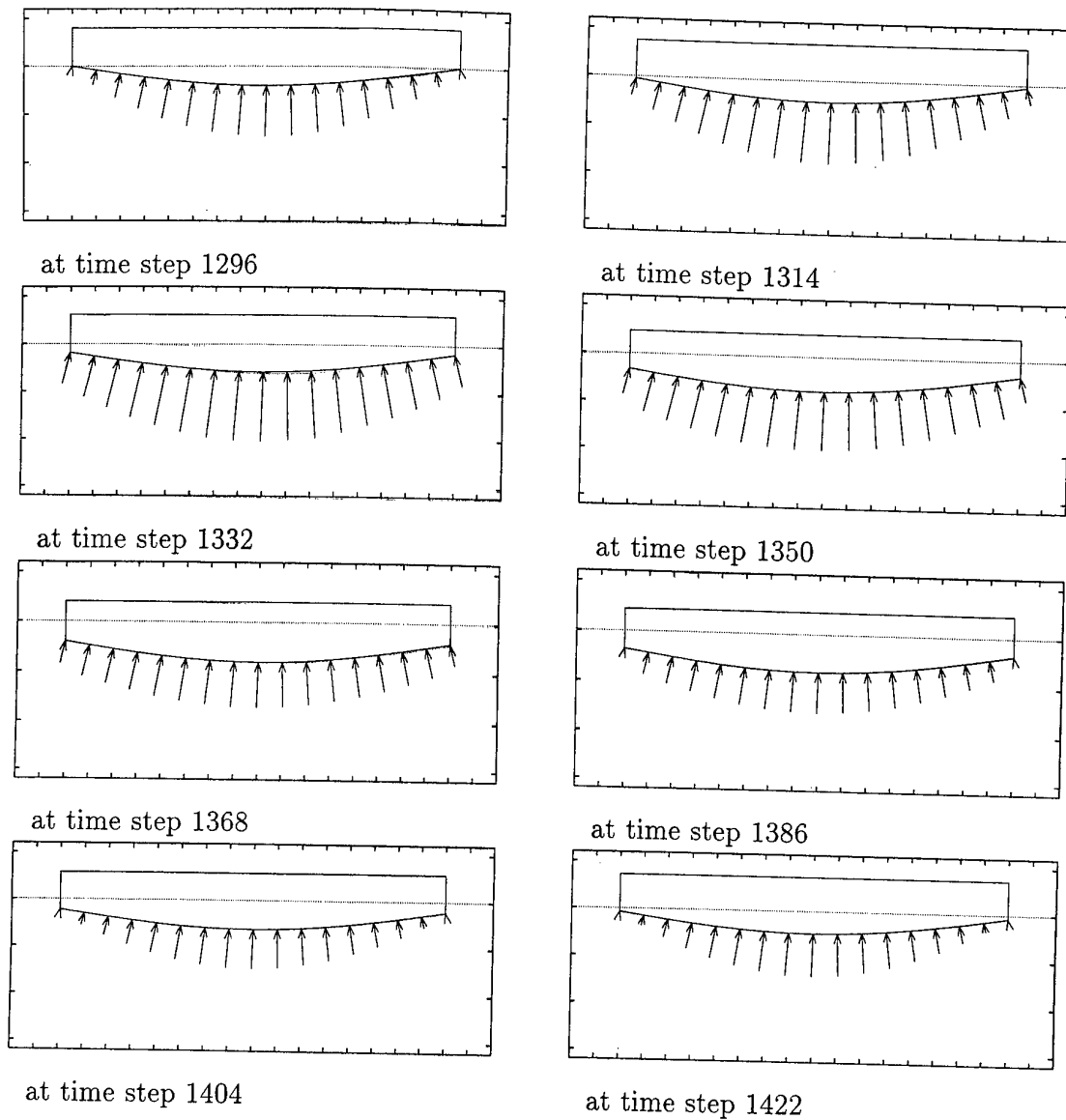


Figure 3: Evolution of the pressure distribution acting on the wetted-surface of the subject trigonometric rigid-body oscillating in shallow water of depth $h = 1$ m at eight representative phases within a full period

References

- Jiang, T., "A Unified Nonlinear Theory for Approximations of Wave-Related Problems in Shallow Water," In preparation, 1999.
- Jiang, T., "Investigation of Waves Generated by Ships in Shallow Water," Proceedings of the 22th Symposium on Naval Hydrodynamics, Washington, DC, 1998.
- Jiang, T. & Sharma, S.D., "Wavemaking of Flat Ships at Transcritical Speeds," Proceedings of the 19th Colloquium on Ship and Ocean Technology, Duisburg, 1998.
- Nwogu, O. "Alternative Form of Boussinesq Equations for Nearshore Wave Propagation," Journal of Waterway, Port, Coastal and Ocean Engineering, Vol. 119, pp. 618-638.
- Schröter, A., "Nonlinear Time-Discretized Seaway Simulation in Shallow and Deep Water (in German)," Institut für Strömungsmechanik und Elektronisches Rechnen im Bauwesen der Universität Hannover, Report No. 42, 1995.

ASYMMETRY AND HORIZONTAL VELOCITY DURING WATER IMPACT

Carolyn Judge, Armin Troesch

Department of Naval Architecture and Marine Engineering
University of Michigan, Ann Arbor

High-speed planing boats are widely popular but little is understood about their stability at high speeds. Many of these craft are known to experience unexpected behavior at operational speeds. Research at the University of Michigan intending to understand dynamic instability has used a water impact model to determine the flow over a cross-section of the hull. The impact model takes a two-dimensional section of the hull and predicts how the flow moves over the bottom as the hull section enters the water. By using a low order strip theory and viewing the planing hull as a series of cross-sections at different points of impact (near the bow the hull is just starting to enter the water while near the transom the hull has mostly entered the water), this model determines the transverse flow characteristics over the entire hull. The resulting boundary value problem can be numerically solved using a two-dimensional vortex distribution.

At the last IWWF conference, the authors discussed Xu's model for asymmetric impact along with the governing equations and problem formulation for symmetric impact with horizontal velocity [1]. The present work begins with a brief review of Xu's work and the motivation for understanding horizontal velocity during impact. The solutions to the governing equations are then presented as well as results for both symmetric and asymmetric impact with horizontal velocity.

Xu [3] developed a model for asymmetric impact which was built on Vorus's [2] work. Vorus's model allowed for arbitrary sectional contour impact, reordering the variables in the first order in a physically consistent manner. Xu described two types of impact due to asymmetry. Type A flow, Figure 1, was when there was small asymmetry and the water moved out towards the chine on both sides of the keel. Type B flow, Figure 2, occurred when there was large asymmetry and the flow separated from the hull at the keel on one side.

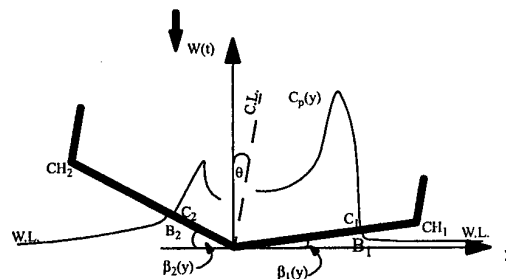


Figure 1: Type A Flow

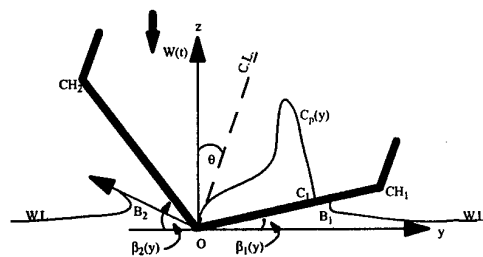


Figure 2: Type B Flow

Xu determined the onset of Type B flow by calculating the initial positions of the zero-pressure points (C_1 and C_2) for different values of θ $\{ \theta = \frac{1}{2}(\beta_2 - \beta_1) \}$. As θ increases, C_2 moves closer towards the keel.

When C_2 reaches the keel, the flow becomes Type B. The limiting angle of β_2 versus the corresponding β_1 is plotted in Figure 3 and suggests that the critical value of β_2 is relatively insensitive to β_1 .

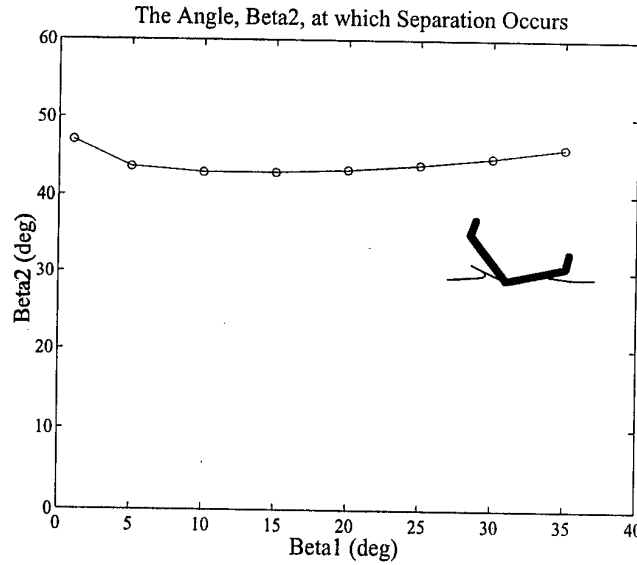


Figure 3: For each β_1 , the value of β_2 which causes Type B flow due to vertical impact

Horizontal velocity, as well as asymmetry, is very important when considering transverse plane motions. In order to predict stability in the transverse plane, horizontal velocity during impact needs to be taken into consideration. Consider a symmetric impact with horizontal velocity, Figure 4. When roll is constrained, this type of impact will produce Type A and Type B flows. Using the solutions to the governing equations shown here, the ratio of horizontal to vertical impact velocity required for Type B flow can be calculated. In addition, the results for an asymmetric impact with horizontal velocity can be determined.

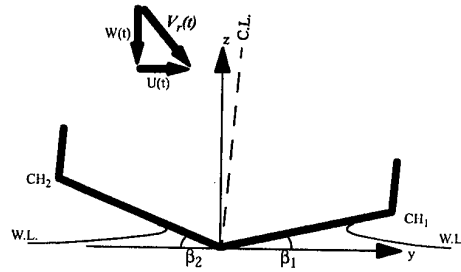


Figure 4: Symmetric Impact with Horizontal Velocity

The model for determining the locations of the zero-pressure points for the initial conditions is defined by the dynamic boundary conditions, the kinematic boundary condition (or kutta conditions), and the displacement continuity condition. The initial conditions are determined for flat-sided contours with constant impact velocity. The dynamic boundary condition is the zero pressure requirement outside the zero-pressure points and gives the velocities of the jet roots.

$$Y_{B1t} = \frac{\tilde{V}_s^2(b_1) - V_n^2(b_1) - V_s^2(b_1)}{2(\tilde{V}_s(b_1) - V_s(b_1))}$$

$$Y_{B2t} = \frac{\tilde{V}_s^2(-b_2) - V_n^2(-b_2) - V_s^2(-b_2)}{2(\tilde{V}_s(-b_2) - V_s(-b_2))}$$

Y_{b1t} and Y_{b2t} are the jet velocities and \tilde{V}_s and V_s are the total (fall plus perturbation) and fall velocities, respectively, in the tangential direction and V_n is the fall velocity in the normal direction. The jet-spray roots and zero-pressure point locations are non dimensionalized by the right-hand side zero-pressure point and are b_1 , b_2 , 1, and c_2 , respectively. The kinematic boundary condition requires zero normal velocity on the hull. This leads to the kutta conditions which must be satisfied at the zero-pressure points, C_1 and C_2 , to guarantee velocity continuity.

$$\frac{1}{2\pi} \int_1^{b_1} \frac{\gamma_s(s)}{\chi(s)(s+c_2)(s-1)} ds - \frac{1}{2\pi} \int_{-b_2}^{-c_2} \frac{\gamma_s(s)}{\chi(s)(s+c_2)(s-1)} ds = \frac{1}{\pi} \int_{-c_2}^1 \frac{\cos \tilde{\beta}(V_n \cos \beta)}{\chi(s)(s+c_2)(s-1)} ds$$

$$\frac{1}{2\pi} \int_1^{b_1} \frac{\gamma_s(s)s}{\chi(s)(s+c_2)(s-1)} ds - \frac{1}{2\pi} \int_{-b_2}^{-c_2} \frac{\gamma_s(s)s}{\chi(s)(s+c_2)(s-1)} ds = \frac{1}{\pi} \int_{-c_2}^1 \frac{\cos \tilde{\beta}(V_n \cos \beta)s}{\chi(s)(s+c_2)(s-1)} ds + \frac{1}{2\pi} \left[\int_1^{b_1} \gamma(s) ds + \int_{-b_2}^{-c_2} \gamma(s) ds \right]$$

where $\tilde{\beta}(\xi) = \text{atan}(\sin \beta)$, $\chi(\xi) = \frac{\kappa(\xi)}{\sqrt{(\xi+c_2)(1-\xi)}}$ and for constant deadrise, $\kappa(\xi) = \left| \frac{1-\xi}{\xi} \right|^{\frac{\tilde{\beta}_1}{\pi}} \left| \xi+c_2 \right|^{\frac{\tilde{\beta}_2}{\pi}}$.

The displacement continuity condition is a conservation of mass requirement. It requires that the displacement of the cylinder and the free surface contours combine to be a continuous nontrivial function of y to the second order. The displacement continuity condition must be satisfied at the jet-spray root locations, B_1 and B_2 .

$$\int_{-c_2^*}^1 \frac{\cos \tilde{\beta}(V_n^* \cos \beta)}{\chi^*(s)(s+c_2^*)(1-s)} ds = \int_{-c_2^*}^1 \frac{\cos \tilde{\beta}H_c(s)}{\chi^*(s)(s+c_2^*)(1-s)} ds$$

$$\int_{-c_2^*}^1 \frac{\cos \tilde{\beta}(V_n^* \cos \beta)}{\chi^*(s)(1-s)} ds - \int_{-c_2^*}^1 \frac{\cos \tilde{\beta}H_c(s)}{\chi^*(s)(1-s)} ds = \int_{-c_2^*}^1 \frac{\cos \tilde{\beta}(V_n^* \cos \beta)}{\chi^*(s)(s+c_2^*)} ds - \int_{-c_2^*}^1 \frac{\cos \tilde{\beta}H_c(s)}{\chi^*(s)(s+c_2^*)} ds$$

where c_2^* is the ratio of the left-hand jet-spray root location to the right-hand jet-spray root location,

$\chi^*(\xi)$ is $\chi(\xi)$ with c_2^* plugged in for c_2 and $V_n^* = \int_0^t V_n d\tau$.

The results for a symmetric impact with horizontal velocity are shown in Figure 5. The ratio of horizontal to vertical impact velocity required for Type B flow is greatly dependent on deadrise angle. For low deadrise angles, the horizontal velocity must be much greater than the vertical velocity for separation to occur. However, as the deadrise angle increases the necessary ratio reduces rapidly at first and then begins to flatten out.

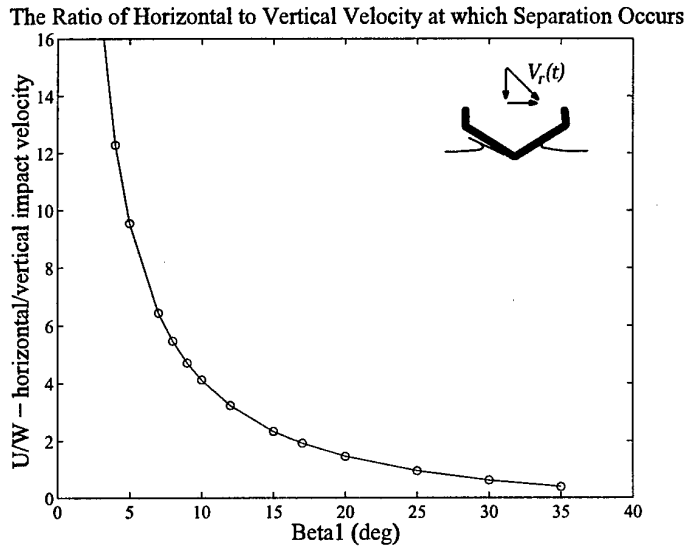


Figure 5: U/W required for Type B flow for symmetric hulls of varying deadrise angles

In understanding transverse stability of planing hulls, the interaction of asymmetry and horizontal velocity is important. For a given ratio of horizontal to vertical velocity, the angle β_2 required for separation can be determined. In Figure 6 the limiting angle of β_2 versus the corresponding β_1 is plotted for different ratios of horizontal to vertical velocity. For each of the different ratios, the dependence of β_2 on β_1 for initiation of Type B flow is small. The increase in horizontal velocity decreases the value of β_2 required for separation. Therefore, the more a planing boat is heeled over, the less horizontal velocity is required to get separation off the keel. Likewise, the larger the horizontal velocity, the smaller θ needs to be for Type B flow.

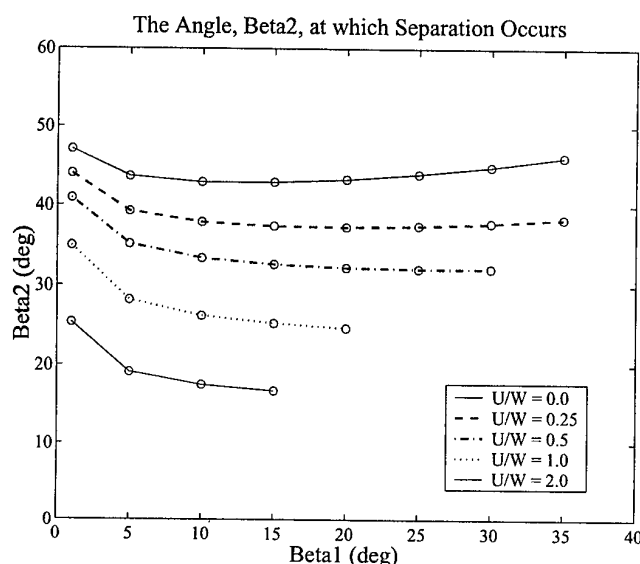


Figure 6: β_2 for Type B flow with corresponding β_1 for varying U/W

The results of an impact model that included both asymmetry and horizontal velocity could be incorporated into a nonlinear motion simulator in order to provide an analytical transverse stability tool. The results would allow for a dynamic righting arm curve to be developed for high speed planing craft. Horizontal velocity is a significant component of transverse planing stability and therefore needs to be addressed. That is the goal of developing the model presented here.

Acknowledgment

This research has been supported by the Department of Defense, Office of Naval Research and the Link Foundation. The authors would also like to thank Lixin Xu for his hypergeometric function software and discussions on his model and problem derivation.

References

- [1] Judge, C., Xu, L., and Troesch, A.W. 1999 Water impact model with horizontal velocity. *14th International Workshop on Water Waves and Floating Bodies*. Port Huron, MI
- [2] Vorus, W.S. 1996 A flat cylinder theory for vessel impact and steady planing resistance. *Journal of Ship Research*, 40, 2
- [3] Xu, L. 1998 A theory of asymmetrical vessel impact and steady planing. *Ph.D dissertation*, Department of Naval Architecture and Marine Engineering, University of Michigan, Ann Arbor
- [4] Xu, L., Troesch, A.W., and Vorus, W.S. 1998 Asymmetric Vessel Impact and Planing Hydrodynamics, *Journal of Ship Research*, 42, 3

WAVE INTERACTIONS WITH A MULTITUDE OF FLOATING CYLINDERS

by Masashi KASHIWAGI

Research Institute for Applied Mechanics, Kyushu University
6-1 Kasuga-koen, Kasuga-city, Fukuoka 816-8580, Japan

1. Introduction

A column-supported type very large floating structure (VLFS), consisting of a thin upper deck and a multitude of buoyancy columns, is considered to be advantageous in that the wave forces and hence wave-induced responses are small relative to a box-shaped pontoon type. However, when a large number of identical bodies are placed in an array with equal separation distance, near-resonant modes may occur between adjacent bodies at some critical frequencies, and cause large wave forces on each element of the array.

In this paper, 64 truncated cylinders arranged in 4 rows and 16 columns are considered as a part of a real structure to check occurrence of near-resonant modes and performance of the wave interaction theory based on the potential flow. Experiments are conducted to measure the wave forces on a couple of element cylinders, as well as the total force on all cylinders, and the wave elevation along the longitudinal center line. Numerical computations are also performed using Kagemoto & Yue's interaction theory, with special care paid on the numerical accuracy and convergence.

Attention is focused on variation of the wave elevation and forces near critical frequencies. Since the reflection of waves is related closely to the steady drift force and moment, computations of the mean drift force and moment based on the momentum-conservation principle are implemented and compared with corresponding experiments.

2. Wave Interaction Theory

We consider a column-supported type VLFS, in which a great number of identical columns are placed in a rectangular array with equal separation distance. The elementary column considered here is a truncated circular cylinder with radius a and draft d . The distance between centerlines of adjacent cylinders is $2s$ in both x - and y -axes. The positive z -axis is directed downward, with $z = 0$ the undisturbed free surface and $z = h$ the constant water depth. Incident plane waves propagate in the direction with angle β relative to the positive x -axis.

The boundary conditions are linearized and the potential flow is assumed. Then, we express the velocity potential in the form

$$\Phi(x, y, z, t) = \text{Re}[\phi(x, y, z) e^{i\omega t}], \quad (1)$$

$$\phi = \frac{gA}{i\omega} \left[\phi_I + \phi_S - K \sum_{k=1}^{\infty} \frac{X_k}{A} \{ \phi_k + \varphi_k \} \right], \quad (2)$$

where g , A , ω and K are respectively the gravitational acceleration, the amplitude of an incident wave, the circular frequency, and the wavenumber given by ω^2/g .

ϕ_I is the incident-wave velocity potential expressed by

$$\phi_I = \frac{\cosh k_0(z-h)}{\cosh k_0 h} e^{-ik_0(x \cos \beta + y \sin \beta)}, \quad (3)$$

where k_0 is a solution of the wave dispersion relation, $k_0 \tanh k_0 h = K$.

ϕ_S in (2) represents the scattering potential. Let the number of floating bodies be denoted by N_B . Then the scattering potential due to the j -th body, ϕ_S^j , may be expressed in the form

$$\phi_S^j = \{A_S^j\}^T \{\psi_S^j\}, \quad (4)$$

where $\{A_S^j\}$ is the unknown coefficient vector, and $\{\psi_S^j\}$ is the vector comprised of the progressive and evanescent wave components, which can be expressed as

$$\{\psi_S^j\} = \begin{Bmatrix} Z_0(z) H_m^{(2)}(k_0 r_j) e^{-im\theta_j} \\ Z_n(z) K_m(k_n r_j) e^{-im\theta_j} \end{Bmatrix}. \quad (5)$$

Here

$$Z_0(z) = \frac{\cosh k_0(z-h)}{\cosh k_0 h}, \quad Z_n(z) = \frac{\cos k_n(z-h)}{\cos k_n h}, \quad (6)$$

and k_n is the evanescent-mode wavenumbers satisfying $k_n \tan k_n h = -K$ ($n = 1, 2, \dots$). The local cylindrical coordinate system (r_j, θ_j, z) has been used, with the origin placed at the center of the j -th body. The number of terms in the θ -direction, m , is taken as 0, $\pm 1, \pm 2, \dots$.

Using the wave interaction theory developed by Kagemoto & Yue, the unknown coefficient vector in (4) can be determined, with all effects of interactions with other bodies taken into account exactly in the framework of the potential theory.

In the radiation problem, X_k in (2) denotes the complex amplitude of the k -th mode of motion. In the definition of the mode, not only rigid-body motions but also a set of "generalized" modes to represent elastic deflections of a deck are assumed to be included. ϕ_k is the velocity potential due to the single-body oscillation with unit velocity in the k -th mode (without any interactions), and φ_k is the remaining part due to hydrodynamic interactions with other bodies.

By solving the boundary-value problem for a single body, ϕ_k may be explicitly given in the form

$$\phi_k^j = \{\mathcal{R}_k^j\}^T \{\psi_S^j\}, \quad (7)$$

where $\{\mathcal{R}_k^j\}$ is known and referred to as the vector of radiation characteristics.

The problem for φ_k is essentially the same as the scattering problem, and thus its solution is given by

$$\varphi_k^j = \{A_k^j\}^T \{\psi_S^j\}, \quad (8)$$

where $\{A_k^j\}$ is unknown but can be determined in exactly the same way as for the scattering problem.

Collecting all contributions due to the body disturbance, the velocity potential except for ϕ_I in brackets of (2) (let us denote this potential by ϕ_B) can be expressed as

$$\left. \begin{aligned} \phi_B &= \sum_{j=1}^{N_B} \{A^j\}^T \{\psi_S^j\}, \\ \{A^j\} &= \{A_S^j\} - K \sum_{k=1}^{\infty} \frac{X_k}{A} \left(\{\mathcal{R}_k^j\} + \{A_k^j\} \right). \end{aligned} \right\} \quad (9)$$

Then using (9), the wave elevation at any point on the free surface ($z = 0$) can be computed by

$$\zeta(x, y) = A \left[\phi_I(x, y, 0) + \phi_B(x, y, 0) \right]. \quad (10)$$

3. Velocity Potential at Far Field

At a large distance from the structure, evanescent-wave components decay. Thus we may consider only the progressive waves in (9) expressed by the Hankel function.

In terms of the global coordinate system $O-r\theta z$, the Hankel function can be written by Graf's addition theorem in the form

$$H_m^{(2)}(k_0 r_j) e^{-im\theta_j} = \sum_{\ell=-\infty}^{\infty} J_{m-\ell}(k_0 L_{j0}) e^{-i(m-\ell)\alpha_{j0}} \{H_\ell^{(2)}(k_0 r) e^{-i\ell\theta}\}, \quad (11)$$

where L_{j0} and α_{j0} are the radial distance and azimuth angle of the origin of the global coordinate system when viewed from the center of the j -th body, and r must be larger than L_{j0} for (11) being valid.

Substituting the above relation into (9), the disturbance potential at far field can be written as

$$\phi_B = \sum_{\ell=-\infty}^{\infty} A_\ell \{Z_0(z) H_\ell^{(2)}(k_0 r) e^{-i\ell\theta}\}, \quad (12)$$

where A_ℓ ($\ell = 0, \pm 1, \pm 2, \dots$) denotes the components of the vector given by

$$\{\mathcal{A}\} = \sum_{j=1}^{N_B} [M_{j0}]^T \{\mathcal{A}^j\}. \quad (13)$$

Here, $[M_{j0}]$ is the matrix when writing (11) in a matrix form, and $\{\mathcal{A}^j\}$ is defined in (9).

The incident-wave potential, ϕ_I given by (3), can be also expressed in terms of the cylindrical coordinate system. Therefore the total velocity potential can be written as

$$\phi = \frac{gA}{i\omega} \sum_{\ell=-\infty}^{\infty} Z_0(z) \left\{ \alpha_\ell J_\ell(k_0 r) + A_\ell H_\ell^{(2)}(k_0 r) \right\} e^{-i\ell\theta}, \quad (14)$$

where α_ℓ is the coefficient explicitly given by $\alpha_\ell = \exp\{i\ell(\beta - \pi/2)\}$.

4. Wave Drift Force and Moment

Based on the conservation principle of linear and angular momentum, we can relate the mean drift force and moment on a structure to the far-field potential. In the present case, necessary integrations with respect to z and θ for a large value of r can be analytically performed in terms of (14). The details of derivation are omitted here, but using orthogonality relations in trigonometric functions and Wronskian formulae for Bessel functions, we can obtain the following results:

$$\bar{F}_x = -\frac{\rho g A^2 k_0}{2} \frac{k_0^2}{K} \frac{1}{K + h(k_0^2 - K^2)} \text{Im} \sum_{\ell=-\infty}^{\infty} \left[2A_\ell A_{\ell+1}^* + \alpha_\ell A_{\ell+1}^* + A_\ell \alpha_{\ell+1}^* \right], \quad (15)$$

$$\bar{F}_y = -\frac{\rho g A^2 k_0}{2} \frac{k_0^2}{K} \frac{1}{K + h(k_0^2 - K^2)} \text{Re} \sum_{\ell=-\infty}^{\infty} \left[2A_\ell A_{\ell+1}^* + \alpha_\ell A_{\ell+1}^* + A_\ell \alpha_{\ell+1}^* \right], \quad (16)$$

$$\bar{M}_z = -\rho g A^2 \frac{1}{K} \frac{k_0^2}{K + h(k_0^2 - K^2)} \text{Re} \sum_{\ell=-\infty}^{\infty} \ell \left[A_\ell A_\ell^* + \alpha_\ell A_\ell^* \right]. \quad (17)$$

5. Experiments

A truncated circular cylinder with diameter $D (= 2a) = 114$ mm was used as an elementary float, and 64 cylinders were arranged in an array with 4 rows (in the y -axis) and 16 columns (in the x -axis) with equal separation distance of $2s = 2D$ between the centerlines of adjacent cylinders in both x - and y -axes. The draft of cylinders was set to $d = D$ and $2D$, but here the results of $d = 2D$ will be mainly shown.

Experiments were carried out in head waves with all motions fixed. Measured items were wave elevations at 16 points along the centerline of the array, wave forces on elementary cylinders placed at No. 1, No. 9, and No. 15 columns along No. 2 row, and at the same time the total forces on 64 cylinders. The frequency range in measurements was $Ks = 0.2 \sim 1.6$ and the wave steepness H/λ (the ratio of wave height to wave length) was set to approximately 1/50.

6. Results and Discussion

After convergence of numerical results was checked for $Ks = 1.0$, $\beta = 0^\circ$ and $h = 3d$, the number of terms in the θ -direction (M) and the number of evanescent modes (N) were determined to be $M = 4$ and $N = 3$, which yields an absolute accuracy of five decimals. In this case, the total unknowns for $N_B = 64$ are $(2M + 1) \times (N + 1) \times N_B = 2304$. To enhance numerical efficiency, the double symmetry relations with respect to the x - and y -axes are exploited, reducing the number of unknowns to 1/4.

Although there are many measured results, only a couple of results are shown here, because of shortage of the space. Fig. 1 shows the wave elevation as a function of Ks , measured at between No. 1 and No. 2 columns (the upwave side). Likewise, Fig. 2 and Fig. 3 are the results near the midst of the array and the downwave side, respectively. We can see rapid variation at the upwave side and large-amplitude waves in the midst of the array for $Ks \simeq 0.8 \sim 1.24$. $Ks \simeq 1.24$ may corresponds to the Neumann trapped mode, discussed by Maniar & Newman. Numerical results agree well qualitatively with experiments, but tend to overpredict as the point compared goes downstream. No breaking waves were observed in the experiments.

Thus the difference from the potential-theory results may be attributed to a decaying mechanism due to development of the oscillatory boundary layer or other viscous effects.

Figure 4 shows the surge drift force in head waves. Analogous to the wave elevation at the upwave side, rapid variation can be seen at frequencies less than $Ks \approx 1.24$. When Ks is greater than this critical value, the waves are mostly reflected and thus the drift force becomes large. Although measured values are scattered, the overall agreement is favorable between computed and measured results.

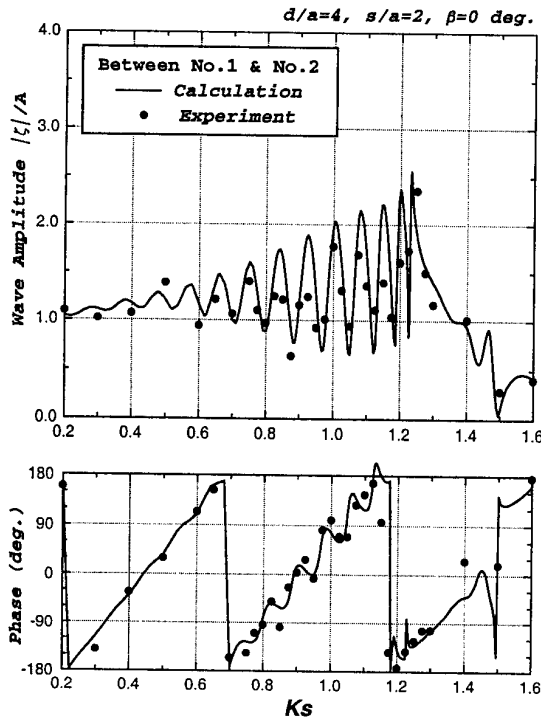


Fig. 1 Wave elevation at upwave side

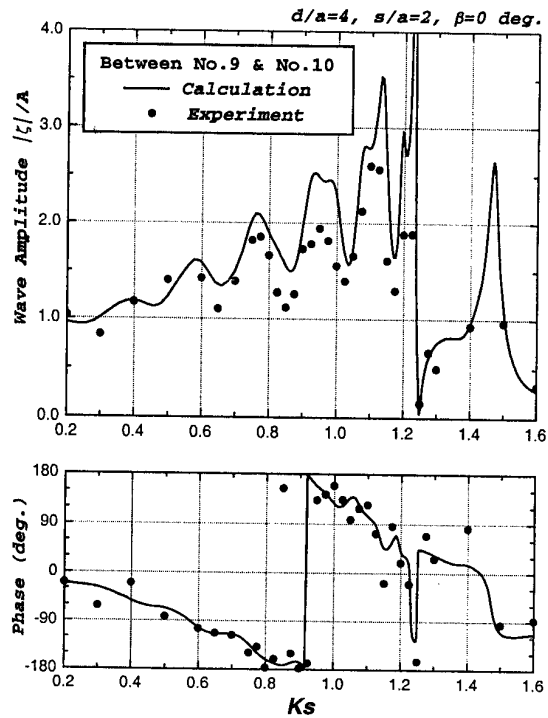


Fig. 2 Wave elevation at midst of the array

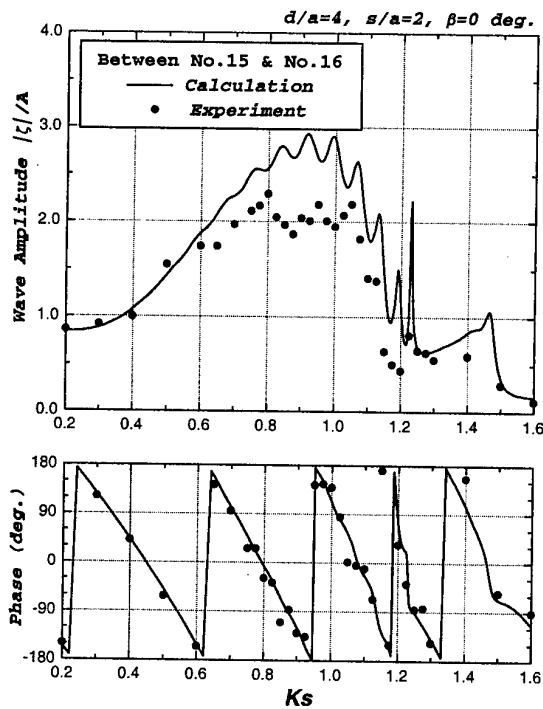


Fig. 3 Wave elevation at downwave side

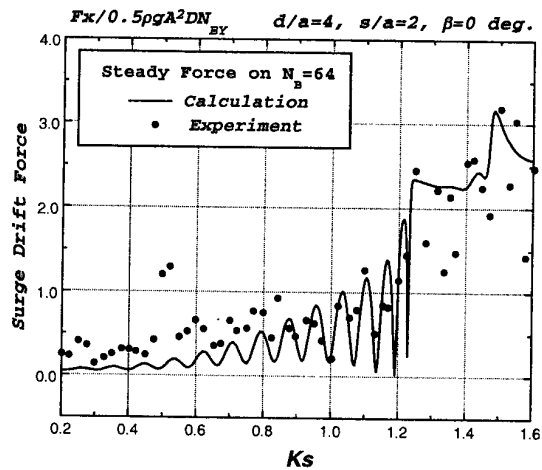


Fig. 4 Surge drift force acting on 64 cylinders arranged in 4 rows and 16 columns in head waves

NUMERICAL ANALYSIS OF SLOSHING PROBLEM

Yonghwan Kim

American Bureau of Shipping
Research Department, Houston, TX, USA

Introduction

Many studies have been reported for the sloshing analysis in liquid containers. One of the major concerns in the marine hydrodynamic field is the accurate prediction of impulsive load on internal structures. During violent sloshing, the sloshing-induced impact load can cause a critical damage on tank structure. Such damage cases have been reported for oil tankers, LNG carriers and bulk carriers. Recently, this problem becomes an important issue in FPSO design.

Many analytical and experimental studies on sloshing were performed in the 1950's and 1960's for the tank design of space vehicles. In the 1970's and early 1980's, the sloshing problem became an important issue in the design of the liquified natural gas (LNG) carriers. Some numerical methods were applied during this time, and such studies can be found in the works of Faltinsen[2], Bridges[1], Mikelis and et al[5]. Some Japanese researchers have continued the study, and many interesting results have been introduced for the two- and three-dimensional sloshing problems. Recently some computational results using the general-purpose flow simulation programs, like FLOW3D, have reported for the sloshing analysis. However, the application of the general-purpose programs may be not proper for the prediction of impulsive loads, since the typical numerical treatment of wall condition can result in unrealistic flow simulation.

In this study, a numerical method has been applied for the simulation of fluid flows in the two- and three-dimensional tanks. The global fluid motion is of interest and local nonlinear phenomena are not considered in detail. The method of solution is a finite difference method, adopting staggered grids. The free surface profile is assumed to be single-valued, so that SURF scheme is applicable to the numerical implementation of free-surface boundary condition. The numerical computation has been carried out for a few models which experimental or other computational results are available. The present results include the computation of impact pressure on tank ceiling. Moreover, the developed computer program was extended to the real-ship application.

Numerical Method

The present study adopts SOLA method for the Navier-Stokes equation. This method is well known, and the details can be found in [3]. In this method, the finite-difference form of the velocity vector in the $(n+1)$ -th time step, $\bar{u}_{ijk}^{(n+1)}$, can be written as follows:

$$\bar{u}_{ijk}^{(n+1)} = \bar{u}_{ijk}^* + \Delta p_{ijk} \frac{\Delta t}{\Delta(x, y, z)}$$

where

$$\bar{u}_{ijk}^* = \bar{u}_{ijk}^{(n)} + \Delta t \left[-\frac{1}{\rho} (\hat{\nabla} p)_{ijk}^{(n)} + \nu (\hat{\nabla}^2 \bar{u})_{ijk}^{(n)} + (\bar{f})_{ijk}^{(n+1)} \right] - \Delta t \{ \bar{u} \cdot \hat{\nabla} \}_{ijk}^{(n)} \bar{u}_{ijk}^{(n)}$$

$$\Delta p_{i,j,k} = - \frac{(\hat{\nabla} \cdot \bar{u}_{ijk}^*)}{2\Delta t (1/\Delta x^2 + 1/\Delta y^2 + 1/\Delta z^2)}$$

and ρ, ν, p, \bar{f} are the liquid density, kinematic viscosity, pressure and external force vectors, respectively. Here, the three-dimensional staggered grids are distributed in whole tank domain, and the subscript i, j, k indicates the cell index. In the present study, a conservative form of the mixed central-upwind difference is applied for the convection term in the Navier-Stokes equation.

The free surface elevation can be obtained from the kinematic condition which takes the following form:

$$\eta_{ij}^{(n+1)} = \eta_{ij}^{(n)} + \Delta t \left[w - u \frac{\partial \eta}{\partial x} - v \frac{\partial \eta}{\partial y} \right]_{ij}$$

The dynamic condition can be imposed using the irregular-star method. In this method, the pressure at the cell near free surface is interpolated from the pressure values at six neighbor points, including the points on free surface.

A no-slip condition is valid when the viscous effect is so significant that the boundary layer thickness is comparable to the cell size. However, generally, the viscous does not influence much on violent sloshing flow. In this study, a free-slip condition is applied on tank walls.

Impact Pressure Computation

Some special numerical treatments are required when the liquid contacts tank ceiling or horizontal members. First of all, the detachment of fluid from ceiling should be properly simulated. When a part of fluid is on the tank top, a typical no-flux condition tends to prevent the vertical detachment. In the present computation, the downward velocity is allowed at the tank top boundary if the free surface is nearby and moves down. In a LNG cargo, the downward velocity should be also allowed when the pressure is less than the vapor pressure.

As pointed in some studies, the typical wall condition on the tank top can produce too large impact pressure. This study adopts the concept of buffer zone, which has been successfully applied by Mikelis and some Japanese. In the buffer zone near the tank top, the free-surface boundary condition is modified to the following form:

$$\kappa \frac{p_f - p_{atm}}{\rho} - (1 - \kappa) \frac{H_B}{\Delta t} w_f = 0$$

where

$$\kappa = \begin{cases} (D - \eta) / H_B & D - H_B \leq \eta < D \\ 0 & \eta \leq D - H_B \\ 1 & \eta = D \end{cases}$$

D is the tank depth and H_B is the size of buffer zone. This is the linear combination of the no-flux wall condition and dynamic free surface condition. Therefore, the existence of wall boundary affects on the fluid motion when the free surface is inside the buffer zone. This condition is valid only when the free surface moves upward. In the real physical phenomenon, the magnitude of impact pressure depends on some other factors, like the air cushion, structural response and liquid compressibility. The concept of buffer zone may reflect a part of such effects during an impact occurs.

Averaging the signal over several time steps is another numerical treatment for the impulsive dynamic pressure. Since the finite number of cells are used in the numerical computation, the computational pressure signal shows the series of discrete impulses. According to the computational experience, the averaged signal shows closer time-history and peak than not-averaged results.

The classical criterias for the numerical stability are valid in the present study. For example, the Courant condition for the velocity and wave should be satisfied. In addition, it is desirable that the time segment should be fine enough for the free surface to experience the boundary condition in the buffer zone.

Computational Results

In the numerical computation, the upwinding factor for the convection term was fixed to be 0.75 and the kinematic viscosity has been set to be $10^{-6} \text{m}^2/\text{sec}$. For the two-dimensional computation, only one mesh sheet was distributed along the transverse direction.

Figure 1 shows a comparison of the instantaneous wave elevation with the linear analytic solution. When a small amplitude excitation with an out-of-resonance frequency, the numerical solution is very close to the analytic solution. In the case of Figure 1, the excitation is near resonance, so that a typical difference between the nonlinear and linear results can be observed.

Figure 2 shows an instantaneous snapshot of fluid motion, and it is compared with experiment. This tank has the same dimensions with Figure 1, but one deep vertical baffle and three horizontal members are in the tank. The experimental result is from [4]. From this figure, we can figure out that the present method provides quite reasonable solution even for a tank with internal members.

Figure 3 shows the computed pressure signals with different meshes. The observation points are the center of corner cells between the tank top and side wall. Generally the larger impact pressure is generated when the mesh size becomes smaller, but it should be noticed that the averaged signals do not show a significant discrepancy.

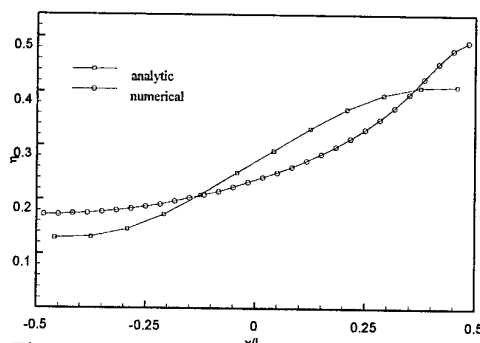
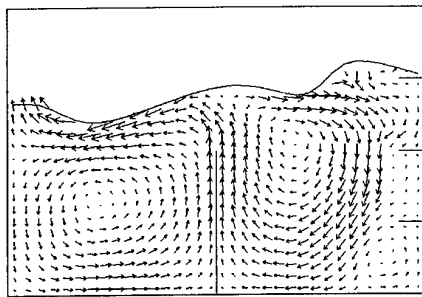
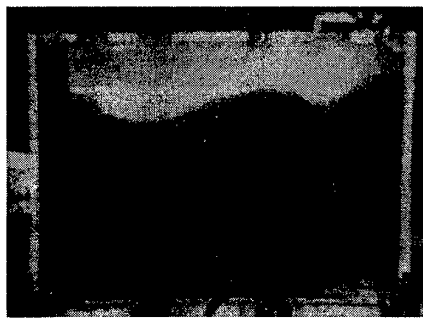


Figure 1. Instantaneous surface profile; 0.8m(L)×0.8m(B)×0.54m(D), 50% filling, $T_1=1.15\text{sec}$, $A_1=0.01\text{m}$, 30×1×20 meshes, no internal members, $t=5.4\text{ sec}$

Figure 4 shows the comparison of the computed and measured pressure signals on the tank top. The measurement shows unsteady peaks, but the maximum pressure is close to the numerical result. According to the computational experience, averaging over 4~6 time steps provides reasonable results.

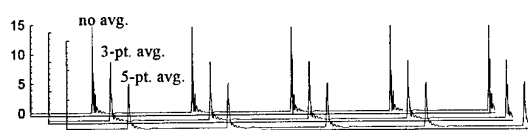


(a) Computed velocity vectors and elevation

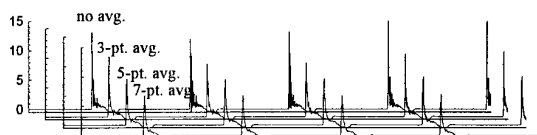


(b) Experiment

Figure 2. Instantaneous snapshots of fluid motion; the same dimension with Figure 1, 70% filling, $T_1=1.08\text{sec}$, $A_1=0.04\text{m}$, $30 \times 1 \times 20$ meshes, with internal members



(a) 30×20



(b) 40×30

Figure 3. Grid dependency of the pressure signal at tank top; the same tank with Figure 1, 80% filling, $T_1=1.175\text{sec}$, $A_1=0.04\text{m}$, 5.5sec time window, $H_B=0.5\Delta z$, peak of experimental data: 9.07kN/m^2

Figure 5 shows the wave profile in a three-dimensional tank, and the tank dimension and excitation conditions are the same with those of [6]. In this case, the excitation frequency is the third mode of natural motion, and both surge and sway motions are under the excitation. The z-coordinate is scaled for the comparison with their result (small figure), and two results show a good agreement.

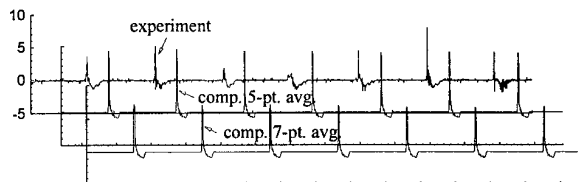


Figure 4. Pressure time-histories on tank top; the same tank with Figure 1, 70% filling, $T_1=0.98\text{sec}$, $A_1=0.038\text{m}$, $30 \times 1 \times 20$ meshes, $H_B=0.5\Delta z$

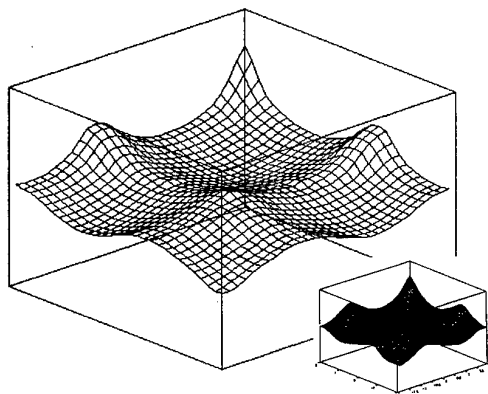


Figure 5. Instantaneous wave profile in a 3-D tank; $L/d=B/d=4$, $T_1\sqrt{g/d} = T_2\sqrt{g/d}=4.13$, $A_1/d=A_2/d=0.0186$, $30 \times 30 \times 30$ meshes (small figure; Wu, Ma & Taylor[6])

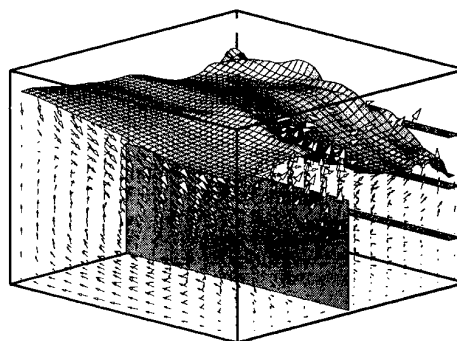


Figure 6. Instantaneous wave profile and velocity vectors in a 3-D tank; the same tank with Figure 2, $B=0.8\text{m}$, $T_4=T_5=1.30\text{sec}$, $A_4=A_5=4\text{deg.}$, $40 \times 40 \times 30$ meshes

Figure 6 shows the instantaneous surface profile and velocity vectors on fluid domain when the tank is under the roll and pitch excitations. The fluid motion in this tank is complicated because of the internal members.

Especially, the deep vertical member plays an important role to block the horizontal motion.

Figure 7 shows the wave elevation at two tank corners of the same side when the roll motion is under excitation. In this case, the horizontal members influence on the fluid motion in some region, resulting in the three-dimensional flows. Therefore, we can observe some time-delay of the pressure impulse at the left and right corners. This is another effect of the horizontal member, which is different with Figure 2. In this figure, the flat crests indicate that the fluid contacts the tank ceiling, and other flat signals are due to the horizontal member.

Figure 8 shows the pressure history at a corner of tank top when the tank is under both surge and sway excitations. In particular, two motions have the same frequency and amplitude but the phase difference is applied in the case of Figure (b). In this case, the 45-deg. phase difference induces the rotational surface motion. Therefore, the impact area on the tank top turns around periodically along the top edges, and the maximum pressure is much less than the case without phase difference.

The present computation is extended to multi-tank sloshing analysis for real ships. Figure 9 shows an application example for a LNG carrier with five tanks. In the real-ship computation, it is desirable to couple a ship-motion program with the sloshing analysis code since the sloshing-induced forces and moments affect on the ship motion. A study for coupling with the three-dimensional ship-motion program is in progress.

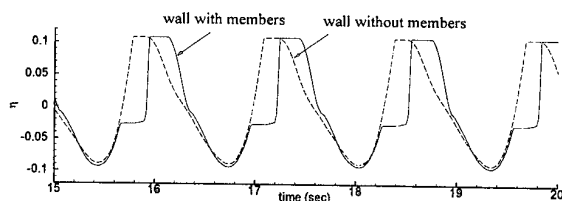


Figure 7. Surface elevation at two corners; the same tank with Figure 2; 80% filling, $T_4=1.30\text{sec}$, $A_4=4\text{deg}$.

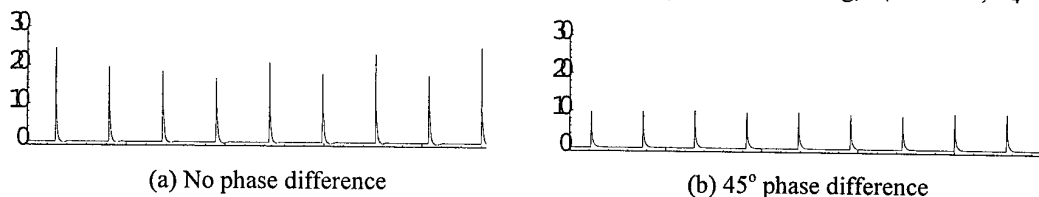


Figure 8. Time histories of pressure on a ceiling corner; $T_1=T_2=1.08\text{sec}$, 45° phase difference, $A_1=A_2=0.02\text{m}$, 30x30x20 meshes, $x/L=y/B=0.983$, 5-pt. averaged

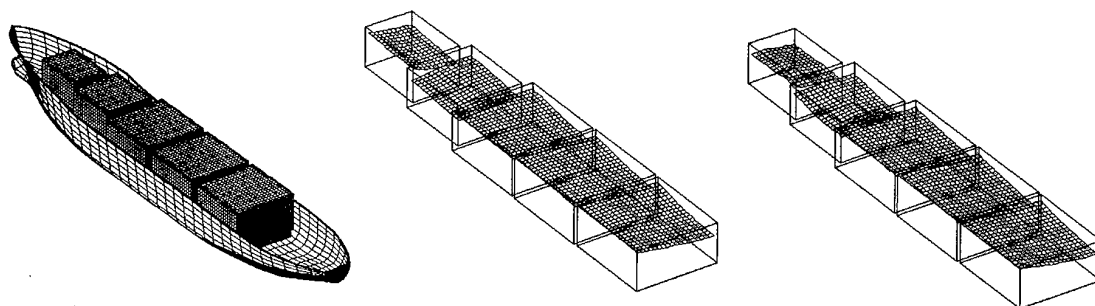


Figure 9. Sloshing in a LNG carrier; LAMP modeling for motion, sway-heave-roll-pitch coupling

Acknowledgement

I appreciate DAEWOO Heavy Machinery Ltd. for admitting to use their experimental data.

References

- [1] Bridges, T.J., 1982, 'A numerical simulation of large amplitude sloshing', *Proc. of the 3rd International Numerical Ship Hydrodynamics*
- [2] Faltinsen, O.M., 1978, 'A numerical non-linear method of sloshing in tanks with two dimensional flow', *Journal of Ship Research*, Vol.18
- [3] Hirt, C.W. & et al, 1975, 'SOLA-A numerical solution algorithm for transient fluid flows', *Report LA-5852*, Los Alamos Scientific Laboratory
- [4] Kim, Y., 1993, 'Development of sloshing analysis system, II', DAEWOO HMI, *Research Report SH-9121*
- [5] Mikelis & et al, 1984, 'Sloshing in partially filled liquid tanks and its effect on ship motions', *Trans. Of RINA*, Vol.126
- [6] Wu, G.X. and et al, 1998, 'Numerical simulation of sloshing waves in a 3D tank based on a finite element method', *Applied Ocean Research*, Vol.20

ON THE BEHAVIOUR OF STEEP SHORT-CRESTED WAVES IN DEEP WATER AND THEIR EFFECTS ON STRUCTURES

OLIVIER KIMMOUN¹ AND CHRISTIAN KHARIF²

¹*Ecole Supérieure d'Ingénieurs de Marseille, IMT-Technopole de Chateau-Gombert, F-13451 Marseille Cedex 20, France*

²*Ecole Supérieure de Mécanique de Marseille, IMT-Technopole de Chateau-Gombert, F-13451 Marseille Cedex 20, France*

Most of the studies on the kinematics and dynamics of surface waves were focused for years on two-dimensional wave fields and not many dealt with three-dimensional wave fields. The so-called short-crested waves due to the nonlinear interaction of two similar uniform wave trains coming from two different directions are one of the simplest genuinely three-dimensional waves of permanent form doubly-periodic in two directions of the horizontal plane. These short-crested waves may occur in a number of important maritime situations. Swell being fully reflected off a vertical sea-wall or jetty results in a short-crested wave field being found adjacent to the reflecting wall. Waves propagating down a vertical-walled channel can assume a short-crested wave form when there is a cross-channel variation of the flow pattern. These waves may also occur when a wave train is diffracted behind an obstacle of finite width. These waves are known to have very steep pyramidal shape that may cause serious damage to vessels or off-shore structures.

The study deals with short-crested waves due to two plane waves intersecting at an angle μ , or by a reflection of a progressive plane wave on a vertical sea-wall at an angle of incidence $\theta = (\pi - \mu)/2$. The derived short-crested waves are progressive in one direction and standing in the perpendicular direction. The values $\theta = \pi/2$ and $\theta = 0$ are, respectively, the Stokes wave and the standing wave (the two-dimensional limits). One considers surface gravity waves on an inviscid incompressible fluid of infinite depth. The flow is assumed irrotational. To put all the equations into non-dimensional form, one scales all the variables with respect to the reference length $1/k$ and the reference time $(gk)^{-1/2}$, where k is the wavenumber of the incident wave and g is the acceleration due to gravity. The governing equations are

$$\nabla^2 \phi = 0 \quad \text{for} \quad -\infty \leq z \leq \eta(x, y, t) \quad (1)$$

$$\nabla \phi \rightarrow 0, \quad \text{as} \quad z \rightarrow \infty \quad (2)$$

$$\eta_t + \phi_t + \frac{1}{2} |\nabla \phi^2| = C \quad \text{on} \quad z = \eta(x, y, t) \quad (3)$$

$$\eta_t + \phi_x \eta_x + \phi_y \eta_y - \phi_z = 0 \quad \text{on} \quad z = \eta(x, y, t) \quad (4)$$

$$\phi_y = 0 \quad \text{on} \quad y = 0 \quad (5)$$

where $\phi(x, y, z, t)$ is the velocity potential, $z = \eta(x, y, t)$ is the equation of the free surface, (x, y) are the horizontal coordinates, z is the vertical coordinate and C is a constant. The wave is assumed to propagate in the x -direction without change of shape.

The above problem admits steady short-crested waves. To prove rigorously the existence of short-crested waves is a difficult task, and so far only capillary-gravity waves with high enough surface tension have been shown to exist. However, there is numerical evidence that short-crested waves exist (see, for example, the numerical result of Roberts, (1983)). Fuchs (1952), Chappellear (1961), Hsu et al (1979) and Menasce (1994) used perturbation expansions to compute from formal point of view the small-amplitude three-dimensional waves. Ioualalen (1993) and Kimmoun et al. (1999) extended the computations to higher order. In the frame of reference (X, Y, Z, t) moving with the wave, the surface elevation and the velocity potential are of the form

$$\begin{cases} \eta = \sum_{i=1}^{\infty} h^i \sum_{m,n} a_{imn} \cos(mX) \cos(nY) \\ \phi = \sum_{i=1}^{\infty} h^i \sum_{m,n} b_{imn} \sin(mX) \cos(nY) e^{(\alpha_{mn} Z)} \end{cases} \quad (6)$$

$$\text{where } \alpha_{mn}^2 = m^2 (\sin\theta)^2 + n^2 (\cos\theta)^2 \quad (7)$$

The wave steepness of the wave is defined by $h = (\eta(0, 0) - \eta(\pi, 0))/2$. The coefficients a_{imn} and b_{imn} are computed up to 27th order.

To study the stability of the short-crested waves, let the perturbative motion be

$$\begin{cases} \eta' = e^{-\sigma t} e^{i(pX+qY)} \sum_{j=-\infty}^{\infty} \sum_{k=-\infty}^{\infty} a_{jk} e^{i(j \sin\theta X + k \cos\theta Y)} \\ \phi' = e^{-\sigma t} e^{i(pX+qY)} \sum_{j=-\infty}^{\infty} \sum_{k=-\infty}^{\infty} b_{jk} e^{i(j \sin\theta X + k \cos\theta Y)} e^{\kappa_{jk} Z} \end{cases} \quad (8)$$

$$\text{where } \kappa_{jk}^2 = (p + j \sin\theta)^2 + (q + k \cos\theta)^2 \quad (9)$$

The infinitesimal disturbances are harmonic perturbations modulated by wave number p and q in the two horizontal directions. Up to $h = 0.30$, Ioualalen & Kharif (1994) have shown that the short-crested waves admit characteristic stability regimes for (i) near standing waves (θ around 0), (ii) fully three-dimensional waves (θ around $\pi/4$) and (iii) near Stokes waves (θ around $\pi/2$). For values of h greater than 0.30 it is found (i) for near standing waves that the dominant instability is a sideband-type instability in the direction of propagation (class Ia), (ii) for fully three-dimensional waves that the dominant instability is a sideband-type instability in oblique direction (class Ib), and (iii) for near Stokes waves that the dominant instability is a *horseshoe-patterned* instability (class IIa). For fully three-dimensional waves, it is interesting to note that instabilities of class IIb become dominant above $h = 0.63$. So it is concluded that the dominant resonant interactions of short-crested waves are four-wave instabilities (class I) except for steep near Stokes waves, and very steep fully three-dimensional waves for which five-wave processes are predominant (class II).

The force exerted by waves on vertical walls is an important design criterion. Fenton (1985) examined the uniform short-crested wave problem to third order and obtained expressions for the depth integrated wave force on the wall and the depth integrated wave

moment about the basis of the wall. Later Marchant & Roberts (1987) via a computer-generated perturbation expansion investigated the uniform short-crested wave to 35th order in wave steepness and extended Fenton's work to oblique incident wave in shallow water. Here the problem is to consider wave forces exerted by more realistic wave patterns such as modulated short-crested. The effect of the modulation for different angle θ and waveheight h is analyzed and results are compared with Fenton and Marchant & Roberts work's.

References

- CHAPPELEAR J.E., 1961, On the description of short-crested waves, *Beach Erosion Board, U.S. Army Corps Engrs, Tech. Memo* 125.
- FENTON J.D., 1985, Short-crested waves and the wave forces on a wall, *J. Water Waves Port. Coast. and Ocean Eng.*, **111**, 693-718.
- FUCHS R.A., 1952, On the theory of short-crested oscillatory waves, *Gravity Waves, U.S. Nat. Bur. Stand. Circular* **521**, 187-200.
- HSU J.R.C., TSUCHIYA Y. & SILVESTER R., 1979, Third-order approximation to short-crested waves, *J. Fluid Mech.* **90**, 170-196.
- IOUALALEN M., 1993, Approximation au quatrième ordre d'ondes de gravité tridimensionnelles en profondeur infinie, *C.R. Acad. Sci. Paris*, **316** II, 1193-1200.
- IOUALALEN M. & KHARIF C., 1994, On the subharmonic instabilities of steady three-dimensional deep water waves, *J. Fluid Mech.*, **262**, 265-291.
- KIMMOUN O., BRANGER H. & KHARIF C., 1999, On short-crested waves: experimental and analytical investigations, *Eur. J. Mech. Fluids*, **18**, 5.
- MARCHANT T.R. & ROBERTS A.J., 1987, Properties of short-crested waves in water of finite depth, *J. Austral. Math. Soc. Ser. B*, **29**, 103-125.
- MENASCE D., 1994, Analyse non linéaire d'ondes de surface bidimensionnelles et tridimensionnelles, *PhD thesis*, Université de Nice Sophia Antipolis, Nice (France).
- ROBERTS A.J., 1983, Highly nonlinear short-crested waves, *J. Fluid Mech.*, **135**, 301-321.

IMPULSIVE FREE-SURFACE FLOW DUE TO A STEADY LINE SOURCE AT THE BOTTOM OF A UNIFORM FLUID LAYER

Maurizio Landrini
INSEAN, The Italian Ship Model Basin
Via di Vallerano 139, 00128 Roma. Italy

Peder A. Tyvand
Department of Agricultural Engineering
Agricultural University of Norway
Box 5065, N-1432 Aas Norway

Introduction

The classical Cauchy-Poisson problem assumes the initial surface elevation and surface velocity to be given at time zero. The resulting free-surface flow is calculated according to linear theory. The present work is concerned with the Cauchy-Poisson problem for constant depth [1, 2]. Specifically, we consider the flow due to normal velocity at the bottom instead of initial surface disturbances.

We will investigate the basic case of a steady source (or sink) located at the bottom by analytical and numerical means. Such singularities, turned on impulsively at time zero, generate interesting classes of nonlinear wave systems governed uniquely by a Froude number. A source will generate a bore, from undular type to breaking dependent on the Froude number. The steady sink may give rise to dip instability, where the free surface collapses into the sink.

Problem formulation

We consider an inviscid, incompressible fluid layer of infinite width and constant depth h^* . The motion is two-dimensional and starts from rest with uniform zero wave elevation. According to Kelvin's theorem the motion is irrotational. A steady source (sink) is turned on impulsively at time $t^* = 0$. It has volume flux Q^* per length unit perpendicular to the plane of motion. The singularity is located at the bottom point $(x, y) = (0, -h^*)$. The relevant dimensionless parameter is the Froude number of the source:

$$F = Q^* / \sqrt{g^* h^{*3}} \quad (1)$$

As unit of dimensionless length we take h^* . Our primary units of dimensionless time and velocity are Q^*/h^* and h^{*2}/Q^* , respectively. This are relevant for the small-time behaviour of the nonlinear free-surface flow. For the large-time evolution, gravity plays an dominant role and we have to resort to the alternative gravitational units of dimensionless time and velocity: $\sqrt{h^*/g^*}$ and $\sqrt{g^*/h^*}$, respectively.

The velocity potential Φ satisfies Laplace's equation, with (fully nonlinear) boundary conditions on the free surface:

$$\frac{\partial \eta}{\partial t} + \nabla \Phi \cdot \nabla \eta = \frac{\partial \Phi}{\partial y} \quad \frac{\partial \Phi}{\partial t} + \frac{1}{2} |\nabla \Phi|^2 + \frac{1}{F^2} \eta = 0 \quad \text{on } y = \eta(x, t) \quad (2)$$

and a no-penetration condition at the bottom.

Analytical and numerical results

For small time t we can solve the nonlinear problem asymptotically by a small-time expansion:

$$(\Phi, \eta) = H(t)[(\Phi_0, 0) + t(\Phi_1, \eta_1) + t^2(\Phi_2, \eta_2) + \dots] \quad -\infty < t < \infty \quad (3)$$

where $H(t)$ is the Heaviside unit step function. To each order, Laplace's equation is valid in the undisturbed fluid domain:

$$\nabla^2 \Phi_n = 0 \quad -1 < y < 0 \quad (n = 0, 1, 2, \dots) \quad (4)$$

The boundary conditions are:

$$\Phi_0 = 0 \quad \Phi_1 = -\frac{1}{2} \eta_1^2 \quad \Phi_2 = -\eta_1(2\eta_2 + \frac{1}{2F^2}) \quad (5a)$$

$$\eta_1 = \frac{\partial \Phi_0}{\partial y} \quad \eta_2 = \frac{1}{2} \frac{\partial \Phi_1}{\partial y} \quad \eta_3 = \frac{1}{3} \frac{\partial \Phi_2}{\partial y} + \frac{1}{6} \eta_1^2 \frac{d^2 \eta_1}{dx^2} + \frac{1}{3} \eta_1 \left| \frac{d\eta_1}{dx} \right|^2 \quad (5b)$$

on the free surface, while on the bottom holds:

$$\frac{\partial \Phi_0}{\partial y} = \delta(x) \quad y = -1, \quad t > 0 \quad (6)$$

only for the zeroth order potential. Upon introducing an (inessential) spatial artificial periodicity (with fundamental wavenumber k) and after some manipulations, the first-order elevation reads:

$$\eta_1 = \frac{1}{2} \operatorname{sech} \pi \frac{x}{2} \simeq \frac{2k}{\pi} \sum_{n \text{ odd}} \operatorname{sech} k_n \cos k_n x \quad (7)$$

where both the exact and the approximate solutions are given, and $k_n = nk$. The second- and third-order solutions can be obtained only in the form of multiple series expansions:

$$\eta_2 = -\frac{1}{2} \left(\frac{k}{\pi}\right)^2 \sum_{n \text{ odd}} \sum_{m \text{ odd}} \text{sech } k_n \text{sech } k_m [k_{n-m} \tanh k_{n-m} \cos(k_{n-m}x) + k_{n+m} \tanh k_{n+m} \cos(k_{n+m}x)] - \sigma \frac{1}{4} \text{sech} \left(\frac{\pi}{2}x\right) \quad (8)$$

and

$$\begin{aligned} \eta_3 = & \frac{1}{3} \left(\frac{k}{\pi}\right)^3 \sum_{n \text{ odd}} \sum_{m \text{ odd}} \sum_{q \text{ odd}} \text{sech } k_n \text{sech } k_m \text{sech } k_q \times \\ & \{ k_{n-m} \tanh k_{n-m} [k_{n-m-q} \tanh k_{n-m-q} \cos(k_{n-m-q}x) + k_{n-m+q} \tanh k_{n-m+q} \cos(k_{n-m+q}x)] \\ & + k_{n+m} \tanh k_{n+m} [k_{n+m-q} \tanh k_{n+m-q} \cos(k_{n+m-q}x) + k_{n+m+q} \tanh k_{n+m+q} \cos(k_{n+m+q}x)] \} \\ & + \frac{2}{3} \sigma \left(\frac{k}{\pi}\right)^2 \sum_{n \text{ odd}} \sum_{m \text{ odd}} \text{sech } k_n \text{sech } k_m [k_{n-m} \tanh k_{n-m} \cos(k_{n-m}x) + k_{n+m} \tanh k_{n+m} \cos(k_{n+m}x)] \\ & - \frac{1}{3F^2} \frac{k}{\pi} \sum_{n \text{ odd}} k_n \text{sech } k_n \tanh k_n \cos k_n x + \frac{\pi^2}{384} \text{sech}^5 \left(\frac{\pi}{2}x\right) [3 \cosh(\pi x) - 5] + \frac{\sigma^2}{12} \text{sech} \left(\frac{\pi}{2}x\right) \end{aligned} \quad (9)$$

respectively. The solution for a sink at the bottom can be obtained simply by changing the sign of η_1 and η_3 .

Figure 1 shows the comparison between the small time expansion and the numerical solution of the exact problem obtained by a boundary integral equation method. Apparently, significant differences between the two solutions appear for $t > 1$. As it can be expected, for a source weak enough, the flow develops in the

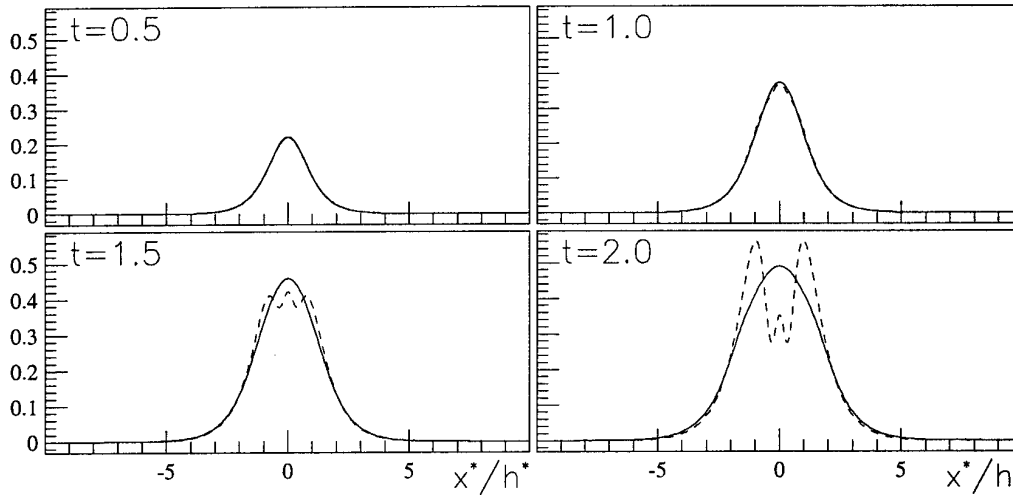


Figure 1: Comparison between the small time expansion solution (dashed lines) and the numerical computations (solid-lines) for $F = 1.0$. Non-dimensional time $t = t^* Q^* / h^{*2}$.

form of an undular bore (cfr. fig. 2) which cannot be followed by the present small time expansion solution. Therefore, for larger time we find alternative analytical solutions. To the purpose, we switch from the units of dimensionless time and velocity above introduced to the gravitational units. By integrating up in time the asymptotic solution given in [2], we get an asymptotic solution for the (linearized) surface elevation

$$\eta = \frac{1}{2} F \int_0^t (2/(t-\tau))^{1/3} \text{Ai}[(2/(t-\tau))^{1/3}(|x| + \tau - t)] d\tau \quad (10)$$

in terms of the Airy function. In this equation we assume that the wave front has propagated many length units. The comparison between the asymptotic formula and the fully nonlinear solution is given in figure 2, where also the linear solution is plotted. Apparently, although the phenomenon is qualitatively well captured, the fully nonlinear bore-front is steeper and propagates faster. These differences are magnified by further increasing the source strength.

The undular bore leaves behind it an almost flat free surface with height $\eta_b = F/2$ according to a linear theory. As it can be seen in the same figure, the fully nonlinear numerical solution predicts a smaller η_b . We now give an analytical estimate of the free surface height η_b past the bore. The analysis follows from a simple mass conservation argument, where we apply the amplitude dispersion $c = 1 + 3\eta_b/2$ given by the

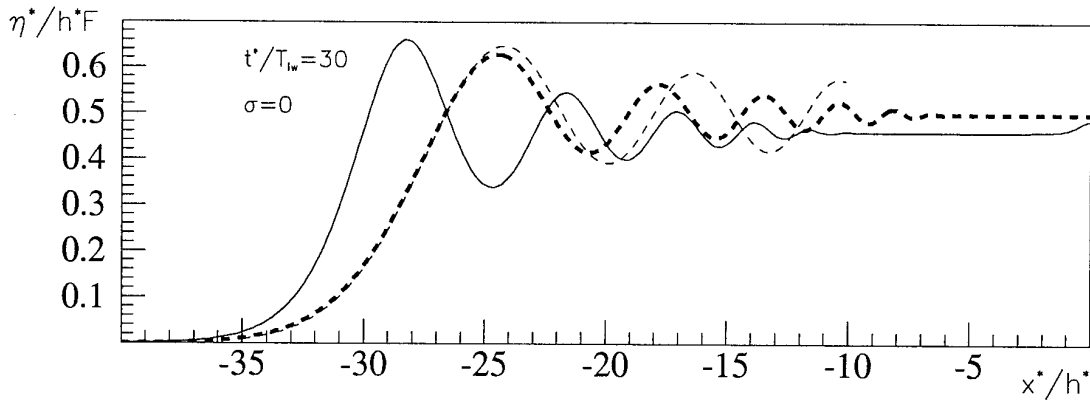


Figure 2: Undular bore due to a steady sink ($F = 0.25$). Bore-fronts as predicted by the asymptotic formula (10) (thin dashed line), linear (thick dashed line) and fully nonlinear computations (solid line).

Korteweg-deVries equation. We consider a trapezoid model where the midpoint of the bore front has half the amplitude dispersion of the bulk of the bore. This gives the analytical formula

$$\eta_b = \frac{2}{3} \left(\sqrt{1 + \frac{3}{2}F} - 1 \right) \quad (11)$$

for the surface elevation in the bulk of the bore, which is in a remarkable good agreement with our numerical computations (for non-breaking cases):

	$F = 0.5$	$F = 0.25$	$F = 0.125$	$F = 0.0625$
η_b from eq. (11)	0.4305	0.4603	0.4785	0.4888
η_b from num. sim.	0.4318	0.4608	0.4786	0.4888

In numerical computations, increasing the source strength, the front of the bore-front steepens and eventually a breaker develops. In particular, for larger F the breaking event appears sooner and a larger plunger is featured (cfr. fig. 3). Our results rely on a fully nonlinear model and improve the earlier shallow-water computations in [3]. A further step could be coupling with the steady breaker solution in [4].

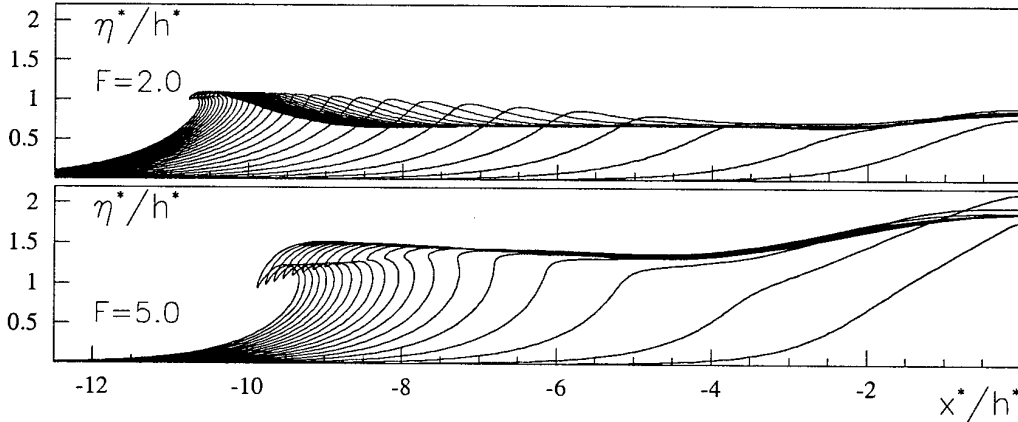


Figure 3: Evolution toward breaking of the bore due to a source, $F = 2$ and 5.

The asymptotic formula (10) equally applies to the case of a submerged sink. Unlike the previous case, nonlinearities delay the propagation of the front which, now, leaves behind it a depression (see fig. 4). As it can be expected, the stronger the sink is, the deeper the depression will be. More peculiar, the free surface is now characterized by a number of high frequency oscillations.

For a stronger suction of the sink, the free surface collapses into the bottom singularity [5, 6, 7]. According to the small-time expansion, the critical Froude number for the early tendency towards dip instability is $F_c = 4/\pi$. For this value we have $\eta_3(0) = 0$ and the nonlinear suction into the sink is exactly balanced by the gravitational rebound to the leading order. Xue & Yue (1998), for the deep water axisymmetric case, evidenced that the dip formation is a strongly nonlinear phenomenon which cannot be decided by small-time asymptotics. Actually, we numerically found an intermediate range of $-F$ (cfr. fig. 5) for which a hump emerges from the nascent dip and gives rise to a couple of symmetric plunging breakers. For increasing $-F$,

the horizontal separation of the breaking waves decreases. For stronger suction, the hump reduces to narrow bulge of fluid and, eventually, to a jet emitted from the collapsing dip. Only for a stronger sink, the fluid collapses continuously toward the singularity.

We have studied nonlinear free-surface flows generated by an impulsive bottom source or sink. Compared with earlier work on submerged singularities in deep water, we observed a much stronger tendency towards wave breaking, due to the weaker dispersion of a wave packet propagating on finite depth. Details of the breaking vary with the Froude number of the source/sink. Wave breaking appears also for sinks somewhat too weak for dip instability: this terminates our computations and thereby disturbs our search for a clear dip instability criterion. For the bottom source, another challenge remains for future work: Is there a steady bore solution of the fully nonlinear free-surface problem?

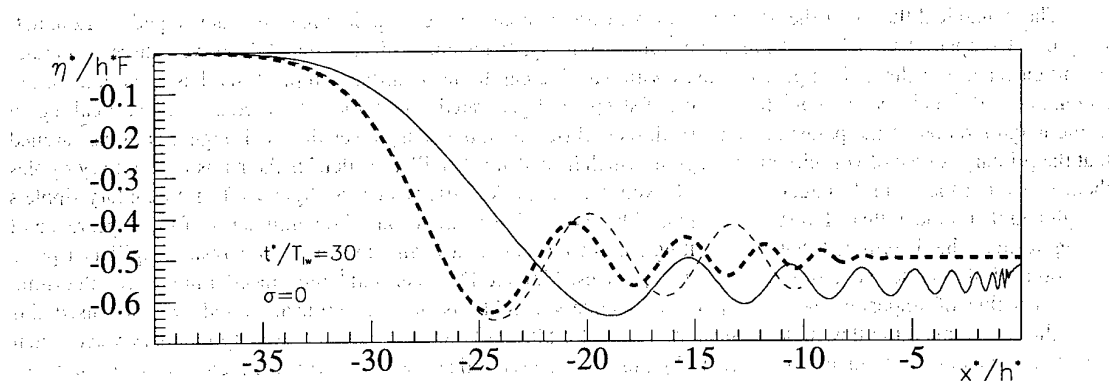


Figure 4: Free surface due to a constant sink ($F = -0.25$). Comparison of asymptotic prediction (thin dashed line), linear (thick dashed line) and nonlinear computations (solid line).

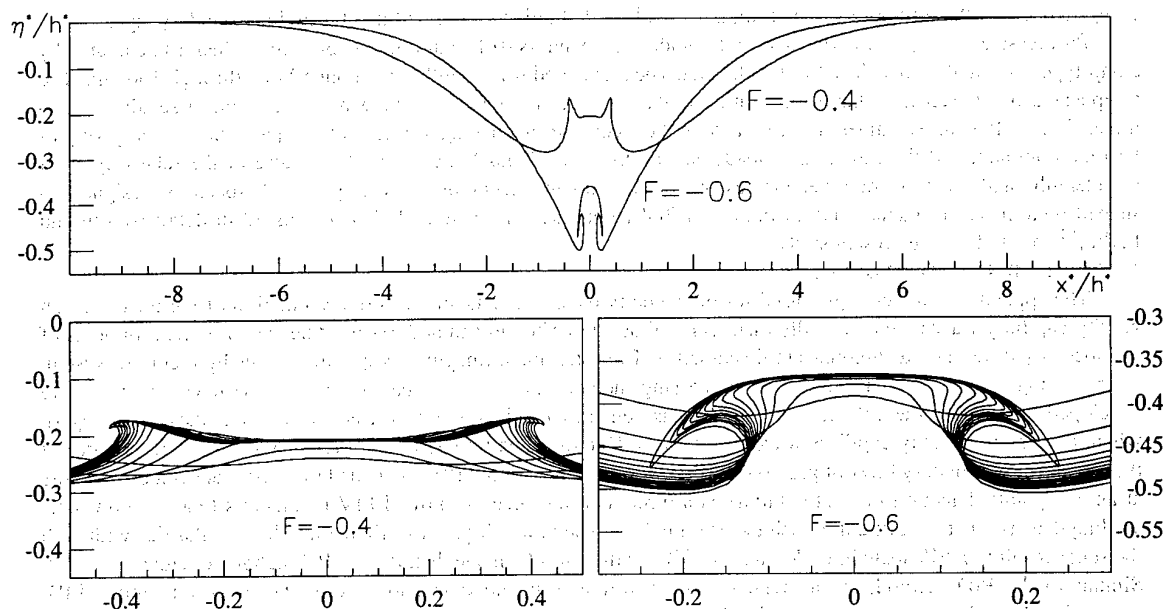


Figure 5: Free surface due to a constant sink. Top: free surface for $F = -0.4$ ($t = 4.42$) and $F = -0.6$ ($t = 2.88$). Bottom: enlarged view in natural scale of the free surface around the sink.

The research activity of M.L. is supported by the Italian *Ministero dei Trasporti e della Navigazione* through INSEAN Research Project 2000-2002.

1. Wehausen, J.V. & Laitone, E. V. 1960 *Handbuch der Physik*, ed. W. Flugge, vol. 9, pp. 446-778, Springer-Verlag.
2. Whitham, G.B. 1974 *Linear and Nonlinear Waves*. J. Wiley, New York.
3. Peregrine, D.H. 1966 Calculations of the development of an undular bore, *J. Fluid Mech.* 25, 321-330.
4. Cointe, R. & Tulin, M. P. 1994 A theory of steady breakers. *J. Fluid Mech.* 276.
5. Tyvand, P.A. 1992 Unsteady free-surface flow due to a line source. *Phys. Fluids A4*, 671-676.
6. Xue, M. & Yue, D.K.P. 1998 Nonlinear free-surface flow due to an impulsively-started submerged point sink. *J. Fluid Mech.* 364, 325-347.
7. Miloh, T. & Tyvand, P.A. 1993 Non-linear transient free-surface flow and dip formation due to a point sink. *Phys. Fluids A5*, 1368-1375.

THE VELOCITY AND VORTICITY FIELDS BENEATH GRAVITY-CAPILLARY WAVES EXHIBITING PARASITIC RIPPLES

H. J. Lin and Marc Perlin, *University of Michigan, Ann Arbor, MI 48109-2125, USA, perlin@umich.edu*

I. INTRODUCTION

The dynamical theory of the generation of parasitic capillary waves (ripples) has been developed by Longuet-Higgins,¹ Crapper,² Ruvinsky and Freidman,³ and Ruvinsky, Feldstein, and Freidman.⁴ However, there is another important feature of these short gravity waves with parasitic capillaries (capillary ripples) that has been pointed out by Okuda *et al.*,⁵ and Ebuchi *et al.*⁶ In the crest of steep wind-generated waves, they observed a strong vortical region in the neighborhood of the parasitic capillary ripples. Based on a boundary-layer theory, Longuet-Higgins⁷ argued that the primary source of vorticity in this region, which he called a "capillary roller," is the parasitic capillary ripples themselves, not the wind. Longuet-Higgins showed that the peak vorticity occurs slightly aft of a capillary ripple's trough and that a mean flux of vorticity is induced by the capillary waves. Based on arguments of the appearance of strong vortices, he determined that the resulting surface currents that form beneath steep parasitic capillary ripples can approach the phase speed of gravity-capillary waves. Mui and Dommermuth⁸ introduced a numerical algorithm that is capable of imposing more complicated boundary conditions on a curvilinear boundary. They used this algorithm to simulate the flow field/vortical structure of a 50 mm long, near-breaking gravity-capillary wave. Their calculation quantitatively matched Longuet-Higgins' model except that the strong vortical region in the crest of the underlying wave is absent in the numerical results. More recently, Lin and Rockwell⁹ observed the near-surface flow field beneath a stationary gravity-capillary wave train (with wavelengths of 100 to 200 mm) generated above a hydrofoil in a recirculating free-surface water channel. They used conventional digital PIV to estimate velocity; however, an accurate velocity/vorticity measurement of progressive waves with short wavelengths has never been completed due to the difficulties of investigating small-scale fluid structure within a fairly thin boundary layer.

Progressive gravity-capillary waves with moderate steepness (0.130 through 0.230) are studied, as generated by a flap-type wave maker in a closed water channel. The associated wavelengths are about 50 mm through 100 mm. The steepnesses are chosen such that the parasitic capillary ripples are present but the wave remains quasi-steady and two dimensional. (For larger values, the interactions between the underlying waves and the parasitic capillary ripples become dominant and the flow is not steady, see Perlin *et al.*¹⁰ and Jiang *et al.*¹¹). Because of the relatively short wavelengths and the moderate steepnesses, novel experimental techniques are required. A specially designed V-shaped-bottom water channel and an improved PIV technique, sub-pattern PIV, as discussed in detail by Lin and Perlin,¹² are used for the present study.

II. EXPERIMENTAL TECHNIQUES

The apparatus and techniques used for the velocity measurements and thus the calculation of vorticity beneath gravity-capillary waves are essentially identical to those described in Lin and Perlin;¹² hence, only the rudiments of the specially developed techniques are discussed. A Brewster angle imaging setup with a laser-light control system for recording images is used with a new processing method known as sub-pattern PIV. These new techniques are developed to improve the velocity flow-field measurement capability within a free-surface boundary layer region where progressive gravity-capillary waves are present. Due to the extremely thin but rather vortical characteristics of the free-surface boundary layer of gravity-capillary waves, conventional PIV methods fail to estimate velocity vectors at an acceptable detection rate. This failure is a direct consequence of optimal PIV parameters (e.g. window size, seeding density) that are difficult to achieve for this flow. The new sub-pattern PIV method has similarities with both the super-resolution PIV technique (Keane *et al.*¹³) and the particle image distortion (PID) technique (Huang *et al.*¹⁴). Similar to the PID method, an artificial image distortion is included in sub-pattern PIV; however, unlike PID, conventional PIV is not adopted for the first iteration as it yields invalid estimates for velocity gradients larger than an allowable value. To determine the required image distortion (that essentially removes the velocity gradient effects and thus facilitates use of conventional PIV techniques), appropriate sub-interrogation windows are used. The length/width of these sub-interrogation windows that gives the best results is 1/3 the length of the full-sized interrogation window. Three properly chosen sub-interrogation windows are required to give a first-approximation to the actual distortion between images. A procedure is used to locate the most-concentrated particle image sub-patterns. The three most-concentrated particle image sub-patterns are chosen as long as each represents independent data. By requiring that the sub-interrogation windows not exceed 1/2 overlap on each other, this is ensured. The technique is robust and shown to yield velocity fields of thin, previously immeasurable, vortical regions.

The second difficulty that arises in these measurements is due to the oscillating and deforming air-water interface—it is mirror-like (i.e. specular) and problematic—it causes very noisy data. The specular interface makes

surface detection in the images difficult. An experimental setup that utilizes the Brewster angle is adopted and the specular effects of the free-surface are reduced dramatically. It proved to be very effective.

The relatively small number of image pixels provided by the system is insufficient for extracting a dense array of velocity vectors; hence, special processing is necessary. Particle images acquired at several locations are analyzed using the PIV correlation method, and the estimated velocity fields are merged (with an overlap of 1/3 the image width) to provide coverage over an entire wavelength. Thus, wave generation repeatability and precise re-location of the imaging system are imperative. The imaging system and laser optics are mounted on a carriage astride a positional horizontal precision rail. The repeatability is examined by replication of the wave elevation profile measurements (Perlin *et al.*¹⁰). The results show that the deviations in the wave profiles are less than the pixel-resolution of the PIV system, as long as all the equipment (wave maker, laser light chopping mechanism, imaging system, etc.) is driven by the same set of electronic signals. Thus, the data-merging technique is shown to be accurate and effective.

A second recording/processing technique with double exposures of photographic film obtains high-resolution, high-accuracy PIV data. A different setup is used. The optical sensor plane of the digital imaging system is replaced by a 4 by 5 inch Kodak T-Max 400 film, and the laser beam is deflected by an acousto-optic modulator (AOM). The AOM acts as an on-off switch for the continuous Argon-Ion laser. The illumination duration is less than 500 μ sec (for each exposure) and the time interval between laser pulses and hence exposures is 4 msec. The digital imager trigger signal controls the AOM. A scanning mirror with feedback is added to the imaging optics, and the oscillation of the mirror is synchronized by the wavemaker driving signal with eight times the primary frequency. The amplitude is adjusted according to the feedback signal to provide a sufficient bias velocity for double-exposure PIV (Adrian¹⁵). This technique proved less effective in surface detection for one primary reason. The upper-most particle images for each single exposure are assumed to represent the water surface. Since the wave's forward (backward) face at the first (second) exposure is overlapped with the near surface region at the second (first) exposure, a sufficiently accurate wave profile is difficult to obtain. Therefore, the data acquired by this (double-exposure photographic film) method are used only to compare to the data recorded by the digital imaging system in the upper region close to the surface. It also provides the lower region data where the digital imaging system results are absent.

III. THE EXPERIMENTS

Three sets of experiments are conducted with different wavemaker frequencies: 4.21 Hz, 5.26 Hz, and 6.70 Hz; the associated wavelengths are approximately 100 mm, 70 mm, and 50 mm, respectively. Each set includes three forcing amplitudes. The wave maker is driven by a sinusoidal signal, and its motion is examined for repeatability. The displacement of the wavemaker matches the primary frequency input signal, while other (harmonic) frequency components show an amplitude less than 0.5% of the primary frequency component. Hence, the wave maker motion is essentially sinusoidal. The capillary ripples or other high-frequency components are present in the wave form due to resonance. They are not due to the presence of higher harmonics in the drive signal. The waves investigated are of moderate steepness ($ka = 0.130$ through 0.225) to maintain two-dimensionality and avoid modulation. The profiles show (almost) phase-locked underlying (primary) waves and ripples. The amplitudes of the primary waves and capillary ripples decrease monotonically in space due to viscous damping; however, their decrease is relatively slow compared to the time scale of the PIV image recording. Hence, the waves are quasi-steady in this steepness range.

Only the 5.26 Hz experiments are presented. These experiments are conducted with three different steepnesses: $ka = 0.225$, 0.200 , and 0.170 with wavelengths 70.0 mm, 67.0 mm, and 64.1 mm, respectively. The vorticity distribution is presented in Fig. 1. Waves of this frequency show seven parasitic capillary ripples along the forward surface of the underlying gravity waves. The $ka = 0.225$ waves shown in Fig. 1 (c) exhibit vorticity greater than 30 rad/sec in three troughs on the forward face, on the second, third, and fourth troughs (as shown by arrows in the figure) from the primary crest. A much weaker clockwise vortex is present in the first trough. The first two of these strong clockwise vortices are accompanied by adjacent upstream counter-clockwise counterparts. For the two lower steepness waves ($ka = 0.200$ and 0.170), strong vortices are not found; here, only one location has vorticity stronger than 10 rad/sec and it is located in the first trough of the steeper wave. Since there is less accuracy in the *wave-form* detection using PIV images, the profiles shown do not exhibit the finer details of those acquired by the vertically magnified images in Jiang *et al.*¹¹ hence, Fig. 2 is included. This figure presents vertically exaggerated surface-elevation profiles for 5.26 Hz waves with about the same steepnesses as those presented in Fig. 1. Evidently, the parasitic capillary waves decayed rapidly as they travelled downstream. About 14 capillaries are seen in the uppermost profile including seven on the rear-facing side of the primary wave. As viscous damping removes energy from the wave train, the number and steepness of the parasitic waves decreases. In the second profile, about 10 parasitic waves are visible, while in the middle profile this number is reduced to about seven. In the farthest downstream profile, the capillaries are barely visible.

IV. DISCUSSION AND CONCLUDING REMARKS

For the 5.26 Hz waves, the wavelength is approximately 70 mm, and the wave profile clearly shows that

capillary ripple amplitudes decay spatially along the forward face of the underlying waves. For the $ka = 0.225$ waves, strong clockwise vortices appear at least in the second, third, and fourth troughs, while the accompanying counter-clockwise vortices in the crests of the capillary ripples are much weaker or absent in one case. Quantitative comparison of the magnitude is difficult since the experimental wave steepness of the capillary ripples cannot be measured accurately. And unlike the numerical simulation or theoretical prediction, the exact vorticity on the surface is unavailable (unless inadvisable extrapolation is used).

In the vorticity fields presented, and the numerical results by Mui and Dommermuth, the "capillary roller" predicted by the theory does not exist. However, similar phenomena are seen in certain experimental situations. The vorticity data presented here have moderate ka values. For higher energy waves (larger wavemaker stroke), the wave profiles become very unsteady, and an entire wavelength vorticity measurement cannot be made with the present equipment. However, by tracking particles captured in the crest area, with $ka = 0.250$ or higher, a jet-like flow immediately in front of the primary crests is found. That is, a small group of waterborne particles seems to travel at about the phase speed, much faster than the particles immediately beneath them. When such a flow is present, the wave profile is neither steady nor stable in any sense, and a turbulent flow field is observed in this area. Also, the wave profile has a decay rate faster than the well-known rate, $\partial a / \partial t = -2\nu k^2 a$.

For the first time, the velocity and vorticity fields beneath progressive gravity-capillary waves with parasitic ripples present are reported. Two new experimental techniques especially developed to facilitate these measurements are discussed briefly. The theoretical prediction, numerical simulation, and experimental investigation all show strong vortices at the capillary troughs. However, the capillary roller in the primary crest is not realized by the numerical simulation, and the experimental observation has difficulty generating temporally periodic waves with the required steepness. On the other hand, a capillary roller is observed qualitatively and reported by several researchers, especially for wind waves, but a careful flow field study (analytically or experimentally) is not available. In general, the vorticity magnitudes in the troughs of the parasitic capillaries are greater than those in the crests, in agreement with theory and numerical prediction. According to our laboratory observation with a mechanically generated wave train, the (spatial) amplitude decay seems to play an important role in the occurrence of capillary rollers. The decay rate is faster than the theoretical prediction presumably due to the unavoidable turbulence that occurs. Such a flow situation requires an experimental technique that can handle unsteady, very fine-scale eddies (turbulence) in a very thin near-surface region. The present effort demonstrates an effective approach utilizing the Brewster angle and the sub-pattern PIV technique.

ACKNOWLEDGMENTS

This research was supported by the Office of Naval Research under the University Research Initiative Ocean Surface Processes and Remote Sensing at the University of Michigan, Contract No. N00014-92-J-1650.

¹M.S. Longuet-Higgins, "The generation of capillary waves by steep gravity waves," *J. Fluid Mech.*, **16**, 238-259 (1963).

²G.D. Crapper, "Non-linear capillary waves generated by steep gravity waves," *J. Fluid Mech.*, **40**, 149-159 (1970).

³K.D. Ruvinsky and G.I. Freidman, "On the generation of capillary-gravity waves by steep gravity waves," *Izv. Atmos. Ocean. Phys.*, **17**, 548-553 (1981).

⁴K.D. Ruvinsky, F.I. Feldstein, and G.I. Freidman, "Numerical simulations of the quasi-stationary stage of ripple excitation by steep gravity-capillary waves," *J. Fluid Mech.*, **230**, 339-353 (1991).

⁵K. Okuda, S. Kawai, and Y. Toba, "Measurement of skin friction distribution along the surface of wind waves," *J. Ocean. Soc. Japan*, **33**, 190-198 (1977).

⁶N. Ebuchi, H. Kawamura, and Y. Toba, "Fine structure of laboratory wind-wave surfaces studied using an optical method," *Boundary-Layer Met.*, **39**, 133-151 (1987).

⁷M.S. Longuet-Higgins, "Capillary rollers and bores," *J. Fluid Mech.*, **240**, 659-679 (1992).

⁸R.C.Y. Mui and D.G. Dommermuth, "The vortical structure of parasitic capillary waves," *J. Fluid Engr.*, **117**, 355-361 (1995).

⁹J.C. Lin and D. Rockwell, "Evolution of a Quasi-steady breaking wave," *J. Fluid Mech.*, **302**, 29-44 (1995).

¹⁰M. Perlin, H. Lin, and C.-L. Ting, "On parasitic capillary waves generated by steep gravity waves: an experimental investigation with spatial and temporal measurements," *J. Fluid Mech.*, **255**, 597-620 (1993).

¹¹L. Jiang, H.J. Lin, W.W. Schultz, and M. Perlin, "Unsteady ripple generation on steep gravity-capillary waves," *J. Fluid Mech.*, **386**, 281-304 (1999).

¹²H.J. Lin and M. Perlin, "Improved methods for thin, boundary layer investigations," *Exp. Fluids*, **25**, 431-444 (1998).

¹³R.D. Keane, R.J. Adrian, and Y. Zhang, "Super-resolution particle imaging velocimetry," *Meas. Sci. Tech.*, **6**, 754-768 (1995).

¹⁴H.T. Huang, H.E. Fiedler, and J.J. Wang, "Limitation and improvement of PIV. Part II: Particle image distortion, a novel technique," *Exp. Fluids*, **15**, 263-273 (1993).

¹⁵R.J. Adrian, "Particle-imaging techniques for experimental fluid mechanics," *Ann. Rev. Fluid Mech.*, **23**, 261-304 (1991).

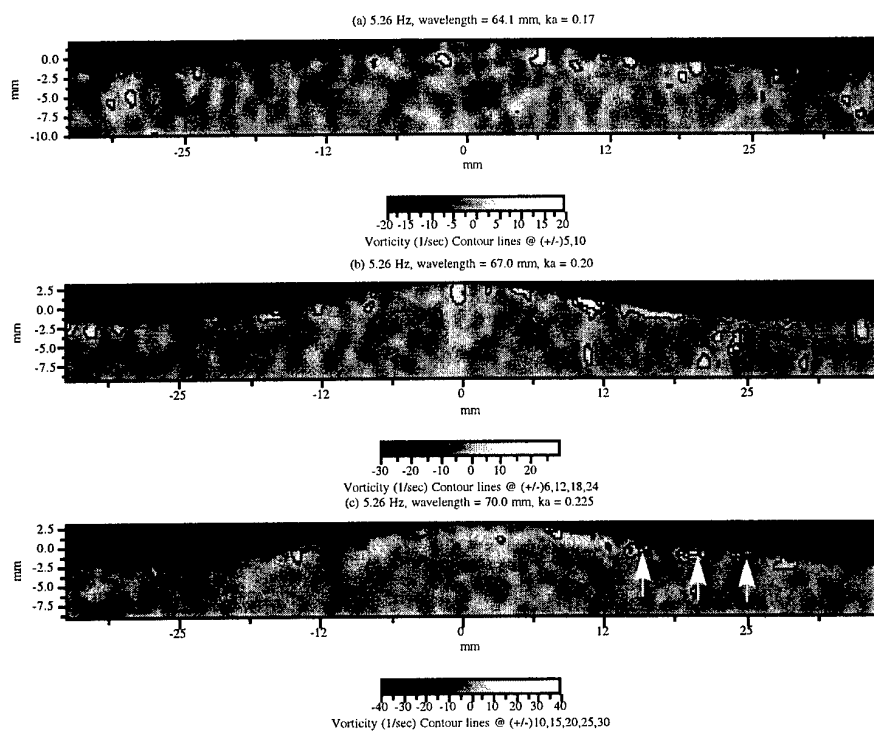


Fig. 1. Vorticity distributions beneath 5.26 Hz gravity-capillary waves with steepnesses, ka , (a) 0.17, (b) 0.20, and (c) 0.225. Axes are in mm. The arrows in the lower figure locate the second, third, and fourth capillary troughs discussed in the text.



Fig. 2. Surface elevation profiles of 5.26 Hz waves measured, in 30 mm intervals, 180 mm (uppermost profile) through 300 mm (lowermost profile) downstream of the wave maker. The wave steepnesses are 0.21 through 0.17, approximately the same range of steepnesses as the waves/vorticity fields shown in Fig. 1. A cylindrical lens system is used to generate the vertical exaggeration of about 5.8 in these images.

AN ALTERNATIVE METHOD FOR LINEAR HYDRODYNAMICS OF AIR CUSHION SUPPORTED FLOATING BODIES

Malenica Š. & Zalar M.

BUREAU VERITAS - DTA, 17bis Place des Reflets, 92400 Courbevoie, France

Introduction

The presence of the air cushions under the floating body can significantly change the overall dynamic behaviour of the body [1]. The idealisation of the problem as a rigid body case is not correct and the effects of the air cushions should be taken into account properly. This is the purpose of the present note. We consider first the hydrodynamic part of the problem which will be solved under the usual assumptions of the linear potential theory. The construction of the boundary value problem for the potential Φ is very similar to the classical problem of the rigid body, except for the condition on the part of the water surface under the air cushion. So we first concentrate on the detailed derivation of this boundary condition.

Boundary condition on the free surface under the air-cushion

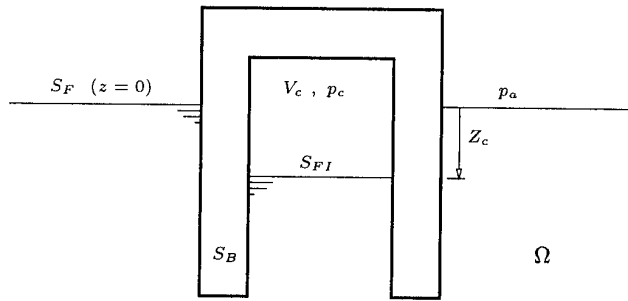


Figure 1: Basic configuration

This boundary condition is derived in the similar way as for the "real" free surface. It is a combination of the following dynamic and kinematic conditions:

$$p_c = -\rho g(Z_c + \Xi) - \frac{\partial \Phi}{\partial t}, \quad \frac{\partial \Xi}{\partial t} = \frac{\partial \Phi}{\partial z} \quad (1)$$

where p_c is the pressure in the air cushion, Z_c is the mean position of the free surface under the air cushion and Ξ is its elevation relative to Z_c .

By taking the time derivative of the first expression in (1) we combine two conditions in one:

$$\frac{\partial^2 \Phi}{\partial t^2} + g \frac{\partial \Phi}{\partial z} + \frac{1}{\rho} \frac{\partial p_c}{\partial t} = 0 \quad (2)$$

By assuming the adiabatic variation of the pressure inside the air cushion [1] we can write:

$$\frac{\Delta p}{p_{cs}} = -\kappa \frac{\Delta V}{V_{cs}} \quad (3)$$

where p_{cs} is the static pressure in the air cushion $p_{cs} = -\rho g Z_c + p_a$ (p_a being the atmospheric pressure), Δp is the variation of the pressure inside the air cushion $\Delta p = p_c - p_{cs}$, V_{cs} is the mean volume of the air cushion, ΔV is the volume change and κ is the adiabatic constant ($\kappa = 1.4$ for the air).

Now we can rewrite the equation (2) in the following form:

$$\frac{\partial^2 \Phi}{\partial t^2} + g \frac{\partial \Phi}{\partial z} - \frac{\kappa p_{cs}}{\rho V_{cs}} \frac{\partial \Delta V}{\partial t} = 0 \quad (4)$$

Furthermore it is possible to relate the volume change ΔV to the body motions and the surface elevation:

$$\Delta V = \iint_{S_{FI}} w dS \quad (5)$$

where w is the relative free surface elevation:

$$w = \zeta_v - \Xi \quad (6)$$

with ζ_v denoting the vertical displacement of the points fixed to the body and positioned on S_{FI} for $t = 0$.

The interior free surface condition becomes finally:

$$\frac{\partial^2 \Phi}{\partial t^2} + g \frac{\partial \Phi}{\partial z} - \frac{\kappa p_{cs}}{\rho V_{cs}} \iint_{S_{FI}} \frac{\partial w}{\partial t} dS = 0 \quad (7)$$

The frequency domain equivalent of this equation is:

$$-\nu \varphi + \frac{\partial \varphi}{\partial z} - \alpha \iint_{S_{FI}} w dS = 0 \quad (8)$$

where $\nu = \omega^2/g$ and:

$$\alpha = -\frac{i\omega\kappa p_{cs}}{\rho g V_{cs}} \quad (9)$$

Potential decomposition and solution methodology

As in the rigid body dynamics we assume now the following decomposition for the unknown potential φ :

$$\varphi = \varphi_I + \varphi_D - i\omega \sum_{j=1}^6 \xi_j \varphi_{Rj} \quad (10)$$

It is easy to deduce the boundary conditions on the interior free surface and on the body for each of these potentials:

Diffraction

$$\left\{ -\nu \varphi_D + \frac{\partial \varphi_D}{\partial z} = \alpha \iint_{S_{FI}} w_D dS + \nu \varphi_I - \frac{\partial \varphi_I}{\partial z} \right\}_{S_{FI}} \quad (11)$$

$$\left\{ \frac{\partial \varphi_D}{\partial n} = -\frac{\partial \varphi_I}{\partial n} \right\}_{S_B} \quad (12)$$

Radiation

$$\left\{ -\nu \varphi_{Rj} + \frac{\partial \varphi_{Rj}}{\partial z} = \alpha \iint_{S_{FI}} w_{Rj} dS \right\}_{S_{FI}} \quad (13)$$

$$\left\{ \frac{\partial \varphi_{Rj}}{\partial n} = n_j \right\}_{S_B} \quad (14)$$

The boundary value problems are completed by the usual free surface condition on the exterior free surface and the Sommerfeld radiation condition at infinity.

As we can see all BVP-s looks similar. The main difficulty lies in the fact that the relative wave elevation w is not known in advance but depends on the solution of the BVP itself. For the sake of clarity let us

now consider the generic boundary value problem of the form:

$$\left. \begin{aligned} \Delta\psi &= 0 & \text{in } \Omega \\ -\nu\psi + \frac{\partial\psi}{\partial z} &= 0 & \text{on } S_F \\ -\nu\psi + \frac{\partial\psi}{\partial z} &= \alpha \iint_{S_{FI}} w dS + C & \text{on } S_{FI} \\ \frac{\partial\psi}{\partial n} &= v & \text{on } S_B \\ \lim[\sqrt{\nu R}(\frac{\partial\psi}{\partial R} - i\nu\psi)] &= 0 & R \rightarrow \infty \end{aligned} \right\} \quad (15)$$

It is eventually possible (source method plus some "tricks") to solve this BVP directly but the most simple way is to develop w in a form of the series of known basis functions with unknown coefficients. We write:

$$w = \sum_{i=1}^{N_I} w_i f_i(x, y) \quad (16)$$

where f_i are the known basis functions and w_i are the unknown coefficients. The total potential ψ is now decomposed as follows:

$$\psi = \psi_0 + \alpha \sum_{i=1}^{N_I} w_i \psi_i \quad (17)$$

The boundary value problems for each of the potentials ψ_i , $i = 0, N_I$ become:

$$\left. \begin{aligned} \Delta\psi_0 &= 0 & \Delta\psi_i &= 0 & \text{in } \Omega \\ -\nu\psi_0 + \frac{\partial\psi_0}{\partial z} &= 0 & -\nu\psi_i + \frac{\partial\psi_i}{\partial z} &= 0 & \text{on } S_F \\ -\nu\psi_0 + \frac{\partial\psi_0}{\partial z} &= C & -\nu\psi_i + \frac{\partial\psi_i}{\partial z} &= \iint_{S_{FI}} f_i dS & \text{on } S_{FI} \\ \frac{\partial\psi_0}{\partial n} &= v & \frac{\partial\psi_i}{\partial n} &= 0 & \text{on } S_B \\ \lim[\sqrt{\nu R}(\frac{\partial\psi_0}{\partial R} - i\nu\psi_0)] &= 0 & \lim[\sqrt{\nu R}(\frac{\partial\psi_i}{\partial R} - i\nu\psi_i)] &= 0 & R \rightarrow \infty \end{aligned} \right\} \quad (18)$$

As we can see the above BVP-s belong to the family of the classical linear diffraction-radiation problems. The only difference is the condition on the interior free surface but this doesn't influence the methodology of numerical solution so that the well known boundary integral equation method can be used in its most simple form as in [2].

The last remark concerns the choice of the basis functions $f_i(x, y)$. In principle any complete set of basis functions can be used, but the most simple choice are the stepwise functions equal to 1 on one panel and 0 on the others, as used in [1]. The numerical solution becomes then quite straightforward, and the unknown coefficients w_i are found from:

$$w_i - \alpha \sum_{j=1}^{N_I} (\nu\psi_j^i + S_j) w_j = \nu\psi_0^i + C^i, \quad i = 1, N_I \quad (19)$$

where S_j is the surface of the j th panel, and superscript "i" means that the value at centroid of the i th panel should be taken.

Comments on the Pinkster's method

The present paper was mainly initiated by the work of Pinkster [1] who treated the same problem using the different methodology. This author use the following decomposition for the potential:

$$\varphi = -i\omega\{\varphi_I + \varphi_D + \sum_{j=1}^6 \xi_j \varphi_{Rj} + \sum_{c=1}^C \xi_c \varphi_c\} \quad (20)$$

where ξ_c and φ_c are roughly equivalent to w_i and ψ_i in the present notations (both for the diffraction and radiation). From [1] it can be shown that on the surface S_{FI} the potential φ satisfies the following condition:

$$\frac{\partial \varphi}{\partial z} = \alpha \iint_{S_{FI}} w dS \quad (21)$$

which represents only the kinematic condition and is different from (8).

In fact it seems that the method used in [1] treats the problem as a multibody interaction problem where the panels on S_{FI} are allowed to perform only the rigid body vertical motions. In this way, after satisfying the kinematic condition (21) on the interface, the dynamic condition is satisfied by solving the "motion equations" for the multibody system composed of the rigid body and the massless panels on the interface (Eqn. (10) or (19) in [1]). Thus, at the end, the total potential satisfy the same condition on the interface, so that the two methods are equivalent.

Numerical results

We show now some preliminary results for two limiting cases $\alpha = 0$ and $\alpha = \infty$. The body is the rectangular box with the length of $150m$, width of $20m$, draft of $10m$ and the "wall thickness" of $4m$. On the figure 2 the results for the heave added mass A_{33} and damping B_{33} coefficients are presented. We can appreciate the important differences between two classes of results, which means that, in the general case ($0 < \alpha < \infty$), the influence of the air cushion must be evaluated correctly in order to have an representative model of the body dynamics.

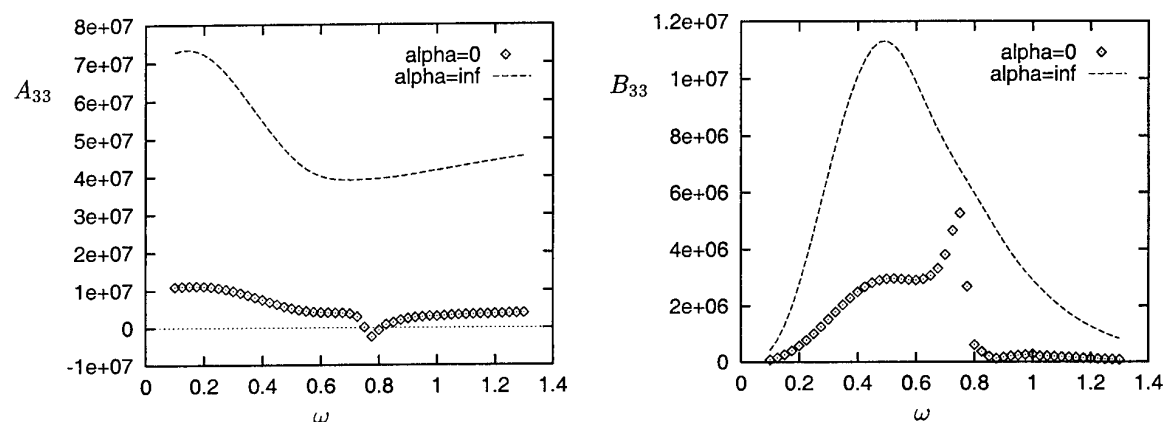


Figure 2: Heave added mass and damping coefficients for rectangular barge.

Conclusion

We presented here an alternative method for solving the linear hydrodynamic problem for air-cushion supported stationary vessels. In contrast to the original method presented in [1], this method seems to be more direct because the boundary value problems for the potentials include both kinematic and dynamic boundary conditions on the interior free surface. In this way the potential decomposition (10) becomes quite natural (as in the rigid body case) and the methodology for determining the body motions straightforward.

References

- [1] PINKSTER J.A., 1997. : "The effect of air cushions under floating offshore structures", BOSS'97, Delft, Netherlands.
- [2] CHEN X.B., MALENICA Š. & PETITJEAN F. 1995. : "Offshore hydrodynamics.", Bulletin Technique de Bureau Veritas. Vol.1, pp.47-66.

On the sloshing modes in moonpools, or the dispersion equation for progressive waves in a channel through the ice sheet

B. Molin, ESIM, 13451 Marseille cedex 20, France, molin@esim.imt-mrs.fr

Barges with large rectangular moonpools housing the upper ends of the risers are now being considered as floating production systems in mild areas like Western Africa. Typical dimensions are 180x60 m for the barge and 80x20 m for the moonpool (the 'well-bay'), the draft ranging from 5 up to 25 m.

An hydrodynamic problem encountered with this concept is how much water motion takes place in the moonpool, under wave induced pressures and barge motion.

At the previous workshop (Molin, 1999) consideration was given to the piston mode, when the bulk of water inside the moonpool heaves up and down nearly like a rigid body. Results were given for the natural frequency and associated shape of the free surface, under the simplifying assumption that the beam and length of the barge be much larger than the breadth and length of the moonpool.

In this sequel, with the same simplifying assumption, we analyze the sloshing modes that take place in the longitudinal direction. An eigen value problem is formulated and natural frequencies and modal shapes are obtained. A striking result is that the natural frequencies of the longest sloshing modes are much larger than could be expected, and that they are quite sensitive to the 'aspect ratio' b/l of the moonpool. Similar effects are obtained for progressive waves in a moonpool of infinite length, tantamount to a channel through the icepack.

The barge is assumed to be a rectangular box of length L , beam B and draft h . The moonpool is located at mid-deck, and is also rectangular with length l and width b . The waterdepth is taken to be infinite. Use is made of a cartesian coordinate system xyz , with its origin located at one of the lower corners of the moonpool. The z axis is upward, $z = 0$ is the bottom of the moonpool, $z = h$ the free surface.

The problem is tackled via potential flow theory. Be $\Phi(x, y, z, t)$ the velocity potential inside the moonpool. When the beam and length of the barge are assumed to be infinite, Φ obeys the boundary condition at $z = 0$

$$\Phi(x, y, 0, t) = \frac{1}{2\pi} \int_0^b \int_0^l \frac{\Phi_z(x', y', 0, t)}{\sqrt{(x-x')^2 + (y-y')^2}} dx' dy'. \quad (1)$$

Φ is sought for under the form

$$\begin{aligned} \Phi(x, y, z, t) &= \Re \{ \varphi(x, y, z) e^{-i\omega t} \} \\ \varphi &= \sum_{n=0}^N \sum_{q=0}^Q \cos \lambda_n x \cos \mu_q y (A_{nq} \cosh \nu_{nq} z + B_{nq} \sinh \nu_{nq} z) \end{aligned} \quad (2)$$

with $\lambda_n = n\pi/l$, $\mu_q = q\pi/b$, $\nu_{nq}^2 = \lambda_n^2 + \mu_q^2$

and, when $n = q = 0$, the hyperbolic functions are to be replaced with $A_{00} + B_{00} z/h$.

The Laplace equation and the no-flow condition at the vertical walls are fulfilled. Only the boundary conditions at $z = 0$ (equation 1) and $z = h$ ($g \varphi_z - \omega^2 \varphi = 0$) remain.

Inserting (2) in (1), multiplying both sides with $\cos \lambda_m x \cos \mu_p y$ and integrating in x and y gives

$$A_{mp} = \frac{2}{\pi b l (1 + \delta_{m0}) (1 + \delta_{p0})} \sum_{n=0}^{\infty} \sum_{q=0}^{\infty} \nu_{nq} I_{mnpq} B_{nq}, \quad (3)$$

where

$$I_{mnpq} = \int_0^l dx \int_0^l dx' \int_0^b dy \int_0^b dy' \frac{\cos \lambda_m x \cos \lambda_n x' \cos \mu_p y \cos \mu_q y'}{\sqrt{(x-x')^2 + (y-y')^2}}. \quad (4)$$

I_{mnpq} is non zero only when both $m+n$ and $p+q$ are even. For the longitudinal sloshing modes, (p, q) are even, and all (m, n) are either odd or even. Advantage is taken of this to reduce the size of the eigen value problem, which is obtained by combining (3) with the free surface equation and eliminating one set of the A_{nq} or B_{nq} coefficients, like in the 2D case (Molin, 1999).

Figure 1 shows a plot of the free surface obtained for the first mode, for a 80x20x5 m moonpool. The maximum elevation is not obtained at the end walls, but at about 10 m. The associated period is 7.36 s, which for a progressive wave in an unbounded ocean corresponds to a wavelength of 84.5 m, quite far off twice the length of the moonpool (160 m)!

For these calculations the double series was truncated at $n = 25$ and $q = 10$. It was found that, when only one term is retained, $n = 1$ (or 2, 3, etc.), $q = 0$, the natural frequency is obtained with a good accuracy, even though the modal shape be not strictly sinusoidal. It is found to be given by

$$\omega_{n0}^2 = g \lambda_n \frac{1 + J_n \tanh \lambda_n h}{J_n + \tanh \lambda_n h} \quad (5)$$

where

$$J_n = \frac{n}{b l^2} \int_0^b dy \int_0^b dy' \int_0^l dx \int_0^l dx' \frac{\cos \lambda_n x \cos \lambda_n x'}{\sqrt{(x-x')^2 + (y-y')^2}} = \frac{n}{b l^2} I_{nn00}. \quad (6)$$

J_n can be expressed as

$$J_n = \frac{2}{n \pi^2 r} \left\{ \int_0^1 \frac{r^2}{u^2 \sqrt{u^2 + r^2}} \left[1 + (u-1) \cos(n \pi u) - \frac{\sin(n \pi u)}{n \pi} \right] du + \frac{1}{\sin \theta_0} - 1 \right\} \quad (7)$$

where $r = b/l$ and $\tan \theta_0 = r^{-1}$.

Figure 2 shows J_n , versus $\lambda_n b = n \pi b/l$, for $n = 1, 2, 10$. It appears that J_n is always less than 1. Hence one can introduce β_n such that

$$J_n = \tanh \beta_n \quad (8)$$

which leads to the dispersion equation

$$\omega_{n0}^2 = g \lambda_n \coth(\lambda_n h + \beta_n). \quad (9)$$

When $\lambda_n b$ goes to zero, so do J_n and β_n . Hence very large values of ω_{n0} can be obtained when both the draft h and the breadth b are small, as compared to the length l of the moonpool. In the case considered here equation (9) gives 7.41 s for the first natural period, to be compared with the exact value of 7.36 s.

At this stage one may conjecture that similar effects should be observed for progressive waves in an infinite length moonpool, that is a cut through a rigid ice sheet. In such case one starts from the expression, for the velocity potential inside the channel

$$\varphi(x, y, z) = e^{i k_0 x} \sum_{n=0}^{\infty} \cos \mu_n y (A_n \cosh \nu_n z + B_n \sinh \nu_n z) \quad (10)$$

where $\mu_n = n\pi/b$, $\nu_n^2 = k_0^2 + \mu_n^2$, and only even values of n are retained. The same boundary condition (1) applies at $z = 0$, giving

$$e^{ik_0 x} \sum_n \cos \mu_n y A_n = \frac{1}{2\pi} \int_{-\infty}^{\infty} dx' \int_0^b e^{ik_0 x'} \frac{\sum_n \nu_n \cos \mu_n y' B_n}{\sqrt{(x-x')^2 + (y-y')^2}} dy' \quad (11)$$

or, setting $x' = x + u$:

$$\sum_n \cos \mu_n y A_n = \frac{1}{2\pi} \int_{-\infty}^{\infty} du \int_0^b e^{ik_0 u} \frac{\sum_n \nu_n \cos \mu_n y' B_n}{\sqrt{u^2 + (y-y')^2}} dy'. \quad (12)$$

Again, multiplying both sides with $\cos \mu_m y$ and integrating in y gives

$$A_m = \frac{1}{\pi b (1 + \delta_{m0})} \sum_n \nu_n B_n I_{mn} \quad (13)$$

with

$$I_{mn} = \int_{-\infty}^{\infty} du \int_0^b dy \int_0^b dy' e^{ik_0 u} \frac{\cos \mu_m y \cos \mu_n y'}{\sqrt{u^2 + (y-y')^2}} \quad (14)$$

and, together with the free surface condition, an eigen value problem can be set to obtain the frequencies ω_n and associated free surface shapes. Most likely, like in the longitudinally restricted case, a good approximation of the frequency ω_0 of the inline mode can be obtained by retaining only the $n = 0$ terms, yielding

$$\omega_0^2 = g k_0 \frac{1 + J_0 \tanh k_0 h}{J_0 + \tanh k_0 h} \quad (15)$$

where

$$J_0(k_0 b) = \frac{k_0 b}{2\pi} \int_{-\infty}^{\infty} du \int_0^1 dy \int_0^1 dy' \frac{e^{ik_0 b u}}{\sqrt{u^2 + (y-y')^2}}. \quad (16)$$

$J_0(k_0 b)$ can be evaluated as

$$J_0(k_0 b) = 1 - \frac{2}{\pi k_0 b} \left(1 - \int_0^1 e^{-k_0 b (1-u^2)^{-1/2}} du \right). \quad (17)$$

It is also shown on figure 2. It is the limiting case of $J_n(\lambda_n b)$ when n goes to infinity, and the same type of dispersion equation applies:

$$\omega_0^2 = g k_0 \coth(k_0 h + \beta_0) \quad (18)$$

where $J_0(k_0 b) = \tanh(\beta_0)$. The differences between J_1 , J_2 , J_n and J_0 are due to end effects, which are most pronounced for the long modes.

Acknowledgments

This work was carried out within an industrial project called: 'Tank testing of the *WELLHEAD BARGE*_® for West African deepwaters applications'. This project is led by Bouygues Offshore associated with the following partners: Elf, ESIM, IFP, Ifremer, Principia and Sedco Forex.

Reference

MOLIN, B. 1999. On the piston mode in moonpools, Proc. 14th Int. Workshop on Water Waves & Floating Bodies, Port Huron, R.F. Beck & W.W. Schultz editors.

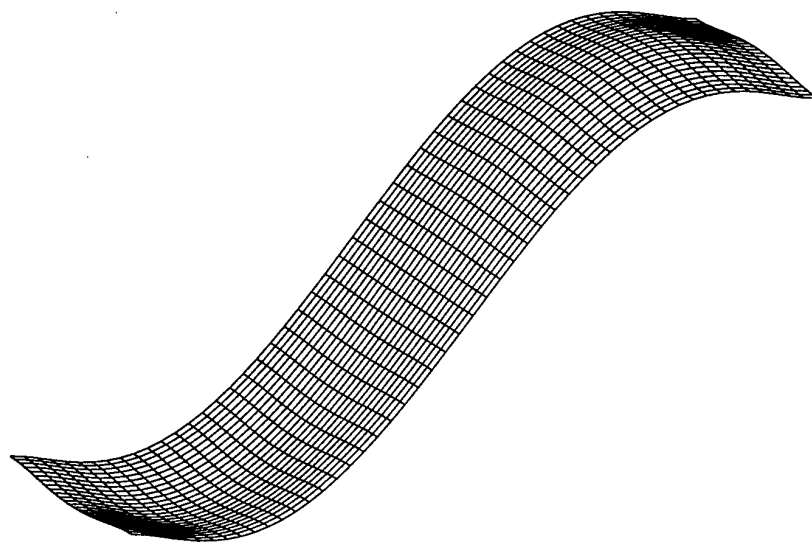


Figure 1: Free surface shape for the first sloshing mode. Moonpool dimensions: 80x20x5.

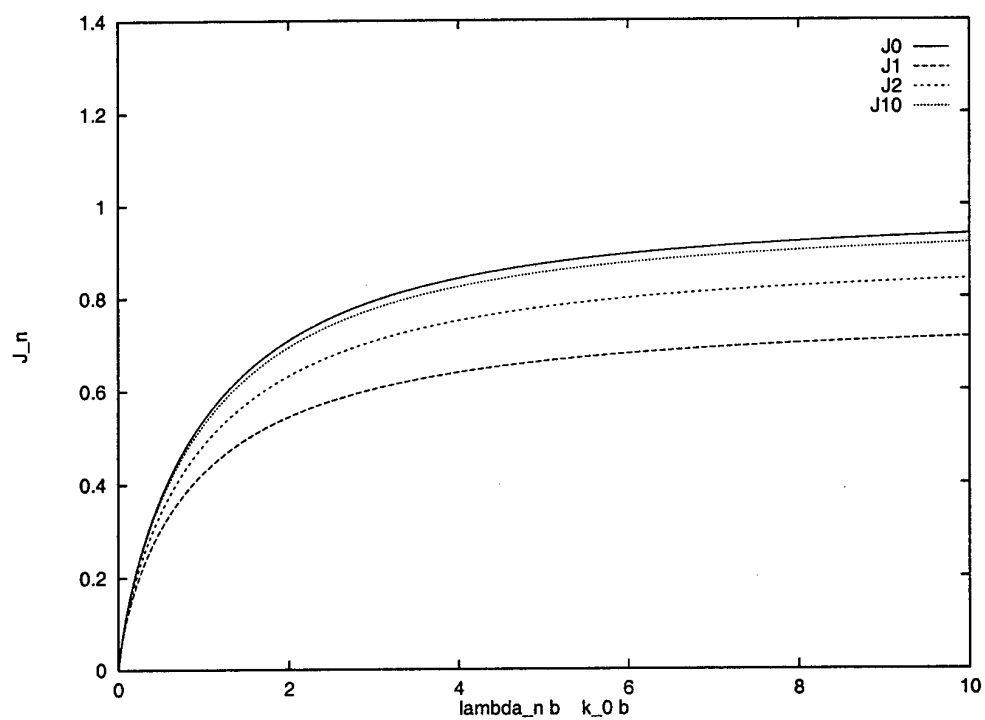


Figure 2: Functions J_1 , J_2 , J_{10} versus $\lambda_n b$ and J_0 versus $k_0 b$.

Wave Making Resistance of a Submerged Hydrofoil with Downward Force

Kazu-hiro Mori
Hiroshima University

Shigeki Nagaya
Ship Research Institute

Submerged hydrofoil with downward force

The wavemaking resistance of a submerged lifting body can be reduced by generation of downward force[1][2]. This phenomenon is interesting from the viewpoint not only from practical applications but from hydrodynamics. However, little has been studied so far. Fig.1 shows the comparison of the computed waves with and without downward force. The latter is computed without satisfying the Kutta condition. The waves with downward force is remarkably less.

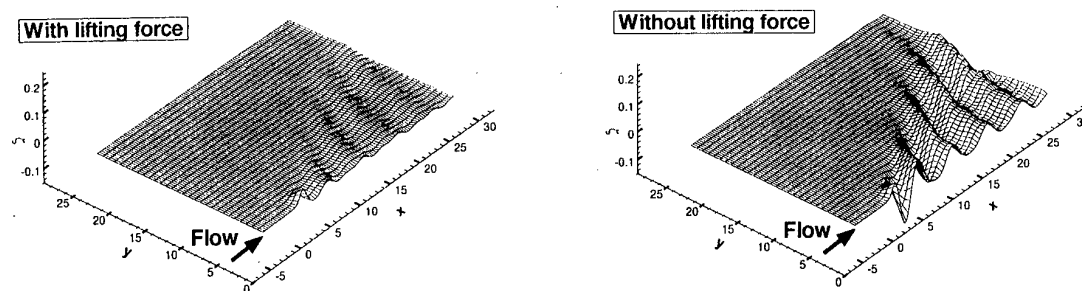


Fig.1 Comparison of wave patterns between with and without lifting force ($\alpha = -2^\circ$)

Results of numerical computations and measurements

For the numerical computation, the flow around a hydrofoil is assumed potential flow and a direct boundary element method is used where the fully nonlinear free-surface boundary conditions are imposed. The Kutta condition at the trailing edge is satisfied by introducing a wake sheet behind the hydrofoil on which the velocity potential has a jump.

Three dimensional rectangular hydrofoils with NACA sections are studied. The total drag coefficient C_T and the lifting force coefficient C_L are obtained by the integration of pressure over the foil while the wave pattern resistance coefficient C_{wp} is determined from the computed wave profiles by the wave pattern analysis. C_B is the buoyancy force coefficient. All the

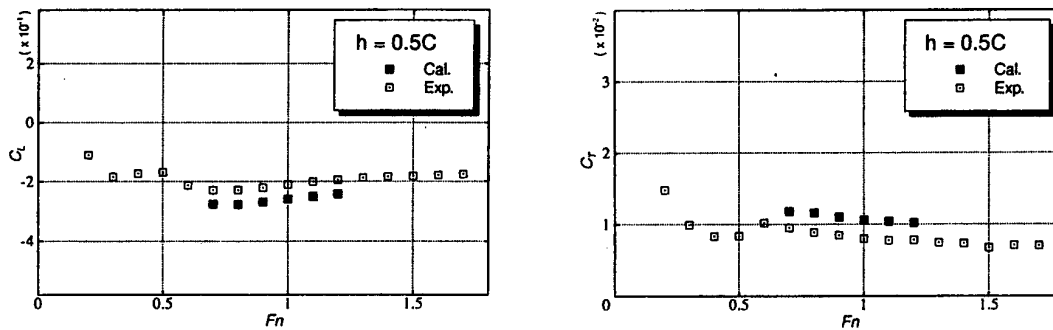


Fig.2 Comparison of drag and lifting force between calculated and experimental results (NACA4412, $Fn=1.0$)

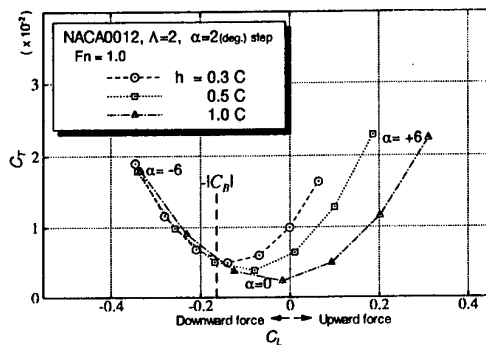


Fig.3 Total resistance at various submergence depth

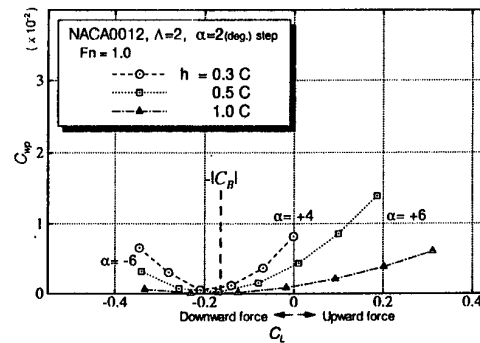


Fig.4 Wave resistance at various submergence depth

coefficients are normalized by $1/2 \rho U^2 S$, where ρ is the fluid density, U , the speed and S , the plane area of the hydrofoil given by a product of the chord length C and span width. Thus C_b depends on the speed although the force itself does not change.

An experiment is carried out to measure the forces acting on the foil. The drag of the flat plate with the same area and the supporting strut has been subtracted from the measured value; C_T gives the sum of the induced drag and wavemaking resistance.

Fig.2 shows the comparison of the computed values with the measured. The computed results agree rather well with those of measured although the lifting force is slightly less than the measured while the drag is larger.

Figs.3 and 4 show C_T and C_{wp} at three different submergence where h , α and λ are the submergence depth, the angle of attack and the aspect ratio of foil respectively. It is clearly demonstrated that the wave pattern resistance is minimum and almost zero where the downward force is equal to the buoyancy force. This finding is proved for the different Froude numbers and for the foils with different displacement volume as seen in Figs.5 and 6.

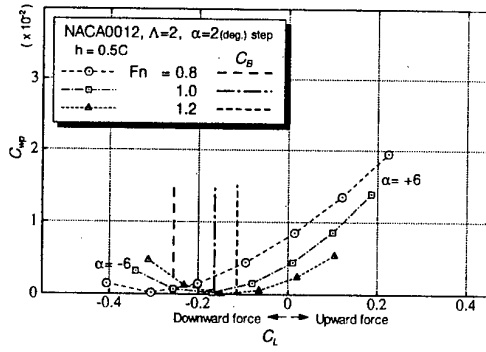


Fig.5 Total resistnace at various Froude number

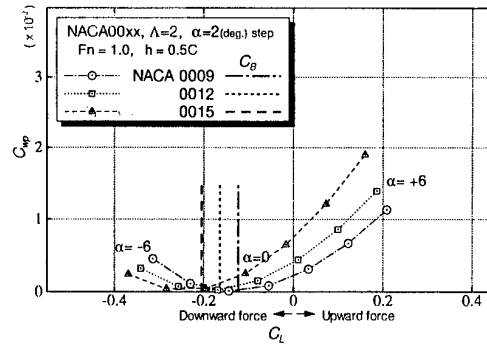


Fig.6 Wave resistance at various displacement volume

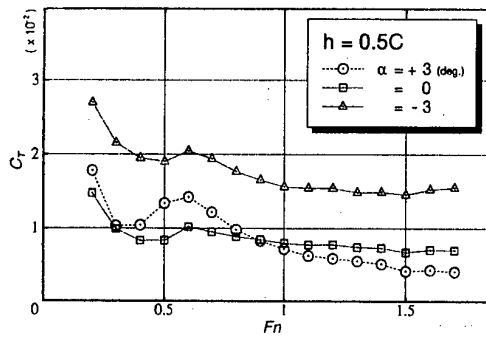


Fig.7 Measured total drag and lifting force (NACA4412)

Fig.7 shows the results of measurements. Because the total drag includes the induced drag, it is not clearly demonstrated, but the total drag is less when the lifting force is equal to the buoyancy force.

Shape in terms of wave-free singularity

Expecting to find a shape of a lifting body with zero-wavemaking resistance, studies have been carried out so far by an optimization method where the shape is iteratively changed to find out that with the minimum wavemaking resistance[3]. Here the shapes generated by a distribution of the wave-free singularity whose velocity potential is given by the combination of doublet and vortex as

$$\Phi(x, z) = Ux + Ua^2 \{ D(x, z+h) - D(x, z-h) - \kappa [V(x, z+h) - V(x, z-h)] \} \quad (1)$$

where

$$D(x, z \pm h) = \frac{x}{x^2 + (z \pm h)^2} \quad V(x, z \pm h) = \tan^{-1} \frac{z \pm h}{x}$$

and (x, z) are the coordinate system where x and z are the streamwise and vortical directions respectively and κ , the wave number given by g/U^2 . (1)

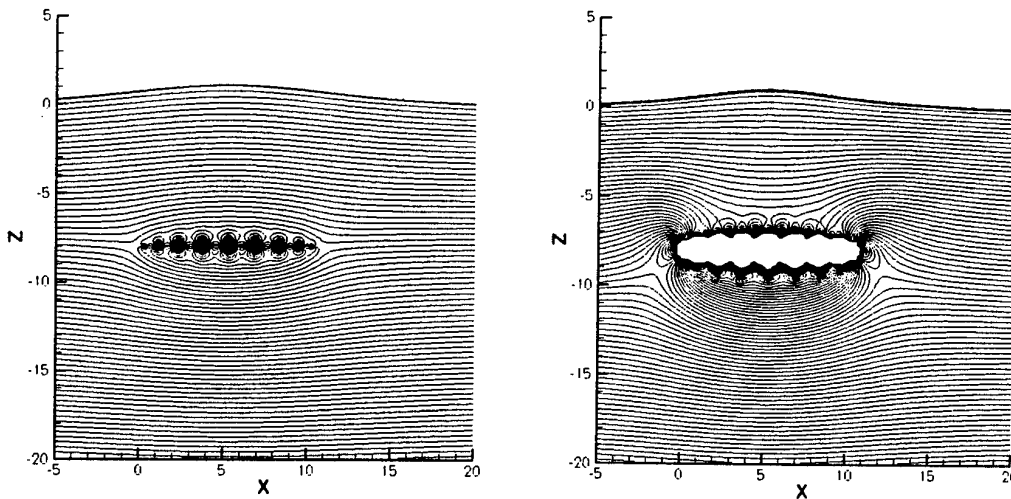


Fig.8 Streamlines (left) and pressure contours (right) of a line distribution of singularity

satisfies the linearised free surface condition.

The streamlines around a line distribution of the discrete singularities given by (1) and its pressure contours are shown in Fig.8 where the free-surface profile is drawn by a thick line. As expected, the pressure field is producing the downward force, but the shape is symmetry and no significant difference can be seen from that only by the dipole distribution. In other words, we cannot expect such a free-surface elevation by the generated shape unless a circulation is realized by any means which is equal to the total intensity of the second term of (1). A distribution along a cambered line with a sharp trailing edge satisfying the Kutta condition may provide the wave-free shape.

Concluding remarks

It is definitely made clear that zero wave making resistance can be realized when the downward force is equal to the buoyancy force. The shape of such lifting bodies can be generated in terms of wave-free singularities, although the relation between the circulation and the shape should be studied more.

References

- [1]Mori K., et al :A Study on Semi-Submersible High Speed Ship with Wings, Jour. of Soc. Naval. Arc. Japan, Vol. 164, (1988).
- [2]Tuck E.O. and Tulin M.P. :Submerged Bodies That Do Not Generate Waves, Proc. of 7th International Workshop on Water Waves and Floating Bodies, val de Reuil, France, (1992).
- [3]Nagaya S., Xu Q., Mori K. :On Resistance of a Submerged Lifting Body which Generates Downward Lifting Force, Jour. of Soc. Naval. Arc. Japan, Vol. 182, (1997).

DIFFRACTION OF WATER WAVES BY AN AIR CHAMBER

by J. N. Newman
MIT, Cambridge, MA 02139, USA

The wave-induced loads on a very large floating structure can be reduced by using an air cushion to provide part of the static support. This idea has been advanced by Pinkster *et al* (1997, 1998), with computations and experimental measurements of the motions in waves and the air-cushion pressure. They consider a long rectangular barge with side walls and ends enclosing the air cushion. Further computations have been performed by Lee & Newman (1999) using a more complete description of the acoustic disturbance, with particular attention to the resonant modes of the air cushion which are analogous to the ‘cobblestone effect’ suffered by air-cushion vehicles (Ulstein & Faltinsen, 1996).

Here we consider a simpler two-dimensional diffraction problem, which provides qualitative insight into the coupling between the acoustic and water waves. In the plane (x, y) , water occupies the semi-infinite domain $-\infty < x < \infty$, $-\infty < y < 0$. Air is enclosed within a chamber bounded by vertical walls at $x = \pm a$, a horizontal lid at $y = b$, and by the free surface $-a < x < a$, $y = 0$, as shown in Figure 1. The walls and lid are fixed. Plane waves of amplitude A , frequency ω and wavenumber $k = \omega^2/g$ are incident from $x = -\infty$. The motions of the water and air are assumed sufficiently small to justify a linearized analysis.

With the time-dependence represented by the factor $e^{i\omega t}$, the velocities of the air and water are equal to the gradients of the complex potentials $\Phi(x, y)$ and $\phi(x, y)$. (Upper/lower case symbols or the subscripts a/w are used where appropriate to distinguish the air/water domains, respectively.) The governing equations are the Helmholtz and Laplace equations

$$\nabla^2 \Phi + K^2 \Phi = 0, \quad \nabla^2 \phi = 0, \quad (1)$$

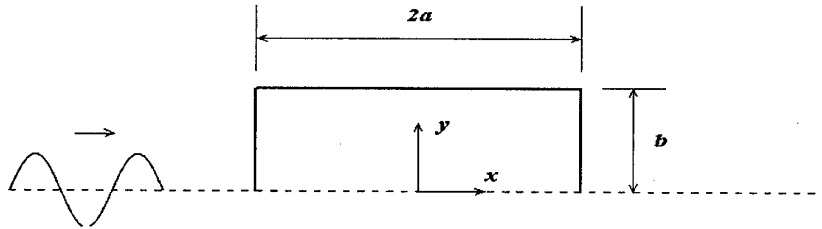


Figure 1: Sketch showing the air chamber and incident wave.

where $K = \omega/c$ is the acoustic wavenumber and c is the sound velocity. The corresponding pressures are given by the linearized Bernoulli equation:

$$P(x, y) = -i\rho_a\omega\Phi(x, y), \quad p(x, y) = -i\rho_w\omega\phi(x, y) - \rho_w gy, \quad (2)$$

where ρ is the density. The aerostatic pressure $-\rho_a gy$ is neglected on the assumption that $c \gg g/\omega$.

Zero normal velocity is prescribed on the ends and lid of the chamber. On the air-water interface the kinematic and dynamic conditions are combined in the usual manner to give the linear free-surface condition

$$\rho_w(\omega^2\phi - g\phi_y) = \rho_a\omega^2\Phi. \quad (3)$$

The boundary-value problem for ϕ is completed by imposing the conventional conditions, including the homogeneous form of (3) on the the exterior free surface, the requirement that ϕ vanishes as $y \rightarrow -\infty$, and an appropriate radiation condition in the far field.

The potential in the air chamber can be expanded in the form

$$\Phi = i\omega A \sum_{m=0}^{\infty} \xi_m \Phi_m(x, y), \quad (4)$$

where

$$\Phi_m(x, y) = f_m(x) \frac{\cosh v_m(b-y)}{v_m \sinh v_m b} \quad (5)$$

and

$$f_m(x) = \cos(u_m(x-a)). \quad (6)$$

Here

$$u_m = \frac{m\pi}{2a}. \quad (7)$$

The normalizing factors are chosen such that $\Phi_{my}(x, 0) = f_m(x)$. The elevation of the interface is

$$\eta(x) = A \sum_{m=0}^{\infty} \xi_m f_m(x). \quad (8)$$

The eigenfunctions $\Phi_m(x, y)$ satisfy homogeneous Neumann conditions on the ends and top of the chamber. The coefficients v_m follow from the Helmholtz equation:

$$v_m^2 = u_m^2 - K^2. \quad (9)$$

These coefficients are either real or imaginary, and the eigenfunctions Φ_m are real.

The potential in the water can be derived by superposition of the incident-wave potential

$$\phi_I = \frac{igA}{\omega} \exp(ky - ikx) \quad (10)$$

with the solution for an oscillatory pressure imposed on the free surface (Wehausen & Laitone, 1960, equation 21.17). After adapting to the present notation it follows that

$$\phi = \phi_I - \frac{i\omega}{\pi\rho_w g} \int_{-a}^a P(\xi, 0) d\xi \int_0^\infty \cos \kappa(x-\xi) e^{\kappa y} \frac{d\kappa}{\kappa - k}. \quad (11)$$

In the integral with respect to κ the contour of integration passes below the pole $\kappa = k$, in accordance with the radiation condition. After substituting (2) and (4-5),

$$\phi = \phi_I + i\omega A \sum_{m=0}^{\infty} \xi_m \phi_m, \quad (12)$$

where

$$\phi_m = -\frac{k\rho_a}{\pi\rho_w v_m \tanh v_m b} \int_{-a}^a f_m(\xi) d\xi \int_0^{\infty} \cos \kappa(x - \xi) e^{\kappa y} \frac{d\kappa}{\kappa - k}. \quad (13)$$

After imposing the kinematic boundary condition $\phi_y = i\omega\eta$, multiplying by $f_n(x)/a$, and integrating over $(-a, a)$, a linear system of equations is derived for the unknown coefficients ξ_m in the form

$$\sum_{m=0}^{\infty} \xi_m C_{mn} = D_n, \quad (14)$$

where

$$C_{mn} = \frac{1}{a} \int_{-a}^a f_n(x) \left[f_m(x) - \frac{k\rho_a}{\pi\rho_w v_m \tanh v_m b} \int_{-a}^a f_m(\xi) d\xi \int_0^{\infty} \cos \kappa(x - \xi) \frac{\kappa d\kappa}{\kappa - k} \right] dx \quad (15)$$

and

$$D_n = \frac{1}{a} \int_{-a}^a f_n(x) e^{-ikx} dx = -\frac{2i^n ka}{(u_n^2 - k^2)a^2} \sin\left(ka + \frac{n\pi}{2}\right). \quad (16)$$

The integrals in (15) with respect to x and ξ are elementary, and the remaining integral with respect to κ can be evaluated in terms of sine and cosine integrals.

The simplest physical parameters to consider are the vertical exciting force and pitch moment, due to the acoustic pressure P acting on the ends and lid of the air chamber. Neglecting the contribution to the pitch moment from the ends, the force and moment are given by

$$\begin{pmatrix} X_3 \\ X_5 \end{pmatrix} = \int_{-a}^a \begin{pmatrix} 1 \\ -x \end{pmatrix} P(x, 0) dx. \quad (17)$$

After normalizing by the long-wavelength (hydrostatic) limits of the force and moment for a flat plate of the same width, it follows that

$$\frac{X_3}{2\rho_w g a A} = \frac{\rho_a k \xi_0}{\rho_w v_0 \sinh v_0 b} \quad (18)$$

and

$$\frac{X_5}{\frac{2}{3}\rho_w g k a^3 A} = -\frac{12\rho_a}{\pi^2 \rho_w} \sum_{\substack{n=1 \\ (n \text{ odd})}}^{\infty} \frac{\xi_n}{n^2 v_n \sinh v_n b}. \quad (19)$$

For asymptotically large wave periods the normalized heave force tends to a value less than the usual hydrostatic limit of 1.0, due to the compressibility of the air. The pitch moment tends to zero more quickly than the corresponding hydrostatic moment for a conventional floating body, due to equalization of the pressure throughout the chamber when the period is very large.

Preliminary computations indicate a very large pitch exciting moment in relatively short waves, at the resonant frequency of the first anti-symmetric acoustic mode ($Ka = \pi/2$). The maximum heave force occurs in longer waves. More complete computations of the heave force, pitch moment, and modal amplitudes ξ_n will be presented at the Workshop.

REFERENCES

- Lee, C.-H. & Newman, J. N. 1999. 'Wave effects on large floating structures with air cushions,' *Proc. 3rd Intl. Workshop on Very Large Floating Structures*, Honolulu, pp. 139-148
- Pinkster, J. A., 1997. 'The effect of air cushions under floating offshore structures,' *Proc. 8th Intl. Conference on the Behaviour of Offshore Structures*, Delft, The Netherlands, Vol 2, pp. 143-158.
- Pinkster, J. A., Fauzi, A., Inoue, Y. & Tabeta, S., 1998. 'The behaviour of large air cushion supported structures in waves,' Proceedings, *Proc. 2nd Intl. Conf. on Hydroelasticity in Marine Technology*, Fukuoka, Japan, pp. 497-505.
- Ulstein, T., & Faltinsen, O. M., 1996. 'Cobblestone effect on surface effect ships,' *Schiffstechnik / Ship Technology Research* Vol. 43, pp. 78-90.
- Wehausen, J. V. & Laitone, E. V., 1960. 'Surface waves,' *Encyclopedia of Physics* Vol. 9, pp. 446-778. Springer-Verlag.

Steady free-surface potential flow due to a point source

Noblesse F.*, Yang C.**, Hendrix D.*

* David Taylor Model Basin, NSWC-CD

** Institute for Computational Science and Informatics, George Mason University

Consider the linearized free-surface potential flow generated by a point source of unit strength advancing with constant speed \mathcal{U} along a straight path submerged a depth $\delta = D/L$ below the mean free-surface plane $z = 0$. Here L is an arbitrary reference length. This reference length may be chosen as $L = D$ or $L = \mathcal{U}^2/g$, which respectively yield $\delta = 1$ or $\delta = gD/\mathcal{U}^2$. The flow is observed from a moving system of coordinates attached to the source and thus appears steady. The z axis is vertical and points upward. The x axis is chosen parallel to the path of the moving source and points in the direction of motion of the source. The origin of the system of coordinates is chosen above the source, which is then located at the point $(0, 0, -\delta)$.

BASIC FLOW REPRESENTATION

The disturbance velocity field \vec{u} due to the unit source can be expressed as

$$\vec{u} = \vec{u}^W + \vec{u}^S + \vec{u}^L \quad (1)$$

where the simple-singularity component \vec{u}^S corresponds to a simple Rankine singularity and the wave component \vec{u}^W and the local component \vec{u}^L account for free-surface effects.

The **wave component** \vec{u}^W is given by

$$\begin{Bmatrix} u^W \\ v^W \\ w^W \end{Bmatrix} = (1 - \text{sign} x) \frac{1}{\pi F^4} \int_0^\infty dt \alpha \begin{Bmatrix} \cos \varphi^x \cos \varphi^y \\ -t \sin \varphi^x \sin \varphi^y \\ \alpha \sin \varphi^x \cos \varphi^y \end{Bmatrix} \exp \frac{(z-\delta) \alpha^2}{F^2} \quad (2a)$$

$$\text{where} \quad \varphi^x = \frac{x \alpha}{F^2} \quad \varphi^y = \frac{y t \alpha}{F^2} \quad \text{with} \quad \alpha = \sqrt{1 + t^2} \quad (2b)$$

The **simple-singularity component** \vec{u}^S is given by

$$\begin{Bmatrix} u^S \\ v^S \\ w^S \end{Bmatrix} = \frac{1}{4 \pi r^2} \begin{Bmatrix} x/r \\ y/r \\ (z + \delta)/r \end{Bmatrix} \quad \text{with} \quad r = \sqrt{x^2 + y^2 + (z + \delta)^2} \quad (3)$$

The **local component** is the object of this note and is considered hereafter. Let

$$r' = \sqrt{x^2 + y^2 + (z - \delta)^2}$$

In the **farfield** $r'/F^2 \rightarrow \infty$, the local component \vec{u}^L can be evaluated using an asymptotic approximation which can be obtained from *Bessho (1964)* and *Ponizy (1994)* :

$$4 \pi F^4 \begin{Bmatrix} u^L \\ v^L \\ w^L \end{Bmatrix} \sim \begin{Bmatrix} u_1^{LF} + u_2^{LF} \\ v_1^{LF} + v_2^{LF} \\ w_1^{LF} + w_2^{LF} \end{Bmatrix} \quad \text{as} \quad r'/F^2 \rightarrow \infty \quad (4a)$$

where \vec{u}_1^{LF} and \vec{u}_2^{LF} are given by

$$\begin{Bmatrix} u_1^{LF} \\ v_1^{LF} \\ w_1^{LF} \end{Bmatrix} = \left(\frac{F^2}{r'} \right)^2 \begin{Bmatrix} x/r' \\ y/r' \\ (z - \delta)/r' \end{Bmatrix} \quad \begin{Bmatrix} u_2^{LF} \\ v_2^{LF} \\ w_2^{LF} \end{Bmatrix} = 4 \left(\frac{F^2}{r'} \right)^3 \begin{Bmatrix} (A - B - 1) x/r' \\ (A + B - 3) y/r' \\ 1 - \frac{3}{2} (Y_\infty^2 + Z_\infty^2) \end{Bmatrix} \quad (4b)$$

$$\text{with} \quad Y_\infty = \frac{y}{r'} \quad Z_\infty = \frac{\delta - z}{r'} \quad B = \frac{Z_\infty}{1 + Z_\infty} \left(\frac{3}{2} - \frac{Z_\infty/2}{1 + Z_\infty} \right) \quad (4c)$$

$$A = \frac{Z_\infty}{1 + Z_\infty} \left(\frac{9}{2} + \frac{Z_\infty}{1 + Z_\infty} \left(\frac{1}{2} + \frac{3}{2} Z_\infty \right) \right) + \frac{Y_\infty^2}{(1 + Z_\infty)^2} \left(4 + \frac{Z_\infty}{1 + Z_\infty} \left(\frac{1}{2} + \frac{3}{2} Z_\infty \right) \right) \quad (4d)$$

In the **nearfield**, the local component \tilde{u}^L is given in *Noblesse (1978)* and *Ponizy (1994)* as

$$4\pi F^4 \begin{Bmatrix} u^L \\ v^L \\ w^L \end{Bmatrix} = \begin{Bmatrix} u_1^{LN} + \text{sign}x (u_2^{LN} + u_3^{LN} + u_4^{LN}) \\ v_1^{LN} + v_2^{LN} + v_3^{LN} + v_4^{LN} \\ w_1^{LN} + w_2^{LN} + w_3^{LN} + w_4^{LN} \end{Bmatrix} \quad (5a)$$

The components \tilde{u}_1^{LN} and \tilde{u}_2^{LN} are singular at $r' = 0$ and are given by

$$\begin{Bmatrix} u_1^{LN} \\ v_1^{LN} \\ w_1^{LN} \end{Bmatrix} = - \left(\frac{F^2}{r'} \right)^2 \begin{Bmatrix} x/r' \\ y/r' \\ (z - \delta)/r' \end{Bmatrix} \quad \begin{Bmatrix} u_2^{LN} \\ v_2^{LN} \\ w_2^{LN} \end{Bmatrix} = \frac{F^2}{r'} \begin{Bmatrix} 2Z_0 \\ 2Y_0 Z_0 \\ 1 + Y_0^2 - Z_0^2 \end{Bmatrix} \quad (5b)$$

where $Y_0 = y/(r' + |x|)$ and $Z_0 = (\delta - z)/(r' + |x|)$. The component \tilde{u}_3^{LN} is given by

$$\begin{Bmatrix} u_3^{LN} \\ v_3^{LN} \\ w_3^{LN} \end{Bmatrix} = \begin{Bmatrix} \ln(F^2/r') + \ln(1 + Y_0^2 + Z_0^2) - (\gamma + 1/2 - \ln 2) + (Y_0^2 - Z_0^2)/2 \\ Y_0(1 + Y_0^2/3 - Z_0^2)/2 \\ -4/3 - Z_0(3 + Y_0^2 - Z_0^2/3)/2 \end{Bmatrix} \quad (5c)$$

where $\gamma \approx 0.577$ is Euler's constant. The component \tilde{u}_3^{LN} is $O(1)$ as $r' \rightarrow 0$. Finally, the component \tilde{u}_4^{LN} is $O(r'/F^2)$ as $r' \rightarrow 0$ and is given by

$$\begin{Bmatrix} u_4^{LN} \\ v_4^{LN} \\ w_4^{LN} \end{Bmatrix} = \frac{2}{\pi} \int_{-1}^1 dt \sqrt{1 - t^2} \begin{Bmatrix} \Re \mathcal{F}(Z) \\ t \Im \mathcal{F}(Z) \\ \sqrt{1 - t^2} \Im \mathcal{F}(Z) \end{Bmatrix} \quad (5d)$$

$$\mathcal{F}(Z) = \exp(Z) E_1(Z) + \ln(Z) + \gamma \quad Z = \left(\frac{z - \delta}{F^2} \sqrt{1 - t^2} + \frac{y}{F^2} t + i \frac{|x|}{F^2} \sqrt{1 - t^2} \right) \sqrt{1 - t^2}$$

Here, $E_1(Z)$ is the exponential integral. $\mathcal{F}(Z)$ and consequently \tilde{u}_4^{LN} vanish as $r'/F^2 \rightarrow 0$.

Let the coordinates $(x, y, z - \delta)$ be defined in terms of the polar coordinates (r', θ, φ) :

$$\begin{Bmatrix} x = r' \cos \theta \cos \varphi \\ y = r' \cos \theta \sin \varphi \\ z - \delta = -r' \sin \theta \end{Bmatrix} \quad \text{with} \quad \begin{Bmatrix} 0 \leq \theta \leq \pi/2 \\ -\pi < \varphi \leq \pi \end{Bmatrix}$$

The foregoing farfield and nearfield representations show that the local flow $F^4 \tilde{u}^L$ is a function of the 3 variables $(r'/F^2, \theta, \varphi)$ and that $4\pi (r')^2 \tilde{u}^L$ is $O(1)$ for $0 \leq r'/F^2 \leq \infty$.

GENERALIZED FLOW REPRESENTATION

Expressions (2) for the wave component \tilde{u}^W show that v^W and w^W vanish as $x \rightarrow 0$. However, u^W has a finite discontinuity at $x = 0$. Specifically, we have

$$\pi F^4 u^W \sim (1 - \text{sign}x) J \quad \text{as } x \rightarrow 0 \quad \text{with} \quad J = \int_0^\infty dt \alpha \cos \frac{y t \alpha}{F^2} \exp \frac{(z - \delta) \alpha^2}{F^2}$$

The nearfield representation (5) of the local component \tilde{u}^L shows that v^L and w^L are continuous at $x = 0$. However, u^L has a finite discontinuity at $x = 0$. Specifically, we have

$$\pi F^4 u^L \sim \text{sign}x (u_2^{LN} + u_3^{LN} + u_4^{LN})/4 \quad \text{as } x \rightarrow 0$$

Continuity of the velocity $u^W + u^L$ at $x = 0$ yields $4J = [u_2^{LN} + u_3^{LN} + u_4^{LN}]_{x=0}$. The wave component \bar{u}^W may be expressed in the form $\bar{u}^W = \bar{u}_*^W + \bar{u}_L^W$ where the component \bar{u}_*^W is defined by (2) with $\text{sign}x$ in (2a) replaced by a function

$$\Theta \equiv \Theta\left(\frac{\sigma x}{F^2}\right) \text{ of the type } \quad \text{erf}\left(\frac{\sqrt{\pi}}{2} \frac{\sigma x}{F^2}\right) \quad \tanh\left(\frac{\sigma x}{F^2}\right) \quad \frac{x}{\sqrt{x^2 + (F^2/\sigma)^2}} \quad (6a)$$

Here, σ is an arbitrary positive real number. Note that we have

$$\Theta \sim \sigma x / F^2 = (\sigma r' / F^2) x / r' \quad \text{as} \quad x \rightarrow 0 \quad (6b)$$

The component \bar{u}_L^W is given by

$$\begin{Bmatrix} u_L^W \\ v_L^W \\ w_L^W \end{Bmatrix} = (\Theta - \text{sign}x) \frac{1}{\pi F^4} \int_0^\infty dt \alpha \begin{Bmatrix} \cos \varphi^x \cos \varphi^y \\ -t \sin \varphi^x \sin \varphi^y \\ \alpha \sin \varphi^x \cos \varphi^y \end{Bmatrix} \exp \frac{(z-\delta) \alpha^2}{F^2}$$

The component \bar{u}_L^W represents a local flow, which can be grouped with \bar{u}^L . Thus, the flow representation (1) becomes $\bar{u} = \bar{u}_*^W + \bar{u}^S + (\bar{u}^L + \bar{u}_L^W)$. In the limit $x \rightarrow 0$, we have $v_L^W \rightarrow 0$, $w_L^W \rightarrow 0$, and $\pi F^4 u_L^W \sim (\Theta - \text{sign}x) J \sim (\Theta - \text{sign}x) (u_2^{LN} + u_3^{LN} + u_4^{LN})/4$. Thus, $\text{sign}x$ in (2a) and (5a) may be replaced by a function Θ of the type (6) if σ is sufficiently large. This substitution is used hereafter.

SIMPLE ANALYTICAL APPROXIMATION TO THE LOCAL FLOW

The farfield and nearfield representations (4) and (5) yield

$$4\pi F^4 \begin{Bmatrix} u^L \\ v^L \\ w^L \end{Bmatrix} \approx Q \left(\frac{F^2}{r'} \right)^2 \begin{Bmatrix} x/r' \\ y/r' \\ (z-\delta)/r' \end{Bmatrix} \quad \text{with} \quad \begin{cases} Q \rightarrow 1 & \text{as } r'/F^2 \rightarrow \infty \\ Q \rightarrow -1 & \text{as } r'/F^2 \rightarrow 0 \end{cases}$$

A simple function Q that satisfies these two limiting conditions is $Q = (r' - F^2)/(r' + F^2)$. Thus, the local flow \bar{u}^L may be approximated as $\bar{u}^L \approx \bar{u}^{LA}$ with \bar{u}^{LA} given by

$$4\pi F^4 \begin{Bmatrix} u^{LA} \\ v^{LA} \\ w^{LA} \end{Bmatrix} = - \left(\frac{F^2}{r'} \right)^2 \begin{Bmatrix} x/r' \\ y/r' \\ (z-\delta)/r' \end{Bmatrix} + \frac{2F^2/r'}{r'/F^2 + 1} \begin{Bmatrix} x/r' \\ y/r' \\ (z-\delta)/r' \end{Bmatrix}$$

This approximation to the local flow \bar{u}^L is asymptotically equivalent to the first (dominant) terms in the farfield and nearfield approximations (4) and (5), and the relative error associated with the approximation \bar{u}^A is $O(F^2/r')$ in the farfield and $O(r'/F^2)$ in the nearfield.

The second term in the approximation \bar{u}^{LA} is $O(F^2/r')$ in the nearfield, like the second term \bar{u}_2^{LN} defined by (5b) in the nearfield approximation (5a). The modified approximation given by

$$4\pi F^4 \begin{Bmatrix} u^{LA} \\ v^{LA} \\ w^{LA} \end{Bmatrix} = - \left(\frac{F^2}{r'} \right)^2 \begin{Bmatrix} x/r' \\ y/r' \\ (z-\delta)/r' \end{Bmatrix} + \frac{2F^2/r'}{(r'/F^2 + 1)^2} \begin{Bmatrix} x/F^2 \\ y/F^2 + Y_0 Z_0 \\ (z-\delta)/F^2 + (1+Y_0^2 - Z_0^2)/2 \end{Bmatrix} \quad (7a)$$

$$\text{where} \quad r' = \sqrt{x^2 + y^2 + (z-\delta)^2} \quad Y_0 = \frac{y}{r' + |x|} \quad Z_0 = \frac{\delta - z}{r' + |x|} \quad (7b)$$

is asymptotically equivalent to the first term in the farfield approximation (4) and the first two terms in the nearfield approximation (5). In fact, (7) yields

$$4\pi F^4 \begin{Bmatrix} u^{LA} \\ v^{LA} \\ w^{LA} \end{Bmatrix} \sim \begin{Bmatrix} u_1^{LF} \\ v_1^{LF} \\ w_1^{LF} \end{Bmatrix} - 4 \left(\frac{F^2}{r'} \right)^3 \begin{Bmatrix} x/r' \\ y/r' - Y_0 Z_0 / 2 \\ (z-\delta)/r' - (1+Y_0^2 - Z_0^2)/4 \end{Bmatrix} \quad \text{as } \frac{r'}{F^2} \rightarrow \infty \quad (8a)$$

$$4\pi F^4 \begin{Bmatrix} u^{LA} \\ v^{LA} \\ w^{LA} \end{Bmatrix} \sim \begin{Bmatrix} u_1^{LN} \\ v_1^{LN} + v_2^{LN} \\ w_1^{LN} + w_2^{LN} \end{Bmatrix} + 2 \begin{Bmatrix} x/r' \\ y/r' - 2Y_0 Z_0 \\ (z-\delta)/r' - (1+Y_0^2 - Z_0^2) \end{Bmatrix} \text{ as } \frac{r'}{F^2} \rightarrow 0 \quad (8b)$$

Thus, the *relative* error associated with the approximation (7) is $O(F^2/r')$ in the farfield and $O(r'/F^2)^2$ in the nearfield, as follows from (6b), (5a) and (5b).

For purposes of numerical evaluation, the approximation (7) can be expressed in the form

$$4\pi \begin{Bmatrix} u^{LA} \\ v^{LA} \\ w^{LA} \end{Bmatrix} = \begin{Bmatrix} Px \\ Py - QYZ \\ P(z-\delta) + \frac{1}{2}Q[1 + (Y+Z)(Y-Z)] \end{Bmatrix} \text{ with } \begin{cases} P = R(1 - F^2/r' - S) \\ Q = r'R S \\ R = 1/[(r')^2(F^2 + r')] \\ S = 2F^2/(F^2 + r') \\ Y = y/(r' + |x|) \\ Z = (z-\delta)/(r' + |x|) \end{cases} \quad (9a)$$

Gauss integration rules can be used to integrate \vec{u}^{LA} over a panel except if r' is of the order of the panel size. In this case, \vec{u}^{LA} can be expressed as

$$4\pi \begin{Bmatrix} u^{LA} \\ v^{LA} \\ w^{LA} \end{Bmatrix} = \frac{-1}{(r')^2} \begin{Bmatrix} x/r' \\ y/r' \\ (z-\delta)/r' \end{Bmatrix} + \frac{1}{F^2 r'} \begin{Bmatrix} 0 \\ -2\bar{Y}\bar{Z} \\ 1 + \bar{Y}^2 - \bar{Z}^2 \end{Bmatrix} + \frac{2}{F^4} \begin{Bmatrix} u_* \\ v_* \\ w_* \end{Bmatrix} \quad (9b)$$

where \bar{Y} and \bar{Z} stand for mean values of Y and Z over the panel, and \vec{u}_* is given by

$$\begin{Bmatrix} u_* \\ v_* \\ w_* \end{Bmatrix} = \frac{1}{(1+\rho)^2} \begin{Bmatrix} x/r' \\ y/r' + 2\bar{Y}\bar{Z}(1+\rho/2) + (\bar{Y}\bar{Z} - YZ)/\rho \\ (z-\delta)/r' - (1+\bar{Y}^2 - \bar{Z}^2)(1+\rho/2) + \frac{1}{2}(Y^2 - Z^2 + \bar{Z}^2 - \bar{Y}^2)/\rho \end{Bmatrix} \quad (9c)$$

with $\rho = r'/F^2$. The first two terms on the right of (9b) are singular as $r' \rightarrow 0$ but can be integrated analytically. The term \vec{u}_* is finite as $r' \rightarrow 0$ and Gauss integration can be used. Thus, the component \vec{u}^{LA} can be integrated over a panel in a simple and accurate manner.

CONCLUSION

The analytical approximation \vec{u}^{LA} given by (9) makes it possible to evaluate the flow due to a singularity distribution in a simple and highly efficient manner. Practical applications to the slender-ship source distribution defined in *Noblesse (1983)* show that the approximation (9) is sufficient for many purposes. The approximation (7) also provides a useful starting point to develop accurate approximations to the local flow \vec{u}^L by expressing \vec{u}^L in the form

$$\vec{u}^L = \vec{u}^{LA} + \vec{u}^{LR}$$

The remainder $\vec{u}^{LR} = \vec{u}^L - \vec{u}^{LA}$ is $O(1)$ as $r' \rightarrow 0$ and $O(1/r')^3$ as $r' \rightarrow \infty$. This remainder can be evaluated using table interpolation as in *Ponizy (1994)*, or an analytical approximation based on a composite of the farfield and nearfield approximations (8), (4) and (5).

REFERENCES

- Bessho M. (1964) *On the fundamental function in the theory of wavemaking resistance of ships*, Memoirs of the Defense Academy, Japan, Vol. IV, 99-119
- Noblesse F. (1978) *On the fundamental function in the theory of steady motion of ships*, JI Ship Research, 22, 212-215
- Noblesse F. (1983) *A slender-ship theory of wave resistance*, JI Ship Research, 27, 13-33
- Ponizy B., Noblesse F., Ba M., Guilbaud M. (1994) *Numerical evaluation of free-surface Green functions*, JI Ship Research, 38, 193-202

Analysis of Wave Force on a Large and Thin Floating Platform

M. Ohkusu

Research Institute for Applied Mechanics, Kyushu University, Japan

1 Introduction

Regarding the interaction of waves and a very large floating body of zero draft, whose configuration represents a design concept of floating airports, a question was raised at 14th IWWF on how to evaluate the side force acting on the zero draft body. This issue will be crucial if we are concerned with computation of the steady drift force and slow oscillating drift force in multi-frequency waves; the latter in particular is not computed from the far field behavior of the waves scattered and radiated by the body but to be evaluated with integrating the pressure on the body's side surface. We will need more careful analysis of the flow close to the edges of the thin body to study this problem. In this report we present a result of an attempt to this direction.

2 Solution of the problem

We assume a floating thin plate is very long and the flow when it is in beam seas is taken to be two dimensional with generator parallel to the z axis. The x and z axes are on the mean free surface and the y axis is toward vertically upward. We take the width of the plate is 2 and the draft d , ie the thin plate occupies the region of the mean free surface of $-1 \leq x \leq 1$ and $-\infty < z < +\infty$.

We suppose the regular waves being incident at beam on the plate whose velocity potential is

$$\phi_0(x, y)e^{i\omega t} = e^{ikx+ky+i\omega t} \quad (1)$$

Assumptions for our analysis is that the wave length is very small compared with the width of the plate and the draft is much smaller than the wave length ie.

$$1 \gg k^{-1} \gg d \quad (2)$$

This assumption will be reasonable when we consider the dimensions of a prototype model of floating airport constructed recently in Japan.

Here our analysis is not with a method proposed, for example, by Ohkusu (1998) but it is rather along a traditional line of decomposing the flow into radiation and scattering ones and expanding the vibration of the plate into a series. We introduce an expression for the vertical displacement $\zeta(x)e^{i\omega t}$ of the plate due to the bending vibration

$$\zeta e^{i\omega t} = \sum_n A_n U_n(x) e^{i\omega t} \quad (-1 < x < 1) \quad (3)$$

$U_n(x)$ is Chevyshev polynomials of the second kind. A_n are to be determined by solving the equation of the plate vibration with the edge conditions. Reason for this expression is not that Chevyshevs are mode functions but that they lead to the explicit expression of the hydrodynamic pressure on the plate.

The velocity potential $\phi e^{i\omega t}$ of the flow is decomposed into the radiation potential ϕ_R by the vibration of ζ and the scattering potential ϕ_D by ϕ_0

$$\phi = \phi_R + \phi_D \quad (4)$$

Here ϕ_D contains the effect of ϕ_0 . Hereafter we suppress $e^{i\omega t}$ unless it is needed.

The linear free surface condition for ϕ is

$$-k\phi + \phi_y = 0 \quad (y = 0, \quad x > 1 \text{ or } x < -1) \quad (5)$$

Subscript y denotes the differentiation into its direction. Hereafter this notation will be used.

The free surface condition is further simplified in the outer region of $|x \pm 1| = O(1), y = O(1)$ with the assumption of the fore-part of the assumption (2)

$$\phi = 0 \quad (y = 0, \quad x > 1 \text{ or } x < -1) \quad (6)$$

A solution of ϕ_R in the outer domain is straightforward. In the outer region the draft is too small to be felt and the body boundary condition is imposed on $y = 0$

$$\phi_{Ry} = i\omega \sum_n A_n U_n(x) \quad (y = 0, \quad -1 < x < 1) \quad (7)$$

The problem is a familiar one in the linear wing theory (we impose the condition $\phi_{Rx,y} \rightarrow 0$ at infinity). Integral equation for ϕ_{Rx} is given by

$$i\omega \sum_n A_n U_n(x) = \frac{1}{\pi} \oint_1^1 \frac{\phi_{Rx}(\xi, 0)}{\xi - x} d\xi \quad (8)$$

Here a circle on the integral symbol denotes Cauchy's principal value.

Solution is given by inverse Hilbert transform (Tricomi 1957). ϕ_{Rx} and $-\phi_{Ry}$ except the eigensolution is given by the real part and the imaginary part respectively of

$$-\frac{1}{\pi} \frac{i\omega}{\sqrt{1-z^2}} \int_{-1}^1 \frac{\sqrt{1-\xi^2}}{\xi - z} \sum_n A_n U_n(\xi) d\xi \quad (9)$$

In this equation z denotes a complex coordinate $z = x + iy$ and the principal value is taken if $z = x, |x| < 1$. We notice that we should add a progressing wave train solution in very thin layer close to the free surface ($|x \pm 1| = 1, ky = O(1)$)

After some algebra and discarding the eigensolution with the condition of continuity of $\phi_R(x, y)$ at $x = \pm 1, y = 0$, we have ϕ_R on the plate surface

$$\phi_R(x, 0) = -i\frac{\omega}{\pi} \sum_n \frac{A_n}{n+1} U_n(x) \sqrt{1-x^2} \quad (|x| < 1) \quad (10)$$

Reason for choice of Chebyshev polynomials is clear. Obviously the pressure on the plate is in-phase of the motion and no damping force acts.

We consider the local flow in the region of wave length size $k|x \pm 1| = O(1), ky = O(1)$ around both edges of the plate. We notice this region is yet large enough, the latter part of the assumption (2) says, to let us assume the plate draft is zero. ϕ_R in this region close to $x = 1$ for example has to satisfy the original free surface condition (5) and the body condition

$$\phi_{Ry} = O(k^{-1}) \quad (y = 0, \quad -\infty < x < 1) \quad (11)$$

since in this region other edge $x = -1$ is very far away and its existence is not felt. We may take the right hand side is zero in the lowest order solution.

The problem is a dock problem of semi-infinite length which has been well studied (for example Friedrichs and Lewy (1948), Holford (1964)). In our problem the boundary conditions are all homogeneous; the forcing comes from the matching condition with the solution (10) at $x \sim \pm 1$.

A local solution ϕ_R , for example, in the region at $kz \sim 1$ will be

$$\phi_R = -\sqrt{2}i\omega \sum_n A_n \left(\text{Re}[\sqrt{1-z}] + k^{-\frac{1}{2}} F(k(x-1), ky) \right) \quad (12)$$

where the function F is derived from the result of Holford (1964). When we are concerned with the pressure beneath the plate we may define as

$$F(kx, ky) = \frac{1}{2\pi} \int_0^\infty ds \int_0^\infty d\tau \frac{\Lambda(s)\Lambda(\tau) \cos(\tau ky) e^{-\tau k|x|}}{\tau(\tau-i)(s-i)(\tau+s)} \quad (13)$$

The details of the function $\Lambda(x)$ is not reproduced here for the sake of brevity but it is of $O(x)$ at $x = \infty$ and of $O(\sqrt{x})$ at $x = 0$ (see Holford (1964)).

A local solution of ϕ_R at $kz \sim -1$ is obtained in similar manner. We add two local solutions at $x \sim \pm 1$ and the solution (10) to obtain a composite expression of ϕ_R valid everywhere on the plate

$$\phi_R(x, 0) = \frac{-i\omega}{\pi} \sum_n \frac{A_n U_n(x)}{n+1} \sqrt{1-x^2} - \sqrt{\frac{2}{k}} i\omega \sum_n A_n \left[F(k(x-1), 0) - (-1)^{n+1} F(k(x+1), 0) \right] \quad (14)$$

We should notice that F to produce the out-of-phase part of the pressure is localized to very small region close to the plate edges. It means the damping force due to the vibration acts only at the edges of the plate.

ϕ_D is obtained almost the same way as ϕ_R . In the outer region at $x, y = O(1)$ the solution is an eigensolution satisfying the homogeneous conditions both on the body and the free surfaces: $\phi_{Dy} = 0$ on the plate ($y = 0$) and $\phi_D = 0$ on the free surface. The coefficients are to be determined by the matching with the local solution valid $k(z \pm 1) = O(1)$. The local solution is a solution that satisfies the free surface condition (5) and the condition ensuring the incident and the out-going waves at infinity. It is a dock problem and the solution is found in Holford (1964).

A composite expression of ϕ_D valid everywhere on the plate is

$$\phi_D(x, 0) = \sqrt{\frac{1}{k\pi}} \left[\sqrt{\frac{1+x}{1-x}} - \sqrt{\frac{2}{1-x}} \right] + \frac{\sqrt{2}}{\pi} \int_0^\infty \frac{\Lambda(\tau) e^{\tau k(x-1)}}{\tau(1+\tau^2)} d\tau \quad (-1 < x < 1) \quad (15)$$

We see from this expression that the lowest order part of the wave force is limited in the small area very close to the windward edge.

Equation of the plate bending vibration is obtained immediately with the above expressions for hydrodynamic force:

$$\sum_n A_n \left\{ U_n^{(4)}(x) - \omega^2 \left(m - \rho \frac{\sqrt{x^2-1}}{n+1} - \frac{\rho g}{\omega^2} \right) U_n(x) - i\sqrt{2g} \left(F_- + (-1)^n F_+ \right) \right\} = \phi_D(x, 0) \quad (16)$$

where m denotes mass per unit area of the plate and $F_\pm = F(k(x \pm 1), 0)$ in (14).

3 Steady force

We are able to evaluate steady drift force on the plate by the farfield computation without relying on the pressure integration. Yet the pressure integration will be useful for estimating the local distribution of it. Furthermore the idea proposed here will be extended to the computation of the slowly varying force in random seas whose evaluation needs the pressure integration.

We investigate the asymptotic behavior of the local solution ϕ_D as $k(z-1)$ approaches zero to study the force acting on the side surface of the plate, which extends from $y = 0$ to $y = -d$. For the sake of brief description here we focus on ϕ_D , though almost similar method is applied to ϕ_R .

As $k(z-1)$ goes to zero, the second term of ϕ_D given by (15) will become

$$\phi_D = \sqrt{2} - \frac{\sqrt{2}}{\pi} Re \left[k(z-1) \log k(z-1) \right] + O(k(z-1)) \quad (17)$$

Obviously the first term corresponds to the wave elevation at the edge of the plate $x = 1, y = 0$. In our case, very large body and small wave length, the incident waves are reflected completely. The second term is caused by the regularity condition imposed on the edge flow. When a infinite wave elevation is admitted there, other solution will appear (Stoker (1957)).

It is an accepted method in engineering to account only for the steady pressure acting above the free surface due to the wave elevation with very shallow draft body. Here we consider the second term to confirm its legitimacy.

Rescale the coordinate by d as $Z = k(z - 1)/d$ and rewrite (16) with the first two terms retained, we have

$$\phi_D = \sqrt{2} - \frac{\sqrt{2}}{\pi} X \cdot d \log d + O(d) \quad (18)$$

Φ is a solution of the flow around a semi-infinite dock of finite draft 1 to satisfy $\partial\Phi/\partial Y = 0$ on the mean free surface. Φ must have an asymptotic behavior of (18) as Z goes to infinity. The second term of (18) represents the uniform flow along the X axis; it is a simple problem that is solved by conformal mapping method. Φ will be in the form

$$\Phi = \sqrt{2} - \frac{\sqrt{2}}{\pi} d \log d (X + \Psi(X, Y)) \quad (19)$$

where

$$\Psi(X, Y) = -\frac{1}{\pi} \operatorname{Re}(\cosh \zeta), \quad X - iY = \frac{1}{\pi}(\zeta + \sinh \zeta)$$

We compute the steady force f_S acting on the area projected into the x axis with this solution.

$$f_S = -\frac{\rho g}{2} + \frac{\rho}{2} (d \log d)^2 \int_{-1}^0 \left(\frac{\partial \Psi(0, Y)}{\partial Y} \right)^2 dY \quad (20)$$

In this computation we need not consider the force at $x = -1$ because ϕ_D is zero there (complete reflection). Obviously the second term representing the force acting on the mean wetted side surface is of higher order than as much as d .

The steady force f_B acting on the bottom of the plate which is vibrating is given by

$$f_B = \frac{\rho \omega}{4} \sum_n A_n \int_{-1}^1 U'_n(x) dx \left[\sqrt{\frac{1}{k\pi}} \left(\sqrt{\frac{1+x}{1-x}} - \sqrt{\frac{2}{1-x}} \right) + \frac{\sqrt{2}}{\pi} \int_0^\infty \frac{\Lambda(\tau) e^{\tau k(x-1)}}{\tau(1+\tau^2)} d\tau \right] \quad (21)$$

4 Remarks

Numerical results are presented at the Workshop.

A future problem is the case of $kd = O(1)$. Analytical solution of the semi-infinite dock with finite draft is not available as far as the present author knows. Maybe numerical technique must be introduced in this case.

5 References

- (1) Friedrichs KO and Lewy H: The dock problem, Communications on Appl. Math. 1 (1948)
- (2) Holford RL: Short surface waves in the presence of a finite dock I, Proc. Camb. Phil. Soc. 60 (1964)
- (3) Ohkusu M: Hydroelastic Interaction of a Large Floating Platform with Head Seas, 14th IWWF, Michigan (1998)
- (4) Stoker JJ: Water waves, Interscience, New York (1957)
- (5) Tricomi FG: Integral equations, Interscience, New York (1957)

SIMPLIFIED MODEL OF THE FREAK WAVE FORMATION FROM THE RANDOM WAVE FIELD

Efim Pelinovsky¹⁾ and Christian Kharif²⁾

¹⁾Laboratory of Hydrophysics and Nonlinear Acoustics, Institute of Applied Physics,
46 Ulianov Str., 603600 Nizhny Novgorod, Russia

²⁾Ecole Supérieure de Mécanique de Marseille, Technopole de Château-Gombert,
13451 Marseille Cedex 20, France

1. Introduction

The freak wave appearance is a phenomenon characteristic of many areas of the World Ocean. Mallory (1974) collected data of eleven documented events of catastrophic ship collisions with freak waves in the vicinity of the Indian Coast of South Africa. Probably, last such an event occurred in this area with the ship «Taganrogsky Zaliv» in 1985 (Lavrenov, 1985). Lavrenov (1998) suggested that the main reason of the frequent appearance of the freak waves near the south-eastern shore of the South Africa is the wave amplification on the opposite Agulhas current. Sand et al (1990) analysed prototype records of extreme single waves recorded on the Danish Continental Shelf, and pointed out that such waves are too high, too asymmetric and too steep. They also reported the freak wave records on deep water in the Gulf of Mexico. The statistical methods can predict the probability of the appearance of the freak waves (exactly, the averaged number of the possible events during the storm), but can not answer the question, when and where will be next extreme waves. The physical mechanisms of the formation of the freak waves are wave focusing and superposition of waves of different scales. An interesting example of the freak wave formation in the laboratory tank using the spatial - temporal focusing of the dispersive train was demonstrated by Kjeldsen (1990). Considering this mechanism very important, we analyse herein its effect on 2D and 3D water waves on the basis of the linear theory in the presence of a random wave field.

2. Focusing of dispersive trains

To describe 2D water waves with narrow spectrum we will use the linearised version of the parabolic equation for the complex wave envelope $A(x, t)$ (Mei, 1993):

$$\frac{\partial A}{\partial t} = \frac{i}{2} \frac{\partial^2 A}{\partial x^2} \quad (1)$$

with the dimensionless coordinate and time

$$x' = k_0 (x - c_g t), \quad t' = k_0^2 \left| \frac{dc_g}{dk} \right| t, \quad (2)$$

where k_0 is the carrier wavenumber, and c_g is the group velocity on the carrier wavenumber, calculated from the dispersion wave relation

$$\omega = \sqrt{g \tanh(kh)}. \quad (3)$$

The water depth h is assumed to be arbitrary. Equation (1) can be solved exactly with initial condition in the form of the Gaussian wave packet (see, for instance, Clauss & Bergmann, 1986)

$$A(x,0) = A_0 \exp(-K_0^2 x^2), \quad (4)$$

where A_0 is the wave height and K_0 is the inverse wave impulse length. The solution of equation (1) for either time moment is

$$A(x,t) = \frac{A_0}{\sqrt[4]{1+4t^2 K_0^4}} \exp\left(-\frac{K_0^2 x^2}{1+4t^2 K_0^4}\right) \cos\left[\frac{2tx^2 K_0^4}{1+4t^2 K_0^4} - \frac{a \tan(2tK_0^2)}{2}\right]. \quad (5)$$

This solution describes well-known dispersion effect: its wave amplitude decreases with time, its length increases, and the Gaussian impulse transforms into a wave train. But if we consider expression (5) for any negative time as an initial condition, the wave dynamics will have another behaviour: the wave train will transform into the Gaussian impulse at moment $t = 0$ ("collapse" time), and then the wave packet will disperse again. This focusing of the wave train on the first stage can be very significant, and it depends from parameters, A_0 and K_0 .

Real wind waves are random waves which are usually considered as an ensemble of different spectral components with random phases. Due to nonlinearity of the wave field the correlation between phases is not zero, also the variable wind leads to the appearance of coherent components in the wind wave spectrum. We may consider the solution (5) as an example of such a coherent component. Let us consider the superposition of this coherent component with the random wave field. The latter is the sum of the Fourier-component with different amplitudes and phases, each of them, of course, should be the solution of the equation (1),

$$A = \sum_{n=1}^{\infty} a_n \exp i\left(K_n x - \frac{K_n^2}{2} t + \phi_n\right). \quad (6)$$

For illustration, parameters in (6) are chosen as follows

$$a_n = \frac{(-1)^n}{1+0.25n}, \quad K_n = \frac{(2n)^{1.8}}{n+1.3}, \quad \phi_n = \frac{\pi n^3}{6}, \quad (7)$$

and, qualitatively, the wave field is varied as the random field with the significant wave height about 4 (dimensionless units).

The result of the superposition of the coherent wave component (5) with the random field (6) is displayed in Fig. 1 (numbers - dimensionless time). In fact, except in the vicinity of the "collapse" time ($t = 0$), the coherent component is not identified from the resulting records, but during a short period of time, the impulse wave of an extreme amplitude (in our calculations about 10) is generated and then disappears. This simplified model demonstrates all features of the freak wave phenomenon: its "invisibility" in the random field of the wind waves on the sea surface and occurrence during short time in confined part of the sea surface.

3. Conclusion

The mechanism of the spatial - temporal focusing of the coherent component in the wind wave field is probably the key point in the freak wave phenomenon. Calculations were performed also for 3D water waves within 2D version of the parabolic equation for the wave amplitude (these results are not described here in detail): the resulting wave field is shown in Fig. 2. Three-dimensional effects lead to more narrow domain of appearance of the freak wave and shortened period of time for its "visibility". Next step is to study the nonlinear mechanism of the wave focusing and wave-noise interaction, and also to study of the conditions for generation of coherent component in wind wave field.

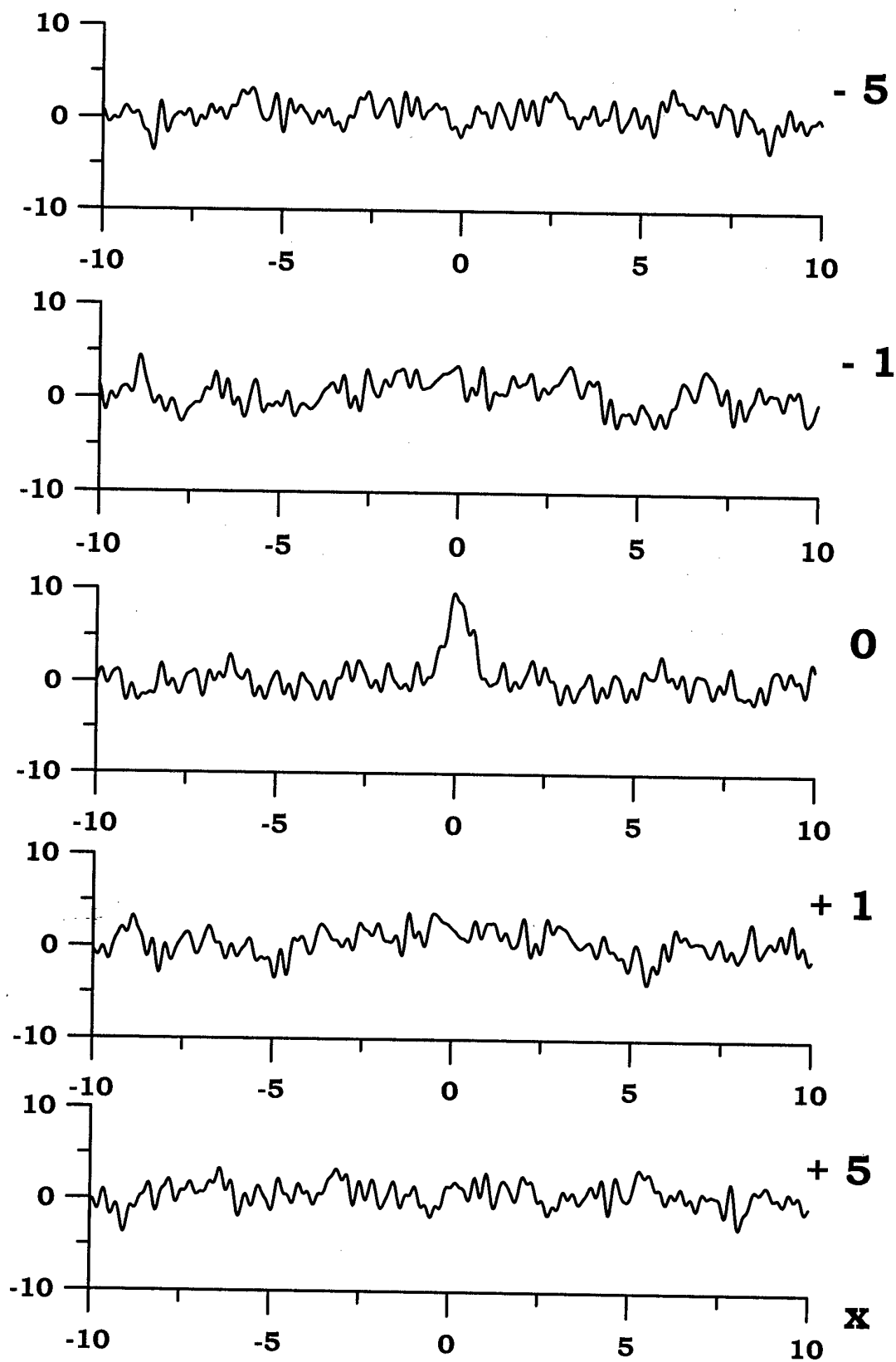


Fig. 1. Evolution of the wave field with the coherent component.

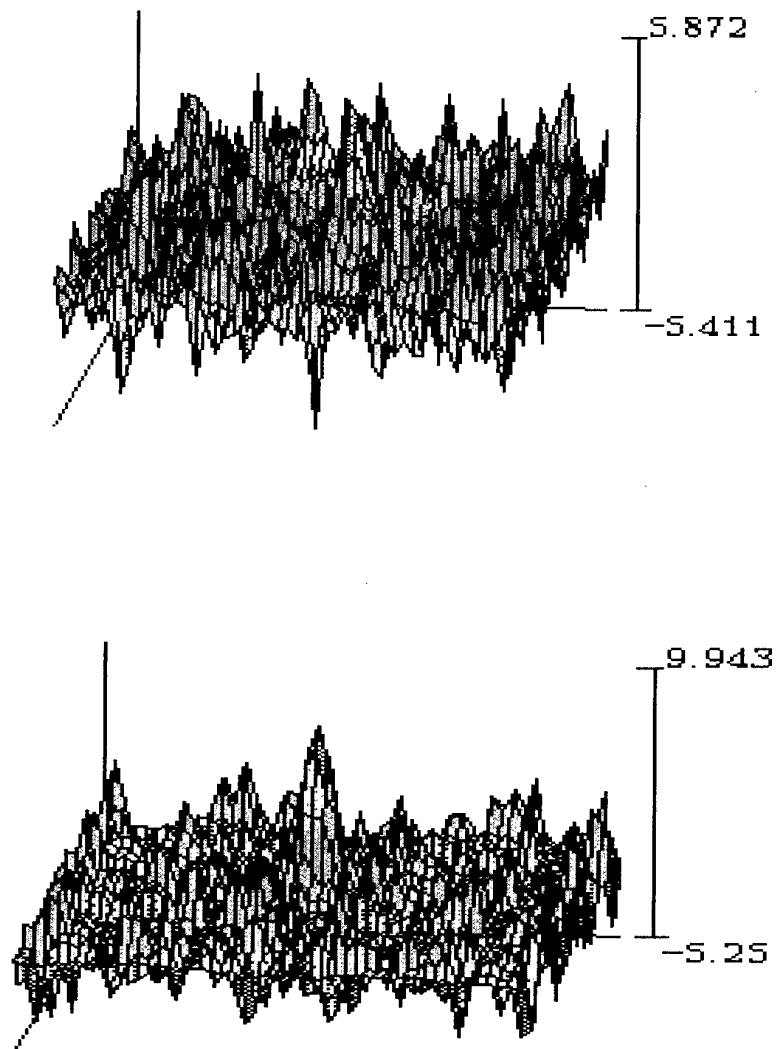


Fig. 2. Focusing of 3D dispersive waves (upper for $t = -1$, below for the "collapse" time).

References

- Clauss G.F., Bergman J.** Gaussian wave packets - a new approach to seakeeping tests of ocean structures. *Applied Ocean Research*, 1986, v. 8, N. 4.
- Kjeldsen S.P.** Breaking waves. *Water Wave Kinematics* (Eds. Torum O., Gudmestad O.T.). Kluwer Academic Publ., 1990, 453 - 473.
- Lavrenov I.** The wave killer accident. *Morskoy Flot*, 1985, N. 12, 28 - 30 (in Russian).
- Lavrenov I.** The wave energy concentration at the Agulhas current off South Africa. *Natural Hazards*, 1998, v. 17, 117-127.
- Mallory J.K.** Abnormal waves in the south - east coast of South Africa. *Int. Hydrog. Rev.*, 1974, v. 51, 99 - 129.
- Mei C.C.** *Applied Ocean Wave Dynamics*. World Sci., Singapore, 1993.
- Sand S.E., Hansen N.E.O., Klinting P., Gudmestad O.T., Sterndorf M.J.** Freak wave kinematics. *Water Wave Kinematics* (Eds. Torum O., Gudmestad O.T.). Kluwer Academic Publ., 1990, 535 - 549.

PRESSURE-IMPULSE THEORY FOR PLATE IMPACT ON WATER SURFACE

Weidong Peng and D. H. Peregrine

School of Mathematics, University of Bristol,
University Walk, Bristol BS8 1TW, England UK

Abstract

For plate impact on water we present a small extension of pressure-impulse theory for the effect of impact on body rotation, and discuss the use of pressure-impulse theory to estimate pressures immediately after impact.

Introduction

The problem of impact on water can be traced back to work by von Karman's (1929) more than a half century ago in studying the landing of sea-planes or flying boats and Wagner (1932) in studying similar wedge entry problem. Their work has been extended by Cointe and Armand (1987) and Cointe (1989). Some extensive surveys of early research have been summarized by Lesser and Field (1983) and Korobkin and Puknachov (1988). More recently, pressure impulse theory has been developed in studying waves breaking against coastal structures and the impact of waves on vertical wall by Cooker and Peregrine (1995) and Wood, Peregrine & Bruce (2000).

In this study we are interested in investigating the value of the simple pressure-impulse approach for the impact of a free falling plate on a water surface. The plate is assumed to be rigid. As the plate strikes on the water surface, abrupt forces are created by impact and decay shortly after. High loading on the impact region generates a pressure field throughout water body. Since impact may not be symmetric we consider both vertical and angular impulses, the plate being allowed to have an angular velocity at impact and after impact. Since, as is usual with this approach, we take a simplified geometry this analysis is straightforward because the pressure impulse satisfies linear equations so angular and vertical motion can be considered

separately and then combined.

As has been discussed by Cooker (1996) the pressure after impact can also be determined from pressure-impulse theory since the post impact velocities can be determined. We have noted that the pressure after impact is greater than the initial pressure in all cases for which we have seen experimental data, which is in agreement with Cooker's results, except for the case of impact of a horizontal plate on flat water where the post impact pressure is less than the initial pressure. This is discussed. There are similarities between this problem and the slamming of ships, Lewison (1970) gives a good discussion motivated by that application.

Pressure-impulse theory

In impact problems, the deceleration of plates and impact loads on fluid boundaries are of large magnitude and short duration so that the dominant terms in the equation of motion for the fluid reduce to inertia and pressure. Further the time scales are so short that the convective terms are negligible in the fluid's acceleration. Thus by integrating over the short duration of the impact the pressure impulse is found and satisfies Laplace's equation if fluid compressibility is negligible. Pressure impulse is defined as

$$P(\mathbf{x}) = \int_{t_b}^{t_a} p(\mathbf{x}, t) dt, \quad (1)$$

where t_a and t_b are the times after and before impact, respectively. Details of boundary conditions etc. may be found in Cooker & Peregrine (1995).

In considering plate motion, let m be the mass of the plate, \mathbf{v} the velocity of the plate, \mathbf{v}_a and \mathbf{v}_b the velocities after and before the impact, ω , ω_a and ω_b its corresponding angular velocities and S the impact area of the plate. During impact, the forces on the plate are due to water pressure and gravity. Thus the equation governing plate motion is

$$m\left(\frac{d\mathbf{v}}{dt} - g\right) = - \int_S (p - p_a) \mathbf{n} dS, \quad (2)$$

where p_a is the atmospheric pressure. Without loss generality, the atmospheric pressure is taken as the reference pressure and set to zero. Since the impact duration is very short and pressures large, the gravity term can be ignored through impact.

The impulse also changes of the angular motion of the plate during the impact. Here we consider only two dimensional motion for simplicity. Let $\mathbf{r} = (r_1, r_2)$ be a position vector on S and $\mathbf{n} = (n_1, n_2)$ the normal to S , then we obtain

$$I_0(\omega_a - \omega_b) = \int_S (r_2 n_1 - r_1 n_2) P dS \quad (3)$$

where I_0 is the moment of inertia about $\mathbf{r} = \mathbf{0}$.

A further boundary condition is that in the impact zone and immediately after impact, the velocity of fluid is equal to the velocity of plate.

In order to solve the problem, we use the linearity of the pressure-impulse to split the problem into two, one relating to the translational motion of the center of mass and the other involving rotation about the center of mass. We can then solve each separately.

Results

The solution of pressure impulse for the plate translational motion can be obtained, in terms of $z = x + iy$, as

$$P_1 = -\rho u_{a0} L \Re\{i(z + \sqrt{z^2 - 1})\} \quad (4)$$

where ρ is the density of water, v_{b0} is the plate's downward velocity just before impact, \Re stands for the real part and where

$$u_{a0} = \frac{mv_{b0}}{m + \frac{1}{2}\rho L^2 h \pi} \quad (5)$$

is the plate velocity after impact and h and L are the plate width (in the third dimension) and length respectively.

For the rotational motion, we have

$$P_2 = \rho \omega_a L^2 \bar{P}_2 = \frac{1}{4} \rho \omega_a L^2 \Re\{i(z - \sqrt{z^2 - 1})^2\} \quad (6)$$

and if we define

$$G = \int_{-1}^1 x \bar{P}_2 dx, \text{ we have } \omega_a = \frac{I_0 \omega_b}{I_0 + \rho L^3 h G}.$$

Thus the total pressure impulse due to a plate falling on the horizontal water surface is written as

$$P = \rho L \Re\{-i[u_a(z - \sqrt{z^2 - 1}) + \omega_a L(z - \sqrt{z^2 - 1})^2/4]\}. \quad (7)$$

On the plate, the pressure-impulse for translational motion from (4) is

$$P_1 = \rho u_{a0} L (1 - x^2)^{\frac{1}{2}}. \quad (8)$$

The total impulse for the translational motion is obtained as $\frac{\pi}{2} \rho u_{a0} L^2$. An experimental result provided by Lloyd, Stansby and Wright (1999) for pressure impulse at the center of the plate is about 1.052 (kpa ms) with $m = 118$ kg, $L = 0.5$ m, $h = 0.5$ m and the travelling speed at 5.4 m/s at impact. The recorded peak pressure is about 255 kpa. Our theoretical result of the pressure impulse is about 1.014 (kpa ms). If the gravity is also considered and $v_b + g\Delta t$ replaces v_b , the theoretical result is about 1.029 (kpa ms), which is in fair agreement with experimental result. The peak pressure can also be estimated using approximate formula $p = 2P_1/\Delta t$.

Post-impact pressure

In the studies of wave impact on walls the pressure after the impulsive peak is always greater than the initial pressure, with a few exceptions when especially large air pockets are trapped between wave and wall. Similarly in the experiments of Lloyd et al (1999) when a plate lands on a wave crest the pressure after the impact is greater than the initial atmospheric pressure. However, Lloyd et al also give pressures from a plate falling onto flat water, and these show post-impact pressures that are significantly below atmospheric pressure. This is an aspect of considerable interest since should

this be the case in a slam impact of a vessel the resulting change in direction of pressure forces on the structure could be especially dangerous if the structure is weakened by a slam.

This negative pressure has been measured and remarked upon before. Lewison (1969) gives a very full discussion of the plate, air and water motion and attributes the negative pressure to the volume available to the trapped air increasing due to the water being accelerated to a velocity larger than the plate's final velocity. However, in comparable wave impact problems there has to be an unusually large volume of air trapped to give such an effect. Indeed in experiments to study the effect of trapped air at a wall by comparing a modified pressure-impulse theory with measured pressures there were generally positive pressures.

The pressure immediately after the impact may be obtained from the pressure-impulse theory, from the values of velocities just after the impulse. This has been discussed in Cooker (1996) which indicates that the pressure is *increased* by $\frac{1}{2}\rho u_b^2$. We see no reason to suppose that an especially large air pocket is trapped beneath a falling plate. One difficulty is that Cooker's approach has some difficulties when the velocities after impact have a singularity, as they do in this case.

We are investigating this problem both from the pressure impulse approach, bearing in mind the results of Wood et al. (2000), and also from a more detailed point of view, and anticipate useful discussion at the Workshop.

We acknowledge the financial support of the United Kingdom Engineering and Physical Science Research Council.

References

- Cointe, R. 1989 Two-dimensional water-solid impact. *J. Offshore Mechanics and Arctic Engng.* **111** 109-114.
- Cointe, R. & Armand, J. -L. 1987 Hydrodynamic impact analysis of a cylinder. *J. Offshore Mechanics and Arctic Engng.* **109** 237-243.
- Cooker, M. J. 1996 Sudden changes in a potential flow with a free surface due to impact. *Q. Jl Mech. appl. Math.*, Vol. **49**, pp 581-591.
- Cooker, M. J. & Peregrine, D.H. 1995 Pressure-impulse theory for liquid impact problems. *J. Fluid Mech.* **297** 193-214.
- Korobkin, A. A. & Pukhnachov, V. V. 1988 Initial stage of water impact. *Ann. Rev. Fluid Mech.* **20** 159-185.
- Lesser, M. B. & Field, J. E. 1983 The impact of compressible liquids. *Ann. Rev. Fluid Mech.* **15** 97-122.
- Lewison, G. R. G. 1970 On the reduction of slamming pressures *Trans. RINA* **112** 285-306.
- Lloyd, P.M., P. K. Stansby & Wright, J. R. 1999 Slam forces and pressures on a flat plate due to impact on a wave crest. (Private communication)
- Wood, D.J., Peregrine, D.H. & Bruce, T. 2000 Wave impact on a wall using pressure-impulse theory. 1 Trapped air. *J. Waterways, Port, Coastal & Ocean Engng.* ASCE to appear.

AN INSTANTANEOUS MEASURE OF THE STRENGTH OF A BREAKER: "FOOT AND TOES"

D. H. Peregrine (d.h.peregrine@bris.ac.uk)

School of Mathematics, Bristol University, University Walk Bristol BS8 1TW, England

M. Brocchini (brocchin@idra.unige.it)

Dipartimento di Ingegneria Ambientale (DIAM), Via Montallegro 1, 16145 Genova - Italy

Abstract:

Development of suitable averaged boundary conditions for a free surface that is disturbed by strong turbulence leads to consideration of the origin of turbulence in a breaker, especially where the water falling down the front meets smooth water. A simple consideration of the averaging and a variation on the usual terminology leads to an instantaneous measure of breaker strength.

We consider spilling breakers, bores and the fully breaking bow waves of moving vessels. The masses of water tumbling down the front of such breakers fall onto the smooth incoming water at the leading edge of the breaker, which is where the major generation of turbulence takes place. Traditionally this is usually envisaged as a "roller" riding on the front of a wave meeting smooth water at its foot. In a paper that stimulated, or informed, a number of experimental measurements (e.g. Battjes & Sakai, 1981; Stive, 1980, 1984), Peregrine & Svendsen (1978) pointed out that the turbulent flow in a spiller can not easily be separated into a "roller" and the rest. There is a stream of turbulence initiated at the foot of the spiller, from which a roller can only be divided once mean streamlines are determined. Also the fluctuating velocities are just as large as the mean velocities. Hence, we choose not use the term "roller": though the concept is useful in indicating forward flow in the surface layer down the face of a breaker. We use "breaker" instead. We are keen to be able to model unsteady waves, and for such waves there is then no unambiguous way of determining a separation streamline to define a roller's boundary.

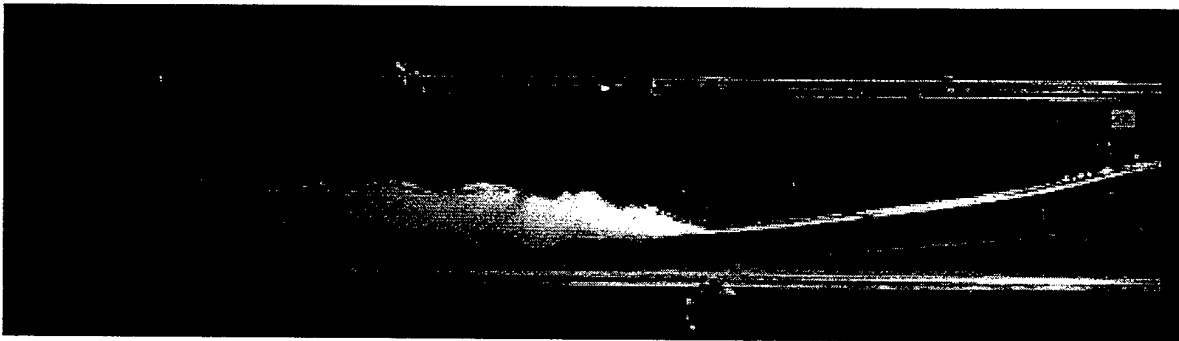


Figure 1. Turbulence at a hydraulic jump revealed by the mixing of a layer of tiny bubbles originally on the surface of the undisturbed water flowing over a weir.

There is another piece of traditional terminology that it seems advisable to change. The forward edge of a breaker's turbulent splashing front is sometimes referred to as the "toe" of the breaker. Measurements, especially of hydraulic jumps, show a continuous mean surface through the breaker at this point. However, there are problems in defining a mean surface at an unsteady irregular boundary as the turbulent flow moves over the smooth surface in front. A very similar problem discussed in Brocchini & Peregrine (1996, §3) for the swash zone on a beach and the

same ideas hold in this problem. If one considers the mean height of water as one moves through from smooth water to a breaker there is a smooth transition as mentioned, and as perceived in figure 1. However, if one looks from above at the breaker's boundary it is not smooth and an averaging along the base of the breaker will give a mean position for the base of the breaker which is not the same as where its mean profile departs from the smooth water surface. We propose that a mean position for base of a breaker, however determined from the three-dimensional character of the turbulent flow, should be called the "foot" of the breaker. In addition we propose that the fluctuations of the boundary between smooth and turbulent flow at the water surface be called the "toes" of the breaker, see figure 2. The effect of this is that at the foot of the breaker there is a finite depth of water above the smooth water level.



Figure 2. Turbulence and splashing of breaking waves (part of a tidal bore in the River Severn) showing the non-uniformity of the foot of the breakers..

This apparently simple change of terminology brings with it a real benefit to the modelling of breakers. There are problems in defining the strength of a breaker. For example, comparisons are often made with hydraulic jumps of the same height in order to estimate dissipation, with varying success. The concept of a breaker foot, with toes fluctuating around it, may be combined with results from our study towards defining free surface boundary conditions in the presence of strong turbulence (Brocchini & Peregrine 2000a,b). Strong turbulence at a water-air free surface can lead to splashing and a disconnected surface as in a breaking wave. In Brocchini &

Peregrine (2000b) we approach from the Reynolds averaging ideas common in turbulence. Averaging to obtain boundary conditions for such flows first requires equations of motion for the two-phase region which we designate as a "surface layer". These are derived using an integral method, then averaged conservation equations for mass and momentum are obtained. Boundary conditions appropriate for use with averaged equations in the body of the water are obtained by integrating across the two-phase surface layer. A number of terms arise for which closure expressions must be found for practical use. Knowledge of the properties of strong turbulence at a free surface is insufficient to make such closures. However, preliminary discussions are given for two simplified cases in order to stimulate further experimental and theoretical studies.

Two dominant parameters appear from our analysis. One is the equivalent depth of the surface layer, d , i.e. the thickness of water in the two-phase layer, the other is its mean velocity, U . Thus, given the position of a breaker's foot, the two-phase layer at that point yields, at least, these two parameters, which may be used as a measure of breaker strength. Such measures are in principle functions of time for unsteady breakers, and hence appropriate parameters for unsteady modelling. Much work needs to be done to learn what suitable closure equations should be for these surface layer variables.

One possible approach to parameterisation at the breaker's foot would be to follow up Peregrine & Svendsen's (1978) suggestion that the primary generation of turbulence occurs at the foot of a breaker in a similar manner to a mixing layer. This is not quite the traditional mixing layer that has been the subject of many studies clarifying its turbulent structure, since the velocities of the two layers that come together at the breaker's foot are in opposing directions relative to the foot rather than in the same direction, or with one being at rest. Thus breaker turbulence is initiated in a more violent fashion, especially since one of the layers is already strongly turbulent. Indeed a measure of the size of the "toes" may also be a useful strength parameter for this turbulence. However, an extrapolation of mixing layer data would be a sensible starting point until comparisons with more relevant experimental data becomes possible.

At present we are unaware of any measurements of an appropriate type at a breakers foot. There are, of course, substantial difficulties in making measurements in a splashing environment, though for small breakers, up to about 3cm in height, surface tension ensures a smooth surface, so measurements may be easier. However, we hope that we may stimulate such studies.

The "foot and toes" concept seems sound at over a wide range of scales. At large scales there is substantial splashing of blobs of water, as may be seen when viewing a breaker head on at near water level. At small scales surface tension restrains the blobs so that there is no splashing but as shown there are still significant toes. It is only at the smallest scale where ripples might ride ahead of the breaker that the toes may be smoothed. Even so figure 3 shows two small breakers, one with ripples and one without, where the turbulence is strong enough to cause the three-dimensional irregularities.

Our suggestion is that the two variables, d and U , at the breakers foot are worthy of further investigation, both experimentally and as parameters in models of breakers.



Figure 3. Turbulent breakers dominated by capillary effects. The left-hand wave shows how turbulent fluctuations influence the amplitude of ripples, whereas the turbulence overwhelms ripple production for the right-hand wave.

We gratefully acknowledge useful discussion with Ib Svendsen, and funding from the European Commission with contract MAS3-CT97-0081 Surf and Swash Zone Mechanics (SASME), and from the Office of Naval Research in its NICOP program, award no. N00014-97-1-0791.

References

- Battjes, J.A. & Sakai, T. (1981) Velocity field in a steady breaker. *J.Fluid Mech.* **111**, 421-437.
- Brocchini, M. & Peregrine, D.H., (1996) Integral flow properties of the swash zone and averaging, *J. Fluid Mech.* **317**, pp.241-273.
- Brocchini, M. & Peregrine, D.H., (2000a) The dynamics of turbulent free surfaces. Part 1. Description of strong turbulence at a free surface. *Preprint*. 25pp.
- Brocchini, M. & Peregrine, D.H., (2000b) The dynamics of turbulent free surfaces. Part 2. Free-surface boundary conditions. *Preprint* 33pp.
- Peregrine, D.H. (1985) Water waves and their development in space and time, *Proc. Roy. Soc. Lond. A* **400** pp.1-18.
- Peregrine, D.H. & Svendsen, L.A. (1978) Spilling breakers, bores and hydraulic jumps, *Proc. 16th Inter. Conf. Coastal Engng.* **1** pp.540-550.
- Stive, M.J.F. (1980) Velocity and pressure field of spilling breakers. *Proc.17th Coastal Engng.Conf. A.S.C.E.* **1**, 547-566.
- Stive, M.J.F. (1984) Energy-dissipation in waves breaking on gentle slopes, *Coastal Engineering*, **8**, pp.99-127.

TRANSIENT MOTION OF A VERTICAL CYLINDER: MEASUREMENTS AND COMPUTATIONS OF THE FREE SURFACE

C. H. RETZLER*, J. R. CHAPLIN* & R. C. T. RAINEY**

*Department of Civil & Environmental Engineering, University of Southampton, **WS Atkins, London

1. Introduction

In recent years there have been concerns in the offshore oil industry over the violent motions of the water surface produced around a vertical cylinder by relatively large steep waves (say height/diameter = 1, height/length = 0.1). The concerns are threefold: (1) the water may reach the deck of the platform, as for example on Shell's Brent Bravo platform in the north Sea in January 1995; (2) the local pressures may damage the platform, as for example on BP's Schiehallion platform in the eastern Atlantic in November 1998; (3) a transient ringing vibration may be excited, as observed for example in the model tests of the Norwegian Draugen, Troll and Heidrun platforms in 1992. Figure 1 shows the water surface motion in question, as observed during earlier experiments (Chaplin *et al.*, 1997). The jet shown on the left (which is more pronounced if the wave is steeper) is thought to be associated with (1) and (2). The mound of water on the right that forms after the crest has passed appears to be associated with the 'secondary loading cycle' (see Chaplin *et al.*, 1997) which is an important feature of (3).

It was argued by Rainey (1997) that some of these features would also be seen in the simpler case of a vertical cylinder undergoing a transient motion in still water. The present experiments explore this suggestion. The experimental set-up, and initial results with harmonic cylinder motion, were reported in Chaplin *et al.* (1999).

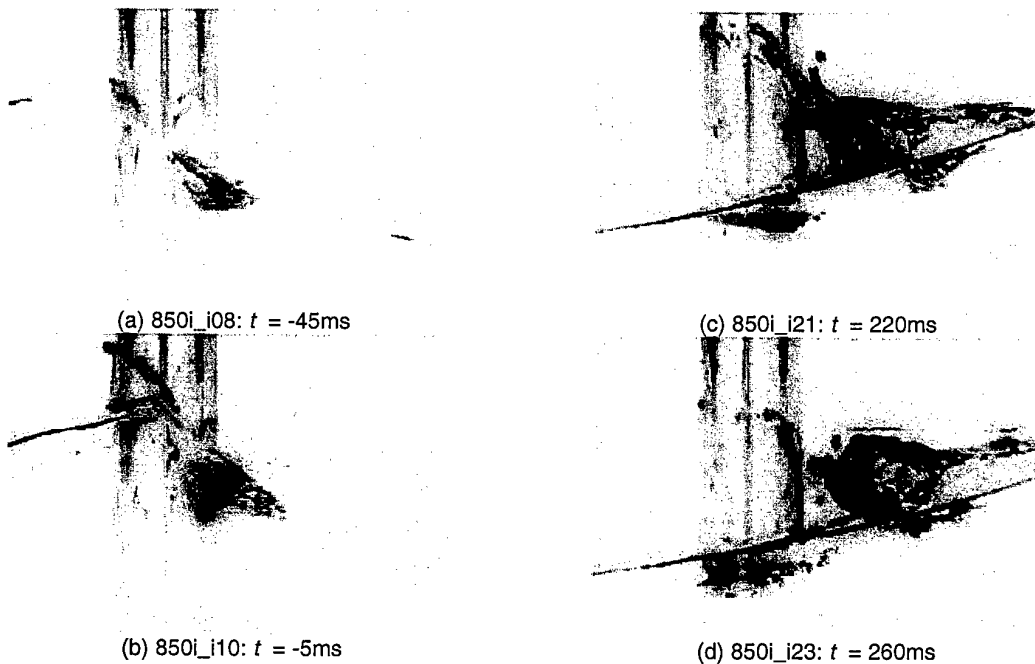


Figure 1. Negative images of a focused wave passing a cylinder of diameter 0.1m: height/diameter ≈ 1.8 , height/length ≈ 0.1 (case 770 of Chaplin *et al.*, 1997). Images (a) and (b) show the jet on the front face of the cylinder. At its peak, the elevation of the top of the jet was almost one diameter higher than that shown in (b). Images (c) and (d) show the water surface rise at the rear.

2. The misleading nature of the small-time expansion scheme

In Rainey (1997) it is pointed out that the small-time expansion scheme predicts violent motion of the water surface around a cylinder moving from rest with a finite initial acceleration. In fact, the same is true if the motion starts arbitrarily smoothly – that is to say, with only the N th derivative of cylinder velocity v being given a finite

value initially (say $v = t^N$). This is because the lowest-order term in the velocity potential, say ϕt^M , must satisfy the boundary-condition $\phi = 0$ on the horizontal plane of the still water surface. Otherwise the dynamic free-surface condition would produce a term proportional to t^{M-1} in the free-surface elevation, from which the kinematic free-surface condition would produce a term proportional to t^{M-2} in the velocity potential. This would contradict our assumption above that the lowest-order term was ϕt^M .

Moreover, the cylinder-surface boundary condition is a velocity proportional to t^N , given the cylinder velocity assumed above, so we deduce that $M = N$, for otherwise ϕ would be zero everywhere. Thus as well as having $\phi = 0$ on the still water surface, ϕ gives unit cylinder velocity. It is therefore the velocity potential given in Rainey (1997), which has infinite vertical velocity at the waterline around the cylinder. By contrast, our experiments show no such violent water surface motion. The same observation, for the case of "impulsive accelerations", is made by Wang & Chwang (1989). It thus appears that the small-time expansion method is fundamentally misleading in this regard. It would be interesting to know if the same is true for the improved small-time expansion schemes, developed hitherto only in 2-D, by Joo et al (1990) and King & Needham (1994).

3. The linear solution for arbitrary transient motion of a vertical cylinder in still water

For the purpose of identifying non-linear behaviour in the observations, comparisons can be made with the linear time domain solution developed by McIver (1994). The case of sinusoidal motion is described in Chaplin *et al.* (1999). From an arbitrary velocity $V(t)$ imposed on the cylinder, McIver's solution is based on a theorem stated by Mei, (1983). This gives a velocity potential for the flow as

$$\phi = \Omega V(t) + \int_{-\infty}^t \Gamma(t-\tau) V(\tau) d\tau \quad (1)$$

where $\Omega V(t)$ is the 'infinite frequency' potential and (as in the case of ϕt^M above) $\Omega = 0$ on the still water plane $z = 0$. For the purposes of computing the free surface elevation $\eta(r, \theta, t)$ from the dynamic boundary condition, the first term in (1) plays no part, and

$$\eta = - \int_{-\infty}^t \left. \frac{\partial \Gamma(t')}{\partial t'} \right|_{t'=t-\tau, z=0} V(\tau) d\tau, \quad (2)$$

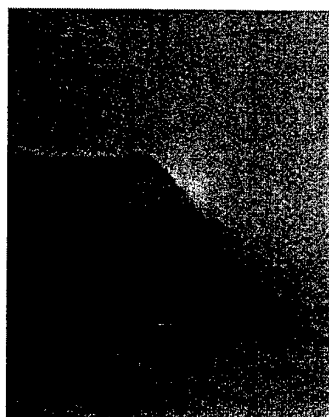
taking length and acceleration scales such that the cylinder's radius and acceleration due to gravity are both unity. The kernel in (2) is given by

$$\left. \frac{\partial \Gamma}{\partial t} \right|_{z=0} = - \frac{2 \cos \theta}{\pi} \int_0^\infty \frac{\cos Wt \tanh qh C_1(qr)}{q |H_1'(q)|^2} dq, \quad (3)$$

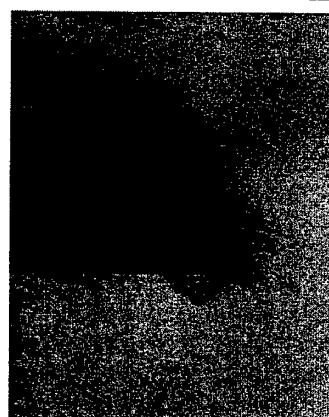
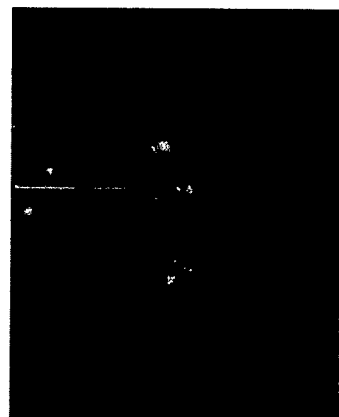
where h is the water depth, C_1 and H_1 are functions defined in McIver (1994), and $W^2 = q \tanh qh$.

4. Experimental results, compared with the linear solution.

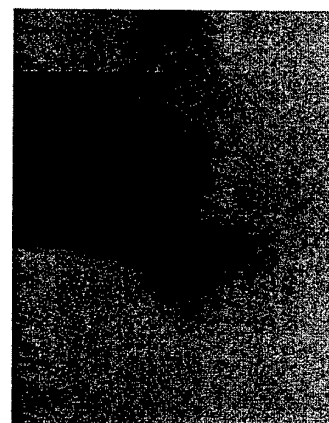
The experiments were carried out in a tank which is equipped with a servo-controlled carriage, to which the 200mm diameter vertical test cylinder was mounted. Measurements are presented here for cases where the cylinder was accelerated horizontally from rest, driven at constant velocity, and then brought to rest again. The overall displacement in each test was equivalent to 75% of a diameter. In figure 2 measurements of the resulting water surface displacements obtained from wave gauges at the front and rear faces of the cylinder are compared with computed time-series. These were obtained as described above for the same points, using the velocity of the cylinder, and taking its cylindrical coordinates as moving with it. (Conventionally, the coordinates are taken as fixed, but the difference is the second order and thus theoretically immaterial.) Agreement deteriorates as the Froude number is increased, and in particular the linear theory overestimates the motion of the water surface on both sides of the cylinder during and after its deceleration. It is worth recalling that the predictions do not capture the effect of that part of the pressure distribution on the cylinder that is related to the square of its velocity. This is on the scale of the stagnation pressure, which, in steady flow in the absence of separation, would act on both the front and rear faces. Broken lines in figure 2 show the effect simply of adding the corresponding head to the water surface elevations at each point. The result is a marginal improvement in the agreement.



(a) 100ms. There is no sign of the violent surface motion predicted by the small-time expansion. Instead, the surface motion is well-behaved and closely follows the linear solution in accordance with the conclusions of Wang & Chwang (1989).



(b) 200ms. The surface is more elevated at the front of the cylinder than in the linear prediction, and shows the first signs of breaking. At the back of the cylinder, a steep localised mound begins to form, similar to that seen in figure 1. This is absent in the linear prediction.



(c) 300ms. The cylinder has just stopped. At the front, the breaking crest is well separated from the cylinder's surface. At the back, the mound is pronounced and has formed two plunging jets. In front of the cylinder the water surface remains close to the still water level, and does not follow the steep descent of the linear solution.



(d) 400ms. At the front of the cylinder, the breaking crest has moved about one radius away from the cylinder surface. At the back of the cylinder, the jets have broken, and are travelling forwards circumferentially. A vertical jet has started to form at the cylinder surface.

Figure 3. Images obtained from high speed video recordings (in the top row) and the linear solution (below) for the case shown in the right hand column of figure 2. Times are measured from the start of the motion.

In figure 3, images of the observed water surface are shown above those obtained from linear predictions for the same motion and at the same times.

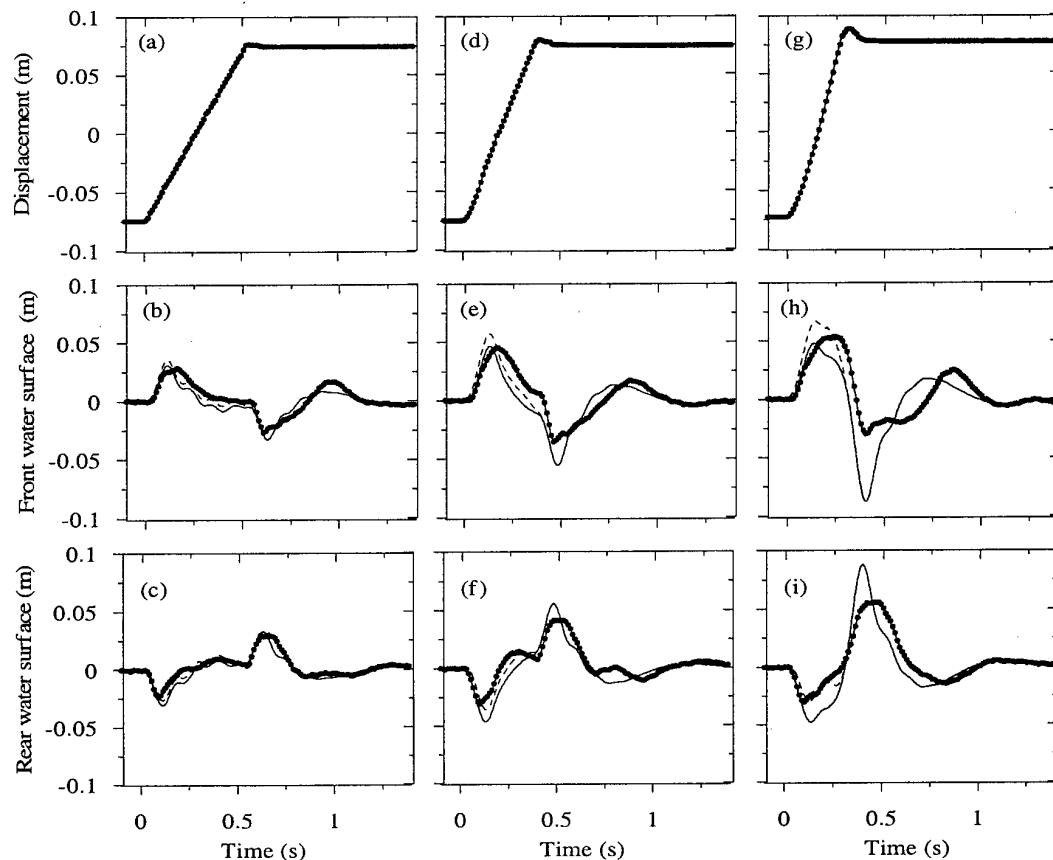


Figure 2. Measurements (points) and predictions (lines) of water surface elevations at the front (b,e,h) and the back (c,f,i) of the cylinder undergoing the displacements shown in (a,d,g). Froude numbers were 0.20, 0.28, 0.36 for cases in the left hand column, in the centre, and on the right respectively.

This work was supported by EPSRC (grant GR/L69879), with support in kind from WS Atkins plc.

References

- Chaplin J.R., Retzler C.H. & Rainey R.C.T., 1999 Waves generated by a vertical cylinder moving in still water. Proc. 13th WWFEB
- Chaplin, J.R., Rainey, R.C.T. & Yemm, R.W., 1997 Ringing of a vertical cylinder in waves. *JFM* **350**, 119-147.
- Joo S.W., Schultz W.W. & Messiter A.F., 1990 An analysis of the initial-value wavemaker problem. *JFM* **214**, 161-183.
- King, A.C. & Needham, D.J., 1994 The initial development of a jet caused by fluid, body and free-surface interaction. Part 1. A uniformly accelerating plate. *JFM* **268**, 89-101.
- McIver, P., 1994 Transient fluid motion due to the forced horizontal oscillations of a vertical cylinder. *Applied Ocean Research* **16**, 347-351
- Mei, C.C., 1983 *The applied dynamics of ocean surface waves*. John Wiley, New York.
- Rainey, R.C.T., 1997 Violent surface motion around vertical cylinders in large, steep waves – is it the result of the step change in relative acceleration? Proc. 12th WWFEB, 215-218, Marseilles [ed. B.Molin].
- Wang, K-H & Chwang, A.T., 1989 Free-surface flow produced by accelerating vertical cylinder *J.Eng. Mech.* **115**(7) 1559-1566.

DAMPING OF SLOSHING DUE TO TANK ROOF IMPACT

Olav F. Rognesbakke and Odd M. Faltinsen
Department of Marine Hydrodynamics
Norwegian University of Science and Technology
N-7491 Trondheim, Norway

A partially filled smooth tank will experience violent fluid motion when forced to oscillate with a period close to the highest natural period of the fluid motion. When the free surface hits the tank roof, a water impact similar to slamming occurs, and energy is dissipated. A statistical treatment of sloshing demands time efficient calculations. Thus, the analytic approach proposed by Faltinsen et al. [1] is well suited for the task. However, the analytical model does not account for impact of water on the roof. By estimating the kinetic and potential energy loss in the jet generated during the impact and relating this to the total energy in the fluid, an equivalent damping term can be introduced in the analytical model. A Wagner's method [2] is applied. When the impact angle between the rising free surface and a chamfered tank roof is large, results from a similarity solution are utilized to correct the estimated energy loss. Numerical simulations for the free surface elevations for a heavy impact case are compared with experimental results. Numerical force calculations and experimental data for different fluids are presented for an LNG tank model.

Consider a rectangular smooth and rigid tank forced to oscillate harmonically in surge. The fluid is incompressible and the flow is two-dimensional and irrotational. The height and the breadth of the tank are H and l . The coordinate system (x, z) is fixed relative to the tank with origin in the mean free surface and in the center of the tank (See Fig. 1.). Violent fluid motion will occur due to resonant motions and small damping. For non-impacting fluid flow, the damping is very small and mainly due to viscosity in the boundary layers [3]. Nonlinearities are significant and cause finite amplitudes at resonance.

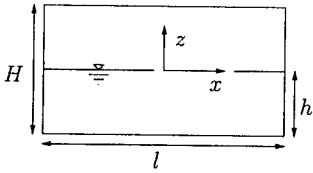


Figure 1: Coordinate system and tank dimensions.

When the fluid motion does not impact the tank roof, [1] is applied. This is based on a Bateman-Luke variational principle and use of the pressure in the Lagrangian of the Hamilton principle. This results in a system of nonlinear ordinary differential equations in time. The unknowns are generalized coordinates β_i of the free surface elevation. The procedure applies to any tank shape as long as the tank walls are vertical near the mean free surface. The equation system for the rectangular tank excited in surge, heave and pitch follows. The free surface elevation ζ is written as

$$\zeta = \sum_{i=1}^N \beta_i(t) \cos\left(\frac{\pi i(x + 0.5l)}{l}\right) \quad (1)$$

The forced oscillation amplitude is assumed small and of $O(\epsilon)$. Further $\beta_i = O(\epsilon^{\frac{1}{3}})$, $i = 1, 3$. Higher order terms than ϵ are neglected in the nonlinear equations. The following system of nonlinear ordinary differential equations for the generalized coordinates describing the free surface are derived for forced motions

$$\begin{aligned} (\ddot{\beta}_1 + \sigma_1^2 \beta_1) + d_1(\ddot{\beta}_1 \beta_2 + \dot{\beta}_1 \dot{\beta}_2) + d_2(\ddot{\beta}_1 \beta_1^2 + \dot{\beta}_1^2 \beta_1) + d_3 \ddot{\beta}_2 \beta_1 + P_1(\dot{v}_{0x} - S_1 \dot{\omega} - g\psi) + Q_1 \dot{v}_{0z} \beta_1 &= 0, \\ (\ddot{\beta}_2 + \sigma_2^2 \beta_2) + d_4 \ddot{\beta}_1 \beta_1 + d_5 \dot{\beta}_1^2 + Q_2 \dot{v}_{0z} \beta_2 &= 0, \\ (\ddot{\beta}_3 + \sigma_3^2 \beta_3) + d_6 \ddot{\beta}_1 \beta_2 + d_7 \ddot{\beta}_1 \beta_1^2 + d_8 \ddot{\beta}_2 \beta_1 + d_9 \dot{\beta}_1 \dot{\beta}_2 + d_{10} \dot{\beta}_1^2 \beta_1 + P_3(\dot{v}_{0x} - S_3 \dot{\omega} - g\psi) + Q_3 \dot{v}_{0z} \beta_3 &= 0, \\ \ddot{\beta}_i + \sigma_i^2 \beta_i + P_i(\dot{v}_{0x} - S_i \dot{\omega} - g\psi) + Q_i \dot{v}_{0z} \beta_i &= 0, \quad i \geq 4. \end{aligned} \quad (2)$$

Here v_{0x} and v_{0z} are projections of translational velocity onto axes of Oxz and $\omega(t)$ is the value of angular velocity of coordinate system $Oxyz$ with respect to an earth fixed coordinate system. The calculation formulas for the coefficients σ_i , P_i , S_i , Q_i , $i \geq 1$ and d_j , $j = 1, \dots, 10$ are given in [1]. The equation system is solved numerically by a fourth order Runge-Kutta method.

When the water impacts on the tank roof, fluid damping is believed to occur. The hypothesis is that the kinetic and potential energy in the jet flow caused by the impact is dissipated. Fig. 2 shows the evolution of an impact in the upper left corner of an LNG ship tank. The formation and overturning of the jet are evident. The linear damping terms $2\xi\sigma_i\dot{\beta}_i$ are included in each of eq. 2. The damping is found as an equivalent damping so that the energy ΔE removed from the system during one full cycle is equal to the kinetic and potential energy lost in the impact, i.e. $\xi = \frac{1}{4\pi} \frac{\Delta E}{E}$. E is the total energy in the system, which is found from $\dot{E} = F_x v_{0x}$ for forced surge motion. An iterative procedure is followed. A simulation over one



Figure 2: Snapshots of upper left corner of LNG tank during impact

period is started with no damping. A first estimate of ξ is found. The simulation is repeated, which results in a new ΔE and thereafter a new ξ . This is done for iteration $i > 1$ as $0.5 \frac{\Delta E_i + \Delta E_{i-1}}{\bar{E}} = 4\pi\xi$. Typically, 5 iterations are sufficient for convergence.

The impact model is based on a generalized Wagner's approach [2]. The tank is assumed rigid so possible hydroelastic effects are ignored. The inflow velocity $V(t)$ and the slope of the impacting surface can be found directly from Eq. 1. The impact velocity is approximated by a linear function $V(t) = V_0 + V_1 t$. $t = 0$ is the time of impact. The impacting surface is approximated by a parabola with radius of curvature R . The wetted length $c(t)$ follows from Wagner's integral equation. This solution can be corrected by accounting for the tank walls and bottom. Details can be found in [4]. However, this effect is not important and thus is not included here. The Wagner's analysis assumes a small angle between undisturbed free surface and tank roof. A similarity solution presented by Zhao and Faltinsen [5], valid for large angles, is applied to correct the energy estimates when this is not the case. The energy estimates obtained from Wagner's analysis are multiplied by a reduction factor. Fig. 3 gives the definitions of symbols used in the slamming analysis. $c(t)$ is the horizontal distance from $x = 0$ to the spray root, δ is the thickness of the jet, u_c is the velocity of the control surface following the spray root and u_a is the fluid velocity in the jet direction at the spray root. Fig. 4 introduces symbols applied in the similarity solution. s_j is the length of the jet, β is the deadrise angle of the wedge, β_0 is the angle of the triangular jet and ζ_L and ζ_B are the vertical distances to the jet root and tip of the jet, respectively.

The similarity solution is derived for a constant impact velocity. However, the reduction factor found for the energy loss for a constant speed is also applied for the linearly decreasing impact velocity.

The kinetic energy flux into the jet is calculated for both the similarity solution and Wagner's approach for a wedge and constant impact speed. The kinetic and potential energy flux through the jet can generally be found as

$$\frac{dE_{kin}}{dt} = \frac{\rho}{2} u_a^2 \delta u_f, \quad \frac{dE_{pot}}{dt} = \rho g (H - h) M_{flux} \quad (3)$$

when a constant velocity across the jet is assumed, and the potential energy loss is estimated as the potential energy the mass of the water in the jet has relative to the level of the mean free surface. u_f is the relative velocity between the fluid velocity and the control surface velocity, $u_f = u_a - u_c$. $M_{flux} = \delta u_f$ is the flux of mass into the jet. Wagner's solution gives [5]

$$u_a = 2 \frac{dc}{dt}, \quad u_c = \frac{dc}{dt}, \quad c = \frac{\pi V t}{2 \tan(\beta)}, \quad \delta = \frac{\pi V^2 2c}{16 (\frac{dc}{dt})^2} = \frac{\tan(\beta) V t}{4} \quad (4)$$

The kinetic energy flux and mass flux is then

$$\left. \frac{dE_{kin}}{dt} \right|_w = \frac{\rho V^4 \pi^3 t}{16 \tan^2(\beta)}, \quad M_W = \frac{dc}{dt} \delta = \frac{\pi V^2}{8} t \quad (5)$$

The jet in the similarity solution is assumed to be triangular, giving

$$\frac{s_j}{Vt} = \frac{\zeta_B - \zeta_L}{Vt \sin(\beta)}, \quad \frac{\delta}{Vt} = \frac{s_j}{Vt} \tan(\beta_0) \quad (6)$$

The mass flux into the jet is then equal to

$$M_S = \frac{d}{dt} \left[\frac{1}{2} s_j \delta \right] = \frac{d}{dt} \left[\frac{1}{2} \left(\frac{\zeta_B - \zeta_L}{\sin(\beta)} \right)^2 \tan(\beta_0) \right] = \left[\frac{\zeta_B - \zeta_L}{Vt \sin(\beta)} \right]^2 \tan(\beta_0) V^2 t \quad (7)$$

A constant flux velocity in the similarity solution is found as $u_f = \frac{M_S}{\delta}$. By observing that the z component of u_c must be equal to $d\zeta_L/dt$ plus the constant downward velocity V , u_c can be estimated as

$$u_c = \frac{d\zeta_L/dt}{\sin(\beta)} + \frac{V}{\sin(\beta)} \quad (8)$$

Again, substituting in Eq. 3, the kinetic energy flux for the similarity solution is

$$\left. \frac{dE_{kin}}{dt} \right|_S = \frac{\rho V^4 t \tan(\beta_0)}{2 \sin^4(\beta)} \left[\left(\frac{d\zeta_L/dt}{V} \right) + 1 + \frac{\zeta_B - \zeta_L}{Vt} \right]^2 \left[\frac{\zeta_B - \zeta_L}{Vt} \right]^2 \quad (9)$$

Figs. 5 and 6 show the difference in kinetic energy and mass flux for Wagner's approach and the similarity solution. The numerical results are based on numbers presented in [5]. When $\beta \rightarrow 0$, the results by the similarity solution and Wagner agree. It is planned to derive a solution for finite deadrise angle that matches the local jet flow and the global solution. This will give more rational estimates of energy loss during an impact with changing impact velocity. Using analytically based computations are advantageous relative to a direct numerical approach due to the extremely fine discretization needed both in time and space in order to capture the details of a jet flow.

The free surface elevation is compared with experimental results for a heavy impact case in Fig. 7. The tank is rectangular with $l = 1.73\text{m}$, a filling height $h = 0.5\text{m}$ and a total height of $H = 1.02\text{m}$. The tank roof is horizontal. The period and amplitude of the sway excitation are $T = 1.71\text{s}$ and $\epsilon_0 = 0.05\text{m}$, respectively. The figure suggests that a satisfactory estimate of the impact velocity $d\zeta/dt$ can be calculated. This value is important in the prediction of slamming loads.

Fig. 8 shows the dimensions of the prismatic LNG tank model for which computational and experimental results of horizontal forces are presented in Fig. 9. The experimental results are found in [6]. A small ever-present non-impact damping was introduced and time series of 400s simulated in order to reach a steady state motion. The chamfer angle is 45 degrees. This gives a reduction factor for the kinetic energy loss of 0.27 and a factor of 0.22 for the potential energy loss. Wagner's approach heavily over-predicts the energy loss for large angles. A good agreement is seen for results away from resonance. At resonance the current approach predicts too large forces. However, if no impact damping was introduced, the maximum force was far larger, about 1.4 times the one presented. Sources of error are discussed below.

The energy loss through the jet and evolution of the wetted length $c(t)$ are shown in Fig. 10. In this special case, approximately 1/5 of the total energy in the fluid is lost during the two impacts of one cycle. The kinetic and potential energy loss are of similar magnitude. The main part of the energy loss happens during the initial phase of the impact. Hence, the errors due to an assumption of a linearly decreasing impact velocity and constant free surface curvature should not be large. At $t = 35.425$ the impact moves past the chamfered part of the roof.

There are several uncertainties and sources of error in the presented methodics, of which some have been discussed already. The accuracy of the nonlinear flow model is of great importance. Missing nonlinear effects can for an excitation close to resonance result in a misprediction of the maximum free surface elevation, leading to a relatively larger error in the estimation of the damping level. This will be investigated by using a fifth order theory, which is a further development of [1]. Local downward vertical accelerations above $1g$ are calculated for some impact cases. According to Penney and Price [7] this is a criterion for breaking of a standing wave. The only back-coupling from the impact to the analytic model is through damping. When the duration and spatial extent of the impact are large, this simplification may no longer suffice.

Force calculation neglects the horizontal force directly caused by the impact. It means that the horizontal force is calculated like in [1]. The additional force has a magnitude of approx. 10% of the total force for a heavy impact in the LNG tank. The impulse is close to zero.

Further work will also focus on the continued development of a nonlinear boundary element method designed for calculating the impact jet flow. This approach will serve to validate the current methodics, as well as provide an alternative damping estimate for heavy impact situations. The wish to still use the nonlinear analytical method for the non-impact flow is motivated by the dramatic difference in simulation time.

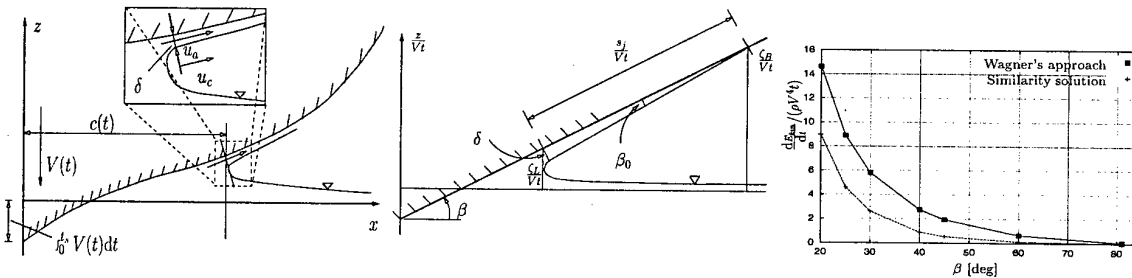


Figure 3: Definitions for the slamming analysis

Figure 4: Definitions used in the similarity solution

Figure 5: Kinetic energy flux

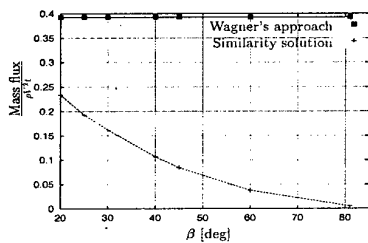


Figure 6: Mass flux

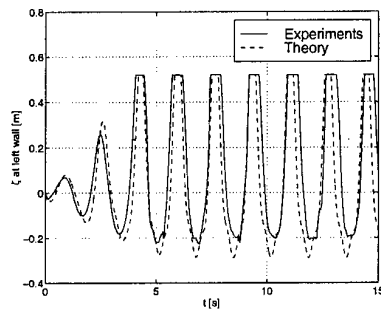


Figure 7: Free surface elevation for a case of heavy roof impact

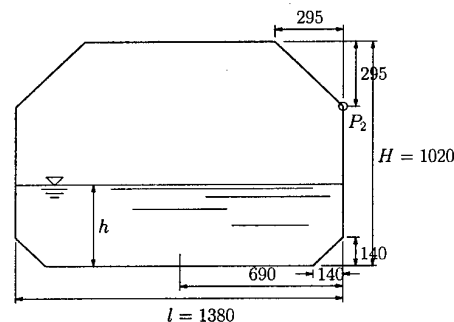


Figure 8: Prismatic LNG tank model. All numbers in [mm]

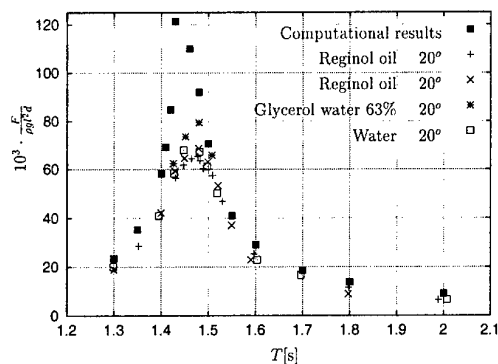


Figure 9: LNG tank $\frac{h}{l} = 0.4$, $\frac{e_0}{l} = 0.01$. Computational results and experimental data for various fluids

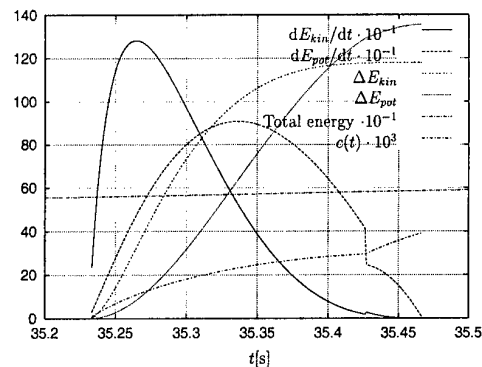


Figure 10: LNG tank $\frac{h}{l} = 0.4$, $\frac{e_0}{l} = 0.01$ and $T = 1.43$ s. Change of energy during an impact

Acknowledgements

This work is part of a Ph. D. thesis sponsored by the Research Council of Norway.

References

- [1] FALTINSEN, O. M., ROGNEBAKKE, O. F., LUKOVSKY, I. A., TIMOKHA, A. N. Multidimensional modal analysis of nonlinear sloshing in a rectangular tank with finite water depth. Accepted for publication in *J. Fluid Mech.*
- [2] WAGNER, H. (1932) Über Stoss- und Gleitvorgänge and der Oberfläche von Flüssigkeiten. *Zeitschr. F. Angew. Math. und Mech.* **12**, 193-235
- [3] KEULEGAN, G. H. (1958) Energy dissipation in standing waves in rectangular basins. *J. Fluid Mech.* **6**, 33-50
- [4] FALTINSEN, O. M., ROGNEBAKKE, O. F. (1999) Sloshing and slamming in tanks. *HYDRONAV'99-MANOEUVERING'99* Gdansk-Ostrada, Poland
- [5] ZHAO, R., FALTINSEN, O. M. (1993) Water entry of a two-dimensional bodies. *J. Fluid Mech.* **246**, 593-612
- [6] FALTINSEN, O. M., OLSEN, H. A., ABRAMSON, H. N., BASS, R. L. (1974) Liquid slosh in LNG carriers. Det Norske Veritas, Publication No. 85
- [7] PENNEY, W. G., PRICE, A. T. (1952) Finite Periodic Stationary Gravity Waves in a Perfect Liquid. *Phil. Trans. Royal Soc. (London)* **A 244**, 254-284

DESIGN OF THREE-DIMENSIONAL BODIES SUBJECT TO WATER IMPACT

Scolan Y.-M., ESIM, 13451 Marseille, France

Korobkin A.A., Lavrentyev Institute of Hydrodynamics Novosibirsk 630090, Russia

1. Introduction

In spite of increasing needs of offshore industry and shipbuilding, the three-dimensional impact problem is far to be well solved yet. However, within the classical assumptions of Wagner's theory [1] there exists a way to derive exact solutions of the 3D impact problem thus providing preliminary qualitative results. This can be done with the help of so-called inverse Wagner's problem [2].

Wagner's approach is formally valid for the initial stage of a blunt body impact onto the liquid free surface. During this stage the boundary conditions can be linearised and imposed on the initial position of the free surface. In the direct problem of impact the body shape and the velocity of its entry are given. For the most general configurations this problem is very complicated and difficulties are connected with the coupled resolution for both the liquid flow and the position of the contact region between the entering body and the liquid. The impact problem is non-linear even within the linearised Wagner's theory. The direct Wagner's problem has been effectively solved for both two-dimensional and axisymmetric cases [3]. Three-dimensional effects are handled at present mainly by using aspect-ratio correction factors.

The inverse problem offers an attractive alternative. Within this problem the body velocity and the contact region shape are prescribed at any instant and it is required to determine the liquid flow and to reconstruct the body shape. The inverse problem of impact is linear and, even in the most complicated cases, can be reduced to integral equations and quadratures. For elliptical contact regions the calculations can be performed analytically.

For various applications of industrial interest the case of elliptic contact regions is general enough to cover a wide range of physical configurations [3]. Semi-axes of the contact region at any instant of time can be either given in advance (inverse Wagner's problem) or defined by additional constraints (optimization problem). It should be noted that the optimization problem includes the solution of the inverse Wagner's problem but can be much more complicated if the constraints are complex. In the present report a free fall of a blunt body onto an initially calm liquid free surface is considered. The mass of the body M is given, and the hydrodynamic force on the body $F(t)$, where t is the time, is prescribed for t being small enough. We shall reconstruct the body shape, entry of which provides the given resistance force. The problem is considered under the following assumptions: (i) the liquid is ideal and incompressible; (ii) the liquid flow is three-dimensional and irrotational; (iii) the contact region between the liquid and the body is elliptic; (iv) the eccentricity of the contact region e is independent of time; (v) the boundary conditions on the liquid surface can be linearised and imposed on its initial position. The considered problem can be reduced to the inverse Wagner's problem and effectively analyzed. The obtained theoretical results may be of help for preliminary design of bodies subject to water impact.

2. Formulation of the problem

Initially ($t = 0$) the resting liquid occupies the lower half-space, $z < 0$, and a body touches the liquid free surface, $z = 0$, at a single point which is taken as the origin of the Cartesian coordinate system $Oxyz$. The vertical velocity of the body $U(t)$ is governed by the second Newton's law:

$$MU_t = Mg - F(t) \quad t > 0, \quad \text{and} \quad U(0) = U_0, \quad (1)$$

where g is the gravity and $F(t)$ is the hydrodynamic force acting on the entering body. According to hypotheses mentioned above, the velocity potential $\phi(x, y, z, t)$ satisfies the following equations:

$$\begin{cases} \phi_{xx} + \phi_{yy} + \phi_{zz} = 0 & z < 0 \\ \phi = 0 & z = 0, (x, y) \notin D(t) \\ \phi_z = -U(t) & z = 0, (x, y) \in D(t) \\ \phi \rightarrow 0 & x^2 + y^2 + z^2 \rightarrow \infty \end{cases} \quad (2)$$

where $D(t)$ is the contact region between the liquid and the moving body. The boundary of $D(t)$ is referred to as the contact line, position of which is convenient to describe in the implicit form: $t = t_c(x, y)$. It is clear that $t_c(0, 0) = 0$ and $D(t) = \{x, y \mid t_c(x, y) < t\}$. If the body position is given at any instant as $z = f(x, y) - h(t)$ —where the function $f(x, y)$ describes the body shape and the function $h(t)$ is the penetration depth, $h_t = U(t)$ and $h(0) = 0$ —the matching condition on the contact line follows from the time integration of the kinematic free surface condition:

$$f(x, y) = h(t_c(x, y)) + \int_0^{t_c(x, y)} \frac{\partial \phi}{\partial z}(x, y, 0, \tau) d\tau \quad (x, y) \in R^2. \quad (3)$$

The hydrodynamic force $F(t)$ (within the Wagner's approximation) is then introduced in equation (1) to give the velocity:

$$F(t) = \frac{d}{dt} [M_a(t)U(t)] \Rightarrow U(t) = \frac{M(U_0 + gt)}{M + M_a(t)} \quad (4)$$

where $M_a(t)$ is the added mass of the floating disk $D(t)$. It is worth noting that the force depends on the shape of the contact region and the body velocity but not directly on the body shape. If the function $t_c(x, y)$ is given, the shape of the contact region $D(t)$ is known at any instant of time. The added mass $M_a(t)$ is then calculated; equation (4) yields the entry velocity $U(t)$ finally providing the penetration depth $h(t)$. The vertical velocity of the liquid free surface $\phi_z(x, y, 0, t)$ follows from (2) and the function $f(x, y)$ is calculated from (3). The procedure is straightforward and provides exact solutions of the Wagner's problem. Inverse Wagner's problem for self-similar flows was discussed by Borodich [4].

Analysis of the described procedure indicates that a main difficulty in the inverse problem is to calculate the distribution of the velocity potential $\phi(x, y, 0, t)$ over the disk $D(t)$ from the boundary-value problem (2). Once the distribution has been found the computations are reduced to quadratures which can be evaluated with a given accuracy. Accuracy of the numerical solution of problem (2) is not easy to control; that justifies the importance of its exact analytical solutions.

3. Inverse problem for elliptic case

Analytical solution of problem (2) is known [5] for elliptic region $D(t)$. This solution can be derived as a limiting case of the well-known solution for an ellipsoid moving in an unbounded liquid. The boundary of the contact region is given by equation: $x^2/a^2(t) + y^2/b^2(t) = 1$. For given semi-axes $a(t)$ and $b(t)$, $b(t) > a(t)$, the function $t_c(x, y)$ is obtained by resolving this equation with respect to time t . The solution of (2) provides the distribution of the velocity potential over the contact region

$$\phi(x, y, 0, t) = -\frac{U(t)a(t)}{E(e)} \sqrt{1 - \frac{x^2}{a^2(t)} - \frac{y^2}{b^2(t)}}, \quad e = \sqrt{1 - a^2/b^2}, \quad (5)$$

and the vertical velocity of the liquid free surface

$$\frac{\partial \phi}{\partial z}(x, y, 0, t) = -\frac{U(t)}{E(e)} \left[E\left(\arcsin \frac{b(t)}{\sqrt{\lambda + b^2(t)}}, e\right) - \sqrt{\frac{b^2(\lambda + a^2)}{\lambda(\lambda + b^2)}} \right], \quad \frac{x^2}{a^2(t) + \lambda} + \frac{y^2}{b^2(t) + \lambda} - 1 = 0, \quad (6)$$

where $\lambda(x, y, t)$ is the positive root of the second equation, and $E(\theta, e)$ and $E(e)$ are the elliptic integrals of the second kind. The added mass of the elliptic disk is $M_a = (2\pi/3)\rho a^2 b/E(e)$. The entry velocity $U(t)$ is given by (4) and the vertical velocity of the free surface by (6) for any x and y . Evaluation of the integral in (3) finalizes the reconstruction of the entering body shape.

The case of constant entry velocity is more simple. In that case, it is shown [2] that the entry of elliptic paraboloid provides an elliptic contact region. Elliptic paraboloid with two parameters is a quite general shape to approximate almost any blunt body near the impact point. The obtained analytical solution can be used to evaluate the aspect-ratio correction factor and to analyse the

accuracy of results given by the strip theory for elongated bodies.

4. Design of entering body shape

The problem of reconstruction of entering body shape which provides a prescribed history of the resistance force $F(t) = F_*\beta(t/T)$ is considered. Here F_* is the constant, T is the time scale and $\beta(t')$ is the non-dimensional function, $t' = t/T$. The entering body shape has to be determined for given function $\beta(t')$ and given constants M , U_0 , F_* , T and e . Two cases are considered: (i) $\beta(t') = 1$ and (ii) $\beta(t') = t' \exp(-t')$. The first case is expected to provide the body shape, for which the entry velocity reduces in an optimal way without high acceleration. The second case roughly imitates a typical history of the impact force.

In the first case the body acceleration is constant, $U(t) = U_0(1 - c_0 t_1)$, and the semi-axis are:

$$b(t) = b_0[t_1/(1 - c_0 t_1)]^{\frac{1}{3}}, \quad a(t) = b(t)\sqrt{1 - e^2},$$

$$t_1 = \frac{gt}{U_0}, \quad c_0 = \frac{F_*}{Mg} - 1, \quad b_0^3 = \left(\frac{3}{2\pi} \frac{E(e)}{1 - e^2} \right) \frac{F_*}{g\rho}$$

It is seen that $b(t) = O(t^{\frac{1}{3}})$ as $t \rightarrow 0$, which indicates that $f(x, y) = O([x^2 + y^2]^{\frac{3}{2}})$ close to the impact point. With known semi-axes of the contact region, the inverse Wagner's problem is solved according to the procedure described in section 3.

In the second case the semi-axes are given by the formulae $a(t) = b(t)\sqrt{1 - e^2}$,

$$b(t) = b_0 \delta^{\frac{1}{3}} \left[\frac{\gamma(t_1/\delta)}{1 + t_1 - \delta(c_0 + 1)\gamma(t_1/\delta)} \right]^{\frac{1}{3}}, \quad \delta = \frac{gT}{U_0}, \quad \gamma(\xi) = 1 - (1 + \xi) \exp(-\xi).$$

Now $f(x, y) = O([x^2 + y^2]^{\frac{3}{4}})$ close to the impact point. Calculations were performed for $U_0 = 4.43\text{m/s}$, $F_* = 29333\text{N}$, $T = 0.0113\text{s}$ and $M = 100\text{kg}$, which correspond to the falling height of 1m and the maximum deceleration of 10g. Two cases were considered: $e = 0.1$ and $e = 0.9$. The time variations of the body acceleration and velocity are illustrated in figure 1a. The time growths of the semi-axes $a(t)$ and $b(t)$ are depicted in figure 1b. It should be noted that the penetration depth $h(t)$ is always smaller than the characteristic lengths of the contact region, which is in accordance with the hypothesis of linearization of the Wagner's theory. The calculated body shapes are plotted in figures 2. In addition the free surface shape is drawn up to its contact with the body. The contact line for $e = 0.9$ is clearly a three-dimensional curve. The deformations of the free surface for a 3D configuration vanish more rapidly than for the 2D case as the distance increases from the body. Side views show the wetted parts of the body surface; there the horizontal lines present the positions of the contact line for different times with the time step $\delta t = 0.0048\text{s}$. The calculated shapes can be used in drop experiments to justify the presented approach.

5. References

1. Wagner H., 1932, "Über Stoss- und Gleitvorgänge an der Oberfläche von Flüssigkeiten.", ZAMM 12, pp 193-215.
2. Scolan Y.-M. & Korobkin A.A., 1999, "Three dimensional theory of impact problem. Part 1: Inverse Wagner problem.", submitted to publication.
3. Korobkin A.A. & Pukhnachov V.V., 1988, "Initial stage of water impact.", Ann. Rev. Fluid Mech., Vol. 20, pp 159-185.
4. Borodich F.M., 1988, "Similarity in the three-dimensional penetration problem of solid bodies into an idel incompressible fluid.", Zh. Prikl. Mekh. Tekh. Fiz. 5, pp 127-132.
5. Leonov M.J., 1940, "Problems and applications of the theory of potential.", Prikl. Mat. Mech. Vol. 4, 5-6, pp 73-86.

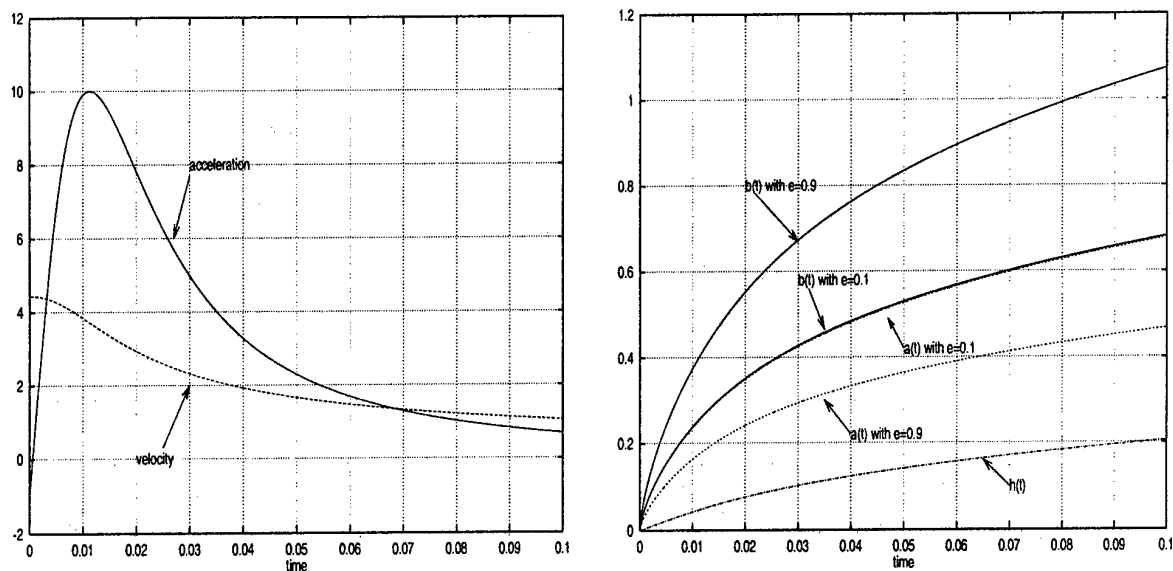
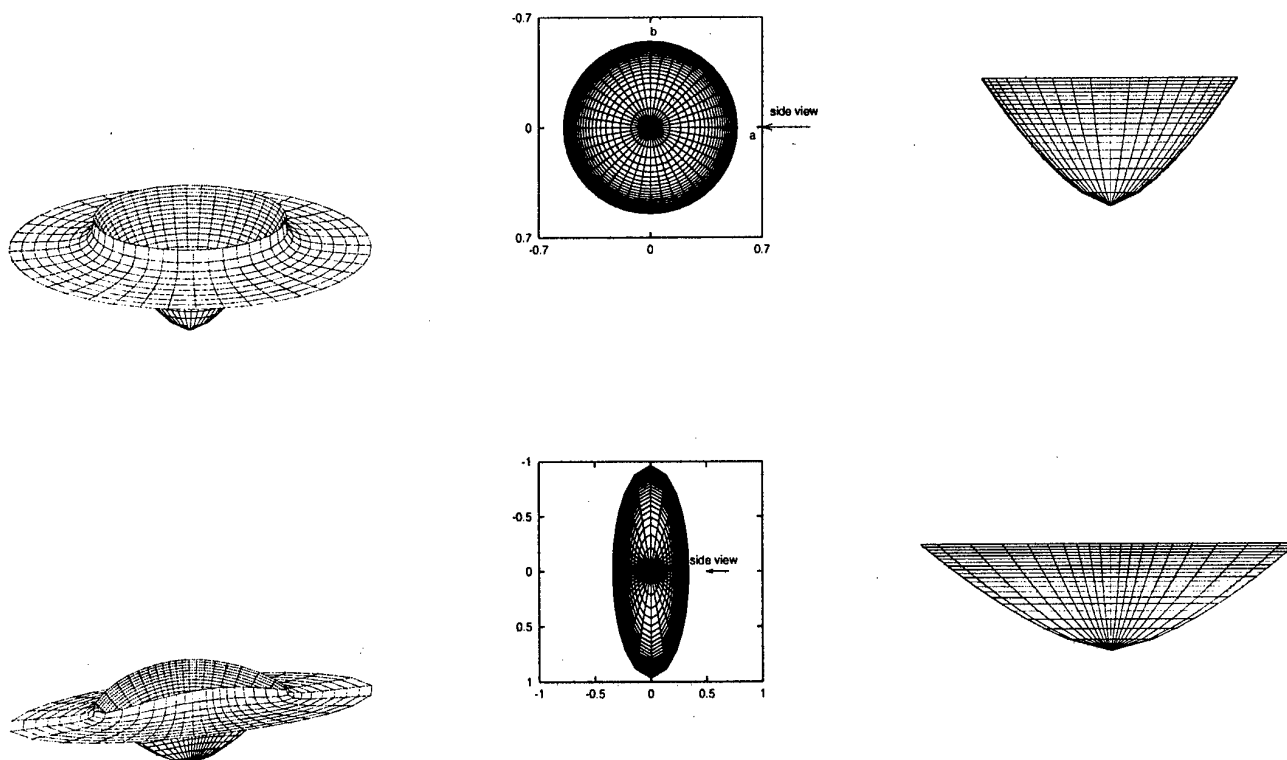


Figure 1: a) Time variations of the velocity and non-dimensional acceleration (in absolute values); b) time variations of the semi-axes: $a(t)$ and $b(t)$ and penetration depth $h(t)$ for two eccentricities: $e = 0.1$ and $e = 0.9$.

Figure 2: *left*: generated shapes with eccentricities $e = 0.1$ and $e = 0.9$ drawn at instant $t = 0.1s$; *center and right*: upper and side views of the shape under the undisturbed free surface; the vertical size is stretched with respect to the horizontal dimensions (factor 3:left, 4:right).



NONLINEAR WAVE GROUP EVOLUTION IN DEEP AND INTERMEDIATE-DEPTH WATER: EXPERIMENTS AND NUMERICAL SIMULATIONS

L. Shemer, Haiying Jiao and E. Kit

Department of Fluid Mechanics, Faculty of Engineering, Tel-Aviv University Tel-Aviv 69978, Israel

Among model equations which describe evolution of nonlinear waves, the Zakharov (1968) equation and the Dysthe modified nonlinear Schrödinger (MNLS) equation (Dysthe 1979, Lo & Mei 1985) are considered to be the most general. Stiassnie (1984) showed that this MNLS equation, which is valid for higher wave steepness than the conventional cubic Schrödinger equation, could be derived from the Zakharov equation assuming narrow frequency spectrum approximation. The use of Zakharov equation to simulate the modification of propagating wave groups, hence, can be advantageous lifting the limitation of narrow band spectrum. Although those equations are known for decades, only in a limited number of studies the theoretical predictions based on those models are directly compared with the experimental results. Such a comparison is carried out here. We report on systematic and accurately controlled experiments in which evolution of the well-defined wave groups in deep and intermediate-depth water is studied along the tank. The spatial evolution of the same wave groups is studied numerically by solving properly discretized Zakharov equations as well as the Dysthe equation. The selection of this problem is due to two main reasons. First, transformation of wave groups propagating toward the beach has significant practical consequences, while being of considerable scientific importance for understanding the nonlinear dynamics of water waves. Second, in an earlier study of this problem (Shemer et al. 1998) it was demonstrated that the cubic Schrödinger equation is incapable to describe correctly the complicated pattern of the spatial evolution of nonlinear wave groups, in particular the asymmetric shape of the evolving group envelope. The application of more advanced models is thus warranted.

Experiments were carried out in an 18 m long, 1.2 m wide and 0.6 m deep wave tank. A computer-controlled paddle-type wavemaker is located at one end of the tank, while a wave-energy-absorbing beach is placed at the far end. A probe-supporting bar with four wave gauges is mounted on a separate carriage, which can be moved along the tank. The distance between the two consecutive probes is 0.4 m. Detailed measurements of instantaneous surface elevation are carried out at eight fixed measuring stations, thus covering 32 distances from the wavemaker. Wave groups with a Gaussian envelope have been studied. The following periodically repeated driving signal is applied to the wavemaker:

$$s(t) = a_0 \exp[-(t/5T)^2] \cos(\omega_0 t), \quad \omega_0 = 2\pi/T, \quad -16T < t < 16T. \quad (1)$$

This signal produces wave groups, which are widely separated and have a relatively broad discrete spectrum. Experiments are carried out for two carrier wave periods, $T=0.7s$ and $T=0.9s$, satisfying nearly deep-water conditions, and for three values of the driving amplitude a_0 , corresponding to a nearly linear, nonlinear, and strongly nonlinear regimes. In the vicinity of the wavemaker, the maximum values of wave steepness $\varepsilon = A_0 k_0$, in the group were 0.07, 0.14 and 0.21, respectively (A_0 and k_0 being the carrier wave amplitude and number).

The MNLS coupled system of equations, which describes the evolution of the envelope $A(\eta, \xi)$, where $\eta = \varepsilon^2 kx$, $\xi = \varepsilon \omega(x/c_g - t)$, and c_g is the group velocity, and of the potential of the induced mean current ϕ , in the fixed coordinates is:

$$A_\eta + i A_{\xi\xi} + i |A|^2 A + 8\varepsilon |A|^2 A_\xi + i 4\varepsilon A \phi_\xi|_{z=0} = 0 \quad (2)$$

$$4\phi_{\xi\xi} + \phi_{zz} = 0 \quad (-h < z < 0) \quad (3)$$

with ϕ satisfying the following boundary conditions:

$$\phi_z = |A|^2_\xi \quad z = 0, \quad \phi_z = 0, \quad z = -h. \quad (4a, b)$$

Following Lo and Mei (1985), equations (2) - (4) are solved using the pseudo-spectral method and the split-step Fourier method.

A modification of the Zakharov equation is necessary to describe the spatial evolution of the wave spectrum, in contrast to the temporal evolution described by the conventional version of this equation. The spatial discrete Zakharov mode-coupled equations describe evolution of the complex "amplitude" $B_j(x)$ of each free wave in the spectrum due to four-wave interactions in a unidirectional space domain, which satisfy the near resonant condition:

$$\omega_0 + \omega_1 - \omega_2 - \omega_3 = 0, \quad |k_0 + k_1 - k_2 - k_3| \leq O(\varepsilon^2 k_0). \quad (5)$$

Equation for the spatial evolution of each component can be written as (Agnon 1999):

$$i \cdot c_g \frac{\partial B_0}{\partial x} = \sum_{\omega_1, \omega_2, \omega_3} T_{0,1,2,3} B^*_{\omega_1} B_{\omega_2} B_{\omega_3} \delta_{0+\omega_1-\omega_2-\omega_3} e^{-i(k_0+k_1-k_2-k_3)x}, \quad (6)$$

where $T_{0,1,2,3}$ is the interaction coefficient. Since the variable in (6) has the same dimensions as in the conventional Zakharov equation, the expressions for calculating the bound components and the kernels used e.g. in Stiassnie & Shemer (1984) are valid for (6) as well. After the number of free modes is chosen and the resonating quartets are selected, evolution equation is written for each free mode. The spatial evolution of the whole wave field along the tank is thus expressed as a set of mode-coupled nonlinear complex ordinary differential equations (ODEs), which can be solved using the modified Runge-Kutta method.

The development of asymmetry of the group envelope can be seen in the simulated surface elevations. In Fig. 1, the experimental results at $x = 2.89$ m and $x = 8.67$ m are presented in Figs. 1a, b, respectively. The corresponding MNLS model simulations at these two locations are presented in Figs. 1c, d, whereas the Zakharov model simulations are given in Figs. 1e, f. At $x = 2.89$ m, both these simulations are quite similar to the experimental result, the agreement being slightly better for the Zakharov model. This similarity between the simulated surface elevations in both models and experimental observations is retained away from wavemaker, at $x = 8.67$ m.

The instantaneous surface elevation at a given location in the Zakharov model is obtained as a superposition of all spectral modes, including free and bound waves. It thus seems natural to compare the evolution of the wave amplitude spectra measured at various locations along the tank, with the corresponding simulations based on the present version of the Zakharov model. Such a comparison is carried out in Fig. 2. The spectrum widening along the tank observed in the experiments (left column) is faithfully reproduced in the simulations (right column). The evolving along the tank spectra in Fig. 2 become gradually more asymmetric, resembling the spatial evolution of the envelope shape observed in Fig. 1.

The present study is thus characterized by experiments and numerical simulations carried out in an inter-related fashion. A convincing agreement between the simulations and the experimental results is obtained. In particular, impressive correspondence can be noted between the skewed wave group shapes at relatively remote locations in the experiments and the numerical simulations. The similar results obtained from two completely different mathematical models confirm the validity of the simulations according to both methods. Under present experimental conditions, both the MNLS and the Zakharov models perform quite well, with the Zakharov model representing the experiments somewhat more faithfully.

References

- Agnon, Y. (1999). Private communication.
- Dysthe, K. B. (1979). "Note on a modification to the nonlinear Schrödinger equation for application to deep water waves." *Proc. R. Soc. London, A* **369**, 105-114.
- Lo, E., and Mei, C. C. (1985). "A numerical study of water-wave modulation based on a higher-order nonlinear Schrödinger equation." *J. Fluid Mech.* **150**, 395-416.
- Shemer, L., Kit, E., Jiao, H.-Y., Eitan, O. (1998) Experiments on nonlinear wave groups in intermediate water depth. *J. Waterway, Port, Coast. & Ocean Engng.* **124**, 320-327.
- Stiassnie, M. (1984). "Note on the modified Schrödinger equation for deep water waves." *Wave Motion.* **6**, 431-433.

Stiassnie, M., and Shemer, L. (1984). "On modifications of the Zakharov equation for surface gravity waves." *J. Fluid Mech.* **143**, 47-67.

Zakharov, V. E. (1968) Stability of periodic waves of finite amplitude on the surface of a deep fluid. *J. Appl. Mech. Tech. Phys.* **9**, 190-194.

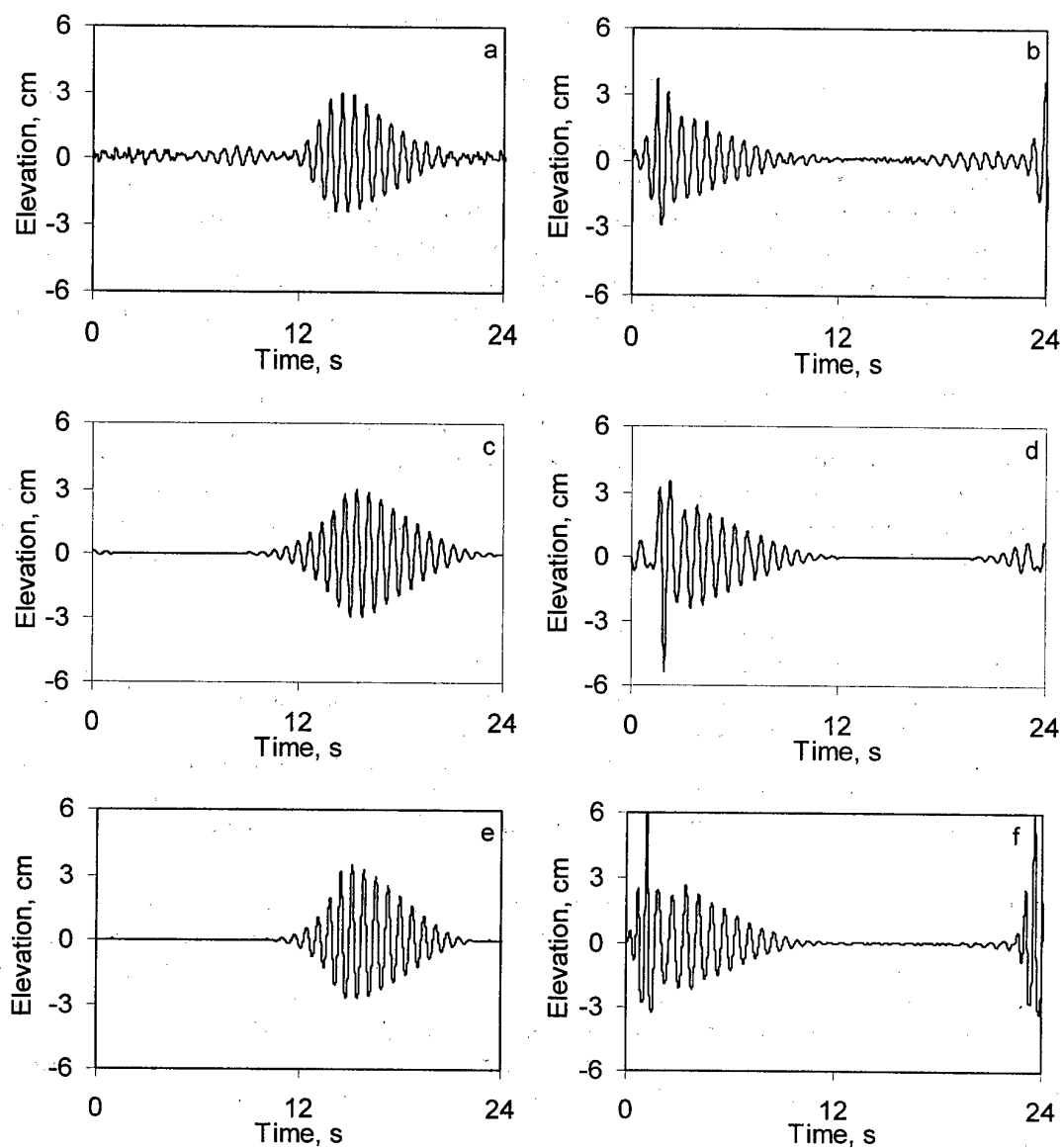


Figure 1 (a) & (b) Experimental results for $\varepsilon=0.21$, $T=0.7$ s at $x=2.89$ m and $x=8.67$ m; (c) & (d) MNLS simulations at the corresponding locations; (e) & (f) Zakharov simulations with 39 free modes.

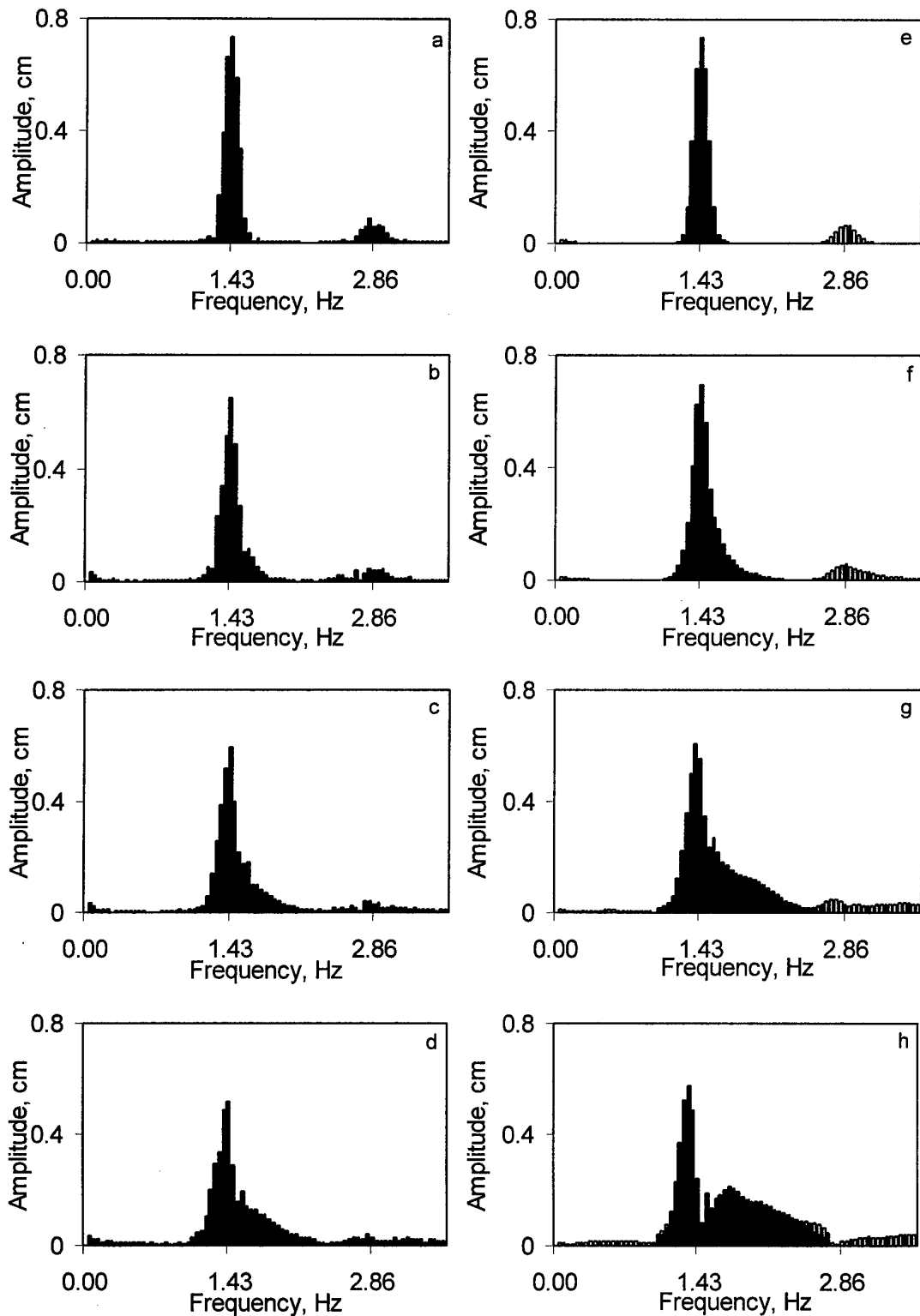


Figure 2. (a - d) Amplitude spectra of measured surface elevation for the conditions of Figure 1. Locations along the tank: (a) $x = 0.24$ m, (b) $x = 2.89$ m, (c) $x = 5.78$ m, and (d) $x = 8.67$ m; (e - h) Simulated amplitude spectra using Zakharov model with 39 free modes at the corresponding locations.

Suppression of Wave Breaking in Nonlinear Water Wave Computations Including Forward Speed

Anil K. Subramani and Robert F. Beck
University of Michigan, Ann Arbor, Michigan 48109, U.S.A.

INTRODUCTION

Much progress has been made over the years in the development of numerical methods for the prediction of nonlinear water waves and wave loads on structures (e.g., Beck, 1998). However, due to inherent limitations in the mathematical model in most of the prevalent methods, a major and persistent difficulty has existed in the simulation of highly nonlinear free-surface flows: the characteristic occurrence of spray and wave breaking causes the computations to terminate abruptly.

Motivated by the desire to prevent even a fleeting generation of spray and breaking waves from curtailing the numerical simulations, a variety of artifices have been formulated in order to overcome the difficulty. Examples include the works of Haussling and Coleman (1979); Wang et al. (1993); and Subramani et al. (1998). The present work describes recent advances in the suppressing of wave breaking.

The approaches above consist essentially of two parts: (1) detecting the likely incidence of wave breaking and then (2) controlling the wave breaking locally. In an improvement over the previous techniques, Subramani et al. (1998) devised a general yet simple numerical criterion, based on the local free-surface curvature, for the likely incidence of wave breaking. The wave breaking was then suppressed in a manner similar to Haussling and Coleman's (1979)—by exerting an additional pressure distribution on the wave, in the vicinity of the breaking wave.

However, the approach proved not to be robust: it was difficult to determine the appropriate amount of damping and there were also problems with extending the technique to calculations involving forward speed, especially in three dimensions. These limitations are overcome through a new, improved technique, which is used in conjunction with the existing, curvature-based criterion for wave breaking. In this paper, we will provide background and describe the technique briefly. Sample calculations will also be presented, including gravity waves in a two-dimensional numerical wave tank and two-dimensional transom stern calculations at forward speed.

BACKGROUND

On the basis of empirical studies, Subramani et al. (1998) proposed the following criterion as a "trigger" for the activation of localized wave damping in their fully nonlinear computations. A wave may go on to break if it satisfies the relation, $|ka| > 0.35$, where a is the wave amplitude and k is the free-surface curvature. Using this criterion and an additional free-surface pressure distribution (as in Haussling and Coleman, 1979), they demonstrated the successful suppression of the breaking wave observed in the physical experiment of Grue et al. (1993). This is reproduced in figure 1.

The curvature-based criterion for breaking is simple and easy to implement, even when waves of different frequencies are present. The curvature may be computed easily—in two dimensions at least—using a local three-point formula arising from the fitting of a circle through three consecutive free surface nodes. This formula gives agreeable results with the analytically obtained curvatures for wave-like profiles.

The new, localized-fairing technique continues to use the exceeding of the threshold $|ka|$ to flag "problem" free-surface nodes. The difference lies in how a breaking wave (the growth of the flagged nodes) is subsequently suppressed. The working of the technique is depicted in figure 2 (a detailed snapshot of the wave surface at the end of a time-step at time, $t=11.30$) and is described below.

METHODOLOGY

The technique lends itself well to Euler-Lagrange methods for solving water wave problems, but its “post-processing nature” also renders it adaptable to other kinds of methods. For illustrative purposes, consider an instant within the UM-DELTA method (Beck, 1998) when the boundary-value problem has been solved and the free surface has been updated by the growths, $\partial h / \partial t$ and $\partial f / \partial t$ (h being the wave elevation and f , the velocity potential). The updated free surface, before fairing, is given by the dashed line in figure 2, with the free-surface nodes marked by hollow circles. Wave breaking, when it occurs, is manifested as a large growth in h at certain nodes.

The use of the curvature-based criterion enables us to flag such nodes (which satisfy $|ka| > 0.35$) and simply to fair through them. As sketched in figure 2, we fit a cubic spline through the non-flagged nodes and re-position the problem nodes on this faired wave surface. In essence, we “bridge” through the flagged, problem free-surface nodes. Extensive tests have shown that a cubic spline gives reliable results.

This technique is essentially a variation of Wang et al.'s (1993) “peeling” technique; however, “bridging” may be more apt a description of the present treatment. In their studies on wave group evolution and deformation, Wang et al. had performed an ad hoc reduction—based on a limiting value of hk , where k is the wave number—of the wave crest at the leading wave front. Another important difference between the two techniques is that we do an identical fairing for f – in order to ensure that there is no mismatch between h and f for nodes on the new free surface. Wang et al. prescribed an exponential decay in elevation when faced with evaluating f for nodes on a free surface that had been lowered because of a peeling-away.

Note that implied in our technique is the discarding of the computed values of $\partial h / \partial t$ and $\partial f / \partial t$ for the nodes that seem poised—on the basis of the local curvature—to break. The flagged nodes by themselves are not discarded, it is important to add. Following the fairing and the setting of updated Dirichlet boundary conditions for the free surface, all the free-surface nodes are carried into the boundary value problem at the next time step. Also, the fairing process is carried out at the end of each intermediate time-step in the 4th-order Runge-Kutta time-stepping algorithm.

The post-fairing calculation, in which the tendency to break has been suppressed at a particular instant of time, is also shown in figure 2. Note also that the difference seen between the “post-fairing wave surface” and the “without damping” calculation is a cumulative result of the damper having been activated over the previous time-steps.

Given the fairing-through of the problem free-surface nodes that occurs, there is an inevitable but slight loss of mass in our calculations. Figure 3 shows the extent to which mass conservation is controlled in the calculation discussed above. In the figure are plotted the percentage change of fluid volume in the tank (obtained by integrating the wave heights throughout the tank) for both, a typical “no breaking involved” calculation and one in which the breaking-wave damper is activated. For the calculation in question, the mass loss (about 0.05%) is much less than the uncertainty that creeps into the calculations (about 0.20%) due to an in-between-sources non-satisfaction of the body boundary condition at the ends of the tank.

FORWARD SPEED CALCULATIONS

One of the advantages of the present technique is its ease of application and robustness for instances of wave breaking in calculations involving forward speed. Consider, for example, the breaking wave behind a two-dimensional transom stern (in inviscid flow). This is a problem that has been tackled by several researchers, including—recently—Scorpio and Beck (1997). The first wave crest behind the transom stern has been observed to break in the case of dry-transom flow at F_H (Froude number based on transom depth) of 2.3.

In his doctoral work, Scorpio (1997) used a variant of Haussling and Coleman's artificial surface-pressure distribution to damp this breaking wave successfully. However, this approach is difficult to rely on because the appropriate amount of damping is not easily determined. Furthermore, questions also exist as to the optimal form of the damping term for forward speed calculations.

On the other hand, no such difficulties exist in the present fairing technique. Its ability to suppress the transom stern breaking wave is shown in figure 4. Convergence of the damped solutions is demonstrated in figure 5.

The technique holds promise for three-dimensional ship wave calculations as well. The wave-breaking criterion may be used to detect the likely occurrence of wave breaking along the predominant wave-propagation direction. The fairing technique may then be used to suppress any wave breaking. We have been using this technique to overcome the numerical instabilities otherwise experienced in the calculation of the bow wave. Some of the discrete free-surface nodes in the vicinity of the ship's bow are flagged and faired through, as previously described.

CONCLUSIONS AND FUTURE WORK

A new, improved technique has been developed for suppressing wave breaking in the computations of nonlinear water waves. The technique may be applied, in conjunction with Subramani et al.'s (1998) curvature-based criterion for the detection of likely wave breaking, within a variety of numerical methods for simulating free-surface flows.

The technique has been successfully tested for a wide range of water wave computations—gravity waves in a two-dimensional tank; waves behind a two-dimensional transom stern; and the spray sheet at the bow of several three-dimensional surface ships. Future work will involve the continued testing of the technique for extreme cases of wave breaking in three-dimensional ship-wave computations.

ACKNOWLEDGMENTS

This research was funded by the Office of Naval Research. The computations were supported by allocations of high performance computing resources through the U.S. Department of Defense's High Performance Computing Modernization Program and the National Partnership for Advanced Computational Infrastructure. AKS is thankful for the financial support provided by the Rackham School of Graduate Studies in the form of a Dissertation Fellowship.

REFERENCES

- Beck, R.F., "Fully Nonlinear Water Wave Computations Using a Desingularized Euler-Lagrange Time-Domain Approach," Nonlinear Water Wave Interaction, International Series on Advances in Fluid Mechanics, U.K., 1998.
- Grue, J., Bjorshol, G., and Strand, O., "Higher Harmonic Wave Exciting Forces on a Vertical Cylinder," Pre-Print Series, Department of Mathematics, University of Oslo, 1993.
- Haussling, H.J. and Coleman, R.M., "Nonlinear Water Waves Generated by an Accelerated Circular Cylinder," Journal of Fluid Mechanics, vol. 92, part 4, 1979, pp. 767–781.
- Scorpio, S.M., "Fully Nonlinear Ship-Wave Computations Using a Desingularized Method," Ph.D. Dissertation and Report No. 334, Department of Naval Architecture and Marine Engineering, University of Michigan, 1997.
- Scorpio, S.M., and Beck, R.F., "Two-Dimensional Inviscid Transom Stern Flow," Proceedings, 12th International Workshop on Water Waves and Floating Bodies, Carry le Rouet, France, 1997.
- Subramani, A.K., Beck, R.F., and Schultz, W.W., "Suppression of Wave Breaking in Nonlinear Water Wave Computations," Proceedings, 13th International Workshop on Water Waves and Floating Bodies, Alphen aan den Rijn, The Netherlands, 1998.
- Wang, P., Yao, Y., and Tulin, M.P., "Wave Group Evolution, Wave Deformation, and Breaking: Simulations Using LONGTANK, a Numerical Wave Tank," Proceedings, 3rd International Offshore and Polar Engineering Conference, Singapore, 1993.

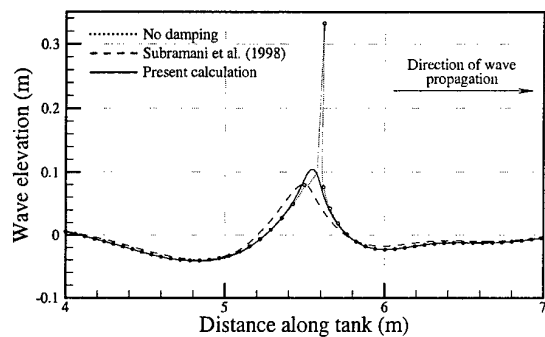


Figure 1. Snapshot of the wave surface at $t=11.35$ in a simulation of the physical experiment of Grue et al. (1993).

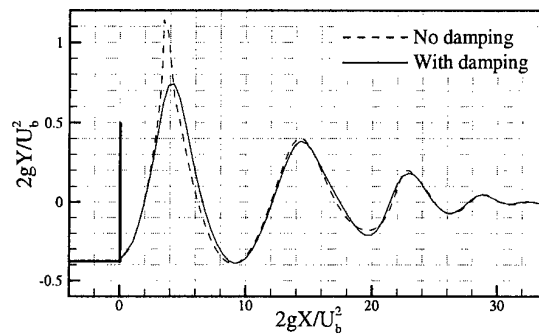


Figure 4. Application of the fairing technique to the breaking wave behind a two-dimensional transom stern.

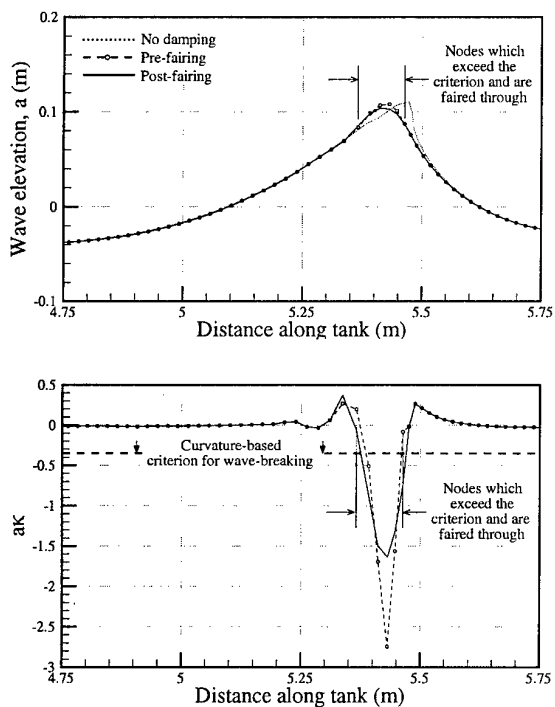


Figure 2. Damping of a breaking wave at $t=11.30$, using a new fairing technique in conjunction with the curvature-based criterion for wave-breaking.

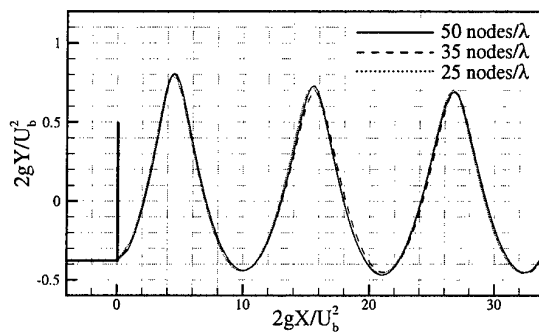


Figure 5. Convergence of solutions obtained using the fairing technique.

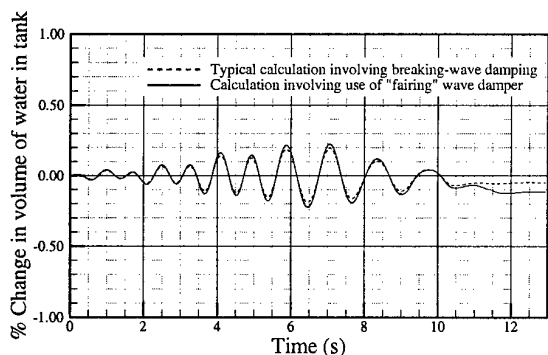


Figure 3. Estimation of mass lost in the process of suppressing the breaking wave in figures 1 and 2.

NUMERICAL SOLUTION FOR UNSTEADY TWO-DIMENSIONAL FREE-SURFACE FLOWS

E. O. TUCK

Department of Applied Mathematics, The University of Adelaide, Australia 5005

An efficient computational procedure is developed for solving fully nonlinear unsteady free-surface problems in two dimensions under gravity. Specifically, we solve here a nonlinear Cauchy-Poisson problem for a flow commencing from rest with a given initial free surface. Our task is thus to solve Laplace's equation $\phi_{xx} + \phi_{yy} = 0$ for the velocity potential $\phi(x, y, t)$, with vanishing velocity at infinity for all finite time t , and two nonlinear boundary conditions on an (unknown) free surface, namely the requirement that it be a material surface, and that the pressure on it be equal to atmospheric.

We use a semi-Lagrangian approach, in which the equation of the free surface is specified parametrically at any time t as $x = X(s, t), y = Y(s, t)$ where s is a marker of a given free-surface point, notionally the initial arclength along the free surface. Then there are three equations determining the free surface evolution, namely (at fixed s , i.e. for each separate free-surface point)

$$\begin{aligned}\frac{dX}{dt} &= u \\ \frac{dY}{dt} &= v \\ \frac{d\Phi}{dt} &= \frac{1}{2}(u^2 + v^2) - gY\end{aligned}$$

where $\Phi(s, t) = \phi(X(s, t), Y(s, t), t)$, and $u = \phi_x, v = \phi_y$.

It is convenient to consider this system of equations as three ordinary differential equations for the functions (X, Y, Φ) of time t , at each fixed free-surface point s . These ODE's can be advanced forward in time by any convenient numerical code, providing the quantities on the right are known at the current time t . If the current potential Φ is known for all s , the tangential velocity can be computed immediately, but not the normal velocity.

At some point in the solution process, the actual Laplace equation must be solved, and this is that point. We therefore must solve a Dirichlet problem with $\phi = \Phi$ assumed known (at the present time t) on the present free-surface boundary, which is assumed temporarily fixed and known. This Dirichlet solution gives $\phi(x, y, t)$ everywhere, and hence allows determination of both velocity components (u, v) , so we can proceed to the next time step $t + \Delta t$. During that step the shape of the free surface via $X(s, t + \Delta t), Y(s, t + \Delta t)$, and the value of $\phi = \Phi(s, t + \Delta t)$ on the free surface are updated.

To solve the Dirichlet problem, we simply assume that the velocity potential we require is a sum of N sources, namely

$$\phi(x, y, t) = \sum_{j=1}^N q_j \log R,$$

for some to-be-determined source strengths q_j , where R is the distance from the j 'th source to the field point (x, y) . The sources are located at prescribed positions (X_j, Y_j) , the only essential requirement for which is that they lie outside the field of flow, i.e. above the free surface. Given values $\Phi_i = \phi(x_i, y_i)$ on a general surface defined by N given discrete collocation points (x_i, y_i) , $i = 1, 2, \dots, N$, it is then only necessary to solve the linear system of equations

$$\sum_{j=1}^N A_{ij} q_j = \Phi_i,$$

The resulting computational method is very fast, economical and accurate. In particular, it is not necessary to "smooth" the free surface during the course of the computation. Such smoothing seems to have been needed to remove spurious grid-scale oscillations ever since the original work of Longuet-Higgins and Cokelet [1], and recent versions of this algorithm have required smoothing routines of a very high degree of sophistication. In contrast, the present results seem inherently smooth.

Solutions of similar problems for sloshing in a rectangular tank were given in [3], the region of flow being then bounded by two vertical side walls and a horizontal bottom. Any such additional boundaries require a modification of the fundamental source potential $\log R$. For example, plane walls and circular cylinders are easy to accommodate by suitable image sources. Even in the present study for an unbounded domain, it is convenient to assume that the initial elevation and hence the resulting flow is symmetric about $x = 0$, which means that the flow is the same as if there was a vertical wall at $x = 0$. Building in this wall by use of an image source reduces the size of the matrix by half.

Nevertheless we must now allow the flow to extend to $x = +\infty$, which is at first sight potentially more difficult than the finite-domain studies of [3]. However, a simple approach of distributing the required sources and collocation points on a grid that smoothly extends toward infinity seems to work quite satisfactorily. A number of such grids have been tried, but a simple and effective choice is one in which, after assigning half of the points (equally spaced) to the non-zero initial free-surface elevation, the remaining points initially are placed on the x -axis with a spacing that increases geometrically, at present with a ratio of 1.1. For example, with $N = 160$ the furthest point is at about $x_N = 400$. Note that in the present semi-Lagrangian method, these nodal points (and the corresponding source points) move with the flow, and hence change with time. It seems that the more remote sources have little effect on the flow in the finite part of the domain, and their strengths tend to zero quite rapidly.

The first results shown here are for an initial surface displacement similar to that used in [3], namely an initial semi-circular depression of unit radius. Without loss of generality, we can scale $g = 1$. This particular run used $N = 640$ points, with a source offset distance of 3 times the local grid spacing and a fixed Runge-Kutta time step of 0.02, although profiles are shown only at intervals of 0.1, up to $t = 3.6$. Up to that time, the results are the same to graphical accuracy with much lower N (typically $N = 80$), and also with much larger timesteps, and offsets between 2 and 4 times the local grid spacing. Finer grids and time steps are needed to pursue the computations nearer to the breaking crisis which occurs at about $t = 3.7$. Figure 1 shows only the portion of the free surface for $x < 2$; the free surface smoothly approaches zero beyond that point. At the last time shown ($t = 3.6$) the free surface is about to break near $x = 1$. At the earlier time $t = 3.0$, a maximum positive elevation of about $y = +1.6$ has occurred at the central point $x = 0$, and this sharp but smooth spike has begun to fall, remaining well captured by the program until computations are stopped at about time $t = 3.7$ by actual physical breaking near $x = 1$.

Figure 2 shows corresponding results for initially semi-elliptical depressions with drafts of 0.5 and 0.3, computed with $N = 160$. At draft 0.5, the central spike with maximum height of about 0.7 occurring at about time $t = 2.6$ is much sharper (though lower), and this presents difficulties to the present implementation of the program which cause it to fail at about $t = 3.4$, a time when it is not yet possible to tell whether breaking will occur.

On the other hand, at draft 0.3, the program is able to continue essentially indefinitely; results are now shown for $x < 3$ at a plotting interval of 0.4, up to $t = 6.8$. The central spike occurring at about time $t = 2.4$ has reduced to a mere gentle peak, and the main smooth crest subsequently moves off toward infinity without breaking, followed by subsidiary troughs and crests.

These particular configurations are studied because of possible relevance to the flow immediately behind the transom of a slender ship moving at high speed. For example, the outward moving crests in the results for the ellipse with draft 0.3 represent diverging waves in that model.

for q_j , where

$$A_{ij} = \log \sqrt{(x_i - X_j)^2 + (y_i - Y_j)^2}.$$

The far-field boundary condition can be enforced at this stage by adding a constraint that the total source strength be zero, or more simply by replacing the computed value of the last free-surface height y_N by zero; even more simply, it can be ignored provided the domain extends far enough, and this is the option presently implemented.

In practice, this is a totally straightforward and computationally efficient task, the matrix A_{ij} requiring only a small number of elementary arithmetic operations to compute, and solution for q_j being done by a standard linear equations routine. The velocity components u, v are then also available by summation of elementary functions. This technique is efficient both in programming and computing time, relative to techniques where the singularities are smoothed out over panels.

The only sophistication needed in the technique is in choice of the appropriate source location points (X_j, Y_j) , defined by a certain offset distance and direction outside the fluid domain. Most reasonable choices work well for gentle disturbances, but there is value in careful placement of sources for violent free-surface motions. See [2, 3] for further discussion of this matter.

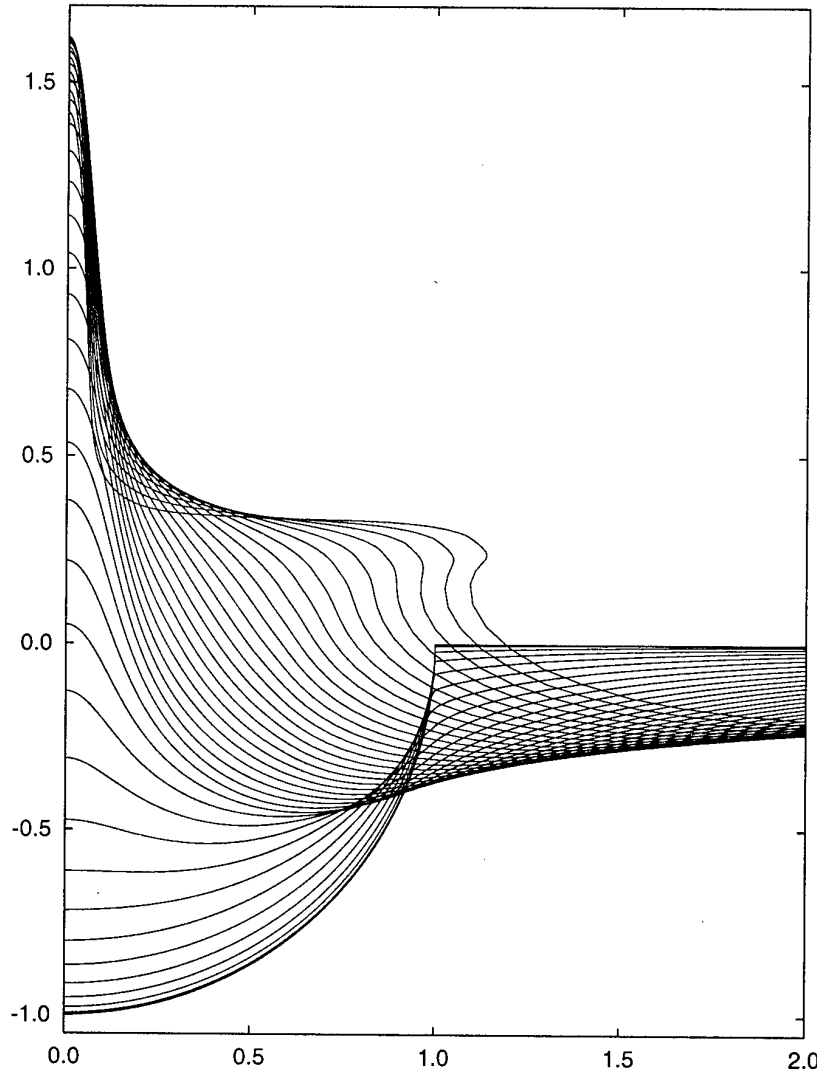


Figure 1: Evolution from rest of an initially semi-circular depression in a plane free surface.

Acknowledgement: This work was supported by the Australian Research Council. Assistance with the most recent computations and graphical presentations has been provided by Dr David Scullen and Dr Sergey Simakov.

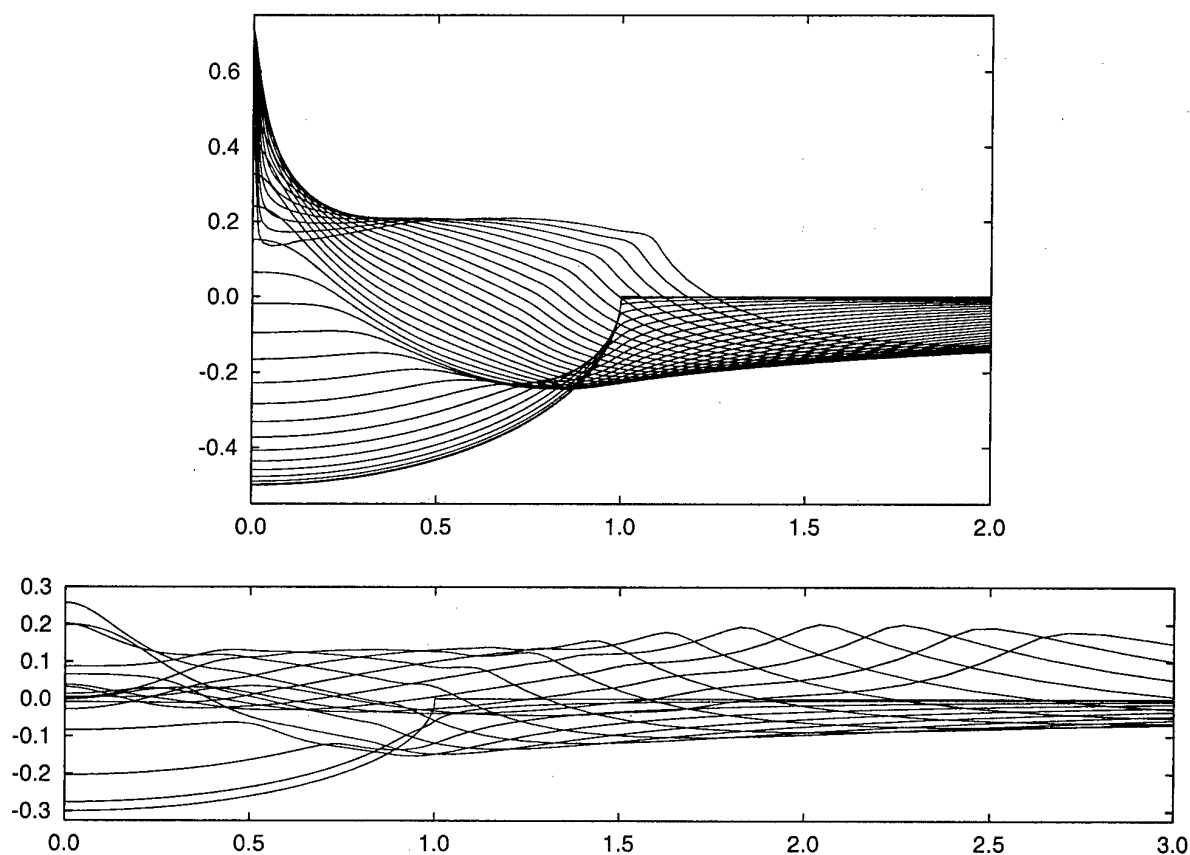


Figure 2: Initially semi-elliptical depressions with drafts 0.5 and 0.3.

References

- [1] Longuet-Higgins, M.S. and Cokelet, E.D., The deformation of steep surface waves on water. I. A numerical method of computation, *Proc. Roy. Soc. Lond. Ser. A*, **350**, 1976, 1–26.
- [2] Scullen, D. and Tuck, E.O., Nonlinear free-surface flow computations for submerged cylinders, *J. Ship Res.*, **39**, 1995, 185–193.
- [3] Tuck, E.O., Solution of nonlinear free-surface problems by boundary and desingularised integral equation techniques, in *Proc. 8th Biennial Computational Techniques and Applications Conference*, ed. J. Noye *et al.*, World Scientific, pp. 11–26, 1997.

THE METACENTRE IN THE STABILITY OF SHIPS. SOME DIFFICULTIES

F. URSELL

Department of Mathematics, Manchester University, M13 9PL, U.K.

1 Introduction

The conventional theory of the metacentre is presented in many textbooks, e.g. in [1] and [2]. I have always had difficulties with this piece of theory, which I shall try to explain in the present note. We consider a body floating in equilibrium on the surface of a fluid, the immersed volume being V . Let the body be subjected to an external couple, so that it takes up an inclined position; when the fluid has come to rest it is assumed that the immersed volume is again equal to V . If the external couple is now removed, does the floating body tend to return to its equilibrium position? This is the problem which is treated in textbooks in the following manner.

We take axes $OXYZ$ fixed in the body. It is almost obvious that the possible constrained positions with immersed volume V are defined by two independent angular parameters. The possible positions of the free surface in the system $OXYZ$ are the *Planes of Flotation*, all of which touch the *Surface of Flotation*. In any such inclined position the force system consists of the constraining couple, together with the force of flotation and the (vertical) weight of the body through its centre of gravity. The force of flotation is the resultant of the hydrostatic pressures acting on the immersed part of the body, it is a vertical upward force and is equal and opposite to the weight. As is well known, its line of action (*Line of Buoyancy*) goes through the *Centre of Buoyancy* which is the centroid of the immersed part of the body for that inclination. When the inclination is varied, it is seen (since there are two independent parameters) that the centres of buoyancy form a surface, the *Surface of Buoyancy*, in the coordinate system $OXYZ$ fixed in the body.

The lines of buoyancy form a doubly infinite system of straight lines (i.e. a linear congruence) in the system of axes fixed in the body. It can also be shown that the lines of buoyancy are the normals to the surface of buoyancy, see [1], Art.49. For any given inclination we can readily find the relevant line of buoyancy, because it is vertical. So far no mention has been made of the metacentre.

The conventional theory now proceeds as follows: it is assumed that the body is rotated about its longitudinal axis, and that we are interested only in certain small angles of inclination. The corresponding lines of buoyancy then form a one-parameter set, with a cusped envelope. To a close approximation it may now be assumed that these lines of buoyancy pass through the cusp which is given the name of metacentre. Then the relative positions of the cusp and of the centre of gravity determine the direction of the constraining couple, and thus they determine the stability of the body in the inclined positions which we have been considering.

There are some difficulties which will have occurred to many readers of this piece of theory. The first difficulty is concerned with the lines of buoyancy, the remaining difficulties are concerned with the fluid motion.

1. The lines in a one-parameter or two-parameter set of lines do not intersect in general, and therefore do not form an envelope.
2. The calculation refers to the body at rest in its constrained position, whereas stability refers to a body in motion.
3. When the constraint is removed, the body begins to move, and so does the fluid. The inertia of the fluid should enter into the calculation.
4. The stability is not determined at the initial instant, it is the end result of a motion in time. This motion starts when the constraint is removed, and ends when the body and fluid finally come to rest. An additional stability argument is considered in the Discussion below.

5. To follow the motion which has just been described we should have to solve a system of non-linear equations in time. These equations describe the motion of both the body and the fluid.
6. Even if the original inclination is small, the resulting linearized wave motion is not readily treated. (See [3] for a related but simpler calculation which involves the coefficients of virtual mass and moment of inertia and the coefficients of damping for all frequencies.)

These difficulties suggest that we may perhaps hope to find an initial motion. When the constraining couple is removed, how does the body begin to move ?

2 A modified problem: To find the initial acceleration

As before, we consider a body floating in equilibrium on the surface of a fluid, the immersed volume being V . Let the body be subjected to an external couple, so that it takes up an inclined position; when the fluid has again come to rest it is assumed that the immersed volume is again equal to V . If the external couple is now removed, what is the initial linear and angular acceleration of the body ?

Lines of buoyancy, centres of buoyancy, and the surface of buoyancy are defined as above. When the constraining couple is removed the body and the surrounding fluid will immediately be accelerated. We need to know the initial reaction of the fluid on the body. This is determined by solving a boundary-value problem. We take coordinate axes $Oxyz$ fixed in space, such that initially the free surface is at $z = 0$. We denote by $\phi(x, y, z)$ the initial acceleration potential, satisfying Laplace's equation. It can be shown that the boundary condition on the initial free surface $z = 0$ is then $\phi(x, y, 0) = 0$. Thus $\phi(x, y, z)$ can be continued by reflection into the upper half-space by the relation

$$\phi(x, y, z) = -\phi(x, y, -z)$$

and its region of definition is the whole of space, bounded internally by the immersed boundary-surface of the body, and by its reflection in the plane $z = 0$. Together these two surfaces will form a closed body, with a discontinuity of slope along the water-line. To an angular acceleration of the immersed surface about an axis there will correspond an angular acceleration of the reflected surface about the reflected axis, and to a linear acceleration of the immersed body there will correspond a linear acceleration of the reflected body. Thus for any prescribed linear and angular acceleration of the immersed body the potential ϕ is well defined in principle outside the closed (immersed plus reflected) body, and the actual linear and angular acceleration can then be found by applying the equations of motion. The boundary conditions on this closed body do not represent a rigid-body motion and therefore the fluid-force system cannot be expressed by the familiar virtual-mass and virtual-moment-of-inertia tensors. However, the acceleration potential can still be found, at least in principle. The calculation involves the determination, from the body contours, of the lines of buoyancy and of the surface of buoyancy, evidently a demanding task which is simplified because the lines of buoyancy are the normals to the surface of buoyancy.

3 Discussion and comments

The argument in the two earlier sections has not yet involved any envelope or cusp, and therefore no metacentre. These become involved when we include the hydrostatic forces in the calculation of the initial acceleration. As has been noted, the lines of buoyancy, forming a normal congruence, do not in general intersect each other and therefore cannot form an envelope. We now consider the properties of such a congruence, which are well known. Let us take a point P on the surface of buoyancy. Each plane containing the normal at P intersects the surface of buoyancy in a plane curve, with a well-defined curvature at P which depends on the orientation of the plane. It is shown in textbooks of differential geometry that for one orientation the curvature has a maximum

and for another orientation the curvature has a minimum. The corresponding directions on the surface of buoyancy are known as the principal directions of curvature and are orthogonal. To each principal direction there corresponds a centre of curvature, (the normals to the surface pass close to the centre of curvature but do not pass through the centre of curvature) and these centres of curvature lie on a surface of two sheets. Every line of buoyancy is tangent to this surface at each of the two centres of curvature. The lines do not form an envelope, and there are no cusps. It seems possible, however, that for a long ship and for inclinations about the longitudinal axis the lower centre of curvature can be taken as an approximate metacentre, and that the moment of the fluid pressure can be described by a virtual-moment-of-inertia tensor. For a long ship and for an inclination about the longitudinal axis of the ship we see that the lower centre of curvature in the mid-section corresponds to the conventional metacentre. In obtaining these considerations use has been made of well-known results in hydrostatics, hydrodynamics and the differential geometry of surfaces, and the assumptions of the modified conventional theory have been clarified, but not its relevance to the original problem of stability.

I found a history of the metacentre in a classical work of scholarship, the *Encyclopädie der mathematischen Wissenschaften*, published between 1898 and 1920. The most relevant article is by P. Stäckel, [4]. The theory is essentially due to Bouguer [6] who introduced the metacentre, to Euler [5], and to Dupin [7] who introduced lines of buoyancy and surfaces of buoyancy. I believe that Dupin in particular understood very well all the difficulties which I have raised. (I have not myself consulted these works.) In the middle of the nineteenth century it was pointed out that the static couple cannot by itself tell us anything about stability, since the fluid motion has been ignored. (We may perhaps feel that the static couple and the fluid couple must be in the same direction, more or less, but this has not been proved.) It is not suggested in Stäckel's article that the initial acceleration can be found, or that the linearized motion can be found.

There is an additional stability argument based on energy, which may occur to some readers. We consider the system at the instant when the constraining couple has just been removed. The kinetic energy at this instant vanishes. A wave motion then takes place, and energy is transferred to infinity. After a long time the system is again at rest. Evidently the potential energy of the floating body in the final state must be less than the potential energy in the initial state. Thus for stability the vertical distance between the centre of gravity and the plane of flotation must be less in the inclined position than in the upright position. The surface of buoyancy, and therefore the metacentre, is not involved in this argument.

References

- [1] Besant, W.H. and Ramsey, A.S. (1946) *Hydrostatics*, Cambridge.
- [2] Lamb, Horace. (1924) *Statics*, Cambridge, ch. 11.
- [3] Maskell, S.J. and Ursell, F. (1970) The transient motion of a floating body, *J. Fluid Mech*, **44**, 303-313.
- [4] Stäckel, P. (1905) Elementare Mechanik. Schwimmende Körper, *Encyclopädie der mathematischen Wissenschaften*, Leipzig, Band 4, Teil 1, Art 6, **39**, 657-658.
- [5] Euler, L. (1749) *Scientia Navalis*, St. Petersburg.
- [6] Bouguer, P. (1746) *Traité du navire*, Paris.
- [7] Dupin, C. (1822) *De la stabilité des corps flottants*, Paris.

FREE-SURFACE WAVE DAMPING DUE TO VISCOSITY AND SURFACTANTS

J.-M. Vanden-Broeck ⁽¹⁾ and B. Spivak ⁽²⁾

⁽¹⁾ *School of Mathematics, University of East Anglia, Norwich NR4 7TJ, UK*

⁽²⁾ *School of Engineering, University of Tel Aviv, 69978, Israel*

1 Introduction

The steady wave pattern developed on the free surface in inviscid two-dimensional fluid domain is well known. In this work, we investigate the influence of a thin film of insoluble material on air-liquid interface, on the wave characteristics. The linearized version of the titled problem in a two-fluid medium has been considered by Miloh *et al* [1]. We employ a quasi-potential approximation and assume that the main flow is potential, while the effect of surfactants enters the problem via Bernoulli equation. Thus, the problem is formulated in terms of a single potential function. The wave amplitude, consistent with the approximation made may be moderate. We consider a pressure distribution moving to the left with constant velocity $c > 0$, on a two-dimensional deep water air-liquid interface, on which there exists a monolayer film of surface active agents. The equations and boundary conditions are expressed in terms of orthogonal curvilinear coordinates (s, n) . Here s denotes arclength along the free surface and n denotes distance along the straight line perpendicular to the interface, considered positive in the outwards direction (i.e. from the liquid to the air). The pressure problem is formulated as a system of nonlinear integro-differential equations for the unknowns on the free surface. These equations are discretized and converted into a system of nonlinear algebraic equations which are solved by Newton's iterations.

2 Governing equations and numerical procedure

We consider a two-dimensional distribution of pressure P (with compact support) moving to the left at a constant velocity c at the surface of a fluid of infinite depth and constant density ρ . This can be interpreted as an inverse problem for a "two-dimensional" contour moving at a constant velocity c at the surface of a fluid. Here the shape of the contour is not known a priori but is given at the end of the calculations by the shape of the free surface below the support of the pressure distribution. We seek steady solutions in a frame moving with the pressure distribution. We choose Cartesian coordinates with the y -axis directed vertically upwards. We introduce dimensionless variables by choosing c as the unit velocity and c^2/g as the unit length. Here g is the acceleration of gravity.

The full boundary conditions for a Newtonian type interface in the presence of surfactants are given in Edwards *et al* [2]. The derivation of these boundary conditions is based on the so called Boussinesq-Scriven constitutive relationship (Scriven [3]) which is expressed in terms of two quantities μ^s and κ^s , the interfacial and dilatational viscosities respectively. We combine these boundary conditions with the quasi-potential approximation developed by Ruvinsky *et al* [4]. This approximation is valid for slightly viscous fluids. The velocity field is separated into a potential part and an irrotational one. The

resulting coupled equations enable one to solve the potential part and deduce from it the (assumed small) irrotational one. The resulting boundary condition on the free surface for the potential function ϕ is

$$\frac{1}{2}\left(\frac{\partial\phi}{\partial s}\right)^2 + y + P - \frac{2}{R_e} \frac{\partial^2\phi}{\partial s^2} (1 + KB_0) - K(W_e - M_r \frac{\partial\phi}{\partial s}) = \frac{1}{2} \quad (1)$$

Here

$$R_e = \frac{c^3}{g\nu} \quad (2)$$

is the Reynolds number,

$$B_0 = g \frac{\kappa_s + \mu_s}{2\rho\nu c^2} \quad (3)$$

the Boussinesq number,

$$W_e = g \frac{\sigma_0}{\rho c^4} \quad (4)$$

the Weber number and

$$M_r = gE_0/\rho c^4 \quad (5)$$

the Marangoni number. Here ν is the kinematic viscosity, E_0 the Gibbs elasticity, K the curvature of the free surface and

$$\sigma = \sigma_0 - \frac{E_0}{c} \frac{\partial^2\phi}{\partial s^2} \quad (6)$$

the variable surface tension.

Next we introduce, in addition to the potential function ϕ , the stream function ψ . Without loss of generality, we chose $\psi = 0$ on the free surface. Following Asavanant and Vanden-Broeck [5], it can be shown that

$$x'(\phi) - 1 = -\frac{1}{\pi} \int_{-\infty}^{\infty} \frac{y'(\varphi)}{\varphi - \phi} d\varphi \quad (7)$$

Here we use ϕ and ψ as independent variables and denote by $x(\phi)$ and $y(\phi)$ the values of x and y on the free surface $\psi = 0$. The prime denotes derivative with respect to ϕ .

We then express all the derivatives in (1) in terms of $x(\phi)$ and $y(\phi)$. This can easily be done by noting that

$$\frac{\partial\phi}{\partial s} = (x'^2 + y'^2)^{-1/2} \quad (8)$$

$$\frac{\partial^2\phi}{\partial s^2} = -\frac{x'x'' + y'y''}{(x'^2 + y'^2)^2} \quad (9)$$

$$K = \frac{x'y'' - y'x''}{x'^2 + y'^2} \quad (10)$$

For given values of R_e , B_0 , W_e and M_r , relations (1), (7)-(10) define a system of integro-differential equations for the two unknown functions $x(\phi)$ and $y(\phi)$. This system is discretized and the resulting algebraic equations are solved by Newton's iterations. In our calculation we chose

$$P = \epsilon \exp \frac{b}{\phi^2 - a^2} \quad \text{for } |\phi| < a \quad (11)$$

and $P = 0$ for $|\phi| \geq a$.

Once $x(\phi)$ and $y(\phi)$ are known, the free-surface vorticity ω_s is determined from

$$\omega_s = 2K + 2B_0 \frac{\partial^3 \phi}{\partial s^3} - R_e M_r \frac{\partial^2 \phi}{\partial s^2} \quad (12)$$

In (12), K and $\frac{\partial^2 \phi}{\partial s^2}$ are given by (10) and (9) and $\frac{\partial^3 \phi}{\partial s^3}$ is calculated by

$$\frac{\partial^3 \phi}{\partial s^3} = - \left[\frac{x'x'' + y'y''}{(x'^2 + y'^2)^2} \right]' (x'^2 + y'^2)^{-1/2} \quad (13)$$

The numerical results show that there are in general two trains of waves on the free surface (a train of short waves at the front of the distribution of pressure and a train of longer waves at the back). Both trains are damped by viscosity. We will discuss how the various parameters R_e , B_0 , W_e and M_r affect the rate of damping.

Acknowledgments

The authors thank T. Miloh and G. Zilman for drawing their attention to this problem and for constructive discussions.

References

- [1] T. Miloh, O. Oshri and G. Zilman (1998). *Free surface flow with viscosity* (ed P.A. Tyvand), Computational Mechanics Publication, Southampton, 117.
- [2] D.A. Edwards, H. Brenner and D.T. Wasan (1991). *Interfacial Transport Processes and Rheology*, Butterworth-Heinemann, Boston.
- [3] L.E. Scriven (1960). *Chem. Eng. Sci.* **12**, 98.
- [4] K.D. Ruvinsky, F.I. Feldstein and G.I. Freidman (1991). *J. Fluid Mech.* **230**, 339.
- [5] J. Asavanant and J.-M. Vanden-Broeck (1994). *J. Fluid Mech.* **273**, 109.

Long Time Evolution of Unstable Bichromatic Waves

J.H. Westhuis*[†], E. van Groesen*, R. Huijsmans[†]

1 Introduction

The instability of wave trains has been a topic of research since [1] showed that the traveling wave solution of the non-linear water wave problem is unstable to modulational perturbations of its envelope. Many authors have studied these instabilities and confirmed the B-F instability growth-rates. When [7] showed that the Benjamin-Feir instability is also produced by the Nonlinear-Schrödinger (NLS) equation of weakly non-linear wave theory, the long term behavior of the initial instability has been sought in terms of desintegration of the modulated wavetrain into solitary wave envelopes [2, 3].

For applications in hydrodynamic laboratories, the evolution and the resulting maximal wave heights are of practical interest. An experimental study by [4] in which the spatial evolution of a bichromatic wave group envelope is reported, motivated the research of this presentation. We numerically investigate with a nonlinear potential time domain method the long time evolution and spatial distribution of unstable bichromatic wavegroups and observe (in most cases) a recurrence phenomena. For moderate cases a 'simple' periodicity in the spatial evolution of the spectrum may be observed. However, with increasing initial amplitudes, more complicated (periodic) structures may be observed. Our current work aims at classifying these phenomena and find experimentally relations between characteristic quantities. In the final section we derive a stability criterion and a partial theoretical explanation of the phenomena.

2 Numerical method

The fluid is considered two dimensional, incompressible, inviscid and irrotational, which allows the velocity field to be defined by a potential function. The dynamic and kinematic boundary conditions on the free surface are integrated in time using a 5 step, 4th order Runge-Kutta scheme. Evaluating the right hand side of

these equations involves the solution of Laplace's equation on the interior of the fluid. This solution is obtained using a linear Finite Element Method on a grid that is refined near the free surface. An artificial beach is constructed using a combination of pressure damping, grid stretching and Sommerfeld conditions tuned at the critical wavespeed \sqrt{gh} ; the damping properties are remarkably good [6].

At the generating side of the domain, we used three different kind of generators to exclude that the observed effects are related to the specific way of wave generation. i) Moving flap: a moving hinged flap, ii) Linearized flap: the fluxes of the real flap are generated on a static vertical wall iii) Linear solution; the flux generated at the fixed vertical wall is derived from the expression for linear water waves. Although the signals differ from each other (which is to be expected), this difference consists of relatively small phase differences, the characteristic deformation of the wavegroup envelope is still observed (Fig. 1) and power spectra are almost identical. For further calculations we used the linearized flap, because it is easier to perform stable computations than with the moving geometry and it is more similar to a physical wave tank than the imposed linear solution. From these observations regarding the beach and wave generation and from qualitative comparison of our numerical results with the experiments in [4], we conclude that the observed phenomena are only due to the nonlinearity of the equations and are not a consequence of numerical wave generation or absorption.

3 Phenomenon and simulations

We have conducted a series of numerical experiments for bichromatic waves with the two frequencies centered around 2s on a water depth of 5 meter. In all cases, both amplitudes are equal and denoted with q . The experimental model test results of [4] ($T_1 = 1.9s$, $T_2 = 2.1s$, $q = 0.08m$), and recent experiments at MARIN by Huijsmans & Westhuis 1999, show strong asymmetric wave envelope deformation. The numerical simulations reproduce these findings; moreover, the computations have been extended to simulate a 1200 m wavetank ($h=5m$) which uncovers dynamics which is not

*Department of Mathematical Sciences, University of Twente, The Netherlands

[†]Maritime Research Institute Netherlands (MARIN) Wageningen, The Netherlands.

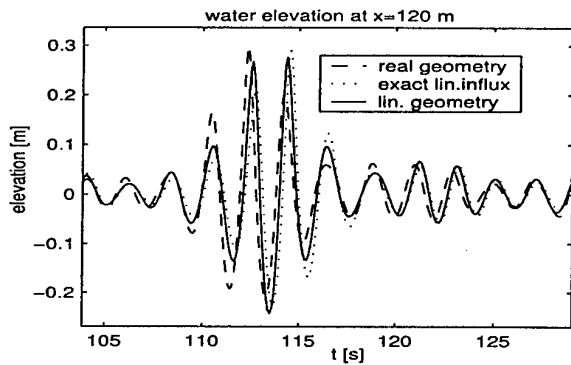


Figure 1: Comparison of the wave elevation of the unstable bichromatic wave generated by a moving hinged flap (dashed line), a hinged flap with linearized geometry (full line) and with the exact linear flux solution of the bichromatic wave prescribed (dotted line).

recognizable in physical laboratories. First we will describe the results for the model test mentioned above; then the evolution of the spectrum for different cases will be compared.

For the model test case, according to linear theory, the modulated wave group would be described by $\eta(x, t) = 2q \cos(\Delta kx - \Delta\omega t) \cos(kx - \bar{\omega}t)$ where $\bar{\omega} = \pi$, $\bar{k} \approx 1$ are the averaged frequency and wave number respectively, and $\Delta\omega \approx \pi/20$, $\Delta k \approx 0.1$ are half the differences. In the figures below, time signals at different positions of the tank show the unstable evolution characterised by large deformations of the envelope: the characteristic temporal beat pattern close to the wave maker is gradually deformed into more confined, much higher waves connected by smaller amplitude waves. For distances of the laboratory, this is shown in Fig. 2; for larger distances, Fig. 3 shows that the smaller waves form a second wave group that splits from the original one and merges with the successive larger group. On even larger distances, Fig. 4, it is seen that the splitting and merger process is a recurrent phenomenon. The temporal behaviour is periodic with period determined by the driving modulation period $\pi/\Delta\omega \approx 20$; the spatial recurrence takes place on an interval of approx. 400 m, much larger than the spatial periodicity of the linear solution which is $\pi/\Delta k \approx 10\pi$.

Now we consider the change in the spectrum of the bi-chromatic waves, and compare the above model test with other cases that have different values of the frequency difference or amplitude. In situations where the initial frequencies are well separated $(T_1, T_2) = (1.8, 2.2)$ no spatial variations have been observed. For smaller frequency differences, such as in figure 5 for $(T_1, T_2) = (1.9, 2.1)$, the spectrum changes with in-

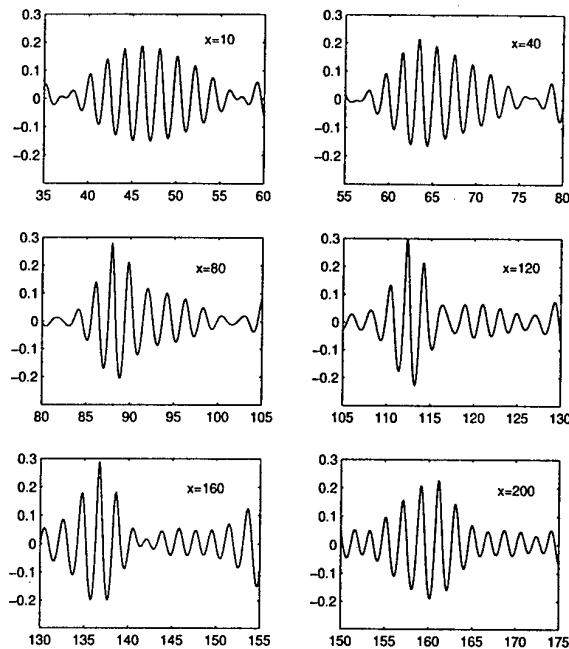


Figure 2: Time signals of a single wave group at different positions, 10, 40, 80, 120, 160, 200 m, from the wave maker, showing the asymmetrisation and increase of amplitude.

creasing distance from the wavemaker, with periodic growth and decay of several sideband modes. The first side band modes $(2\omega_1 - \omega_2, 2\omega_2 - \omega_1)$ are observed for larger amplitudes; for $q = 0.08$, even significant energies at the frequencies $3\omega_1 - 2\omega_2$ and $4\omega_1 - 3\omega_2$ are clearly visible. (Higher initial amplitudes led to breaking within 900 seconds.) For smaller frequency differences, the instability shows itself already for smaller amplitudes.

Examination of the results has shown that there is a correlation between the spatial periods (and growth rates) of the sideband modes and the period of the initial waves. It is remarkable to notice that also the side band frequencies that lay well out of the B-F instability intervals (situations with $q = 0.04, q = 0.06$) show significant growth rates, which indicates that a different kind of analysis is needed when examining the instability of these wavegroups; this will be done next.

4 Theoretical description

It is possible to construct a simplified model to describe and partly explain the observed phenomena by analysing an NLS-type of envelope equation. To that aim, we write in lowest order $\eta(x, t) = a \exp i(K(\bar{\omega})x - \bar{\omega}t + \phi) + c.c.$ with real amplitude a , and phase $K(\bar{\omega})x -$

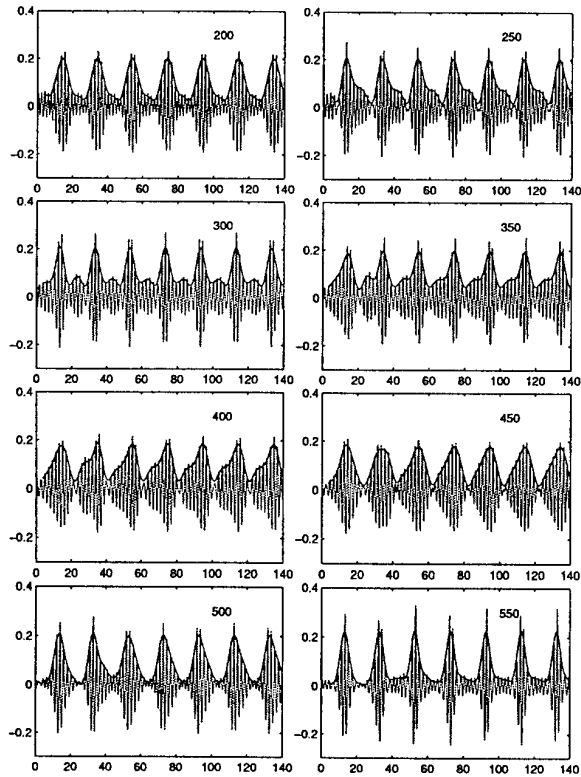


Figure 3: Time signals at larger distances (200 ... 550 m) from the wave maker, showing the splitting and merger of a small wave group.

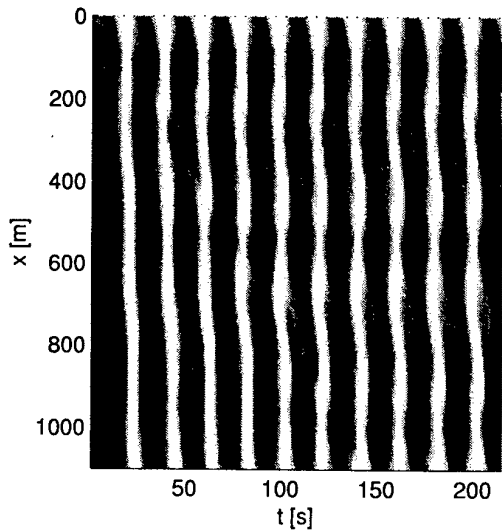


Figure 4: Density plot in a moving frame of reference, showing the splitting and merger of a small wave group.

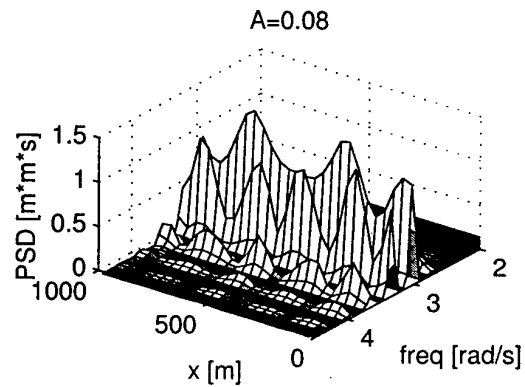
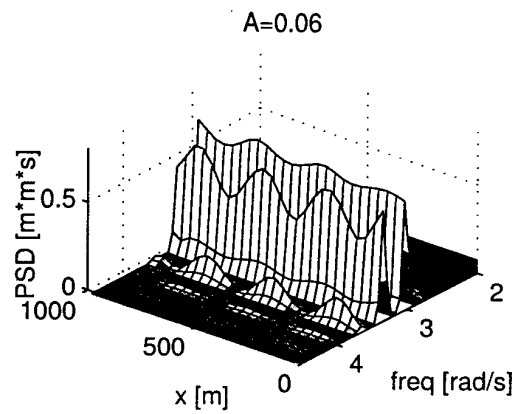
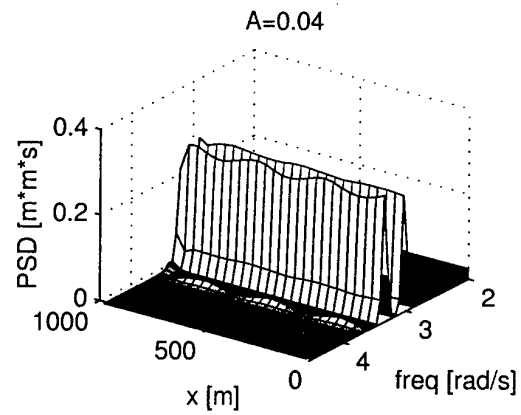


Figure 5: Spatial evolution of the spectrum of the bichromatic wave for different amplitudes. The periods of the bichromatic modes are $(T_1, T_2) = (1.9, 2.1)$ and the depth of the tank is 5 meters. Clearly the periodic structure of the nonlinear spatial evolution is visible for smaller amplitudes. However, for larger amplitudes this simple periodicity does no longer hold.

$\bar{\omega}t + \phi$, where $K(\bar{\omega})$ is the wave number corresponding to the averaged frequency according to linear dispersion. Then the NLS equation contains certain parameters β (from group velocity dispersion) and γ (from nonlinear generation of second harmonic). The parameter β is positive, but the sign of γ depends on the dispersive properties [5]. For applications in laboratories, with relatively short waves, a KdV-type of dispersion is not applicable and would lead to a negative value for γ (and diverging NLS). Instead, using the dispersion relation for small waves of any wave length, i.e. in normalised variables $\omega = \sqrt{k} \tanh k$, the coefficient γ is positive, self-focussing NLS, and the essential features are recovered. To illustrate this, it is simplest to work with the phase-amplitude equations. These can be written in various forms; in the following description, for direct interpretation, we use the physical frequency ω and wavenumber k , and the 'energy', or squared envelope, $E = a^2$. Then, using as variables $\tau = t - x/V_0$, $\xi = x$, with V_0 the central group velocity, energy and wave conservation, the phase equation, are given by, respectively,

$$\partial_\xi E + \partial_\tau [2\beta(\omega - \bar{\omega})E] = 0$$

$$\partial_\xi \omega + \partial_\tau [k - \frac{\omega}{V_0}] = 0, \quad K(\omega) - k = \gamma E + \beta \frac{\partial_\xi^2 a}{a}$$

The last equation is the non-linear dispersion relation (NDR), where the linear dispersion relation is modified with terms that account for a nonlinear correction, and a dispersive driven profile contribution (Yuen & Walker, Fornberg & Whitham).

For the signal problem for the bi-chromatic wave, at $\xi = 0$, the frequency is fixed $\omega = \bar{\omega}$, and the amplitude is the modulation $a = q \cos(\Delta\omega\tau)$. Then, the NDR produces the wave number as $k = \bar{k} - \gamma q^2 \cos^2(\Delta\omega\tau)$, after which the change in frequency is found for increasing ξ , and, consecutively, the change in energy. The result is that initially, in each modulation period, the frequency is skew-symmetric, and the envelope increases in the middle and decreases at the sides. This indicates that near $\xi = 0$, the cosine-profile changes into a sharper peaked pulse profile. With increasing distance, the profile further deforms.

A phenomenological investigation of possible instability can be based on the fact that the model with the correct dispersion is the self-focussing NLS equation and initial data on the whole real line will develop into solitons and residual radiation. For a soliton to exist it is necessary that the quantity $K(\omega) - k$ is positive. The restriction to periodic (temporal) intervals then restricts the possibility for such a soliton to develop in the following way. The energy per period generated at the wave maker is proportional to $q^2/\Delta\omega$. Any NLS-soliton has width inversely proportional to its amplitude, which itself is proportional to its energy. By the

temporal periodicity of the observed phenomena, this means that the soliton amplitude and energy should at least be proportional to $\Delta\omega$. Comparing the generated energy and that of a soliton implies that the quotient $q/\Delta\omega$ should exceed a critical value to explain the appearance of at least one large amplitude soliton within each temporal period, providing a stability criterion that resembles the condition for Benjamin-Feir modulational instability of a uniform wave train.

5 Conclusions

Detailed and accurate numerical simulations of wave forms, their envelopes and spectra of unstable wave-groups were presented on very long spatial and time intervals. It was found that for an initially bi-chromatic wave, instability arises when the wave height or the inverse frequency difference is sufficiently large. The instability was shown to be noticeable in transfer of energy to sideband modes in a quasi periodic manner; taking the spatial structure per mode to be periodic, an experimental dependence between the spatial wavenumber and the wavenumber of the principal mode was found. Theoretically, an instability condition was derived for this case; although it resembles somewhat the BF-instability condition for uniform wave trains, no direct relation has been found between the observed growth rates of side band modes and the standard BF-predictions. A possible explanation may be that the growth rates in the bi-chromatic instability are determined by the enforced periodicity of the envelope and are a manifestation of the development of the confined soliton-type shapes within that period.

References

- [1] T. Benjamin and J. Feir. The desintegration of wave trains in deep water. part 1. theory. *J. Fluid Mech.*, 27:417, 1967.
- [2] V. Chu and C. Mei. The nonlinear evolution of stokes waves in deep water. *J. Fluid Mech.*, 47:337, 1971.
- [3] H. Hasimoto and H. Ono. Nonlinear modulation of gravity waves. *J. Phys. Soc. Japan*, 33:805, 1972.
- [4] C. Stansberg. On the nonlinear behavior of ocean wave groups. *proc. Waves '97*, 2:1227-1241, 1997.
- [5] E. Van Groesen. Wave groups in uni-directional surface wave models. *J. Eng. Math.*, 34:215-226, 1998.
- [6] J. Westhuis. A numerical beach for two and three dimensional fully nonlinear numerical wave tanks. In *Proc. of the 10th ISOPE conference*, 2000. submitted.
- [7] H. Yuen and B. Lake. Nonlinear deep water waves: theory and experiment. *Phys. Fluids*, 18:956, 1975.

INITIAL PRESSURE DISTRIBUTION OVER A WAVEMAKER AFTER AN IMPULSIVE MOTION

by G.X. Wu

*Department of Mechanical Engineering, University College London,
Torrington Place, London WC1E 7JE*

The hydrodynamic problem under consideration is shown in Figure 1. The wavemaker on the left will start moving suddenly with speed U . This is a classic problem and analytical solution based on the potential flow can be obtained easily at the early stage of the motion. Peregrine (1972), for example, solved the problem based on an expansion in terms of time t . His solution reveals that the vertical velocity at the intersection is infinite, which is due to the incompatibility of boundary conditions on the free surface and the body surface at that point. It was later found (Lin, Newman & Yue 1985) that the proper treatment of this singularity is crucial for obtaining accurate numerical solution. Here we will show that this incompatibility also has profound effect on the pressure distribution. Some of features seem not to have been observed before.

As argued by Wu (1998), for this kind of problem due to sudden motion, the initial impact can be divided into two stages: (1) the impulse stage between $0_- \leq t < 0_+$ and (2) the post impulse stage $t = 0_+$. From Peregrine's solution (1972), we can write the velocity potential at $t = 0_+$, or the solution at the second stage, as

$$\phi = \frac{2U}{d} \sum_{n=0}^{\infty} \frac{(-1)^{n+1}}{k_n^2} e^{-k_n x} \cos k_n (y + d) \quad (1)$$

where $k_n = (n\pi + \pi/2)/d$. From this the pressure impulse (Batchelor, 1967, p471) at the first stage can be obtained from $\Pi = -\rho\phi$, where ρ is the density of the fluid. The solution for the pressure at the second stage is, however, less straightforward. In fact it should be obtained from the Bernoulli equation

$$p = -\rho\phi_t - \frac{1}{2}\rho\nabla\phi\nabla\phi \quad (2)$$

In the equation, ϕ is that given in equation (1) while ϕ_t is still unknown. To find the solution for the time derivative term, we notice that the term satisfies the Laplace equation, and the boundary conditions

$$\phi_t = -\frac{1}{2}\nabla\phi\nabla\phi \quad (3)$$

on $y = 0$ and

$$\frac{\partial\phi_t}{\partial x} = -U \frac{\partial^2\phi}{\partial x^2} \quad (4)$$

on $x = 0$ (Wu 1998). It would then be possible to find ϕ_t using a Fourier series similar to that in equation (1). But here there is a short cut. In fact one can easily confirm that the solution for ϕ_t can be written as

$$\phi_t = -\frac{1}{2}(\phi_y^2 - \phi_x^2) - 2U\phi_x \quad (5)$$

despite the product terms. This leads to

$$p = 2\rho U\phi_x - \rho\phi_x^2 \quad (6)$$

On the wavemaker, because we have $\phi_x = U$, the above equation (6) becomes

$$p = \rho U^2 \quad (7)$$

Now at the intersection point A , the pressure is ρU^2 if it is approached along the wavemaker, but it is zero if it is approached along the free surface. Thus the pressure is discontinuous, which is clearly due to the incompatibility of the free surface and the body surface boundary conditions imposed on the potential at the intersection point. This result does not seem to have been noticed before.

If the flow field is the main interest in the time marching analysis, the observed discontinuity in the pressure should not cause too much concern, because the pressure is a product obtained after the potential has been found. It has no feed back to the flow if the body is rigid and fixed. In other cases, such as an elastic plate or a non-fixed rigid body, correct prediction of pressure is an essential part of the analysis, as observed by Lu, He and Wu (2000). Error in pressure will lead to a false response of the body, which will in turn give a false feed back to the flow. It is quite possible that the error will accumulate in the time domain and the numerical solution will depart from the real one and even instability will occur. Thus proper understanding of the pressure behaviour is extremely important in the code development.

Finally, the discontinuity observed above may be confirmed by the numerical results. One can obtain the pressure distribution by solving the boundary values problems for ϕ and ϕ_t . Table 1 shows that the nondimensionalized pressure along the wavemaker. The results are obtained from a boundary element method based on the complex potential with linear elements (Wu & Eatock Taylor 1995). Because the intention is not about computational efficiency, panels with constant length s are used over the boundary of the fluid domain which is truncated at $x = 10d$. The table gives results up to $y/d = -0.20$ to highlight the behaviour of the pressure near the intersection. It shows that $p/\rho U^2$ is near one almost everywhere apart from a small region very close to $y = 0$ where it behaves rather erratically. But the region in which the erratic behaviour can be observed is getting smaller and smaller when the elements are getting smaller and smaller, and at a given point below $y = 0$, the result will tend to one as s decreases. All these are consistent with what is found above.

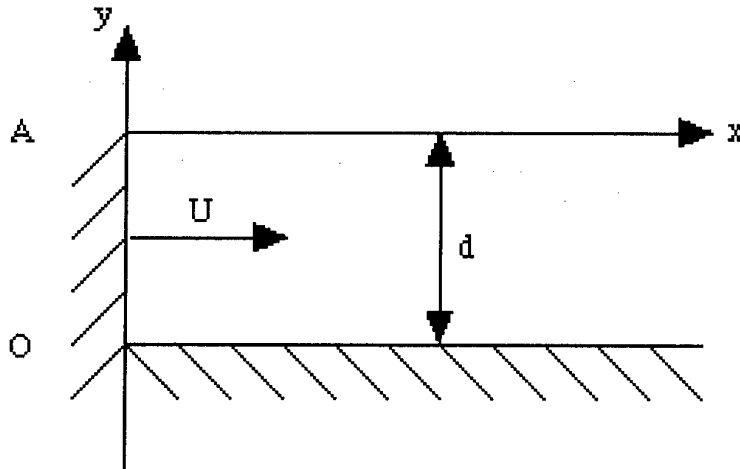


Figure 1. Computational model

Table 1. Pressure along the body surface

y/d	$p/\rho U^2$ ($s/d = 0.01$)	$p/\rho U^2$ ($s/d = 0.02$)	$p/\rho U^2$ ($s/d = 0.04$)
0.00	0.000	0.000	0.000
-0.01	-0.257		
-0.02	0.842	-0.114	
-0.03	0.920		
-0.04	0.954	0.868	0.029
-0.05	0.970		
-0.06	0.979	0.933	
-0.07	0.985		
-0.08	0.988	0.962	0.895
-0.09	0.990		
-0.10	0.992	0.975	
-0.11	0.993		
-0.12	0.994	0.983	0.946
-0.13	0.995		
-0.14	0.996	0.987	
-0.15	0.996		
-0.16	0.996	0.990	0.969
-0.17	0.997		
-0.18	0.997	0.992	
-0.19	0.997		
-0.20	0.998	0.993	0.980

References

- Batchelor, G.K. (1967) *An introduction to Fluid Mechanics*, Cambridge University Press.
- Lin, W.M., Newman, J.N. and Yue, D.K. (1985) "Nonlinear forced motions of floating bodies", *15th Symp. On Naval Hydrodynamics*, National Academy Press, Washington.
- Lu, C.H, He, Y.S. and Wu, G.X. (2000) "Coupled analysis of nonlinear interaction between fluid and structure during impact", *J. Fluids and Structures* (accepted).
- Peregrine, D.H. (1972) "Flow due to vertical plate moving in a channel", Unpublished notes, Department of Mathematics, University of Bristol.
- Wu, G.X. (1998) "Hydrodynamic force on a rigid body during impact with liquid", *J. Fluids and Structures*, Vol.12, pp. 549-559.
- Wu, G.X. and Eatock Taylor, R. (1995) "Time stepping solutions of the two dimensional non-linear wave radiation problem", *Ocean Engineering*, Vol.22, No.8, pp. 785-798.

Numerical Reconstruction of Nonlinear Irregular Wave-Field Using Single or Multiple Probe Data

Guangyu Wu, Yuming Liu & Dick K.P. Yue

Department of Ocean Engineering
Massachusetts Institute of Technology
Cambridge, Massachusetts 02139, USA

1 Introduction

The objective of this work is to develop an effective algorithm for the reconstruction of irregular nonlinear wave-fields using wave records of limited duration at one or more fixed points. With wave reconstruction, we are able to obtain: (i) complete kinematics of entire nonlinear wave-fields; (ii) proper initial conditions for numerical simulations and wave-basin experiments of nonlinear wave-field evolutions; (iii) forecast of nonlinear wave-field evolution dynamics beyond specified wave records; and (iv) data assimilation for quantitative comparisons between numerical simulations and field and wave-basin measurements.

For small to mild waves, the kinematics of the irregular wave-field can be reconstructed based on the linear and second-order Stokes wave theory (e.g. Zhang *et al.* 1999). For moderate to steep waves or long-time wave-field evolutions, higher-order effects must be considered and efficient reconstruction schemes need to be used.

In this work, we develop a multiple-level iterative optimization scheme for the reconstruction of three-dimensional nonlinear wave-fields using single- or multiple-point measurements. For initial (low-level) optimizations, we apply the analytic low-order Stokes wave theory. For high-level optimizations, we employ the Rosenbrock optimization scheme (Bazaraa *et al.* 1993) with an extremely efficient high-order spectral method (HOS) (Dommermuth & Yue 1987) for the computation of nonlinear wave-field evolutions. Since the HOS can follow the evolution of a large number of wave modes and account for their interactions up to an arbitrary order in wave steepness, the present wave reconstruction scheme is capable of regenerating the kinematics of large nonlinear wave-fields for long-time evolutions. As an illustration, the scheme is applied to construct steep two- and three-dimensional irregular waves using wave-basin data. Agreement between the reconstructed wave-field and the measurements is excellent.

2 Problem definition

The mathematic problem of wave reconstruction can be described as follows: given probe data of wave elevations at multiple points in a limited duration ($\bar{\eta}(\mathbf{x}_p, t)$, $p=1, \dots, N_p$, $t \in [0, T]$), find proper initial conditions of the free-surface elevation and velocity potential at $t=0$ ($\eta_0(\mathbf{x}) = \eta(\mathbf{x}, t=0)$ and $\phi_0(\mathbf{x}) = \phi(\mathbf{x}, z=\eta_0, t=0)$) for construction of the nonlinear wave-field such that the difference (\mathcal{E}) between the wave elevations of the reconstructed wave-field at the probes

$(\eta(\mathbf{x}_p, t), p = 1, \dots, N_p)$ and the specified probe data is minimized, i.e.

$$\mathcal{E} = \min \left\{ \frac{1}{N_p} \sum_{p=1}^{N_p} \int_0^T w(\mathbf{x}_p, t) [\eta(\mathbf{x}_p, t) - \bar{\eta}(\mathbf{x}_p, t)]^2 dt \right\} \quad (1)$$

where $w(\mathbf{x}_p, t)$ is a weighting function. This is a nonlinear optimization problem. The main difficulties involved are:

- Evaluation of \mathcal{E} is expensive since it requires to resolve the nonlinear wave-field evolution problem for specified initial conditions.
- The degree of freedom in optimization increases linearly with the duration of the records T and the size of the wave-field.
- There exist multiple solutions satisfying nonlinear equation (1).

Because of these, the wave reconstruction algorithm needs to employ (1) a highly efficient optimization scheme; (2) an efficient and accurate simulation scheme for nonlinear wave-field evolutions; and (3) an effective technique for proper initial solutions of the optimization.

3 Multiple-level optimization scheme

We develop a multiple-level iterative optimization scheme which employs the analytic Stokes wave solutions for low-level optimization and the high-resolution simulation results for high-level optimization. The low-level optimization is conducted analytically while the high-level optimization is performed numerically based on the Rosenbrock method (Bazaraa *et al.* 1993). For the simulation of nonlinear wave-field evolutions, a powerful high-order spectral method (HOS) developed for nonlinear wave-wave interactions by Dommermuth & Yue (1987) is employed. The high efficiency of optimization and HOS simulations allows the reconstruction of large-space/long-time wave-field evolutions including nonlinear wave effects.

The procedure of the multiple-level optimization scheme can be outlined as follows:

- *Level 1:* we use the linear wave solution with N_L free wave modes for $\eta(\mathbf{x}_p, t)$ in (1) and determine the unknown mode amplitudes and phases by analytic optimization.
- *Level 2:* we use the nonlinear (second-order) Stokes wave solution with N_L free wave modes for $\eta(\mathbf{x}_p, t)$ in (1) and determine the unknown mode amplitudes and phases by analytic optimization.
- *Level 3:* using the result of *Level 2* as initial conditions, we conduct HOS simulations with N_H spectral modes and arbitrary order M to determine $\eta(\mathbf{x}_p, t)$. Through an iterative optimization, we obtain a complete solution of $\eta_0(\mathbf{x})$ and $\phi_0(\mathbf{x})$ with N_H spectral wave modes.

Note that with *Level 1* and *Level 2*, we are able to obtain a proper initial guess which speeds up the convergence of the optimization in *Level 3*. In practice, N_H can be as large as $O(10^4)$ and M can be $O(5 \sim 10)$. Thus, we can obtain an accurate reconstruction of nonlinear wave-fields in large domains. Moreover, with the reconstructed wave-field as initial conditions for HOS simulations, we can forecast the evolution of the nonlinear wave-field.

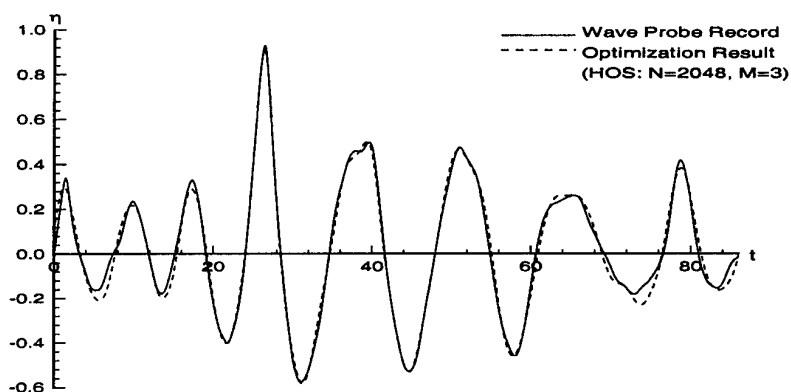


Figure 1: Comparison of computed versus experimentally measured free-surface elevation (*10 meters) at a given point of a two-dimensional wave-field as a function of time (seconds): —, experiments of Stansberg *et al.* (1995); - - -, HOS simulation with $N_H=2048$ spectral modes and $M=3$ order.

4 Results

The present multiple-level optimization scheme is applied to reconstruct both two- and three-dimensional steep irregular wave-fields using single or multiple-points measurements. Figure 1 shows the comparison between the HOS simulation result of the reconstructed wave-field and the experimental measurements of a steep two-dimensional wave-field (Stansberg *et al.* 1995) for about 10 dominant wave periods. The agreement between them is excellent.

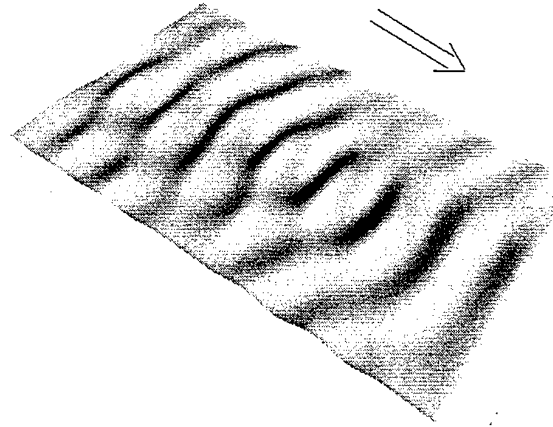
Figure 2 shows the comparison between the HOS simulation results and wave-basin measurements (Liagre 1999) of the three-dimensional steep bull's eye waves. Snapshots of the wave-field are shown in figures 2a and 2b from which it is seen that the reconstructed wave-field contains all key features of the bull's eye waves in experiments. The simulation results of the wave elevations at two positions near the convergence center of the bull's eye wave-field are compared to the experimental data in figures 2c and 2d. Excellent agreement between the HOS simulations and experimental measurements is again obtained.

5 Reference

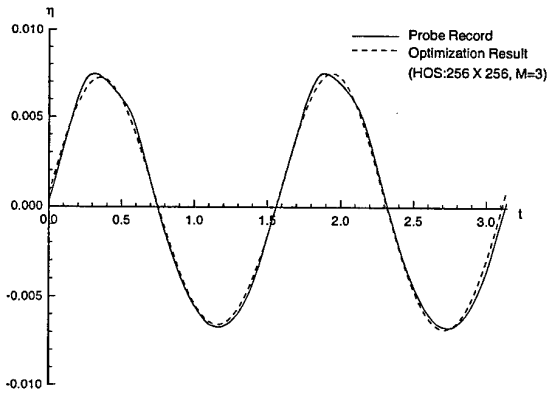
- BAZARAA, M.S., SHERALI, H.D. & SHETTY, C.M. 1993 Nonlinear programming: theory and algorithms, 2nd Edition.
- DOMMERMUTH, D.G. & YUE, D.K.P. 1987 A high-order spectral method for the study of nonlinear gravity waves. *J. of Fluid Mech.* **184**.
- LIAGRE, P.F.B. 1999 Generation and analysis of multi-directional waves, Master Thesis, Texas A&M University.
- STÄNSBERG, C.T., HUSE, E., KROKSTAD, J.R. & LEHN, E. 1995 Experimental study of nonlinear loads on vertical cylinders in steep random waves. *Proc. 5th ISOPE Conference, the Hague, the Netherlands*.
- ZHANG, J., YANG, J., WEN J., PRISLIN I. & HONG K. 1999 Deterministic wave model for short-crested ocean waves — Part I: theory and numerical scheme. *Appl. Ocean Res.* **21**.



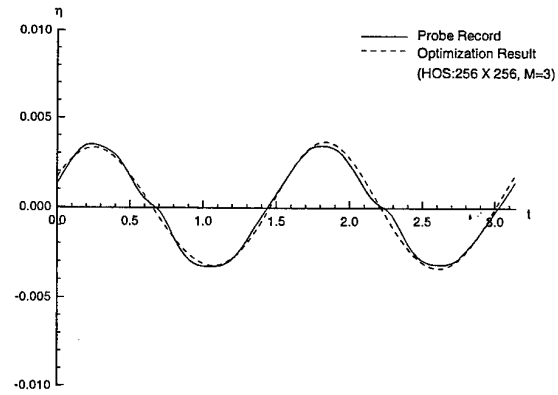
(a)



(b)



(c)



(d)

Figure 2: Comparisons of the reconstructed three-dimensional bull's eye wave-field to the wave-basin measurements (Liagre 1999): free-surface snapshots of the wave-field from the experiment (a) and the HOS simulation with $N_H=256 \times 256$ modes and $M=3$ order (b); and time history of the wave elevations at specified two positions of the wave-field, (c) and (d), from the measurements (—) and the HOS simulation (- - -).

EMBEDDED TRAPPED MODES FOR ARRAYS OF CYLINDERS

J. Zhang, M. McIver, P. McIver & C.M. Linton

Department of Mathematical Sciences, Loughborough University, Loughborough, Leics., LE11 3TU, UK

Introduction

In the problem of the scattering of water waves by a regularly-spaced, finite line of cylinders, it has been observed (see, for example, Maniar & Newman, 1997) that large hydrodynamic forces on individual cylinders occur at frequencies which are close to the trapped-mode frequencies associated with an infinitely-long line of the same spacing. For cylinders of uniform cross-section, these frequencies are determined by reducing the problem to a two-dimensional channel problem by invoking the periodicity of the trapped mode solution and removing the channel depth and time dependence from the problem. Trapped modes are thus non-trivial solutions to the Helmholtz equation in the channel region exterior to the body that satisfy homogeneous boundary conditions and have finite energy. For a fairly general class of cylinders symmetrically placed on the centre-line of the channel, Evans, Levitin & Vassiliev (1994) proved that trapped modes exist at frequencies below the first cut-off for antisymmetric wave propagation down the channel. The solutions are antisymmetric about the centre line of the channel.

More recently Evans & Porter (1998) have provided numerical evidence for the existence of an antisymmetric mode trapped by a circular cylinder on the centre line of the channel, for which the frequency is *above* the lowest cut-off frequency for antisymmetric motion. In other words this mode is embedded in the continuous spectrum. This mode occurs only for a cylinder of one specific radius; this is in contrast to the modes at frequencies below the cut-off which occur for cylinders of any radius. The purpose of this work is to show that this mode is not isolated but is one of a continuous branch of modes which exist for ellipses of continuously varying aspect ratio. A similar branches has also been found for modes supported by rectangular blocks and it is anticipated that such branches exist for a wide class of bodies which are described by two geometric parameters. For the ellipses, the branch of modes begins with a flat plate of specific length aligned along the channel, and ends with a flat plate of a different specific length which is perpendicular to the channel walls. Approximations may be found for the length of the plate aligned with the walls and the trapped mode frequency associated with it. The trapped-mode frequency tends to the second cut-off for antisymmetric motion when the body approaches a perpendicular plate, and an exact asymptotic result for the length of this plate is presented.

Formulation

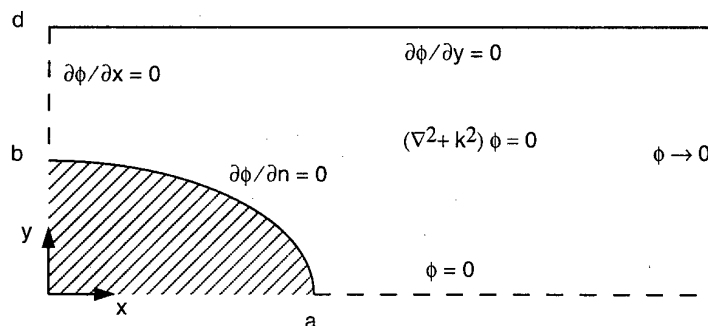


Figure 1: Definition sketch.

A quarter section of the channel and body is illustrated in figure 1 together with the details of the boundary-value problem. The wavenumber k , which is to be found, is directly related to the fluid oscillation frequency. Trapped modes are sought which are symmetric in x , antisymmetric in y , and which have frequencies between the first and second cut-off for antisymmetric wave propagation so that $\pi/2 < kd < 3\pi/2$. Thus the trapped mode potential ϕ satisfies the Helmholtz equation and has zero normal derivative on the quarter body, the channel wall $y = d$ and the line of symmetry $x = 0$. In addition $\phi = 0$ on the centre line of the channel $y = 0$ and $\phi \rightarrow 0$ as $x \rightarrow \infty$.

The method of solution is as follows. A complex, homogeneous integral equation is derived for the trapped mode potential ϕ . This is split into real and imaginary parts and the resulting equations are discretised numerically. A non-zero solution for ϕ which decays at infinity is possible if the determinant of the real matrix is zero and if the eigenvector of this matrix which corresponds to the zero eigenvalue satisfies the imaginary part of the equation. The latter is regarded as a side condition which ϕ must satisfy.

The Green's function for the channel which satisfies the same boundary conditions as ϕ on $y = 0$, $y = d$ and $x = 0$ can be written

$$G = \frac{1}{4}[Y_0(kr) + Y_0(kr_1) + Y_0(kr_2) + Y_0(kr_3)] + \frac{2}{\pi} \operatorname{Re} \int_0^\infty \frac{e^{-k\gamma d} \cosh k\gamma(d-y)}{\gamma \cosh k\gamma d} \cos kxt \cos k\xi t dt$$

$$- \frac{2i}{kd} \sum_{n=1}^{j_a} \frac{1}{\tau} \sin\left(n - \frac{1}{2}\right) \frac{\pi y}{d} \sin\left(n - \frac{1}{2}\right) \frac{\pi \eta}{d} \cos kx\tau_n \cos k\xi\tau_n, \quad (1)$$

where

$$r = [(x - \xi)^2 + (y - \eta)^2]^{1/2}, \quad r_1 = [(x - \xi)^2 + (y + \eta - 2d)^2]^{1/2}, \quad (2)$$

$$r_2 = [(x + \xi)^2 + (y - \eta)^2]^{1/2}, \quad r_3 = [(x + \xi)^2 + (y + \eta - 2d)^2]^{1/2}, \quad (3)$$

$$\gamma(t) = \begin{cases} -i(1 - t^2)^{1/2}, & t \leq 1, \\ (t^2 - 1)^{1/2}, & t > 1, \end{cases} \quad (4)$$

$$\tau_n = [1 - ((n - 1/2)\pi/kd)^2]^{1/2} \quad (5)$$

and

$$(j_a - 1/2)\pi < kd < (j_a + 1/2)\pi. \quad (6)$$

If the frequency is below the first cut-off for antisymmetric modes, that is $kd < \pi/2$, then from (6) $j_a = 0$ and from (1) the Green's function is purely real and decays as $|x| \rightarrow \infty$. This allows a real integral equation to be developed to search for trapped modes in this region. However, if $\pi/2 < kd < 3\pi/2$ then $j_a = 1$ and the Green's function is complex and radiates waves to infinity. In particular

$$\operatorname{Im}[G] = -\frac{2}{kd\tau_1} \sin \frac{\pi y}{2d} \sin \frac{\pi \eta}{2d} \cos k\xi\tau_1 \cos kx\tau_1. \quad (7)$$

Application of Green's theorem to ϕ and G yields

$$\frac{1}{2}\phi(x, y) = \int_{\partial D} \phi(\xi, \eta) \frac{\partial G}{\partial n}(x, y; \xi, \eta) dS, \quad (8)$$

where ∂D is the boundary of the body in the region $x \geq 0$, $y \geq 0$, (x, y) is a point on the cylinder surface, and $\partial G/\partial n$ is the inward normal derivative of G to the body with respect to the variables (ξ, η) . Without loss of generality the function ϕ is assumed to be real and so (8) reduces to the two equations

$$\frac{1}{2}\phi(x, y) = \int_{\partial D} \phi(\xi, \eta) \frac{\partial}{\partial n} [\operatorname{Re}[G(x, y; \xi, \eta)]] dS, \quad (9)$$

and

$$\int_{\partial D} \phi(\xi, \eta) \frac{\partial}{\partial n} [\text{Im}[G(x, y; \xi, \eta)]] dS_q = 0. \quad (10)$$

The integral in (9) is discretised and using collocation a matrix system in the form

$$\sum_{j=1}^n M_{ij} \phi_j = 0, \quad (11)$$

is obtained, where $\phi_j = \phi(\xi_j, \eta_j)$ and (ξ_j, η_j) , $j = 1, \dots, n$, are the collocation points. From (7) the imaginary part of the equation may be discretised to give the side condition

$$S = \sum_{j=1}^n \phi_j \frac{\partial}{\partial n} \left[\sin \frac{\pi \eta}{2d} \cos k\xi \tau_1 \right]_{(\eta, \xi)=(\eta_j, \xi_j)} dS_j = 0. \quad (12)$$

The system of equations in (11) has a non-zero solution for ϕ when $\det(M) = 0$. However this solution only corresponds to a trapped mode if the resulting function ϕ satisfies the side condition (12). Suppose the body is an ellipse with semi-major axis a and semi-minor axis b . For a fixed value of b/a the curve on which $\det(M) = 0$ is plotted in the a/d - kd plane. Rather than look for points on this line on which $S = 0$, the method of Evans & Porter (1998) is followed. At points at which $\det(M) \neq 0$, M has at least one eigenvalue of smallest magnitude, λ say, with corresponding normalised eigenvector ψ . If λ is real then ψ may be taken to be real whereas if λ is complex then ψ must be complex. Nonetheless the curve

$$\tilde{S} = \text{Re} \sum_{j=1}^n \psi_j \frac{\partial}{\partial n} \left[\sin \frac{\pi \eta_j}{2d} \cos k\xi_j \tau_1 \right]_{(\eta, \xi)=(\eta_j, \xi_j)} dS_j = 0 \quad (13)$$

may be drawn in the a/d - kd plane. At the point where the curve $\tilde{S} = 0$ crosses the curve $\det(M) = 0$, $\lambda = 0$ and so $\psi = \phi$ and $S = \tilde{S} = 0$ and the point corresponds to a trapped mode. Numerically this is a more robust method for the calculation of the trapped mode frequencies and points than looking for zeros of the complex determinant because it is found that the curves on which the real and imaginary part of the determinant are zero touch rather than cross in the a/d - kd plane.

Results and discussion

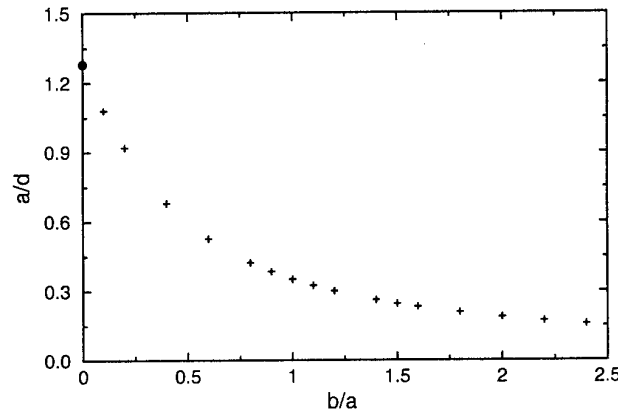


Figure 2: Ellipse geometries that are able to support trapped modes.

Results for embedded trapped modes with $kd \in (\pi/2, 3\pi/2)$ found using the method described in the previous section are shown in figures 2 and 3. These calculations are for ellipses with axis lengths $2a$ in the x direction and $2b$ in the y direction. It is already known (see Evans & Porter, 1998) that an embedded trapped mode exists for the special case of a circle with radius

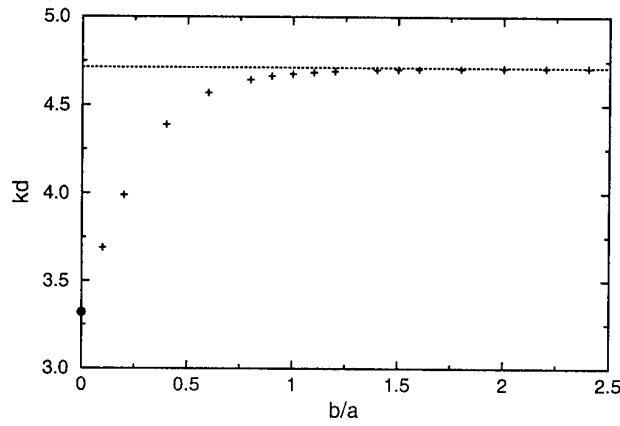


Figure 3: Wave numbers of trapped modes supported by ellipses.

$a/d = b/d \approx 0.352$; the corresponding frequency is given by $kd \approx 1.489\pi$. Figure 2 indicates that the trapped mode for this circle is one of a branch of trapped modes for ellipses with $b/a \in [0, \infty)$. The corresponding trapped-mode wave numbers kd are shown in figure 3. The cut-off at $kd = 3\pi/2$ is indicated by the dashed line and it can be seen that this cut-off is approached as $b/a \rightarrow \infty$.

The limiting case $b/a \rightarrow 0$ corresponds to a thin plate of a specific length aligned with the channel walls. The trapped mode for this problem has been computed by an approximate procedure based on the assumption that the plate is long and it is found that $a/d \approx 1.28$ and $kd \approx 1.06\pi$; these points are marked on the figures by filled circles. The limiting case $b/a \rightarrow \infty$ corresponds to a thin plate perpendicular to the channel walls. An asymptotic analysis may be performed for this case and it is found that the limiting value of b/d is a root of

$$J_1(2\pi b/d) = J_1(\pi b/d). \quad (14)$$

There is only one root for $b/d \in (0, 1)$ with the value $b/d \equiv B \approx 0.392$. The asymptotic analysis also yields the result

$$kd = \frac{3\pi}{2} - \frac{3\pi^3 a^2}{16d^2} [J_1(3\pi B)]^2 + O(a^4/d^4) \quad \text{as } a/d \rightarrow 0 \quad (15)$$

giving the approach to the cut-off illustrated in figure 3.

Further calculations, not shown here, indicate the existence of further branches of embedded trapped modes for elliptical structures that emanate from additional trapped-mode solutions for a flat plate aligned with the channel walls. All of these branches terminate at $kd = 3\pi/2$ for some finite $b/a < 1$. Calculations for a rectangular block are also in progress.

Acknowledgements

The work of the first author is supported by EPSRC grant GR/M30937

References

- EVANS, D. V., LEVITIN, M. & VASSILIEV, D. 1994. Existence theorems for trapped modes. *J. Fluid Mechanics* **261**, 21–31.
- MANIAR, H. D. & NEWMAN, J. N. 1997. Wave diffraction by a long array of cylinders. *J. Fluid Mechanics* **339**, 309–330.
- EVANS, D. V. & PORTER, R. 1998. Trapped modes embedded in the continuous spectrum. *Quarterly J. Mechanics Applied Mathematics* **52**, 263–274.